2019

# High-temperature lubrication mechanism of alkaline borates

Bach Tran
*University of Wollongong*

# High-temperature lubrication mechanism of alkaline borates

A thesis submitted for the conferral of the degree of

**Doctor of Philosophy**

from

**UNIVERSITY OF WOLLONGONG**

by

**BACH TRAN**

B. Eng

School of Mechanical, Materials, Mechatronic and Biomedical Engineering

Faculty of Engineering and Information Sciences

# DECLARATION

I, Bach Tran, declare that this thesis submitted in fulfilment of the requirements for the conferral of Doctor of Philosophy, from the University of Wollongong, is wholly my own work unless otherwise referenced or acknowledged. This document has not been submitted for qualifications at any other academic institutions.

Bach Hoang Tran,
Wollongong, August 2019

# ACKNOWLEDGEMENTS

I am sincerely grateful to Professor Anh Kiet Tieu for giving me the opportunity to embark on my postgraduate study. His constant maintenance, guidance and advices are invaluable to me during all these years.

I owe a thank you to my co-supervisors, Dr. HongtaoZhu and Dr. Shanhong Wan for their support. I also would like to thank Dr. Buyung Kosasih and Dr. Shaogang Cui for their help in the early days of my study. I specifically appreciate the staffs within the Faculty of Engineering and Information Sciences, Mr. Steward Rodd, Mr. Andrew Scobie, Mr. Keith Maywald, Mr. Matthew Franklin, Mr. Carl Rindlisbacher and Mr. Leighton Hill for their kind assistance in sample preparation and equipment repair.

I would like to thank Dr. Mitchell Nancarrow and Dr. David Mitchel for their professional assistance on electron microscope works.

My research would have been impossible without the financial aid from the University of Wollongong.

Finally, I am eternally indebted to my family, particularly my beloved wife Mrs. Dung Tran for her care, encouragement and sharing throughout my journey.

# LIST OF PUBLICATIONS

1. **B. Tran**, A. K. Tieu, S. Wan, H. Zhu, D.R.G. Mitchell, M.J. Nancarrow, Multifunctional Bi-Layered Tribofilm Generated on Steel Contact Interfaces Under High-Temperature Melt Lubrication, **The Journal of Physical Chemistry C**, 2017.
2. **B. Tran**, K. Tieu, S. Wan, H. Zhu, L. Riu, Hot corrosion of borate melt and interface chemistry of borate-coated steel under tribological stimulation, **Corrosion Science**, 2018.
3. **B. Tran**, K. Tieu, S. Wan, H. Zhu, S. Cui, L. Wang, Understanding the tribological impact of alkaline element in lubrication performance of binary borate melt, **RSC Advances**, 2018.
4. **B. Tran**, K. Tieu, S. Wan, H. Zhu, Lubricant as a sticking-scale inhibitor on high temperature sliding contact, **Tribology International**, 2019.
5. S. Wan, **B. Tran**, A. K. Tieu, Y. Xia, H. Zhu, S. Cui, Q. Zhu, The Influence of Water Addition on High-Temperature Tribological Properties of Interstitial Free Sliding against Different Counterparts, **Tribology Transactions**, 2018.
6. S. Wan, A. K. Tieu, Y. Xia, H. Zhu, **B. Tran**, S. Cui, An overview of inorganic polymer as potential lubricant additive for high temperature tribology, **Tribology International**, 2016.
7. S. Wan, A. K. Tieu, Y. Xia, L. Wang, D. Li, G. Zhang, H. Zhu, **B. Tran**, D.R.G. Mitchell, Tribochemistry of adaptive integrated interfaces at boundary lubricated contacts, **Scientific Reports**, 2017.

8. C. Sun, Q. Xue, J. Zhang, S. Wan, A.K. Tieu, **B. Tran**, Growth behavior and mechanical properties of Cr-V composite surface layer on AISI D3 steel by thermal reactive deposition, **Vacuum**, 2017.
9. S. Cui, H. Zhu, S. Wan, K. Tieu, **B. Tran**, L. Wang, Q. Zhu, Effect of loading on the friction and interface microstructure of lubricated steel tribopairs, **Tribology International**, 2017.
10. S. Cui, H. Zhu, S. Wan, **B. Tran**, L. Wang, K. Tieu, Investigation of different inorganic chemical compounds as hot metal forming lubricant by pin-on-disc and hot rolling, **Tribology International**, 2018.
11. S. Wan, H. Wang, Y. Xia, A.K. Tieu, **B. H. Tran**, H. Zhu, G. Zhang, Q. Zhu, Investigating the corrosion-fatigue wear on GrN coated piston rings from laboratory wear tests and field trial studies, **Wear**, 2019.

# ABSTRACT

Like any other metalworking processes, lubrication plays a crucial role in hot metal forming (e.g. hot rolling). An effective lubrication ensures high energy efficiency, low material loss and optimal product quality. The current study investigates potential lubrication properties of alkaline borates at elevated temperature by extensive experimental work. Advanced microscopy analysis allows insights into working mechanics of the lubricants at different scales which help addressing some fundamental questions arise from the past literatures.

Tribological behaviors of sodium borate were thoroughly studied by pin-on-disc testing. With a transition point around 525$^{o}$C, the material exhibits exceptional lubrication performance over the range of 600$^{o}$C-800$^{o}$C on sliding steel pair (GCr15/mild steel). This is demonstrated by remarkable reduction in friction coefficient and wear loss volume on both contact surfaces lubricated by sodium borate compared to the unlubricated case. For instance, under borate lubrication at 800$^{o}$C, the friction coefficient drops by 58% while the wear loss is reduced by 95% and 80% on the disc and the ball, respectively. Detailed analysis revealed tribofilm formation on both contact surfaces. On the ball, a chemically-complex film (~20nm thick) is observed lying on top of ultra-fined grains of iron oxides. Electron Energy Loss Spectroscopy (EELS) indicates a conversion between $BO_4$ to $BO_3$ species in the boundary film which could be triggered by the shearing stress. On the lubricated mild-steel disc, the tribofilm has a dual-layered structure with a total thickness of 50nm: an upper layer rich in Boron (B) and the lower layer rich in Sodium (Na). The Na layer is accountable for good adherence to the oxide surface while the upper film provides

a load-supporting capacity through a self-polymerization mechanism. A static oxidation testing between the borate melt and oxide scale discloses the thermally-activated nature of Na adsorption on the iron oxide interface aided by the ionic characteristics of sodium borate melt at high temperature. The borate tribofilm generated on the disc is significantly depleted in Oxygen that in turn provides a considerable oxidation resistance. This is reflected by reduced thickness of the oxide scale lubricated by sodium borate, the reduction rate is approximately 50% compared to a freely-oxidized surface. Regarding microscopy strategy, High Angle Annular Dark Field (HAADF) imaging technique has shown to be a useful tool to observe B-containing tribofilm.

The roles of Sodium in lubricating mechanics of borate lubricant were revealed by comparing lubrication behavior between two systems: sole $B_2O_3$ and binary oxides $Na_2O$-$B_2O_3$ on sliding steel pairs at 800ºC. The binary system outperforms the singular system in terms of friction and wear loss reduction, which explicitly underlines the critical presence of Na. Further analysis shows that the adsorption of Na on both contact surfaces is regarded as the foundation for the exceptional lubrication performance of sodium borate. While the addition of Na results in the ionic characteristic, $B_2O_3$ provides the polymeric nature which determines the viscous fluid behavior of the lubricant melt on the heated sliding surfaces. A clear correlation between the oxide microstructure and adsorption behavior of Na is established as the Na layer is thicker on oxide scale grown from a highly-alloyed steel substrate. In addition, the role of oxide scale as a supporting medium for lubricant is also emphasized.

Sodium borate demonstrates an ability to eliminate adhesive wear/oxide transfer on sliding High Speed Steel tool surface. This is reflected by reduced thickness of the oxide scale compared to unlubricated case (~88% after 5mins and 80% after 15mins sliding test). The formation of borate tribofilm provides a consistent lubrication, effectively separates asperities contacts and suppresses the sticking tendency of adhesive wear. Prolonged exposure to borate lubrication however alters the oxidation sequence and results in Hematite-to-Magnetite transformation of the underlying oxide scale. Under borate lubrication, the resistance against oxide transfer is also evident in steel rolling contact. Although the passivated rolling module is not able to fully represent actual hot rolling, the contact pressure is set close to real process parameter (>500MPa) and the interactions between sodium borate melt and iron oxides are determined in details. After rolling in the presence of sodium borate melt, the oxide scale experiences a phase transformation as Magnetite becomes the most dominating type while Hematite is prevalent in unlubricated case. This transformation is suggested to facilitate the subsequent pickling process.

A potassium borate was synthesized and evaluated on pin-on-disc testing at maximum temperature of 900$^{o}$C. It displays a superior performance compared to sodium borate at 900$^{o}$C regarding friction and wear loss reduction. The lubrication failure of sodium borate at 900$^{o}$C is mainly due to its low viscosity. Despite the difference in activity between two elements, the working mechanism of potassium borate appears similar to sodium borate.

# LIST OF FIGURES

# LIST OF TABLES

# LIST OF CONTENTS

# CHAPTER 1:

# Introduction

Hot metal forming accounts for the majority of production processes in steel manufacturing. These processes can benefit extensively from a fundamental understanding of the high-temperature tribology which can result in potential process improvements. From a microscopic perspective, the arduous working conditions result in complex functional layers at the interface that remain challenging to be fully resolved. In hot rolling of steel, the reheated steel sheet (body temperature of 850$^{o}$C-1100$^{o}$C) is rolled under heavy loading (<0.8GPa) and high rolling velocity (2-12m/s). The workroll experiences cyclic thermal condition (maximum temperature of 650$^{o}$C) induced by heat transfer and cooling water. Besides classic concerns on friction and wear, surface oxidation, elemental diffusion and interface reactions between contacting bodies (e.g. surfaces, lubricants, atmosphere…) play undeniable roles in the tribological behaviors and therefore should deserve respective considerations.

The use of lubrication to lower friction and minimize material wear losses has been recognized from the early stage of metallurgical age due to its great benefits. In hot metal forming processes, an appropriate lubricant can improve energy efficiency, secure finishing surface quality, and prolong work roll/die lifetime. Although only a number of lubricants can fulfill those criteria due to thermal constraint [1-4], it is still worth exploring the potential candidates and their working mechanism.

This dissertation focuses on the tribological characteristics of a family of inorganic alkaline borates at elevated temperatures, pressure and shear. Friction and wear behaviors of the alkaline borates are thoroughly studied on both sliding and rolling contacts of steel counterparts. In addition, the anti-oxidation capacity of lubricant is also among central subjects. The current work has a strong emphasis on the interface chemistry between the lubricant and oxidized steel since these interactions predominantly govern the lubricant macro-behaviors. Thermally-activated reactions, tribochemical reactions and the effects of oxide microstructures are revealed in details and elaborated regarding their effects on friction, wear and anti-oxidation characteristics. Furthermore, the fundamental roles of each constituent element in the lubricant composition are also explored.

The dissertation starts with investigations on sodium borate, then a synthesized potassium borate is also evaluated at a different temperature range. The outcome in this work is originally applied for hot rolling of steel, but one could find it relevant for other metal forming processes such as hot forging, wire drawing, hot extrusion and seamless pipe manufacturing

# CHAPTER 2:

# Literature review

## 2.1 High temperature tribology

The term “high-temperature tribology” refers to science of interacting surfaces in relative motion at elevated temperature. This temperature is generally assigned to the body temperature of the tribo-component and it varies from one process to another. Such nature of contact can often be found in most hot metal forming processes such as metal sheet rolling, forging, stamping, drawing…Apart from conventional friction and wear aspects, the use of heat results in drastic changes in the bulk properties of the contact materials which in turn affect considerably their tribological behaviors. Microstructural evolution, thermal softening and thermal fatigue are among the critical factors on friction/wear characteristics. In addition, oxidation, heat transfer and elemental diffusion also deserve consideration as their roles on the contact surfaces should not be taken lightly. Figure 2-1 illustrates the complex events that occur during a typical sliding contact at high temperature [5], although one can expect a similarity on rolling contact.

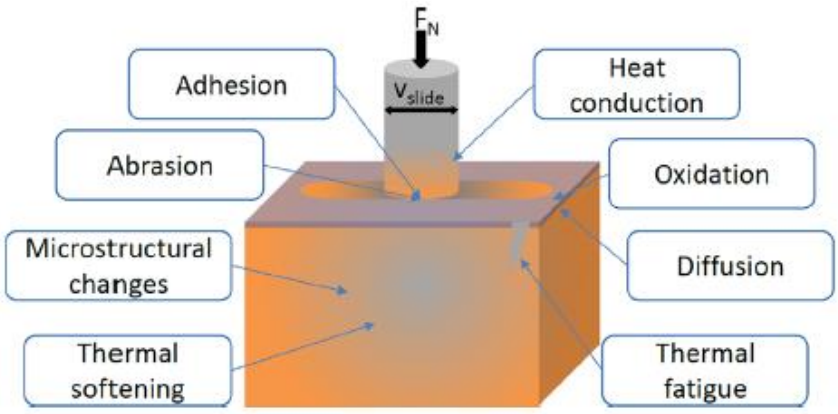


**Figure 2-1:** Involved phenomena during tribological process at high temperature [5]

Although there has been a volume of work dedicated to tribological behaviors of solid lubricants at high temperature (300$^{o}$C-1000$^{o}$C) [1, 3, 4, 6], basic research on the actual lubrication mechanism remains quite limited at this extreme condition. In the presence of lubricant, the tribosystem becomes even more complicated when it has to take into account interface reactions between lubricant elements and sliding surfaces, atomic diffusion within the lubricant and cross-phase diffusion… Because of significant benefits of lubrication, there are always pressing needs to gain further understanding on this particular subject. As the current work revolves around steel processing, past literature on tribological behaviors of the material at high temperature will be summarized.

## 2.2 The roles of oxidation on the contact surface

Oxidation can be regarded as the most influential factor on the contact surfaces since an oxidized surface has totally different mechanical/chemical properties in comparison to a pristine surface. At elevated temperature, steel experiences oxidation under open atmosphere which is manifested by a growing and protective oxide scale on the steel surface. The microstructure and chemical composition of grown oxide scale varies with temperature, exposure time and reactivity of oxidizing atmosphere [7]. Oxidation of low alloy steels has been thoroughly studied in the past [7-10] and a simplified oxidation mechanism under Oxygen atmosphere was proposed in Figure 2-2 [11]. The formation of iron oxide is a result of complex events including the outward diffusion of Fe ions/electron holes, adsorption and diffusion of O molecules and reaction between the reagents. The structural hierarchy stems from complex redox reactions between migrating ions/molecules and the existing oxides layer. In the end, the oxide scale layer generally consists of an

innermost layer of FeO, a middle layer of $Fe_3O_4$ and an outermost layer of $Fe_2O_3$. The layered structure of oxide scale has been widely reported during the hot rolling of steel [12, 13]. Since the oxide scale on the surface is exposed to the contact, their microstructure and mechanical attributes are expected to play a significant role in the tribological behaviors.

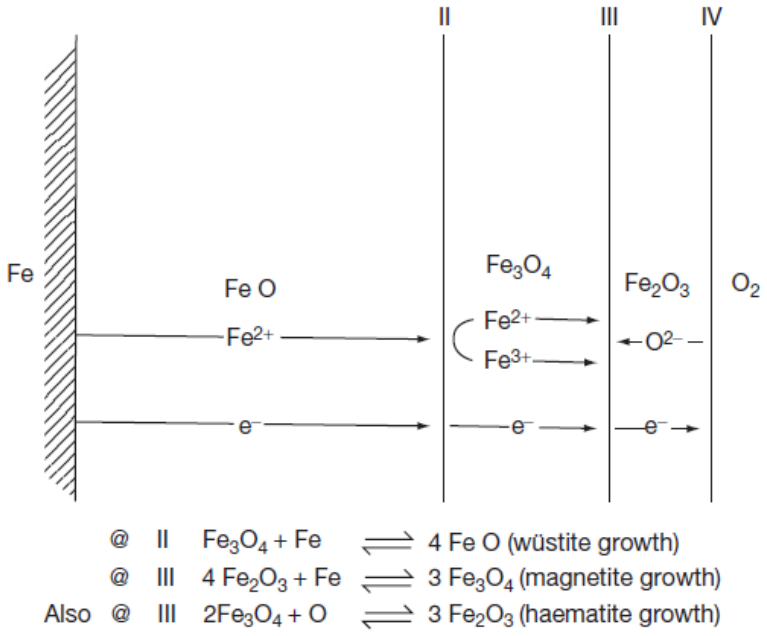


**Figure 2-2:** Oxidation mechanism of pure iron above 570°C [11]

B. Picque et. al. conducted both experimental and numerical studies to determine the mechanical behavior of iron oxide scale at high temperatures [14]. Using a Four-Point Hot Bending Tests, they revealed a close relationship between the hardness ratio of oxide scale/steel base and temperature (Figure 2-3). It is noted that Ex-LC refers to the low-carbon steel specimen and the subsequent number refers to the strain rate. Embrittlement of oxide was found at high strain rate which is normally seen in hot strip rolling. Furthermore, the oxide scale becomes ductile above the critical temperature of 700°C although it is still strain rate-dependent. They also claimed that above this particular point, oxide scale can

demonstrate a high lubricity. Similarly, H. Echsler revealed a concrete dependence of oxide flow stress on temperature and strain rate at 800$^{o}$C-1000$^{o}$C on mild steel [15]. The decreasing flow stress could mean less frictional resistance of the oxide scale under shearing at higher temperature. After conducting a large number of hot rolling experiments, Utsunomiya et al. on the other hand assigned 850$^{o}$C as the transition point between brittle-ductile characteristics of the oxide scale [16]. By comparing different studies, Krzyzanowski et al. [17] detailed plastic behavior variation of the oxide scale with rolling temperature and reduction, as shown in Figure 2-4. It is conclusive that the mechanical properties of oxide scale changes significant with temperature and process parameters (rolling speed, reduction rate…).

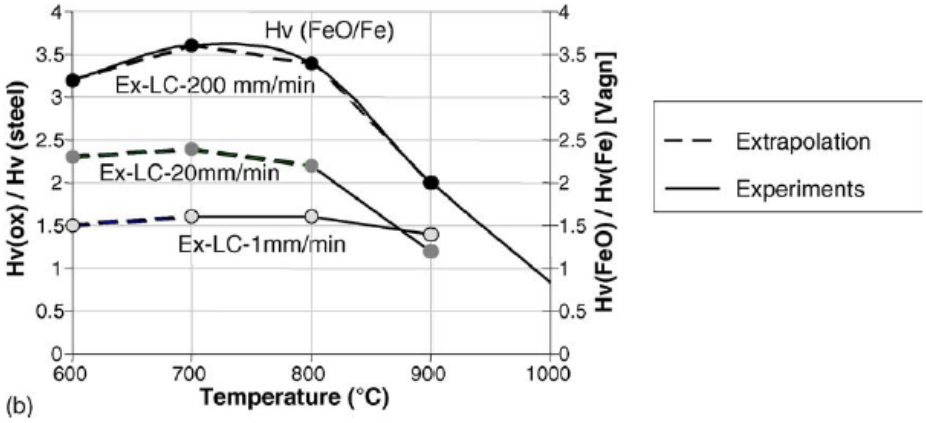


**Figure 2-3:** Hardness ratio between oxide scale and steel substrate as a function of temperature and strain rate by 4 point bending test [14]

Scale thickness also affects friction/wear behaviors in a certain manner. Luong et al. found that thicker oxide scale induces lower friction coefficient in a simulated forging test [18], although they also observed scale pick-up on the die surface which is perceived detrimental. Likewise, a thicker oxide scale reportedly led to a lower friction coefficient in the hot rolling steel [19]. However, Utsunomiya claimed that a thin and uniform oxide

scale (critical thickness is a function of temperature) is preferred since it created a defect-free rolled surface [16], although there was no statement regarding frictional behaviors. During the hot rolling of steel, the same author observed an increase in relative sliding when the oxide scale thickens which subsequently results in ductile-to-brittle transition of the oxide scale at 1000$^{o}$C-1100$^{o}$C [20]. As FeO generally takes up the largest proportion in the oxide scale (FeO thickness is 90-95% of total oxide thickness at 800-1000$^{o}$C [8, 10]), it has received much attention regarding its intrinsic lubricity. A number of researcher indicated that the hot ductility of FeO has a major contribution to the global brittle-to-ductile transition of the oxide scale which leads to a defect-free rolled surface [16, 21]. However, others found negligible influence of FeO in the friction behavior [18]. In short, findings about the tribological response of each individual iron oxide type remain divergent.

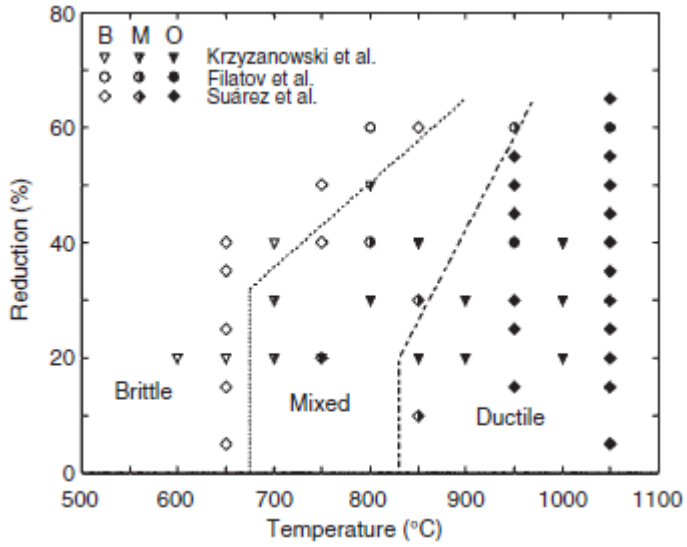


**Figure 2-4:** Plastic behavior of oxide scale as a function of temperature and reduction in hot rolling [17]

Frictional behaviors of oxide scale were investigated in numerous laboratory tribology tests. Interrupted testing in combination with monitoring friction coefficient curve can provide indications about the roles of oxide scale. By using a pin-on-disc configuration, Vergne et al. found a firm correlation between the sliding friction coefficient and the formation of the oxide transfer layer on the pin surface [22, 23]. A typical friction coefficient curve between cast iron pin and AISI 1018 disc at 950°C is given in Figure 2-5. During the running-in period, there are three stages with distinct frictional behavior. The friction drop in the 2nd stage arises from the attrition act of the outgrown oxide scale while the adhesion and wear particles aggregation is believed to trigger the subsequent jump in friction (Stage 3). Zhu et al. revealed a similar pattern by testing mild-carbon steel disc against a High Speed Steel pin [24]. However, they claimed that the spallation of transferred oxide layer on the pin produces a growing friction after the initial drop.

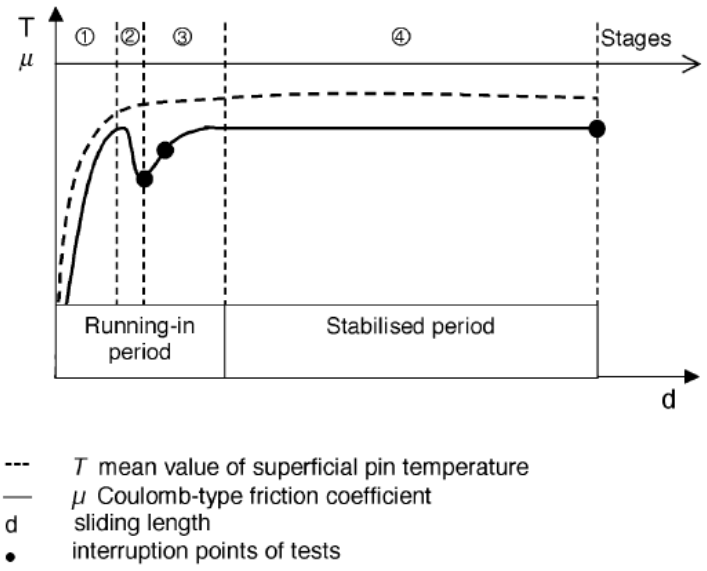


**Figure 2-5:** Friction coefficient evolution of steel pair at 950°C by pin-on-disc testing [22]

There are other microstructural factors that can exert certain impact on the friction and wear behaviors of oxidized steel surface. H. Kato explored critical roles of particles

dimension on the wear rate on sliding pair of carbon steel (~0.45% wt. of C). A clear transition from severe to mild wear regime is observed when the contact is supplied with $Fe/Fe_2O_3$ particles with a diameter less than 0.5µm [25]. On the contact surface, the formation of a protective oxide scale is considered as the origin for such favorable wear transition. It is also evident that the tribo-oxide layer could also lose its efficiency at higher load [26]. Although the above studies were conducted at room temperature, their implications can be translated for a high-temperature contact since the oxide scale grows in different grain size depending on temperature, steel grade and oxidizing atmosphere [7]. Alloying elements indirectly affects the tribological behaviors of parent steel by their participation in the oxidation reaction. In brief, those active elements (Al, Si, Cr…) preferably react with oxygen to form an interlayer on scale/base metal interface [7, 11]. This highly-adherent layer improves significantly the scale adhesion with the base metal which reduces the detachment tendency of the oxide scale upon contact. Figure 2-6 illustrates the growth of layered oxide on steel with inclusion of active elements.

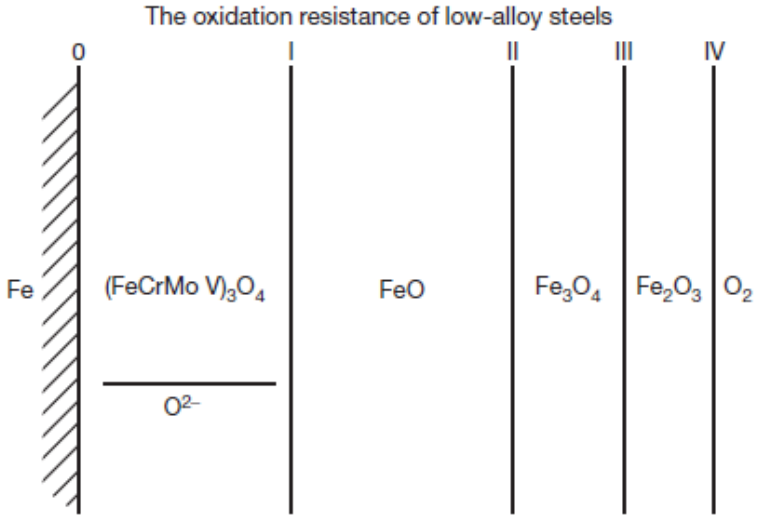


**Figure 2-6:** Schematic of diffusion-controlled growth of multi-layered scales on alloyed steel at high temperature [11]

In lubrication research at room/moderate temperature, the surface chemistry plays a very crucial role. It determines the reactivity towards lubricant elements/additives which is regarded as the central part in the formation of the so-called tribofilm. At high temperature, this aspect is often overlooked due to the limited amount of research related to lubrication.

## 2.3 Lubrication at high-temperature processing

Lubricant is introduced to separate the contact surfaces physically and reduce friction and wear. Frictional force generated upon contact is a function of complex parameters $\eta.v/P$ in which $\eta$ is the lubricant viscosity, $v$ is the relative velocity while P is the applied pressure. A Stribeck curve is given in Figure 2-7 as a visual illustration of the relationship [27]. There are three different lubrication regimes with different frictional behavior. They can be distinguished by the difference of the curve shape (Figure 2-7), or they can be classified by the film thickness-to-composite roughness ratio, namely $\lambda$. Hydrodynamic lubrication is present when $\lambda>3$ and the friction is dominated by the bulk rheological properties of the lubricant film (some identified $\lambda\sim4$ as the upper threshold [27]). In other words, the two contact surfaces are completely separated by the lubricant film in this regime. Mixed lubrication is obtained when $1<\lambda<3$ while the bearing actions of the normal load are supported by both lubricant film and asperities contact. If $\lambda<1$, direct asperities contacts are predominant. In this case, the friction coefficient is less dependent on the bulk rheological attributes of the lubricant while the adsorbed films on the contact surfaces become much more influential.

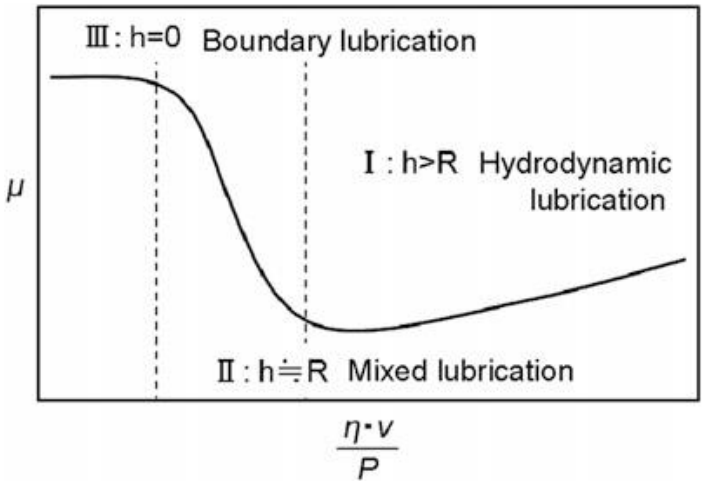


**Figure 2-7:** A typical plot of Stribeck curve [27]

The Stribeck curve was originally derived for journal bearings at room temperature [27], however it can also have some significance for high-temperature tribology. In the hot rolling of steel, there is often a combination of lubrication regimes due to the non-conformity of contact surfaces. Figure 2-8 shows a cross-section of a roll bite in which combined lubrication regimes can certainly exist [2]. The entry zone is often filled with a relatively thick lubricant (hydrodynamic lubrication) while mixed/boundary lubrication are likely found in the middle of the roll bite. As the strip temperature is very high (850-1150$^{o}$C), lubricant film experiences a certain degree of thermal decomposition/transition or boiling upon contact with the strip surface. Thermally-activated reactions, adsorption and diffusion will be accelerated under this extreme condition. Shearing actions on these particular complex layers of material become complicated and often difficult to elucidate fully.

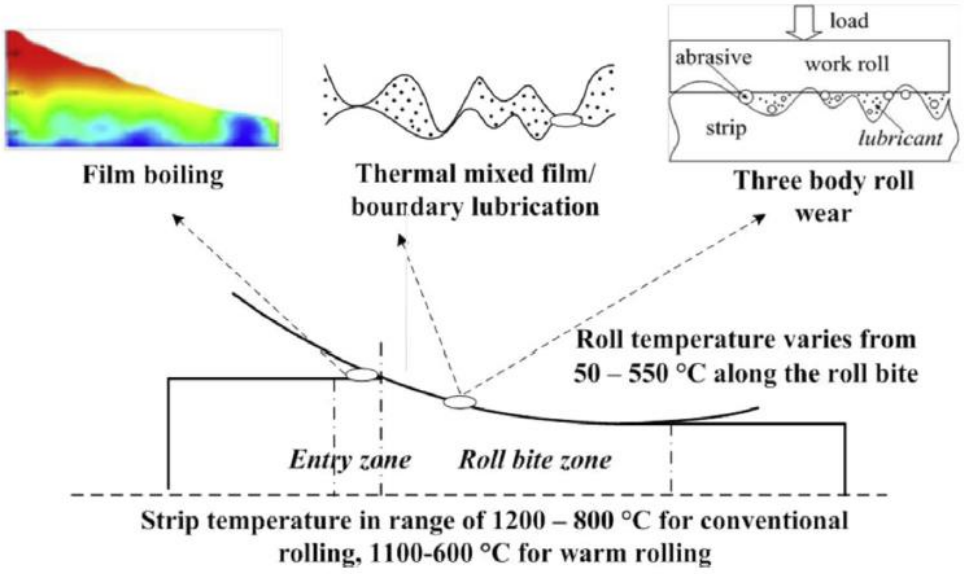


**Figure 2-8:** Coexistence of multiple lubrication regimes at the role bite during hot rolling of steel [2]

### 2.3.1 Oil-based lubricants

From 1960s, oil-based lubricants have been used worldwide in hot rolling of steel to reduce rolling load and increase work roll lifespan. Their performance has been demonstrated through a large number of research work. In general, an oil-in-water emulsion is used since it is more cost-efficiency and delivers cooling effect on the roll. By conducting hot rolling of AISI 1018 steel at 850$^{o}$C lubricated by water, neat oil and oil-in-water (1:1000) emulsion, Shirizly et al. found that the use of either neat lubricant or emulsion reduces the mill load significantly [28, 29]. At low reductions (<30%), the use of lubricant or emulsion decreased the roll force from 15% to 50%. In addition, they also revealed insulating capacity of the lubricant, although it appeared difficult to define the exact optimal oil-to-water ratio. Imae et al. surveyed the effects of emulsion concentration on the rolling load reduction in laboratory rolling test of carbon steel (with a reduction of

50% and a rolling speed of 100m/min). They found that a higher emulsion concentration leads to more reduction in the rolling force [30]. Azushima et al. carried out an in-depth study on the lubricity of a wide range of natural and synthetic oil on sliding-rolling tribo-simulator at 800$^{o}$C while effects of additives/lamellar solid materials (graphite, $MoS_2$, mica) were also investigated [31, 32]. They found an optimal concentration for most lubricants to be 1% regardless of lubricant composition, at which the rolling friction remains relatively low (~0.15). The same authors later proposed two lubrication mechanisms for the optimal oil/water ratio, one above the optimal ratio and one below it. The effects of oil additives on the lubrication performance were rarely reported in hot rolling of steel. Nevertheless, some suggested a strong dependence of lubricity on the operating temperature (up to 500$^{o}$C), as shown in Figure 2-9 [33]. Despite showing significant benefits, the thermal decomposition of oil-based lubricants at high temperature might impose some drawbacks [1, 3, 4].

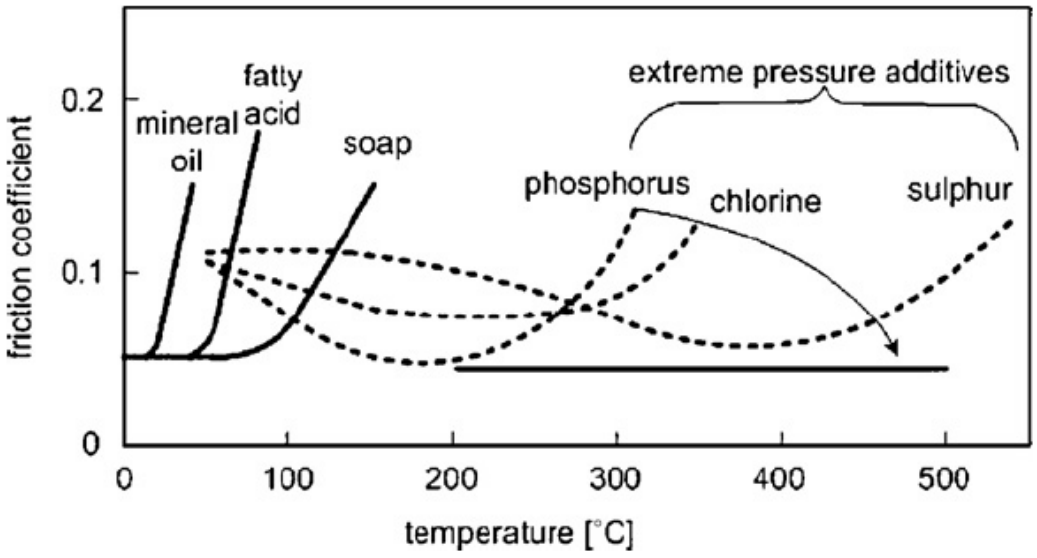


**Figure 2-9:** Working temperature range of additive elements [33]

### 2.3.2 Solid and other lubricants

Apart from dissolvable additives, solid materials have been often formulated in lubricant composition for enhanced performance. Two-dimensional materials gain wide recognition due to their superb lubricity which stems from their low shearing strength. Graphite has been considered the most popular that is stilled used in hot metal forming processes (up to 500$^{o}$C) [34, 35], although lately it becomes more restricted due to environmental concerns [33, 34]. Other candidates can have similar lubrication potential such as transition metal dichalcogenides ($WS_2$, $MoS_2$), hexagonal Boron Nitride (hBN), mica and talc [35, 36]. In general, the 2D materials are dispersed into an aqueous/water-based form to facilitate their application. A. Petrov at el. [37] used ring-compression tests to evaluate the properties of several water-based colloidal lubricants containing either graphite or $MoS_2$. They found that friction coefficient is reduced and die life is significantly increased (by 10%) in the presence of graphite-based lubricant compared to the base lubricant. G. Ngaile [38] investigated the lubrication mechanism in warm forging of aluminum by using two variants of BN-silicone lubricants. While the siloxane is believed to provide hydrostatic/hydrodynamic lubrication, BN acted as a barrier film that reduced friction at 260$^{o}$C. The lubrication mechanism drastically changes at 370$^{o}$C where the depolymerization of siloxanes lead to the formation of $SiO_2$, this eventually combined with BN provide a low shear strength layer. However, most 2D materials lose their intrinsic lubricity above 500$^{o}$C due to thermal degradation, particularly under air atmosphere. For instance, graphite is prone to burn at 450$^{o}$C while $MoS_2$ decomposes to

$MoO_3$ which has inferior lubrication properties compared to its predecessor at 500ºC [35, 39].

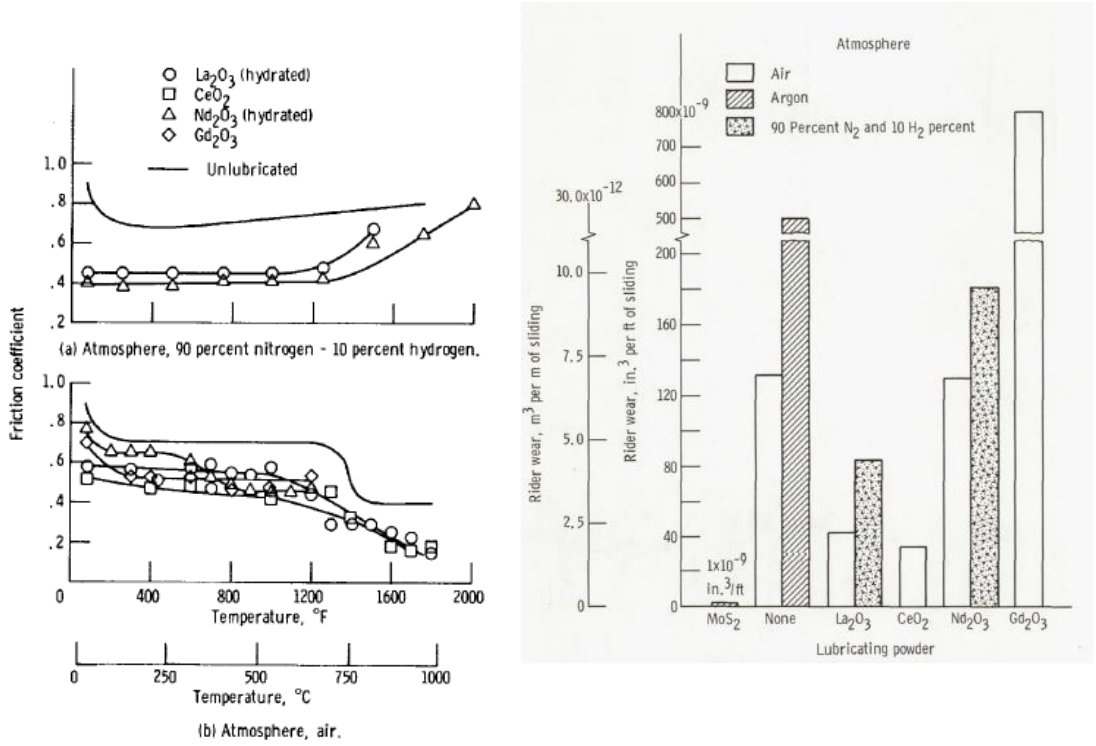


**Figure 2-10:** Friction coefficient curves and wear loss volume from sliding test on rare earth oxides-bonded surface [40]

Lubricious and easily-shearable metal oxides/fluorides are also considered a good alternative, although their applications are limited to coated surfaces [36]. Single oxides of $Re_2O_7$, PbO, $B_2O_3$, AgO are among the most widely used while binary system (a combination of two oxides) can stretch the operational range wider. Sliney [40] explored the lubricity of several rare earth oxides and fluorides in different environments up to 1000ºC. By testing an Inconel 600 pin against Inconel 750 surface at a sliding velocity of 0.03m/s and a 2kg force, most tested oxides exhibit good lubricity compared to unlubricated case, although $La_2O_3$ and $CeO_2$ were found to provide much better wear

resistance (Figure 2-10). In addition, the lubricating oxides perform much better in air atmosphere than $H_2$ atmosphere.

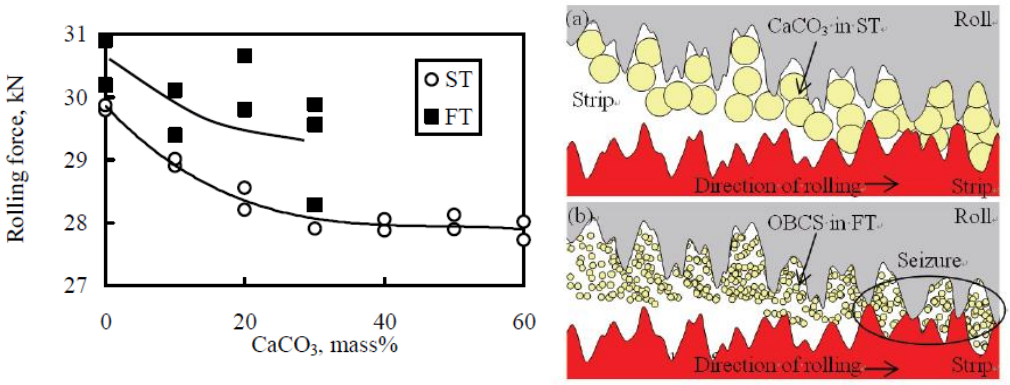


**Figure 2-11:** Rolling force/reduction rate from hot rolling of stainless steel lubricated by $CaCO_3$-added oil and the size effect on anti-seizure performance [41]

Calcium carbonate submicron-particles were reportedly studied as a lubricant additives in hot rolling oil [41]. Naoshi et al. conducted hot rolling of stainless steel (SS440 and SUS444) at 900°C-1000°C with a rolling speed of 0.24m/s, they found that increase in Calcium carbonate content results in a significant drop in the rolling force (shown in Figure 2-11). The effect of $CaCO_3$ particles size was also investigated by testing two lubricants: a semi-fluid type (ST) with a particle size of 1µm and a fluid type (FT) with a particle size of 15nm. It was found that micron-scale particles outperform nano-scale particles in term of rolling force reduction and anti-seizure performance (Figure 2-11). Likewise, $TiO_2$ nanoparticles demonstrated a good lubricity properties in laboratory hot rolling of steel, significantly reduced rolling load and produced a better surface finish [42-44]. N. Ikeda proposed a concept of using high molecular compounds and bonding agents to create an in-situ pseudo lubricant film which can provide an effective lubrication. The compound is extremely viscous when water evaporates [45]. Figure 2-12 shows the working principle of the high molecular lubricant in hot forging [34]. Likewise, Dubois et

al. [46] tested a range of "white lubricants" which basically contains water soluble high-molecular weight polymers and other additives on Warm and Hot Upsetting-Sliding tests to simulate forging contact (maximum contact pressure of 400MPa). They found that the use of "white lubricants" lead to a friction coefficient similar to graphite-based lubricant, however they lose their efficiency as sliding length increases above 10mm.

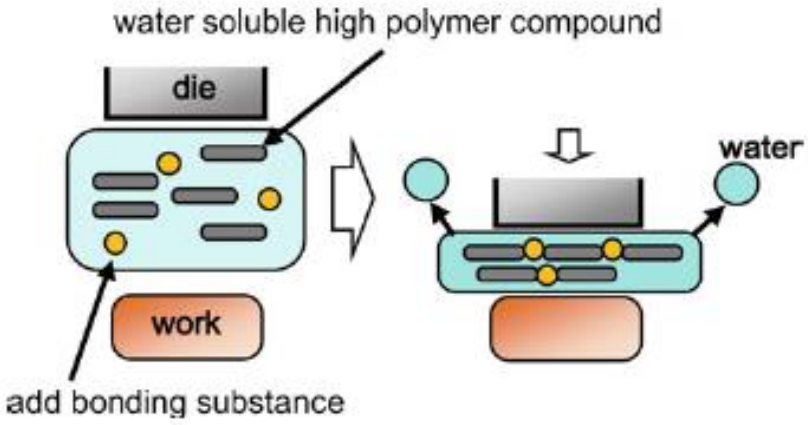


**Figure 2-12:** Proposed working mechanism of high polymer compound in hot forging [34]

## 2.4 Melt lubricant

It has been demonstrated that temperature plays a great role in determining the working range of any type of lubricant. This arises from the thermal stability of each class which closely depends on the molecular structure and reactivity with atmosphere. Figure 2-13 summarizes the working temperature range of typical lubricant classes from sub-zero degree to over 1000$^{o}$C [47]. At the extreme end, only the viscous products that can function effectively are alkali phosphates and glasses. These materials gain lubricity when they transition into viscous melt above their melting point. One of the most remarkable

features of glass-based lubricant is the ability to tune the working range by manipulating chemical composition.

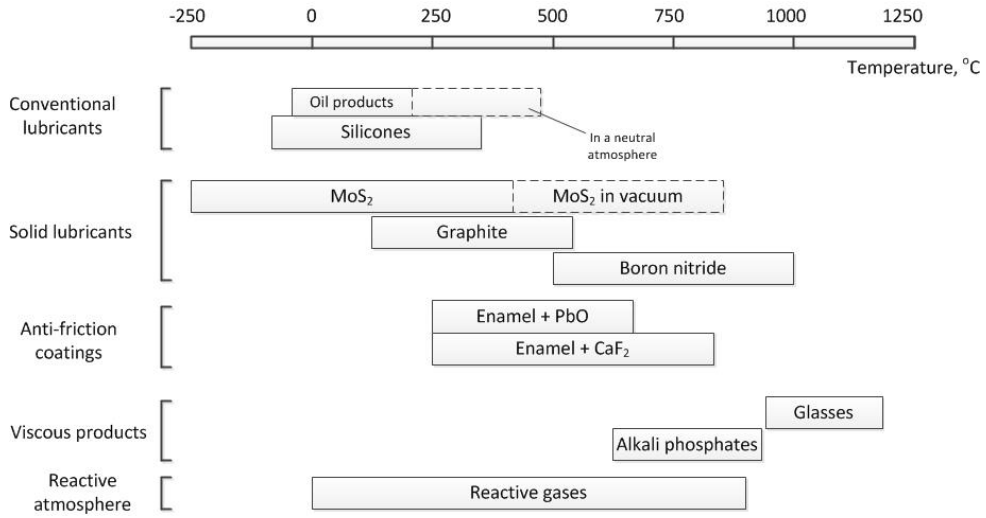


**Figure 2-13:** Working temperature range of different lubricant classes in air atmosphere [47]

In general, a typical glass lubricant is formulated by three major constituents and other minor components as shown in Figure 2-14. The major composition includes alkaline (or alkaline earth) oxides, glass-forming compounds (poly-oxides) and multi-valent metals (Fe, Zn, Mo…). In addition, minor components such as modifiers, binders or coupling agents are often found to improve the overall performance. According to Schey [47], glass-forming compounds are regarded as the building block of glass melt with $P_2O_5$, $B_2O_3$ and $SiO_2$ being the representatives. With a high molecular connectivity, they provide polymeric natures and high melting point for glasses. The inclusion of alkaline (alkaline earth) elements enables active adjustment to both the melting point and viscosity while multi-valent elements are meant to increase the cross-linking which enhances mechanical

attributes of the glass. Despite the great potentials of these lubricants, past research on melt lubrication was often empirical and lacks a systematic approach.

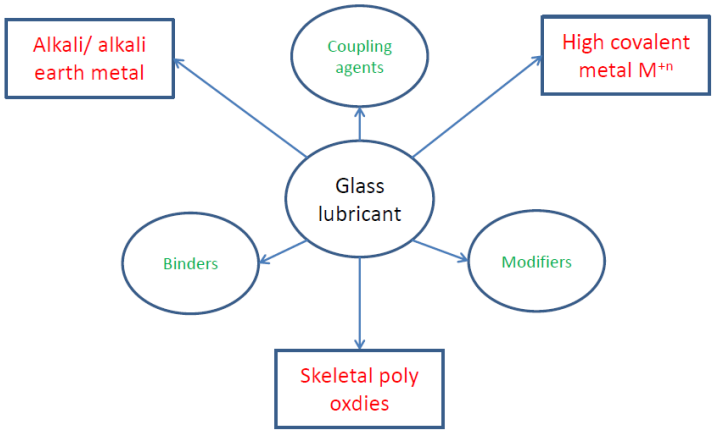


**Figure 2-14:** Typical composition of glass lubricant

### 2.4.1 Brief review

Roger investigated the lubricity of a series of glass in hot extrusion and claimed beneficial effects associated with the softening lubricants [48]. Kaplakjian summarized widely accepted glasses of silicate and borate family with varying composition and corresponding extrusion temperature [49]. By studying the effects of a series of soda lime and borosilicate glass on the hot extrusion of stainless steel at 1000-1200$^{o}$C, Gupta found that only a subtle change in the glass composition can affect its flowability despite having the same melting point [50]. Kovalev [51, 52] proposed a variety of glass composition (predominantly sodium silicate) which can deliver an effective lubrication and desired oxidation resistance in hot forging and stamping while some of them can be applied by means of water-suspension. A complex glass (including borax, binder and other additives) was reportedly used in plastic forging of Ti-alloy at 1050$^{o}$C and demonstrates remarkable protective effects [53]. Li et al. [54] revealed a firm dependence of friction coefficient on temperature and strain rate by means of ring compression test lubricated by a glass with a

softening point of 740°C. They found that the friction coefficient reduces with temperature while it remains insensitive to strain rate at temperature below 950°C. During the hot extrusion of a stainless steel tube, glass lubrication is found to be in hydrodynamic condition which is manifested by a close relationship between the friction coefficient and the melt viscosity [55].

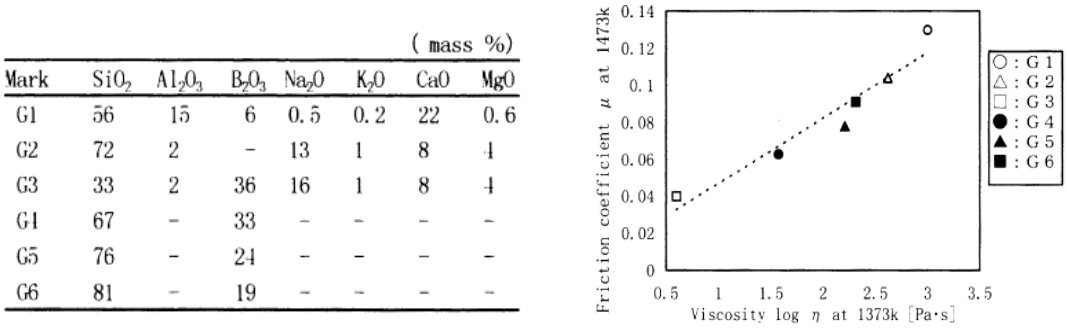

( mass %)

| Mark | $SiO_2$ | $Al_2O_3$ | $B_2O_3$ | $Na_2O$ | $K_2O$ | CaO | MgO |
|---|---|---|---|---|---|---|---|
| G1 | 56 | 15 | 6 | 0.5 | 0.2 | 22 | 0.6 |
| G2 | 72 | 2 | – | 13 | 1 | 8 | 4 |
| G3 | 33 | 2 | 36 | 16 | 1 | 8 | 4 |
| G4 | 67 | – | 33 | – | – | – | – |
| G5 | 76 | – | 24 | – | – | – | – |
| G6 | 81 | – | 19 | – | – | – | – |



**Figure 2-15:** Glass composition and dependence of friction coefficient on glass viscosity at 1373K [55]

Besides publications and technical notes, the use of glass melts in hot metal forming processes have been widely mentioned in patents. Table 2-1 summaries a number of past patents that investigated glass lubrication for a wide range of applications with details related to chemical composition. The roles of each component were occasionally discussed, although the statements were hardly backed with evidence. Likewise, friction and wear reduction resulted by the glass lubricants were sometimes mentioned, but mostly not in a quantitative way. Some information was not available in the original written record.

| Patent number | Working Temperature range (°C) | Load/ pressure range | Compositions | Tribotest types | Applications | Notes | Dispersive medium |
|---|---|---|---|---|---|---|---|
| US3186945 | ~1000 | | Multicomponents lubricant: Alkali oxides/phosphate + divalent metal phosphate and borate<br>Preferable composition: 50-90% alkali metal phosphate, 10-50% alkali borate and balance potassium phosphate<br>Viscosity of 10% solution: 8-10 cP at 50°C Preferable | | Forming austenitic steel tubes, metal rolling | Alkaline cations: make polyphosphate dissolved in water. Polyphosphate: act as lubricant | Water |
| WO 92/01050 | 899-1149 | | Composition: glass powder, binder, rheological agent, weetting and viscosity modifie. Glass frit viscosity $10^2$ ~ $10^4$ P at 900~1150C, softening point 650C with particle size 150micron~ 0.5mm ($Al_2O_3$ + PbO + MgO +CaO +$Na_2O$ +$SiO_2$). Rheological agents: BN, Ni,$Cr_2O_3$ | . | Forging operation, titanium alloy at 950C-1000C, aerospace engines | Glass powder: principle lubricant. Binder: improve surface adhesion. Rheological agents: control liquid flow of glass lubricant, supports the load and prevent asperities contact. | Water |
| EP2014747A1 | ~1200 | | Glass frits composition: first glass frit ($SiO_2$, $Al_2O_3$, CaO and optional MgO, ZnO, $K_2O$), second glass frit, dispersion-suspension agent, other components. Glass frits are different in softening temperatures | Actual production line of seamless steel pipe (with temp. over 1200°C) | Metal working | Each glass frit has corresponding softening point to maintain desired viscosity and adherence | Clay |
| US2010029818 | 700-1300 | | Glass frits composition: calcium phosphate, fatty acid or fatty acid salt, boric acid and akaline metal phosphates with mean grain size <150 micron | Actual production line of seamless pipe (with temp. over 1200°C) | Hot metal processing | Calcium phosphate: suitable trickle flow at high temp Fatty acid: lump formation inhibitor. Boric acid: improves uniform distribution and reduces scaling. Alkali phosphate: contribute to scale dissolution. Small grain size: favor flow characteristics | Not mentioned |
| JPH1192169 | 1000-1300 | | Lubricant composition: $SiO_2$, $Al_2O_3$, $B_2O_3$, alkaline earth metal oxides, alkali metal oxides, $P_2O_5$ | | Hot extrusion | $SiO_2$: glass skeleton. $Al_2O_3$: prevent characteristic change due to phase separation. $B_2O_3$: melt generated scale on surface. Metal oxides: achieve vitrification.$P_2O_5$: lower viscosity | Not mentioned |
| US8846152B2 | 600-1300 | | Glass frits composition: high melting point (m.p) frit ($SiO_2$, $Al_2O_3$, CaO and optional MgO, ZnO, $K_2O$), medium m.p frit, low m.p frit and other components | Mannesmann pipe making process | Anti-scaling in metal production | Each glass frit has corresponding softening point to maintain desired viscosity and adherence | Water |
| NASA TN103776 | ~900 | | Composition: $BaF_2$/$CaF_2$ eutectic was plasma sprayed to form self-lubricating mechanism | Tested on pin-on-disk tribometer in air, $H_2$ and He | Glass forming, metal working, rotary engines, bearings. | | |
| NASA TND7556 | ~900 | 5000psi | Composition: (1) Nichrome-glass, (2) Nichrome-glass-$CaF_2$ associated with plasma sprayed coating | Tested on pin-on-disk tribometer in air, bearing test | Aerospace applications | | |

| | | | | | | | |
|---|---|---|---|---|---|---|---|
| EP0611817A1 | 700-1100 | 50kg/mm2 | Composition: graphite with preferable size of 0.5~30 micron, selected metal oxides ($TiO_2$,PbO, ZnO, CaO,$Al_2O_3$) with particle size of 0.01~20micron | COF test and carburizing test | Hot plastic working | | |
| JPH07118687 | 1100-1200 | | Composition: graphite, water soluble polymer of iron oxide with 10um, glass powder with viscosity of 1000P at 1000C ($SiO_2$, $B_2O_3$, $Al_2O_3$...) | Mannesmann-mandrel mill method | Seamless steel pipe and alloy steel manufacturing | | Water |
| JPH11166188 | 1000 | 200g/m2 | Composition: alkaline earth metal borate (Ca, Ba, Mg, Na salt) with preferable particle size of 2-20um or more preferably 5-15um. | Rolling cylinder | Seamless steel pipe | | Water |
| JPH05271684 | 1000 | 98N/mm2 | Composition: metal oxide powder with preferable particle size of 20-60um. Sodium silicate | Rotating cylinder | | | Water |
| US8082767 | 1000-1300 | | Composition: combination of lamellar silicate, sodium borate, alkali carbonate | 5 stand full retractable mandrell mill | Seamless steel pipe manufacturing | | Water |
| US5691282 | 800-1300 | | Composition: Glass powder, glass frit, graphite, alkali metal silicate, water soluble Na polyphosphate, water in-soluble Na polyphosphate, thickener: polysaccharide, borax. Preferred viscosity at 25ºC: 1000-7000MPa.s | Adhesive ability, film forming ability and mechanical strength at 800-1050C | Hot metal forming | Glass powder: chief component for lubricity (preferred size<100um), glass frit: maintain film-forming property (<100um), graphite (<100um): excellent lubricity, alkali silicate: binder, Na metaphosphate: avoid foam forming, thickener: maintain viscosity and lubricant dispersion, borax: coupling agent | Water |
| US 3254401 | ~1370 | | Composition: Outer harder glass with >94% $SiO_2$, inner softer glass: $SiO_2$-$Na_2O$-$K_2O$-CaO-MgO-$Al_2O_3$ | Oxidation test at 1200C | Hot working operation | As inner softer glass fuses forming protective layer overlying metal surface, outer glass cloth held inner glass from flowing away. As outer harder glass fuses and dissolves into first glass, viscosity increase and reduce flowing-out tendency | Water |
| US 4228670 | ~1000 | | Composition: $SiO_2$, $Na_2O$, CaO, predominant $B_2O_3$, $Al_2O_3$ with preferred diameter of less than 1um | Spraying onto metal surface at 4-5 bar pressure | Forging, pressing | | |
| US 4402838 | >1000 | | Composition: silicate, phosphoric alkali salt, borate | | Forging and extrusion | | Water |
| US 5242506 | >1000 | | Composition: glass powder with preferred size >30um ($Al_2O_3$, PbO, MgO, CaO, $Na_2O$, $SiO_2$), binder, rheological agent, wetting and viscosity modifier | | Forging and extrusion | Glass powder: provide principle lubricity, binder: forming mechanical bond with surface, rheological agent: control the flow and prevent asperities contact | inorganic compounds: xylene |
| US 3293894 | 1500-2200F | | Composition: $SiO_2$, $B_2O_3$, $Na_2O$ | | Tube drawing | | |

| | | | | | | | |
|---|---|---|---|---|---|---|---|
| US 4096076 | ~1800F | | Composition: BN, glass frits ($B_2O_3$, $SiO_2$, CoO), binder | | Forging | BN: provide lubricity, Glass frit: protect BN and form low shear film, CoO: binding agent increase adherence | inorganic compounds: xylene |
| US 3357220 | ~1800F | | Composition: $SiO_2$, $B_2O_3$, $Na_2O$, $Al_2O3$, $K_2O$. Ground to fine powder | Oxidation test at 1800F | Oxidation protection | | |
| US 4358544 | 800-1000 | | Composition: $SiO_2$, $B_2O_3$, $Na_2O$, CaO, $Al_2O_3$ with average size of 20-30um, desired viscosity of $10^4$P at working temperature | | | | acrylic acid, xylene |
| US 8863564 | 700-1200 | | Composition: 2 glass frits with different content of $SiO_2$, $B_2O_3$, $K_2O$, CaO, $Al_2O_3$ and desired viscosity of $10^3$-$10^6$P at 700-1200$^o$C, friction controlling agent and others | Rolling test | Hot rolling process | Each glass frit has corresponding softening point to maintain desired viscosity and adherence | Organic solvent: acrylic or ester. Possibly inorganic powder like bentonite |
| GB 1359430 | ~1100 | | Composition: $P_2O_5$, $B_2O_3$, $Na_2O$, $K_2O$, $Al_2O_3$ and other optional metal oxides | Extrusion, piercing | Hot forming metal | | Water/ highly dispered silica |
| US 4402838 | >1000 | Forging pressure :1000-1600 tons | Composition: (1) $P_2O_5$, $B_2O_3$, $Na_2O$, $K_2O$. (2) Synthetic or natural silica with layered structure suspended in water | | Forging, extrusion | | Water |
| US 5983689 | 850-1000 | | Composition: alkali silicate, silane coupling, alkali compound (carbonate, borate, hydroxide, salt), possibly iron oxide | | Seamless steel pipe | | Water |
| US3248234 | ~1000C | | Composition: $P_2O_5$, $Al_2O_3$, alkali oxides | | alloy drawing | alkali oxides: change fusibility, tendency toward devitrification, $B_2O_3$: increase chemical stability | |
| US 8863564 | 1200-1300 | | Composition: first glass frits, second glass frits containing $SiO_2$, $Al_2O_3$, CaO, optionally MgO, ZnO, $K_2O$ | | Hot metal working | 1. Glass frits with different softening point to provide adaptive viscosity 2. first glass frit viscosity $10^3$-$10^6$ dPas at 1200$^o$C, second glass frit viscosity $10^3$-$10^6$ dPas at 700$^o$C 3. Using controlling agents 4. Can be either used as solid or liquid component atroom temperature | Water/ using dispersion agent like clay, bentonite and organic solvent like acrylic acid ester |
| US 6177386 | 1100-1300 | | Composition: graphite, phosphate mixture, bentonite, sodium silicate, silico-phosphate | | Hot metal working | | |

| | | | | | | | |
|---|---|---|---|---|---|---|---|
| US 5437802 | 800-1200 | | Composition: (A) solid powder of condensed phosphoric acid salt: $KPO_3$, $NaPO_3$, $K_4P_2O_7$, sodium silicate, chromic acid salt, halides.(B) inorganic powder: BN, $Si_3N_4$, amorphous carbon, $K_3PO_4$, $Ca_3(PO_4)_2$, bentonite, $SiO_2$, ZnO. | | Hot rolling process | heat insulating agent (A) with excellent heat conductivity | |
| US 4052323 | >900 | | Composition:(1) graphite, alkylene homopolymer or copolymer, dispersive agent (2) graphite, alkylene homopolymer or copolymer, auxiliary suspension agent, film stabilizer | | | | Water |
| US 3390079 | >900 | | Composition:$B_2O_3$, $SiO_2$, $Na_2O$, CaO, $Al_2O_3$ | | Hot extrusion | Desired viscosity $10^2$-$10^3$ poise at working temperature | Water |
| US 3379642 | ~1000 | | Composition: melamine phosphates, possibly graphite, $MoS_2$, BN | | Hot extrusion | Desired viscosity $10^2$-$10^3$ poise at working temperature | Water |
| JPH 10121088 | 800-1200 | | Composition: oxide-based layered materials (white mica, kaolin, pyrophyllite), binder ($B_2O_3$ and Boron derivaties), metal hydroxide (Ti, Mg, Si, Al…) | | Mannesmann stage | Oxide-based layered materials: provide lubricity at high temperature, binder: provide uniform dispersibility of lubricating agents, metal hydroxide: avoid carburization | Water |
| US 3368970 | 1000 | | Composition: condense phosphate (pyro/poly), alkali metal oxides, ferric oxide, $Al_2O_3$ | | Extrusion of seamless steel tubes | Silicate results in high degree of wear and tear of the work tool. Using combination of $Fe_2O_3$ and $(KPO_3)n$ reduces wear, friction and increases lifespan of the work tool | Water |
| US 3179524 | 1000 | | Composition: alkali metal polymetaphosphate | | | | Water |
| JP-A-7-303915 | 1100-1200 | | Composition: CaO(10-25%), $Al_2O_3$(3-10%),$K_2O$(10-30%), balanced $SiO_2$ | | Hot extrusion | CaO: reduces viscosity, $Al_2O_3$: imparting agent, $K_2O$,$Na_2O$: viscosity adjustment | |
| JP2011-121095 | 1080-1170 | | Composition: $SiO_2$-$Al_2O_3$-$B_2O_3$-CaO | | Hot extrusion | | |
| JP 2015-071521 | 1100-1250 | | Composition: $SiO_2$:47.2-64.8%, $B_2O_3$:4.2-11%, $Al_2O_3$:8.0-17.6%, MgO: 1.6-3.5%. Sum of $Na_2O$ & $K_2O$: 11.0-17% | | Hot extrusion | $B_2O_3$ dissolve scale, $SiO_2$ may dissolve but not sufficiently than $B_2O_3$ | |
| JP 2010-234375 | 1000-1250 | | Composition: <20% $B_2O_3$, $Na_2O$, $K_2O$, $SiO_2$ | | Hot extrusion | Iron oxide melts into the glass, the oxidation of steel surface by glass increases lubricant adhesion | |
| JP 2010-227997 | 1000-1250 | | Composition: 12-30% alkali oxides, total $Al_2O_3$,CaO, MgO:20-40%,<25% $B_2O_3$, balanced $SiO_2$ | | Hot extrusion | Alkali metal oxides are responsible for lubricant adhesion. $Al_2O_3$, CaO, MgO exhibit reducing behavior. $Na_2O$ has more oxidizing capacity than $K_2O$ | |
| JP 2003-113387 | 800-900 | | Composition: glass lubricant with 150-200 mesh size particles. | | Hot extrusion | Application viscosity: 300-100Pas | |

| | | | | | | | |
|---|---|---|---|---|---|---|---|
| JP 11-092169 | 1000-1250 | | Composition: 35-60% $SiO_2$, 10-20% $Al_2O_3$, 12-20% $B_2O_3$, 15-25% alkali earth metal oxides, < 5% alkali metal oxide, <5% $P_2O_5$ | | Hot extrusion | | |
| JP 07-303915 | ~1000C | | Composition: 10-25% CaO,3-10% $Al_2O_3$, 10-30% $K_2O$, balanced $SiO_2$ | | Hot extrusion | Alkaline metal oxides are viscosity modifiers | |
| JP 07-223019 | ~1000-1200 | | Composition: CaO:2-6%, $B_2O_3$:18-22%, $Na_2O$:14-18%, $TiO_2$:8-12%, balanced $SiO_2$ | | Hot extrusion | ZnO imparts chemical durability, $TiO_2$ improves wettability, $Na_2O$ modifies viscosity. 10% reduction of extrusion force was achieved. | |
| JP 2006-188637,A | 500-800 | | Composition: $Na_2O$-$Li_2O$-$P_2O_5$-$B_2O_3$ | | Hot extrusion | | |
| JP 03-100096 | ~1000 | | Composition: 100pts wt. $Cr_2O_3$, 2-10pts wt. $SiO_2$, mixed with water glass. | | Hot rolling | | |
| JP 03-291325 | ~1000 | | Composition: $Al_2O_3$, $SiO_2$, $ZrO_2$ | | Hot rolling | | |
| JP 09-316473 | 1000 | 20-30kgf/m2 | Composition: 80-90% $Fe_2O_3$ (<100um), glass powder | | Hot working | | |
| JP 2014-028395 | 1200 | | Composition: Iron oxides, glass, borax, acid boric. | | Hot rolling | | |

**Table 2-1:** A summarized table of patents using glass lubricants in hot metal forming processes

Oxidation-resistant capacity is also a valuable characteristic of glass-based lubricants. High-temperature oxidation results in the formation of oxide scale which can be considered as material losses and cause many other concerns. For example, about 30% of the yield loss stems from oxide scale-related defects according to the Iron and Steel Institute of Japan [56]. Glass-based coatings have been widely used to enhance corrosion resistance of various alloys at elevated temperatures [57-67]. In hot rolling mill, Riaz et al. [68] proposed a management strategy to suppress oxide scale during re-heating stage by using glass coatings. The application of glass coating resulted in a remarkable reduction in oxide growth. A range of coating composition is given in Figure 2-16 and the corresponding working mechanism of each type is shown in Figure 2-17. Apart from friction and wear reducing-effects, the anti-oxidation capacity of glass compounds lubricants makes them a potential fit for high-temperature lubrication.

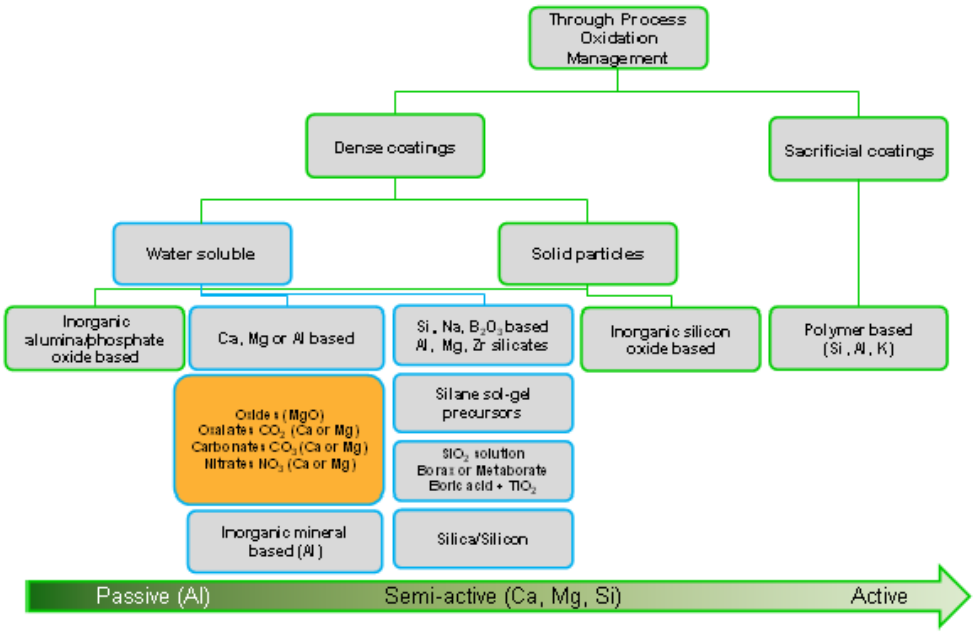


**Figure 2-16:** Type of coatings in reference [68]

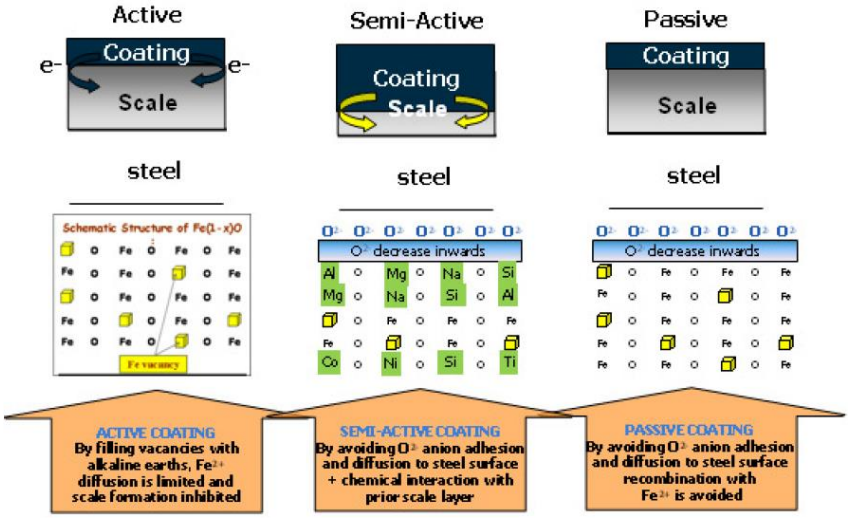


**Figure 2-17:** Working principles of each coating type [68]

### 2.4.2 Glass-like lubrication at low temperature

Glass-like lubrication has been reported at low temperature range. Zinc Dialkyldithiophosphate (ZDDP) is regarded as the most successful oil additive and has been broadly recognized in modern tribology history. It is often formulated in engine oil and many other industrial lubricants due to their exceptional wear resistance. Research has shown that after experiencing complex tribological reaction, ZDDP generally forms a glass-like tribofilm which is mainly constructed from polyphosphate backbones. From the macroscopic point of view, ZDDP generally has a patchy and gradient-like structure with long-chain polyphosphate overlying short-chain phosphate network (as shown in Figure 2-18) [69, 70]. Beside the wear-reducing effect, ZDDPs is also known as an excellent oxidation inhibitors due to their ability to decompose hydroperoxides radicals throughout a complex chemical reactions [69]. The amorphous nature of ZDDP tribofilm renders low-shearing stress which results in low frictional force upon contact [71-73].

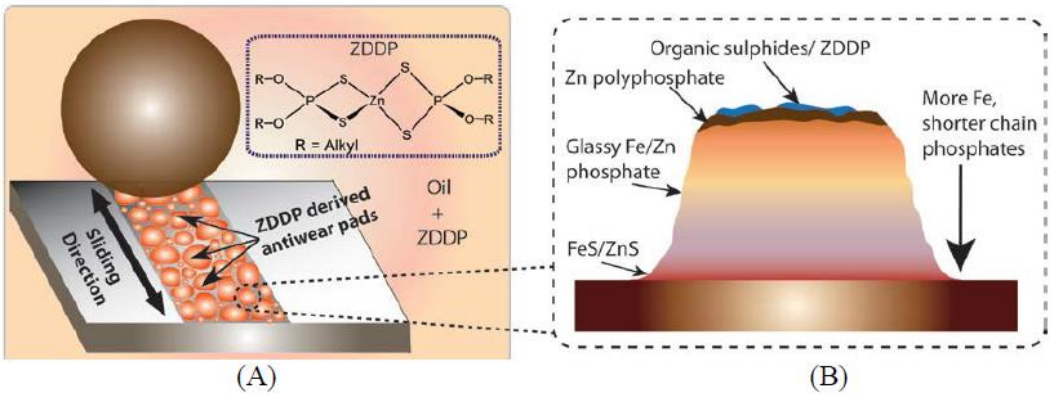


**Figure 2-18:** Compositional gradient within a ZDDP-originated tribofilm [69]

Hard-soft-acid-base theory has been extensively used to elaborate the formation mechanism of ZDDP tribofilm on ferrous contact surfaces [69, 74]. A combination of computational studies and advanced analytical techniques also indicated complex mechano-chemical reactions including wear particles digestion, depolymerization and polymerization of phosphate network [75-77]. Other metal polyphosphates also received attentions regarding their tribological behaviors. Gauvin [78] investigated pure α-$Zn_3(PO_4)_2$ crystalline powder whose structure changes greatly to achieve favorable friction and wear responses. While investigating a number of bulk polyphosphate glass, Spender found that the depolymerized-glassy film favored friction and wear reduction [79]. V.I Kolesnikov [80] proposed an anti-wear and anti-scoring additives in plastic greases used for heavily loaded railway which primarily composes of hetero-molybdophosphate $NaPMoO_6$. Later, Lithium molybdophosphate was proved effective in Puma lubricating oil [81]. In addition, a series of binary metal polyphosphates were found to improve tribological performance of Puma and Buksol lubricants [82, 83]. Adaptive molecular transformation, elimination of oxidizing agents and active adsorption are suggested to be

the principle mechanism of this family of polyphosphate-based lubricant (Figure 2-19) [84, 85].

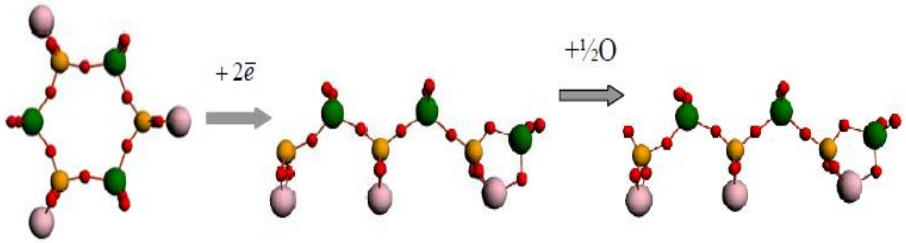


**Figure 2-19:** Structural transformation in Lithium Phosphorowolframates [84]

### 2.4.3 Glass-like lubrication at high temperature

While research on glass-like lubrication received plenty of attention at low/moderate temperature, there has been fewer work carried out at high temperature. Matsumoto investigated tribological performance of water-glass (silicate based) by means of pin-on-disc testing at maximum temperature of 1200$^{o}$C [86]. They found a strong correlation between the friction coefficient and the glass viscosity while the effects of amorphous graphite addition were also illustrated (Figure 2-20). However, no further implications regarding wear reduction and chemical analysis on the worn area were provided. Wan et al. published a review work on the application of inorganic polymer in high temperature tribology and indicated the potential lubrication performance of such class in hot metal forming processes [2].

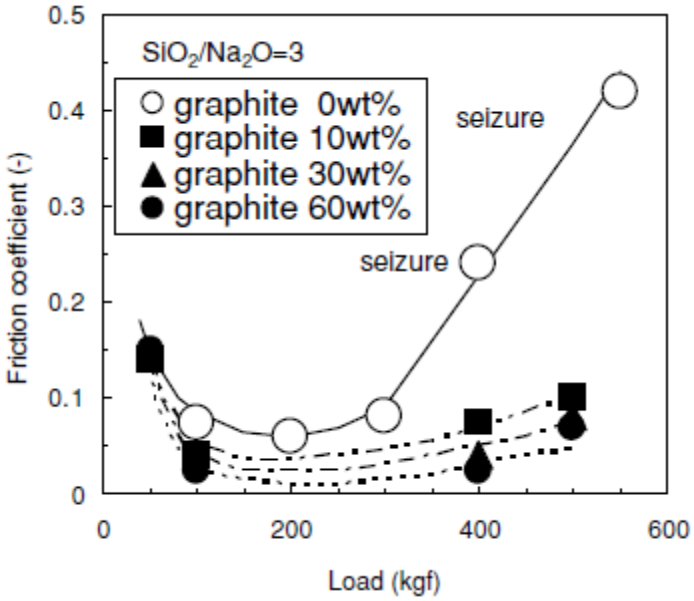


**Figure 2-20:** Friction coefficient as a function of load and amount of graphite inclusion in water glass lubrication [86]

Tieu et al. studied tribological response of an alkaline polyphosphate by means of pin-on-disc testing on steel pair [87, 88]. The polyphosphate composite compound delivers exceptional friction- and wear-reducing effects on the sliding surfaces. A hierarchical structure of the tribofilm was revealed with phosphate melt penetrating deeply into the oxide scale bulk while chemical analysis indicated strong reactions between polyphosphate and iron oxide surface. Later, the compositional complexity of the Na/K polyphosphate tribofilm was resolved by a combination of advanced chemical analysis [89] (Figure 2-21). The lubricant was also capable of reducing rolling force in actual hot rolling of Interstitial-Free (IF) steel, up to maximum 25% compared to unlubricated case. Cui et al. [90] determined the roles of starting molecular structure on tribological behaviors of a range of different Na polyphosphates (orthophosphate, pyrophosphate and metaphosphate). He found that the short-chained polyphosphate lead to a superior frictional and wear behavior

which is quite contrary to what established previously. The lubrication performance of sodium polyphosphate was also justified in laboratory hot rolling of mild-carbon steel [91]. There were also substantial simulation works to substantiate the working mechanism of alkaline polyphosphate melts at high temperature. Ta et al. [92] used Density Functional Theory (DFT) calculations to understand the chemical absorption route of pyrophosphate ($Na_4P_2O_7$) and orthophosphate ($Na_3PO_4$) (at 1073K). They found that Fe-O-P linkage is accountable for the absorption while $Na_4P_2O_7$ was shown to have a stronger binding towards both Fe and $Fe_2O_3$ surfaces than $Na_3PO_4$. Later, Le et al. [93] demonstrated the bonding nature of P-O, Na-O and Fe-O linkages on the immediate interface between pyrophosphate/triphosphate and iron oxide ($Fe_2O_3$). The study illustrates the important role of iron oxide in the decomposition process of phosphate network. The adsorption behavior of a sodium pyrosilicate ($Na_6Si_2O_7$) was also studied in-depth at higher temperature range (maximum 1500K) [94].

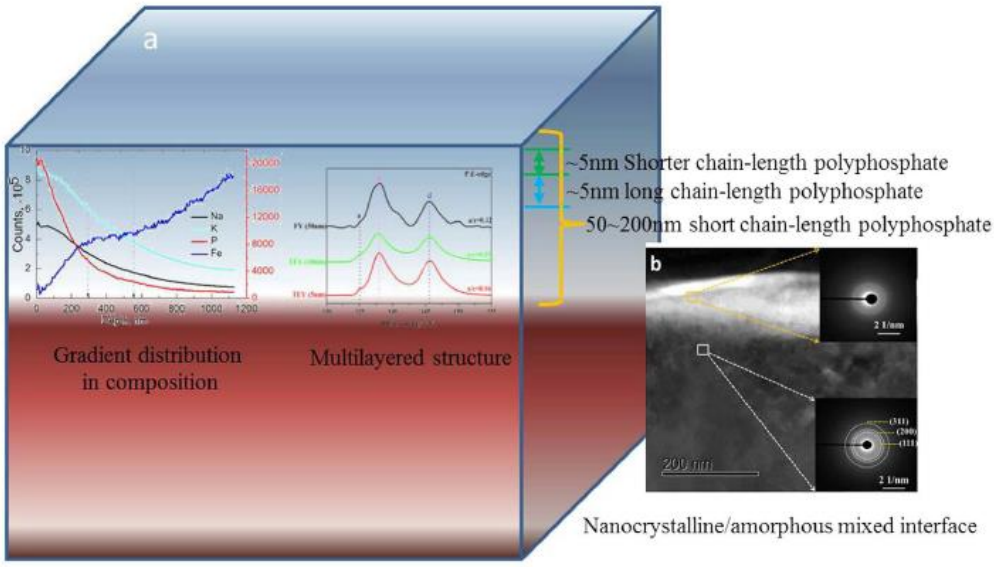


**Figure 2-21:** Compositional gradient of Na/K polyphosphate tribofilm [69]

## 2.5 Research scopes

As stated previously, there are three glass-forming compounds upon which melt lubricant is generally formulated: phosphate, borate and silicate. While phosphate and silicate melts have been investigated thoroughly (particularly phosphate), borate melt received little attention although it has been often included in the lubricant composition for hot metal processing (Table 2-1). Even in the patents that included borate, there were lack of detailed analysis to elucidate the exact function and working mechanism of the material. The current work sets to provide a fundamental understanding about the tribological behaviors of alkaline borates and explore their lubrication potential in the hot rolling of steel which is unprecedented.

- The friction and wear characteristics of sodium borate are studied on sliding steel surfaces at elevated temperatures. Microstructural and chemical characteristics of borate tribofilm are unveiled in details. Experiments are also designed to distinguish thermally-activated reaction and mechanical-chemical reaction.
- The roles of each individual element in borate melt (alkaline element and boron oxide) on the collective lubrication performance are highlighted. This unprecedented piece of understanding allows a better control over lubricant fomulation to fit a specific working circumstance.
- The tribological behavior of sodium borate is investigated in rolling contact. While the passivated rolling module is not entirely representative of actual hot

rolling, the interactions between lubricant and oxide scale under such condition are fully characterized.

- Synthesis of potassium borate is carried out and their tribological behaviors are also determined. Working range of individual alkaline borate is then deduced.

# CHAPTER 3:

# Experimental methodology and characterization

This chapter describes experimental apparatus and analytical instruments used thorough the study. A brief introduction regarding working principle, technical specifications is also included.

## 3.1 High-temperature tribometer

Sliding and rolling contacts are simulated by using high-temperature tribometers under controlled conditions.

### 3.1.1 Ball-on-disc

Friction tests are extensively conducted on a Bruker CETR UMT2 tribometer which is capable of testing up to maximum temperature of 1000$^{o}$C. Ball-on-disc is the mainly used configuration in this study. A 2-dimensional DFH load cell has a minimum force resolution of 10mN while the maximum normal load achievable is 200N. Upper linear stage enables precise positioning down to 1µm. Lower rotary spindle can operate in range of 0.001 to 5000rpm. Both normal and lateral forces are simultaneously recorded by an integrated program (UMT) during the friction test. Tests are performed via designed scripts which allow automated movement of each component. The system provides a highly precise acquisition of friction force with good repeatability. In case of lubrication testing, the lubricant is introduced to the disc through a steel tube with an inner diameter of 2mm. A simplified sketch of the tribometer is given in Figure 3.1.

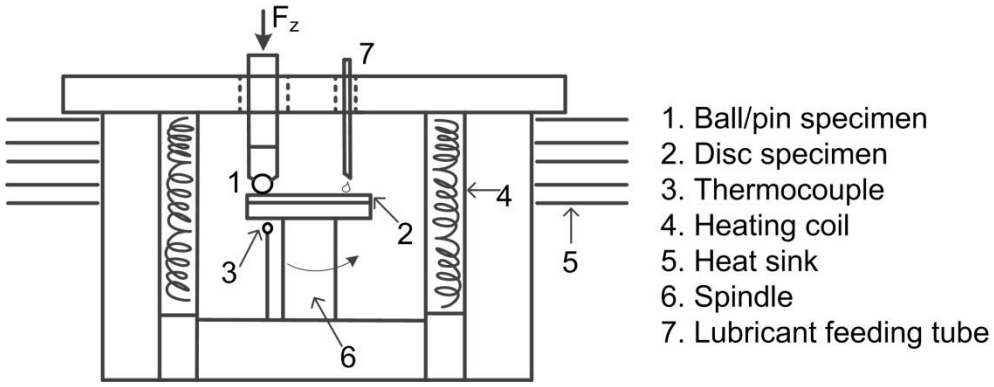


**Figure 3-1:** Simplified schematic of the high-temperature tribometer UMT2

### 3.1.2 Roller on flat

A state-of-the-art Bruker UMT3 was used to simulate the rolling contact at high temperature. It is an upgraded version of the UMT2 with additional utilities, particularly in flexible testing configuration. The module not only allows conventional rotary testing (e.g. ball-on-disc), but also reciprocating testing at high temperature (maximum 1000$^{o}$C). The roller-on-flat is built on the reciprocating unit in which the roller specimen is heavily pressed against the lower flat specimen under back-and-forth reciprocating motion. Although the unit is not able to represent the actual hot rolling condition, high contact pressure during free rolling contact can generate useful insights into the surface-related phenomenon. A detailed apparatus configuration will be provided in Chapter 8.

## 3.2 Analytical methodology

Advanced characterization methods used throughout this study are described below, although there will be some minor tools that are also mentioned when needed.

### 3.2.1 Thermal analysis

High-temperature thermal behavior of interested lubricant was studied by a combination of high-temperature Laser Confocal Microscope (LCM) and Thermal Gravitational Analysis and Differential Scanning Calorimetry (TGA/DSC). *In-situ* LCM allows a real-time observation of surface oxidation, melting, phase transformation under controlled environments at high temperature [95].A schematic illustration of the LCM is shown in Figure 3-2. The specimen is focally heated by a 1.5kW-halogen lamp while the upper CCD camera captures at 25 frames per second and stores into a video file. The instrument allows a direct observation of the lubricant transition close to its melting point.

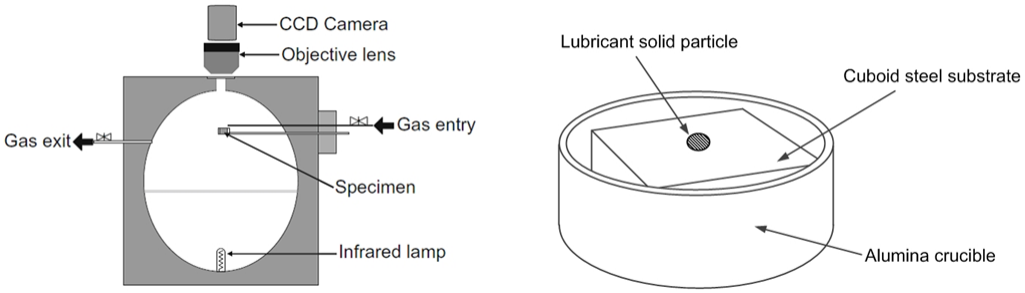


**Figure 3-2:** Cross-sectional schematic of the high temperature LCM and the specimen shape

TGA/DSC is a popular thermo-analytical technique to study thermal behavior of materials. The instrument is capable of detecting melting, oxidation, recrystallization due to the change that is associated with the heat flux of each occurrence, e.g. melting requires energy in form of heat while recrystallization releases energy in the form of heat. In this study, a NETZSCH STA 449 DSC was used and a Rh/PT crucible was chosen for the experiment. The specimen is heated at a rate of $10^{o}$C/min under pure Argon gas.

### 3.2.2 X-ray diffraction

A GBC MMA Diffractometer with a Cu Cu-Kα source and a step size of $0.02^{o}$ was used to determine crystallite structure of interested compounds. The operating voltage and current of X-ray was set at 35kV and 28.6mA, respectively. The received patterns were processed by HighScore Plus with a data base of Powder Diffraction Files (PDF) 4+ 2018.

### 3.2.3 Nanoindentation

Mechanical properties of steel components were determined by a Hysitron Triboindenter TI950. The instrument is calibrated using a standard Quartz specimen with known Hardness and Young modulus. It is equipped with a Berkovich tip with an apex radius of 150nm, this allows an accurate measurement on carbides precipitates in High Speed Steel material (in Chapter 6, 7 and 8).

### 3.2.4 3D Interferometer

Surface topography measurements were made using a 3D Interferometer Optical Microscope (Bruker Contour GT-K). Typical design of the instrument is given in Figure 3-3. The measurement is carried out based on the analysis of interference between the reference wavefront and the reflected wavefront from the sample surface. The output consists of raw quantified data which can be subjected to further processing if necessary. The instrument also enables graphical representation from 3D data set and generation of 2D profiles. On the disc, wear loss volume was calculated by measuring the cross-sectional area of the wear track at 4 different points. In this work, wear loss volume is reported. Table A-4 to A7 (Appendices) refer to specific wear rate.

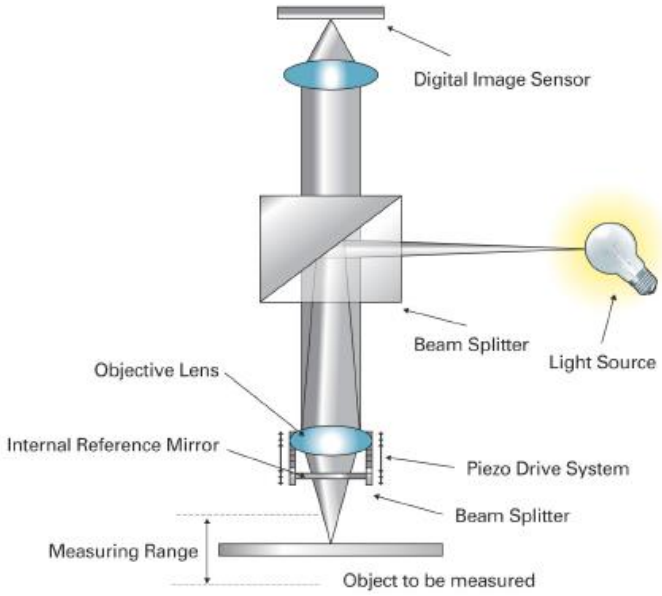


**Figure 3-3:** Typical design of optical interferometer

### 3.2.5 Scanning Electron Microscope (SEM)

Microscopic imaging of sample surfaces was extensively carried out by a JOEL JSM-6490LA Scanning Electron Microscope (SEM). The instrument is equipped with a 30kV conventional tungsten filament and adjustable operating pressure. It has a maximum resolution of 3.5nm at 30kV with 2 main detectors: Secondary Electron (SE) detector and Backscattered Secondary Electron (BSE) detector. The 80x80mm$^2$ SSD Energy Dispersive X-ray (EDX) detector allows a rapid quantitative microanalysis and precise elemental mapping. Microanalysis processing is performed on an integrated Aztec Oxford software suit.

### 3.2.6 Focus Ion Beam Microscope (FIB)

In this work, Focus Ion Beam Microscope (FIB) was mainly used as a sectioning tool to produce a high quality electron-transparent specimen for Transmission Electron Microscope (TEM) work. A FEI Helios NanoLab G3 CX [96] is equipped with Gallium source for ion milling beside conventional functionality of a SEM such as Secondary Electron (SE) imaging and microanalysis (EDS).


**Figure 3-4:** Photograph of the FEI Helios NanoLab G3 CX [96]

### 3.2.7 (Scanning) Transmission Electron Microscope (STEM)

(Scanning) Transmission Electron Microscope has been widely regarded as a powerful tool in materials science research. On the basic of working principle, a high-energy electron beam is illuminated through a thin specimen (<200nm) and the transmitted electrons are recorded on a viewing screen, forming an image. In tribology, the microscope works mostly aim to observe and understand the cross-sectional tribo-interface at the nanoscale. In this thesis, electron-transparent TEM specimens were produced by the FIB mentioned earlier. The STEM work was extensively carried out on a JOEL JEM-ARM200F. The state-of-the-art instrument features aberration-correction probe which is

capable of atomic resolution imaging, <0.08nm at 200kV and <0.14nm at 80kV. The microscope is equipped with a large area SSD EDS detector which allows elemental mapping with atomic resolution. In addition, a Cold Field Emission Gun with a resolution of 0.3V enables atomic-scale determination of electronic structure, e.g. oxidation state, chemical bonding, surface plasmons. Versatile imaging techniques can be performed from a number of available detectors including: High Angle Annular Dark Field (HAADF), Bright Field (BF), Secondary Electron (SE) and Backscattered Secondary Electron (BSE) detectors. Microanalysis processing is conducted by using NSS software suit.

### 3.2.8 Electron Energy Loss Spectroscopy (EELS)

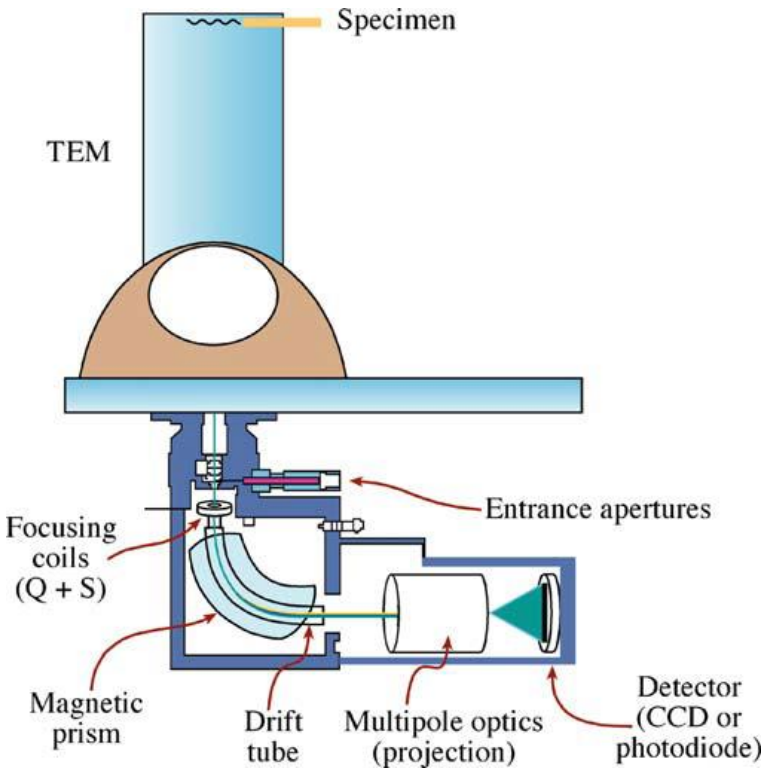


**Figure 3-5:** Cross-sectional view of a typical EELS acquisition assembly below the viewing screen [97]

Another powerful function of the JOEL JEM-ARM200F is its capacity in resolving electronic structure by means of Electron Energy Loss Spectroscopy (EELS). The transmitted electrons experience inelastic-scattering after traversing the thin TEM specimen in which a certain amount of their energy is lost. This energy deviation carries useful information regarding electronic structure of a specific element, which in turn can be correlated to their bonding/valence state and other chemistry characteristics [97]. The JOEL JEM-ARM200F is equipped with a GIF Quantum imaging filter which allows acquisition of energy-loss dispersion spectrum. In this work, EELS was performed on STEM mode and the resulting energy-loss spectrum is processed by a tool in Digital Micrograph software [98]. An image of EELS acquisition assembly is given below [97].

# CHAPTER 4:

# Tribological performance of sodium borate at elevated temperatures

** This chapter content was published in The Journal of Physical Chemistry C, 2017, 121, 45, 25092-25103*

As previously stated, melt lubricants [2] are considered as good candidates for high-temperature lubrication as they possess a desirable set of thermal and chemical characteristics. The concept of melt lubrication is based on utilizing viscous state of the melt lubricant for tribological contact. Sodium polyphosphates reportedly delivered friction and wear reducing effects on sliding steel pairs at the maximum temperature of 800$^{o}$C [87, 99]. It is believed that polymeric melts of boron and silicate can also hold significant potential. Although borates have been studied widely at moderate temperature [100], it is still unclear how the Boron-bearing melts behave in response to tribological exposure at high temperature. The present chapter aims to evaluate tribological properties of an inorganic sodium borate on steel contact at elevated temperature by means of pin-on-disc testing. Hot tribotests were carried out over a wide range of temperature and loading while the lubrication effectiveness is justified by a direct comparison between lubricated and non-lubricated tests. In addition, a thorough analysis was also conducted to reveal microstructure and chemical nature of the tribo-interfaces on both sliding counterparts.

## 4.1 Experimental details

### 4.1.1 Molecular structure and thermal behavior of sodium borate

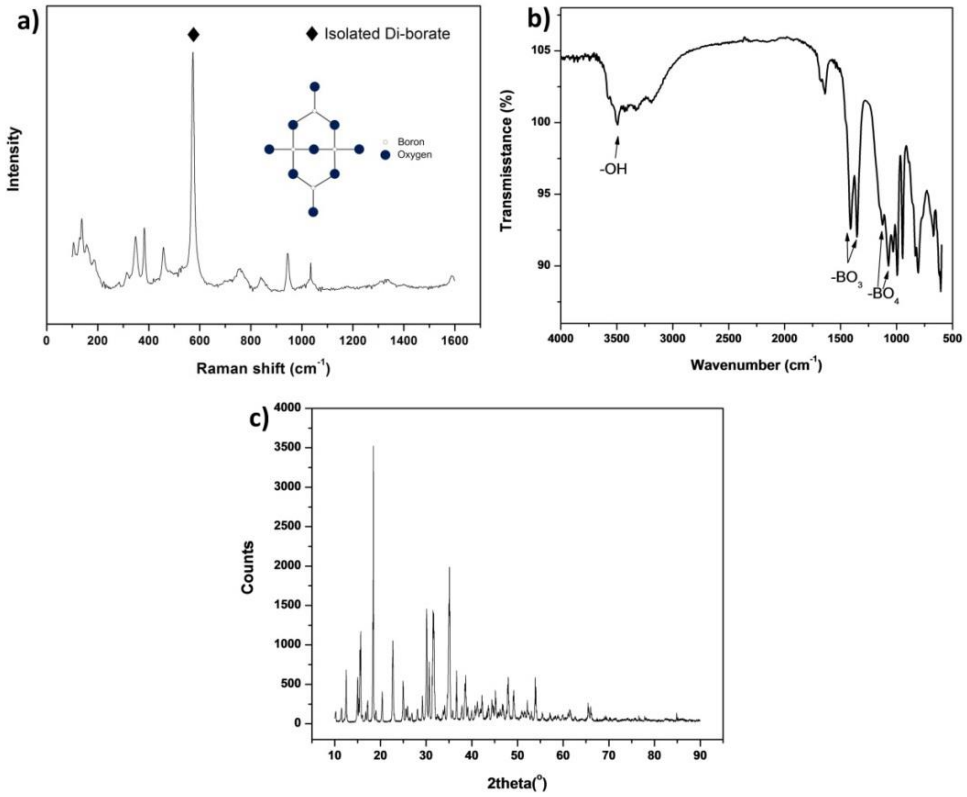


**Figure 4-1:** Vibrational spectroscopy spectrum of sodium borate, a) Raman, b) FTIR and c) X-ray diffraction pattern of the material

Sodium Tetraborate Decahydrate ($Na_2B_4O_7.10H_2O$) was selected for the hot friction test. At room temperature, the naturally-occurring mineral has a crystalline structure as indicated by its XRD pattern (Figure 4-1c). A vibrational spectroscopy analysis was carried out to determine the molecular structure of the compound and the resultant spectrums are shown in Figure 4-1a and 4-1b. In Raman spectrum, the sharp peak located at 580cm$^{-1}$ is assigned to isolated-diborate [101]. Within this dominating structural group, a coexistence of triangular ($BO_3$) and tetrahedral ($BO_4$) boron sites can be expected which

is confirmed by the FTIR analysis. In FTIR spectrum, the band at 3498 $cm^{-1}$ is associated with H-O-H bending while bands at 1411$cm^{-1}$, 1360$cm^{-1}$ and 1127 $cm^{-1}$, 1075 $cm^{-1}$ can be assigned to asymmetric stretching of B-O in $BO_3$ and $BO_4$, respectively [102]. A 5% (weight percentage) aqueous solution of borate was prepared for friction testing.

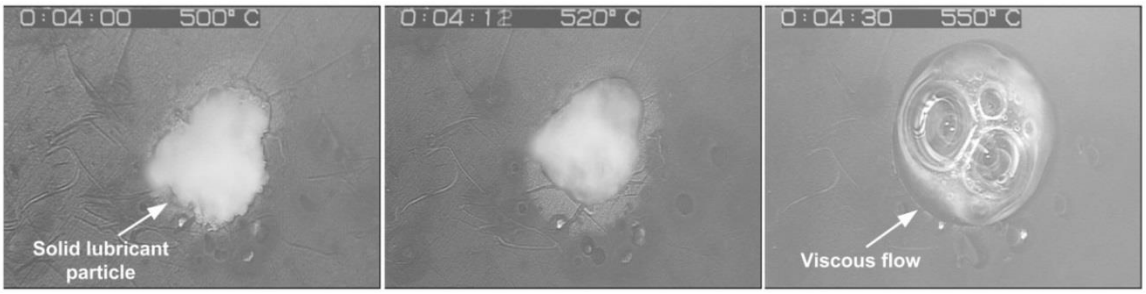


**Figure 4-2:** Snapshots of sodium borate particle through its transition point in Laser Confocal Microscopy

Transition temperature of sodium borate was determined by mean of high temperature Laser Confocal Microscope (LCM) coupled with a CDCD camera. A mild-carbon cuboid substrate (3x3x2.5mm) with roughness of 10nm was fixed onto a 5mm-diameter alumina crucible. A small amount of lubricant powder was gently located on the steel specimen which was subsequently inserted into an ellipsoidal infrared heating furnace. The specimen was then heated by an infrared source to 800$^oC$ at a rate of 1.5$^oC$/s under Argon atmosphere (99.999% Ar). The schematic illustration of the testing apparatus is shown in Figure 3-2. *In-situ* observation of the physical state variation was accomplished by a continuous video recording through objective lens. At 525$^oC$, the solid particle gradually transforms from solid state into a highly viscous liquid (Figure 4-2), marking the transition point of sodium borate.

DSC/TGA analysis was further used to support the melting behavior of borate (Figure 4-3). The material experiences a significant dehydration around 120°C-160°C indicated by two endothermal peaks then it totally melts at ~525°C.

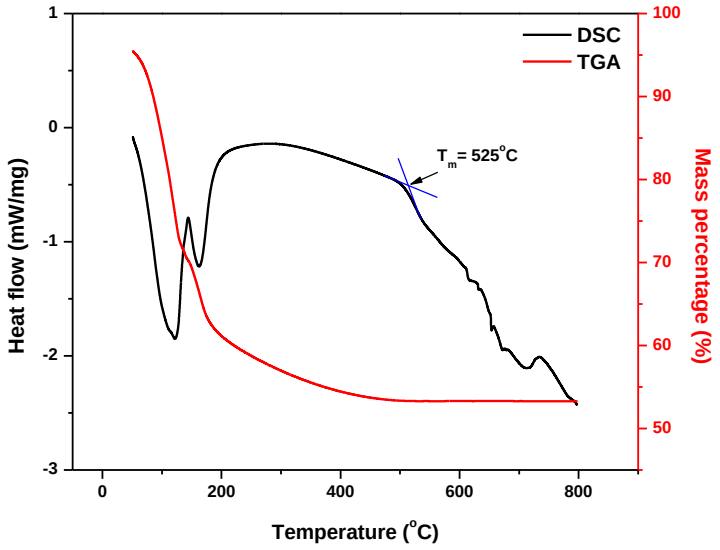


**Figure 4-3:** DSC and TGA curves of sodium borate.

### 4.1.2 Tribopair preparation

A 6.35mm-diameter Chromium GCr15 ball (C:Si:Cr:Fe = 0.98:0.35:1.48:balanced-%wt.) was selected as the stationary component with an initial roughness of ~20nm and a hardness of 5.9GPa. Mild carbon (MC) steel (~0.3%C) with a hardness of 4.7GPa was chosen for the disc material. The round disc of 3mm in thickness and 50mm in diameter, was polished to achieve a roughness of 1µm. Prior to a friction test, both steel components were ultrasonically cleaned by ethanol and acetone respectively for contaminants removal.

### 4.1.3 Friction tests

Hot friction tests were performed on the Bruker UMT2-CETR high temperature ball-on-disc tribometer. Steel counterparts were firstly installed into the tribometer then the furnace was heated to a set temperature. The non-isothermal heating period was divided into multiple sequences to minimize the risk of thermal overshooting. MC disc rotates at 5rpm during heating stage to ensure a homogenous heat distribution while the GCr15 ball is located at 5mm above the disc surface. Sliding tests were carried out at temperature range of 600$^{o}$C-800$^{o}$C while the nominal load was kept at 10N-30N with a linear sliding velocity of 0.1m/s. An external thermocouple was embedded into the ball to monitor its temperature and a typical plot is provided at the set point of 800$^{o}$C in Figure A-1 (Appendices). The maximum contact pressure was calculated according to the reduced young modulus of the oxide scales at testing temperature, reaching a value around 1.14GPa, 1.43GPa, 1.64GPa at 10N, 20N and 30N respectively [103]. The sliding duration is 5 minutes and the tribopairs were immediately retrieved and cooled in air after each test to prevent further oxidation. During the lubrication tests, lubricant solution was fed onto the rotating disc with a rate of 0.01ml/s through an external monitor. The onset of lubricant introduction is 2 minutes before contact engagement. A number of tests were repeated for each testing condition to ensure repeatability.

The maximum contact pressure is calculated by Hertzian stress theory as shown in Equation 4-1[104]. Since the steel tribopair were pre-oxidized prior to sliding test, the Young modulus of oxide scale at different temperature is used to determine the generated stress [103] (Equation 4-2). These equations are used throughout this study to calculate maximum contact pressure, unless stated otherwise.

$$a = \sqrt[3]{\frac{3RF}{4E^*}}$$

a: radius of contact area;

R: ball radius (mm);

$$\frac{1}{E^*} = \frac{1 - v_1^2}{E_1} + \frac{1 - v_2^2}{E_2}$$

F: applied force (N);

$E_1$,$E_2$: young modulus of each contact body (GPa);

$$P_{max} = \frac{3}{2}\frac{F}{\pi a^2} \quad (Eq. 4-1)$$

$v_1$,$v_2$: Poison's ratio of each contact body (=0.3 [81])

$$E^T = E^o_{ox}(1 + n(T - 25) \quad (Eq. 4-2)[103]$$

$E^T$: Young modulus of oxide scale at temperature T ($^o$C)

$$n = -4.7.10^{-4}; E^o_{ox} = 240\text{GPa}$$

### 4.1.4 Characterization

The molecular structure of sodium borate was analyzed by a JY HR800 Raman spectrometer and a Shimadzu Fourier Transform Infrared Spectrometer. Morphologies of worn surfaces were exami**n**ed by JOEL JSM-6490LV Scanning Electron Microscopy coupled with Energy Dispersive Spectroscopy (EDS). Low accelerating voltage (5keV) was used in this case to increase x-ray yield of low-Z atom. Ball loss volume was calculated from the worn scar dimension while the according figure was measured by a Stylus Profiler (Dektak 150 Surface Profilometer) on the disc wear track.

Thin lamellars were produced by Dual Beam FEI Helios NanoLab G3 CX while microscope observations of the cross-sectional interface were performed on aberration-corrected JOEL ARM 200F Scanning Transmission Electron Microscopy (STEM). Since the lubricant melt is formulated with Boron which is typically a light element, detection of

such component is restricted by the low yield of X-ray signal. To overcome this issue, High-angle Annular Dark Field (HAADF) imaging is employed besides conventional Bright Field imaging (BF). Based on Rutherford scattering, collected signal from high-angle incoherent electrons is heavily dependent on atomic number ($Z^2$) [105] of the element. Therefore, STEM-HAADF images can exhibit a high sensitivity toward compositional contrast (with negligible lamellar thickness deviation) and were already used in various applications to differentiate elements with great Z disparity [106, 107]. Spectroscopy (EELS) analysis was operated in STEM mode to mitigate radiation damage with beam dispersion of 0.1eV. The spectra underwent background-subtraction by fitting the pre-edge to a power function law $AE^{-r}$, where E is the energy loss and A and r are constants.

## 4.2 Results

### 4.2.1 Tribological performance of sodium borate over a wide range of testing conditions

Average friction coefficients and wear loss volumes of tribopairs lubricated by sodium borate under different loads (10N, 20N and 30N) at 600ºC, 700ºC and 800ºC are shown in Figure 4-4, 4-5 and 4-6, respectively. The sliding velocity remains at 0.1m/s in every case. It can be seen that friction rises marginally with increasing load, although it still falls in a range of ~0.18-0.2 regardless of testing temperatures. The wear loss volumes share a similar upward tendency when the applied load increases. However, the disc seems to suffer a lower material loss than its counter-surface at harsher condition. The disc loss volume is recorded at 0.122 $mm^3$ at 600ºC under 30N and it jumps to 0.163 $mm^3$ at 800ºC

under the same load. On the other hand, the ball loss volume appears more sensitive to both variables, particularly at a higher temperature range, although the order of magnitude is much lower than the disc. At 600°C, the ball loss volume registers a value of $0.63.10^{-2}$ $mm^3$ under 10N, the figure rises to $0.73.10^{-2}$ $mm^3$ and $0.81.10^{-2}$ $mm^3$ at 20N and 30N, respectively. At 700°C, the corresponding value at increasing load is approximately 3 times higher than those at 600°C. The test at 800°C sees the highest ball loss volumes with a steeper slope than that obtained at lower temperatures as the gap between the two extremes (10N and 30N) is nearly $2.10^{-2}$ $mm^3$. It is clear that borate lubrication yields relatively low friction coefficients under a wide range of conditions, although the wear loss increases slightly with load and temperature. The wear behavior might arise from the varying effect of oxidation on the steel pair which in turn is a function of temperature.

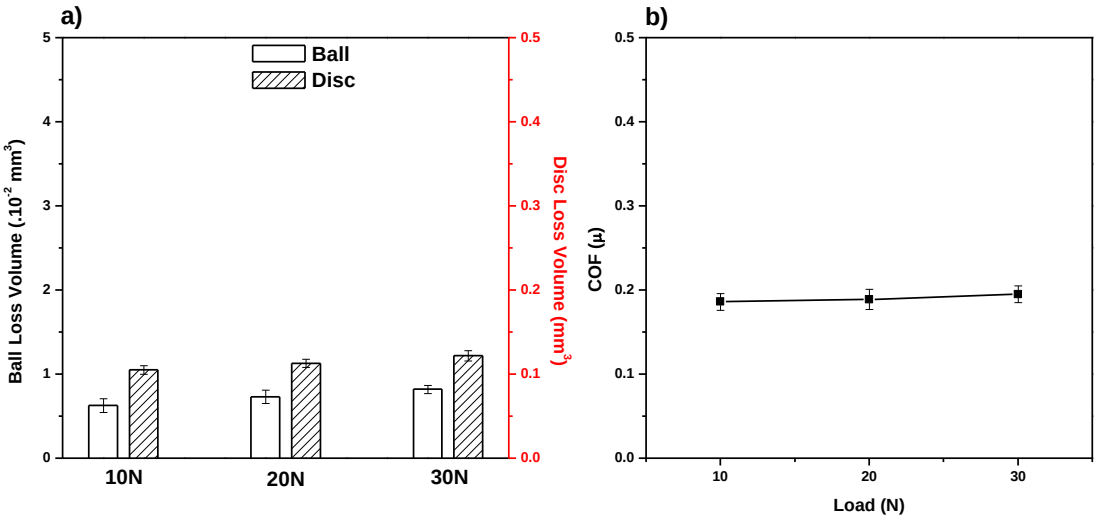


**Figure 4-4:** (a) Wear loss volumes of the tribo-pair and (b) average friction coefficients in lubricated tests versus load at 600°C.

The lubrication effects of sodium borate are clearly demonstrated by the reduction of friction coefficient and wear loss on both steel counterparts in comparison to unlubricated cases. It is noted that the normal load and the linear speed were kept constant at 30N and 0.1m/s, respectively. The evolution of friction coefficient versus sliding time of lubricated and unlubricated tests at 600$^{o}$C, 700$^{o}$C and 800$^{o}$C are displayed in Figure 4-7. During the running-in stage, the friction coefficient fluctuates considerably possibly due to the contact between the hard oxide scale while the steady state sees a stabilization in the friction coefficient. It can be observed that unlubricated sliding contact is characterized by growing friction with increasing temperature. The average friction coefficient is 0.44 at 600$^{o}$C then increases to 0.50 and 0.55 at 700$^{o}$C and 800$^{o}$C respectively. On the other hand, exposure to borate lubrication clearly improves frictional behavior by reducing the coefficient considerably at all testing temperature. Under borate lubrication, the friction coefficients converge at roughly ~0.18-0.2 with the reduction of 60%, 64% and 67% at 600$^{o}$C, 700$^{o}$C and 800$^{o}$C, respectively compared to unlubricated condition at the corresponding temperature.

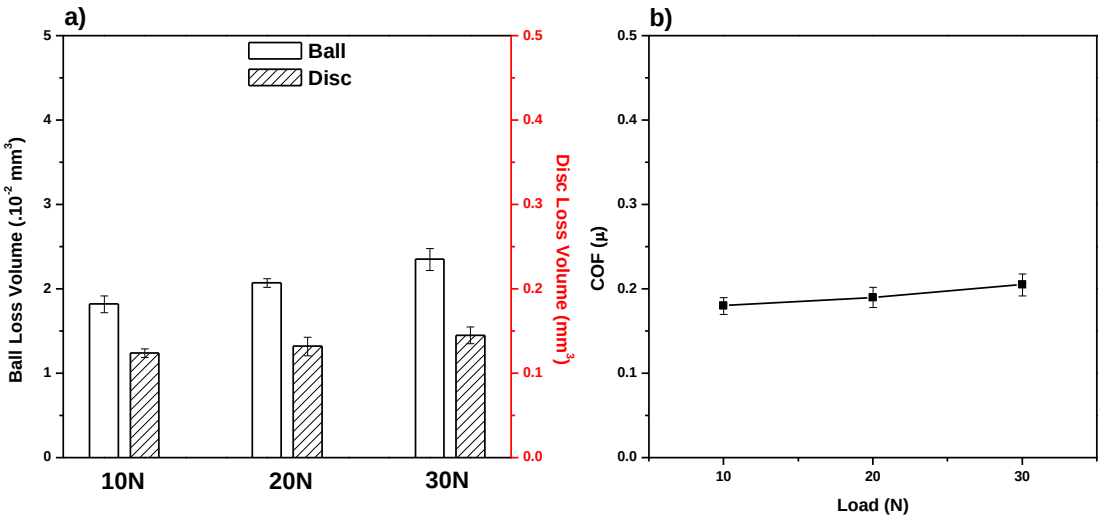


**Figure 4-5:** (a) Wear loss volumes of the tribo-pair and (b) average friction coefficients in lubricated tests versus load at 700$^{o}$C.

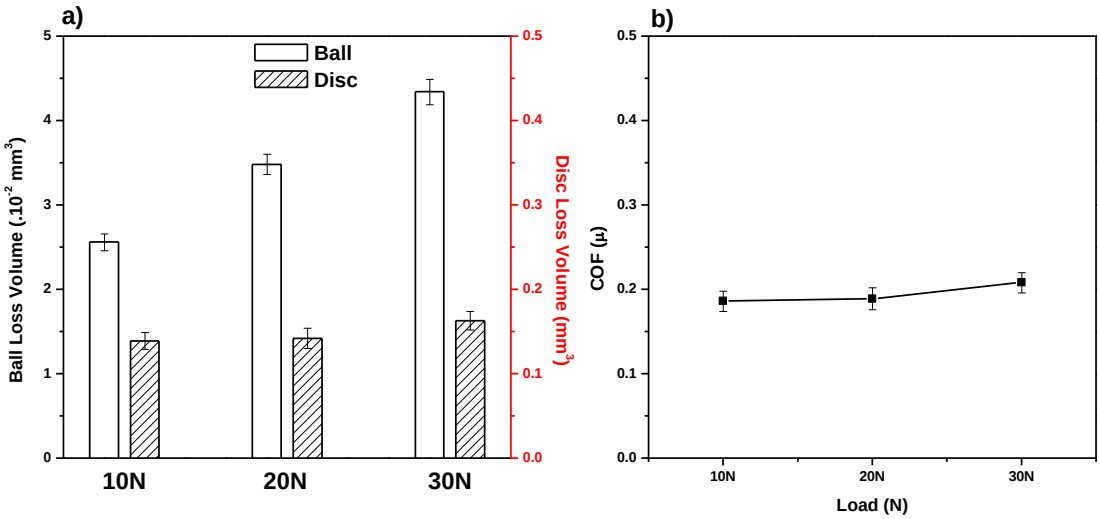


**Figure 4-6:** (a) Wear loss volumes of the tribo-pair and (b) average friction coefficients in lubricated tests versus load at 800°C.

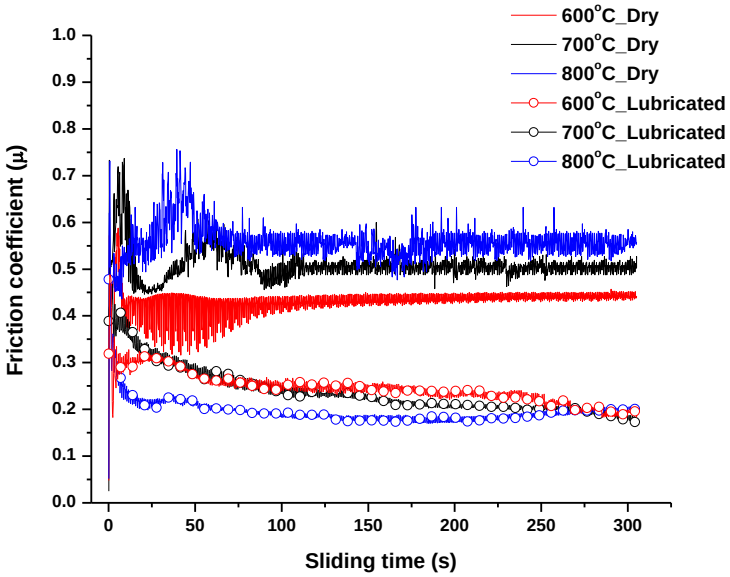


**Figure 4-7:** Friction coefficient curves of dry sliding and lubrication tests at 600°C, 700°C and 800°C (load of 30N, sliding speed of 0.1m/s).

Figure 4-8 shows the wear loss volumes of the sliding pairs in unlubricated and lubricated condition at 600°C, 700°C and 800°C. It is note that the normal load was kept at 30N while sliding velocity was set at 0.1m/s. Dry sliding yields progressive increments of the material loss with temperature on both sliding surfaces, except the loss volume on the MC disc at 800°C which is slightly over half of that at 700°C. The introduction of sodium

borate reduces significantly the wear loss on both sliding counterparts. On the ball, although the wear reduction looks subtle at 600°C, it becomes more significant at higher temperature range as the volume difference increases. Wear losses on the lubricated discs are so minor compared to what recorded in dry sliding condition that the corresponding figures have been represented in a much smaller scale to illustrate the increasing trend (Figure 4-8b). For instance, at 600°C the lubricated disc wears an amount of only 5% of its unlubricated counterpart.

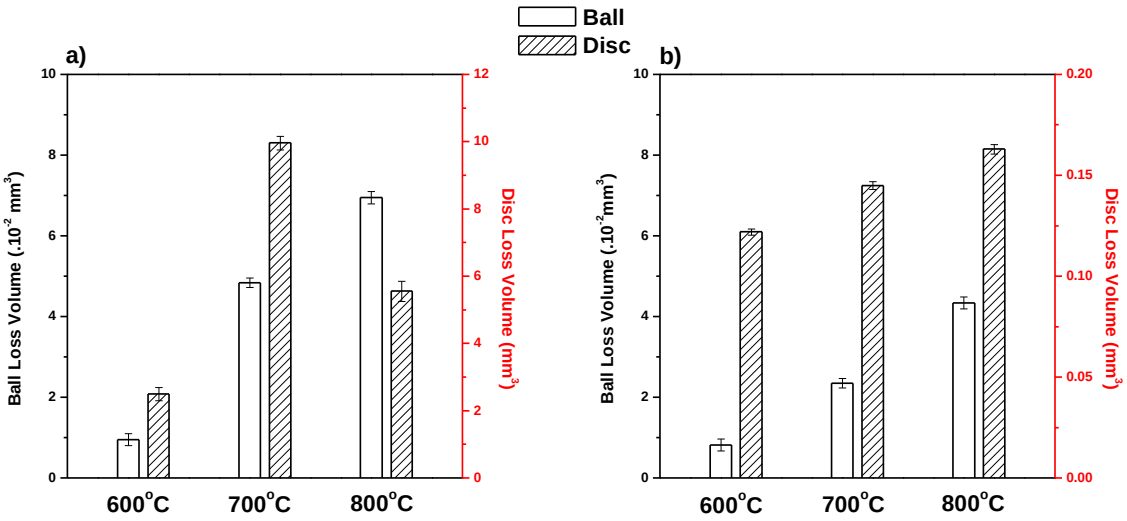


**Figure 4-8:** Wear loss volumes of the tribopair at varying temperatures in (a) dry sliding condition and (b) lubrication condition.

### 4.2.2 Analysis on the worn surfaces at 800°C

This section and the following two provide an in-depth analysis on the worn surfaces after friction test at the temperature of 800°C, those at lower temperatures can be found in Figure A-5 to A-9 (Appendices). Friction coefficient curves and wear loss volumes of unlubricated and lubricated friction tests (at 800°C, 10N, 0.1m/s) are illustrated in Figure 4-9 and 4-10. Again, it can be seen that characteristically high friction coefficient is yielded in the case of dry sliding ~0.42 while the introduction of molten sodium borate

leads to a dramatic drop of friction by approximately 58%. Through the entire lubrication test, the melt lubricant shows a steady and rapid response to sheared stress condition initiated by a 50-second running-in period. In the case of dry sliding test, worn loss volumes were recorded at $5{,}01.10^{-2}$ $mm^3$ and 2,44 $mm^3$ on the ball and the disc, respectively. The corresponding figures recorded substantial drop on both steel counterparts when exposed to the melt lubrication. On the ball, the volume loss is five-fold lower than that produced in unlubricated condition, reaching roughly $1.10^{-2}$ $mm^3$ while the degree of wear reduction registers at remarkably ~95% of that on the opposing disc.

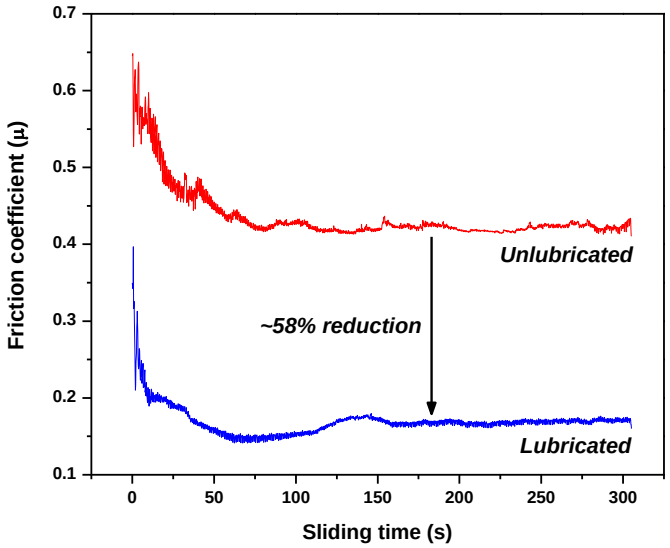


**Figure 4-9:** Friction coefficient evolution of unlubricated and melt-lubricated steel pair (at 800°C, 10N, 0.1m/s).

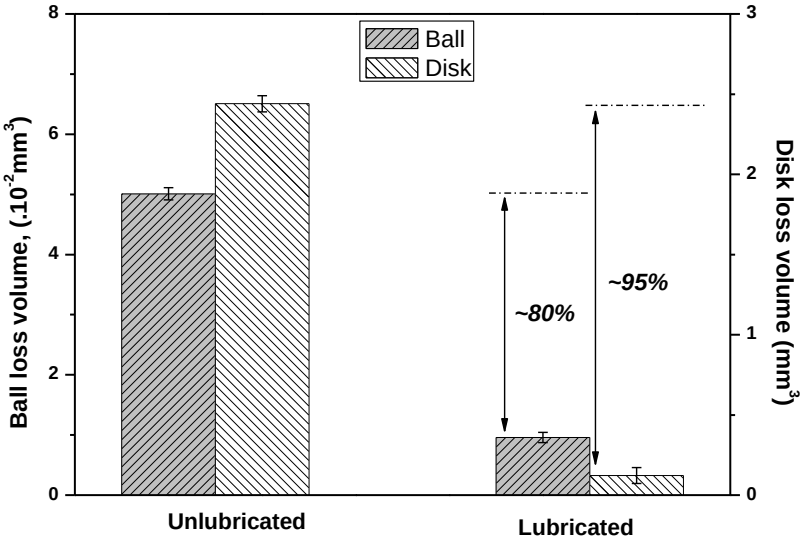


**Figure 4-10:** Wear loss volumes of unlubricated and lubricated steel pair (at 800$^o$C, 10N, 0.1m/s).

After dry sliding test, worn surface morphologies of steel tribo-pair are shown in Figure 4-11. Micrograph of the ball scar shows a variety of surface damages such as microgrooves, ploughing and plastic smearing. Across the worn area, a large amount of wear debris can be observed which can act as a third-body abrasive source. Likewise, the wear track is moderately grooved parallel to sliding direction and featured with dominant iron oxides debris. The magnified zone (in Figure 4-11b) displays a continuous and relatively smooth patch interrupted by multiple shattered fragments of oxides. This can be attributed to the dynamic formation of a compact surface glaze which is originated from sheared stress-induced agglomeration of oxides debris. Some believed that the protective glaze layer can provide a wear resistance in some extent [108, 109]. Under extreme temperature and oxygen availability, the oxidation of abrasive oxide is spontaneous, leading to the formation of Hematite ($Fe_2O_3$) which is the hardest among 3 types of iron oxide [110]. The abrasive Hematite is considered as the main component causing severe fractures on both rubbing surface. It is further evidenced by the X-ray diffraction of debris

oxides (in Figure A-2) where Hematite accounts for the majority accompanied by a small fraction of Magnetite ($Fe_3O_4$). EDS spectra of magnified zones also indicate the predominance of O and Fe on the worn surfaces of mating counterparts (Figure 4-11). The pattern similarity suggests the occurrence of adhesive wear where oxide debris was embedded into the worn area of the ball which yielded plastically. At elevated temperature, it can be deduced that dry sliding contact of steel pairs is characterized by a severe state of abrasive/adhesive wear and plastic deformation which result in high friction and substantial materials loss.

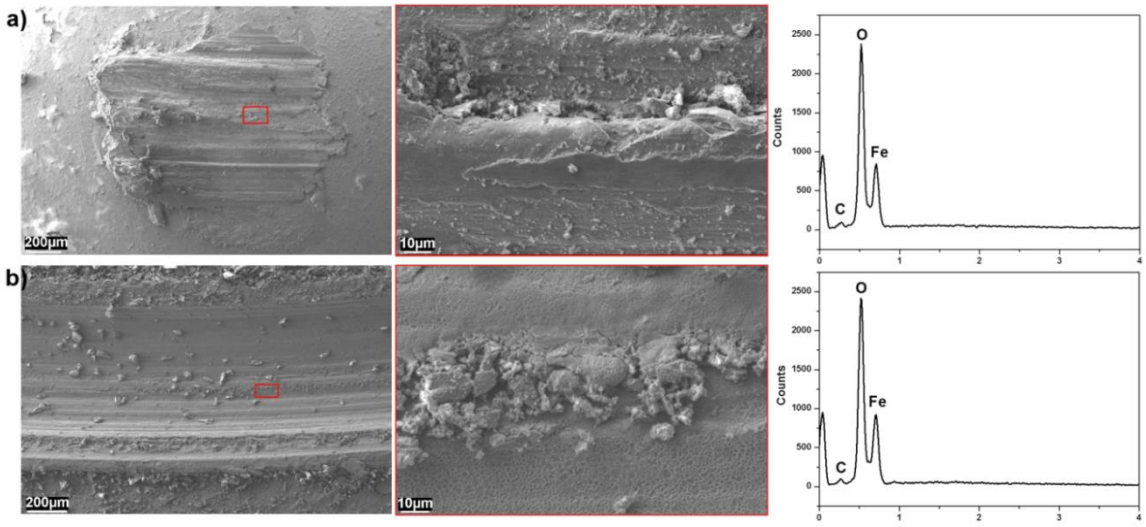


**Figure 4-11:** SEM micrographs of the worn surfaces and the corresponding X-ray spectrum after dry sliding test a) ball, b) disc.

SEM micrographs of steel tribo-pair lubricated by borate melt are shown in Figure 4-12. High-magnification image (Figure 4-12b) displays featureless morphology on the wear track except hexagonal platelets residing on a smooth and glassy surface. Those micro-platelets could be the products of borate melt recrystallization upon cooling. Across the worn scar island-like patches can be observed although it is unclear if they represent the actual morphology of the contact area. X-ray analysis points out the expected lubricant

elements (B, Na and O) on the contact surfaces with relatively weak signal from Fe which implies the presence of a relatively thick film of lubricant melt overlying the worn area. Since the borate melt remains viscous [111] after the friction test, it is likely that the molten lubricant moved back onto the worn area and visually masked the intrinsic rubbing interface. The cooled melt itself transforms into glassy solid whose appearance is clearly not related to shearing action. In order to unfold the true interface, cross-sectional observations are conducted and discussed in the following sections.

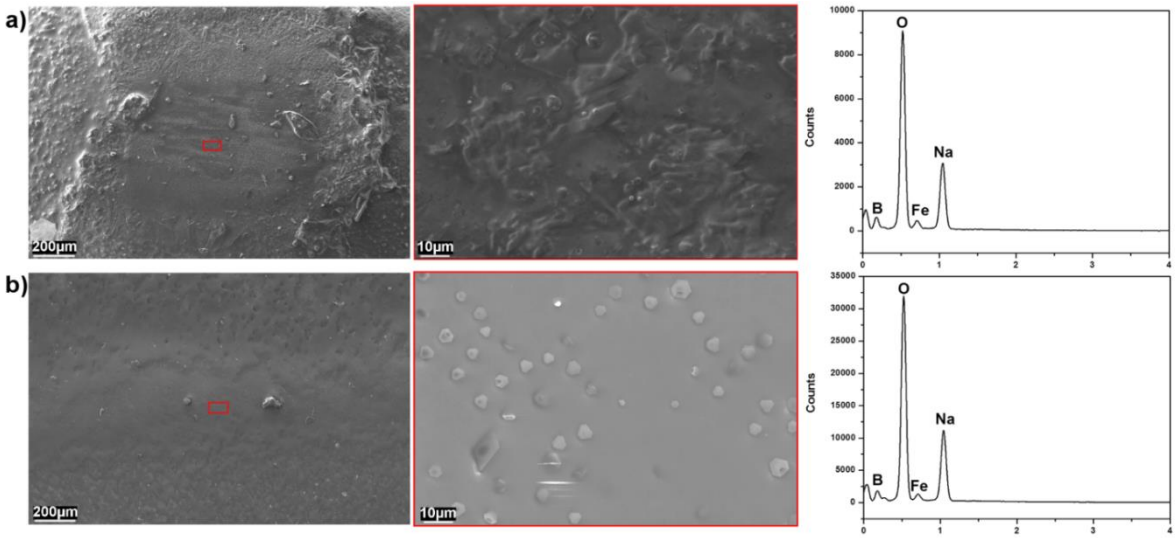


**Figure 4-12:** SEM micrographs of melt-lubricated steel components and the corresponding X-ray spectrum after friction test a) ball, b) disc.

### 4.2.3 Tribo-interface on the ball after test at 800°C

SEM image of the whole thin FIB lamellar (12µmx8µm) extracted from ball scar lubricated by borate melt is given in Figure A-3 (Appendices). As suggested from the top-view EDS analysis on the ball scar, it is confirmed that the interface is covered by an residual lubricant layer with a thickness of 4-5µm (Figure A-3). The cross-section area was selected perpendicular to the sliding direction and the interface appears very smooth. High-magnified BF image of the ball interface is given in Figure 4-13 which displays an ultra-

fine grained region above a coarser base. The nanograin layer is comprised of iron oxide with average size of 50-150nm whereas the confinement range is 200-300nm from the interface boundary. Popularly known for its intrinsically peculiar mechanical properties, the interface-controlled nanolayer can play a significant role in surface characteristics during the sliding contact. By applying Hurst filter to increase textural differences in grey scales, the ultrafine oxide grains are clearly illustrated in Figure 4-13b.

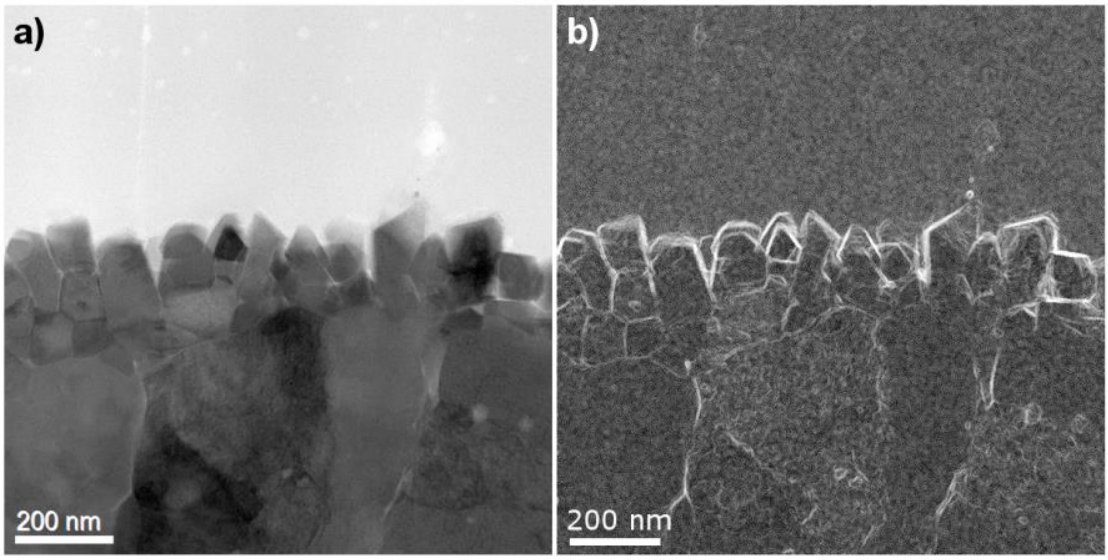


**Figure 4-13:** a) Bright Field (BF) image from the GCr15 ball interface lubricated by borate melt, b) application of Hurst filter underlining the nano-grained interface.

EDS phase mappings of the ball interface are illustrated in Figure 4-14 where three Phases are distinguished with a different chemical makeup. It is noted that Cu comes from the re-deposition of Cu grid during FIB milling which is inevitable. It is obvious that Phase 1 with the predominant composition of Fe and O, is attributed to the oxides scale on the steel ball. Phase 2 can be assigned to the residual melt which is composed of mainly Na, O and B. Accounted for the least area, Phase 3 distributes itself on the boundary region between Phase 1 and Phase 2 with an estimated thickness of 10-20nm. The interfacial film

runs along the outer boundary of the ultrafine grains layer and consists of Na, O, Fe, C and possibly B. EELS characterizations were conducted across the interface region to determine the chemical fingerprints of B-K edge and C-K edge, the resultant spectra and that of the melt reference are shown in Figure 4-15.

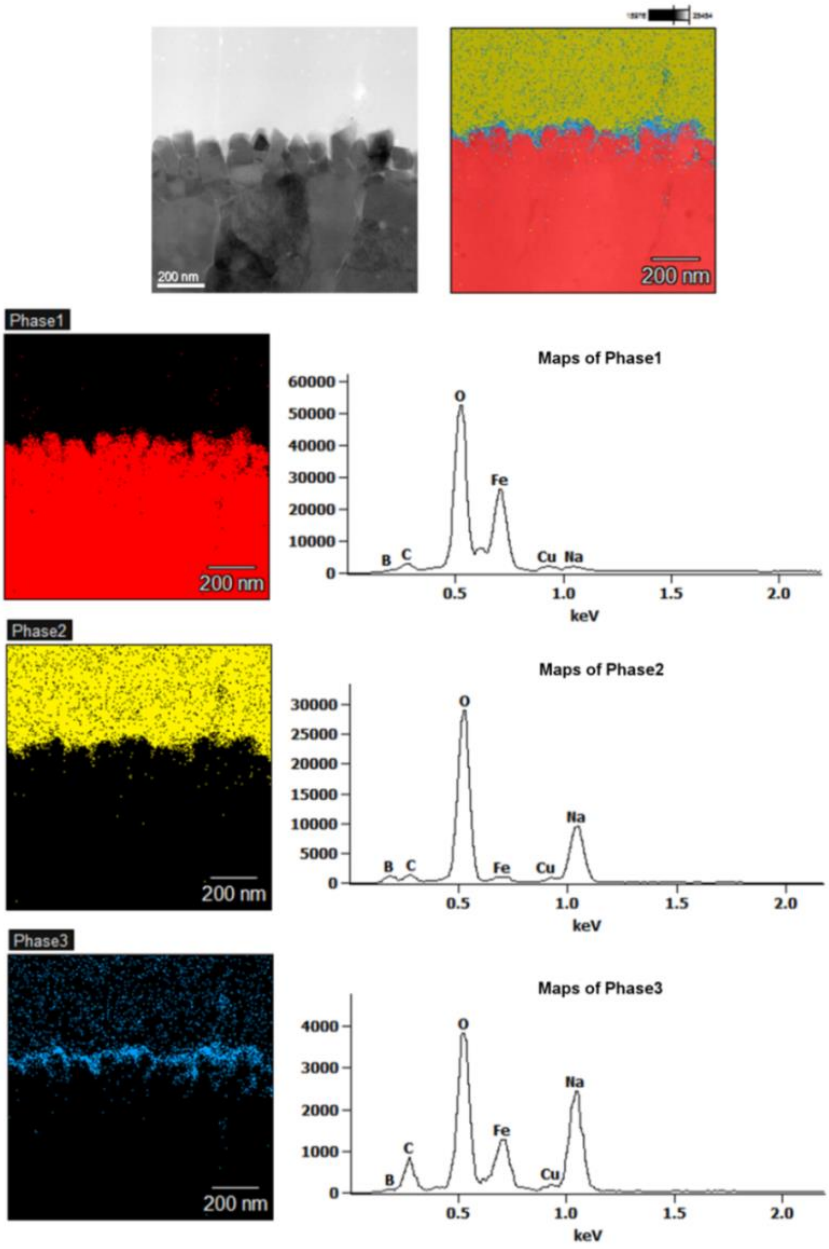


**Figure 4-14:** EDS phase mapping with corresponding composition spectra of the ball interface.

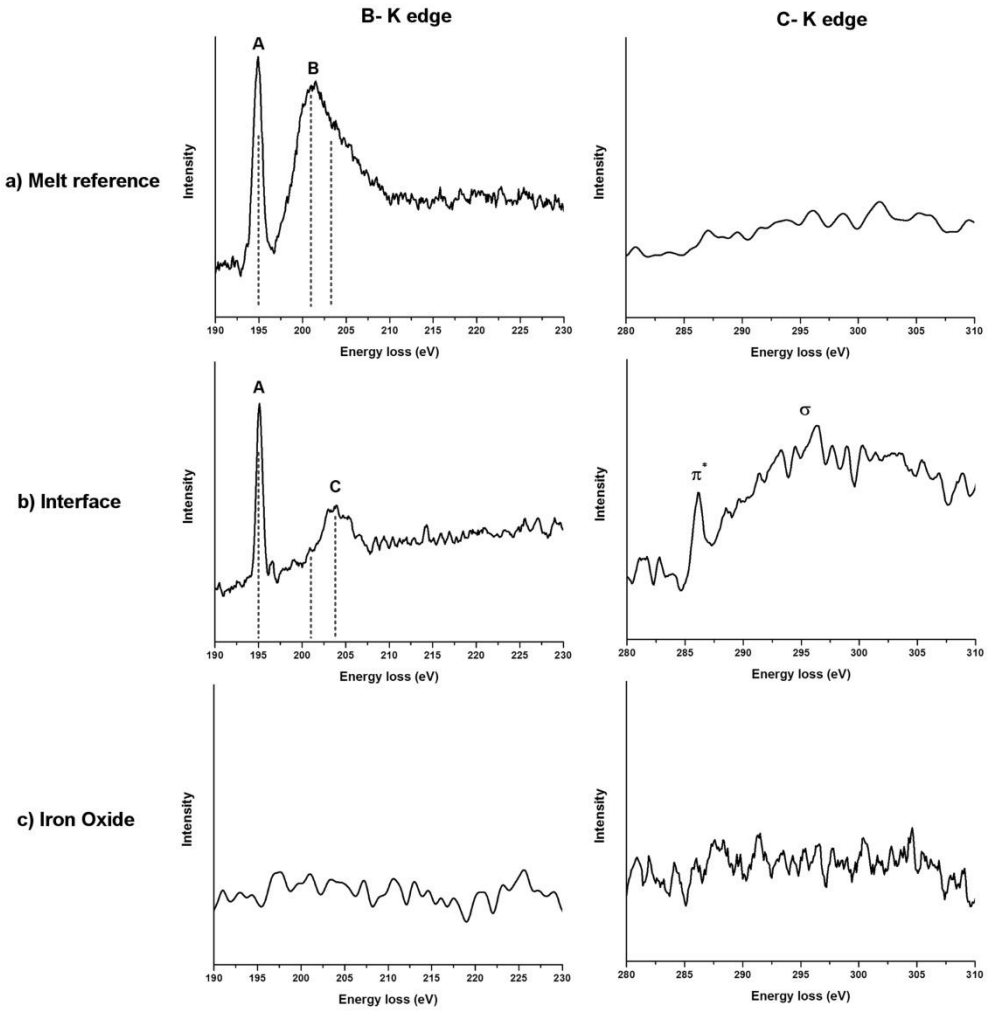


**Figure 4-15:** Extracted EELS spectra of B-K edge and C-K edge from a) melt reference, b) interfacial film (Phase III) and c) iron oxide.

The fine structure of Boron-K edge have been previously resolved with characteristic peaks referring to 2 different configurations of $BO_3$ and $BO_4$ by means of EELS [112, 113]. Previous studies have shown that an intense π* peak at 194eV is assigned to the transition of 1s electron to unoccupied $p_z$ orbital which defines trigonal $^{[3]}$B units, whereas σ* peak at 198.6 eV typically represents tetrahedral $^{[4]}$B units. Peak located 204 eV is mainly associated to three-fold coordinated $^{[3]}$B.

In Figure 4-15, it can be expected that the spectrum from the oxide base without the inclusion of Boron and Carbon, reveals no sign of excitation edge from the elements. The

melt reference spectrum displays a sharp peak A located at 194.8eV followed by a broad hump B with maximum intensity at 202eV (Figure 4-15a). The spectrum shape provides a strong indication about the co-existence of trigonal $^{[3]}B$ and tetrahedral $^{[4]}B$ in the structure of alkali borate glass which is consistent with past studies [114, 115]. In contrast, the spectrum extracted from interfacial film (phase 3) shows an intense peak A at 194.8 eV followed by a broad peak C at 204.2 eV which implies the predominance of planar $BO_3$ within the film composition. The conversion from $^{[4]}B$ to $^{[3]}B$ could be a result of tribochemical reaction. Regarding Carbon, the resultant spectrum suggests the formation of amorphous carbon in the interfacial film (phase 3). The peak located at 286eV is due to the transitions from core 1s state to the π* state followed by a broad peak which is associated to the transition from 1s to σ* state [116, 117]. It is likely that the origin of C arises from decaburization which will be discussed in the following section. It is noted that spikey appearance might be due to partial radiation damages (from intense electron beam) as the glass lubricant is intrinsically non-conductive.

### 4.2.4 Tribo-interfacial on the disc

A FIB thin lamellar (9µmx6µm) of the tribo-interface on the disc is shown in Figure A-4 (Appendices) and the rubbing surface appears rougher than that on the ball. A relatively thick layer of residual melt (2-3µm) can also be observed. Figure 4-16 illustrates a STEM BF image of the disc interface with the corresponding EDS mapping. The formation of a tribofilm can be seen as a continuous and homogenous layer with an approximated thickness of 50-60nm. Close examination suggests that the tribofilm consists of structural layers which can be distinguished by a contrast difference. Elemental mapping of Fe and

melt compositions (except B) are provided to determine their distributions across the tribofilm. Fe is predominantly found in the oxide scale while it is less likely to be included in the tribofilm as well as the residual melt. Apart from homogenous distribution among the residual melt, it is clear that Na heavily concentrates onto the lower region of the tribofilm. On top of that, it is most notable that O is significantly deprived in the tribofilm bulk in comparison to both the residual melt and the underlying oxide scale.

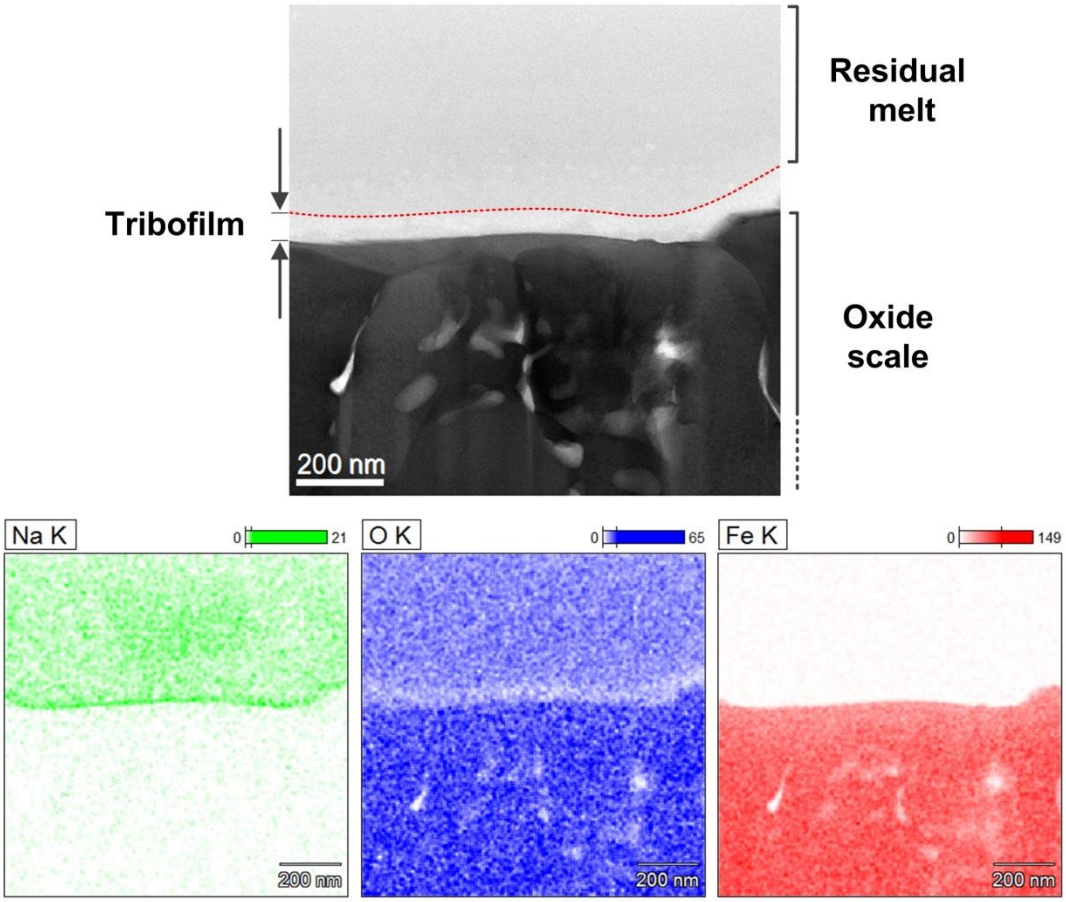


**Figure 4-16:** BF image of the tribofilm generated on the ball and the corresponding EDS mapping.

In order to visually underline the layered structure of the induced tribofilm, HAADF imaging was employed and shown in Figure 4-17. Apart from boundary region, the residual melt presumably contains a homogenous composition from point to point,

exhibiting a uniform contrast. However, a bi-layer structure can be seen in the tribofilm (Figure 4-17b) where the upper layer (II) appears darker than the underlying counterpart (I). In accordance to EDS mapping, it can be deduced that the bottom layer corresponds to the Na-rich region. In addition, it is very likely that the top layer is composed of highly-concentrated light elements characterized by its stark contrast compared to the remaining regions. On the basis of HAADF imaging, the contrast disparity not only suggests compositional differences but also indicates a concentration gradient of heavy/light elements. A representative EDS line scan is given to determine intensity profile across the boundary film of O, Na and Fe (Figure 4-17c). It can be seen that O is significantly depleted within the tribofilm bulk whereas the intensity of Na suddenly increases followed by an abrupt drop when it comes to the oxide substrate. By the combination of EDS and HAADF imaging, the local chemical structure of the bi-layered tribofilm can be revealed and discussed in details in the following section.

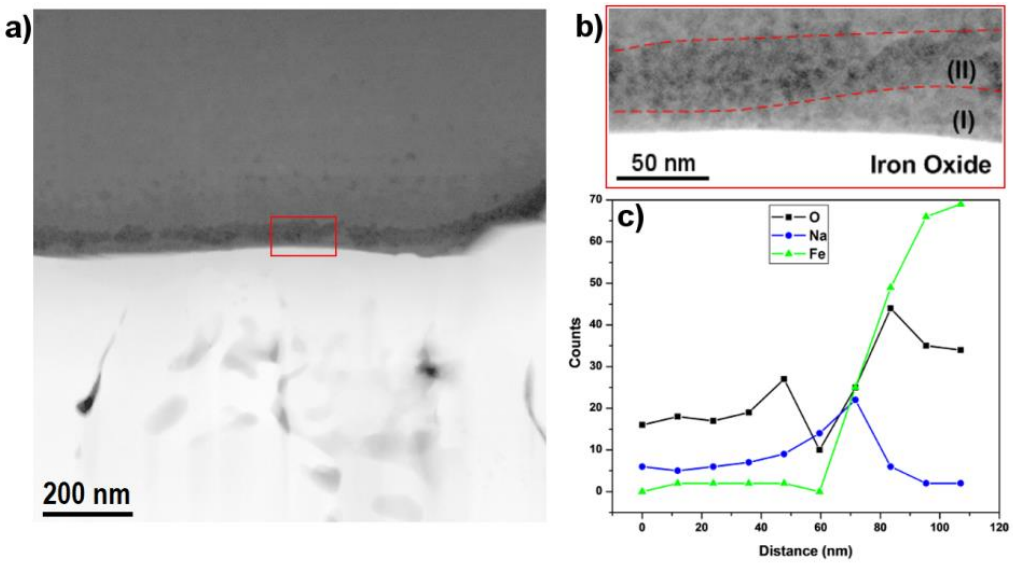


**Figure 4-17:** HAADF image of the tribo-interface generated on the disc (a), detailed image of the dual-layered structure (b) and EDS line scan across the tribofilm (c).

## 4.3 Discussions

The current chapter presents a good lubrication properties of inorganic sodium borate above its melting temperature. The lubrication performance is demonstrated by a considerable reduction in friction coefficient and wear loss over a wide range of testing conditions on the steel tribopair. In order to understand the mechanism of melt lubrication, the physical chemistry aspect of the molten inorganic poly-oxides deserves further consideration. In the molecular structure of sodium borate, there is coexistence of covalent bonding and ionic bonding: the former one is largely attributed to B-O linkage while the latter refers to O-Na interaction. Upon melting, the compound transitions from a rigid state into a highly viscous liquid. The melt viscosity drops progressively with temperature which is associated with a gradual breakdown of the large anionic segments within the glassy network [118]. Eventually, the vitreous melt is characterized by the formation of charged individuals: cationic Na and anionic B-containing units (predominantly $BO_3^{3-}$). The ionic disassociation has been previously proven by the increased electric conductivity at the molten state [118, 119]. The lubricant melt thus could be considered as a high-temperature ionic liquid which dictates the tribological responses.

As illustrated in the TEM images, there appears a bi-layered tribofilm generated on the disc interface after the friction test. The chemical composition of each layer is correlated to different response of ionic components under shearing effect at high temperature. It is evidenced by EDS mapping that the Na-dense layer (~10-20nm thick) is the foundation of the bi-layered structure. The oxide surface is expected to be rich in electron to attract the Na ions in the lubricant melt. This could stem from exo-electron emission [120] or the

intrinsic chemistry nature of the oxide scale at high temperature [7]. Generally, the bottom layer plays a critical role in the properties of a boundary film, notably governing the adhesion strength between that film and the underlying surface. Within the tribofilm structure generated by Zinc Diakyldithiophosphate – the most widely used additive in engine oil, the Sulfur-concentrated layer is accountable for the extreme pressure tolerance and increased scuffing resistance [121, 122].

Since the observation of Boron distribution by EDS mapping is difficult due to its low atomic number, HAADF imaging was used as an alternative approach. With a high sensitivity towards Z-number differences reflected by an image contrast, the technique is capable of distinguishing elements with great Z disparity and providing the concentration gradient. It is shown by X-ray spectra and EELS analysis that the melt lubricant is comprised of B, O and Na with an increasing atomic number Z = 5, 8 and 11, respectively. From HAADF image of the disc interface (Figure 4-17), a stark contrast between oxide base and the overlaying glassy film can be seen as the substrate appears much brighter than the remaining region. These arise from the presence of Fe in the oxide scale which is much heavier (Z=26) than any other melt elements. Within the tribofilm, the dual layers exhibit different contrast as the upper layer is darker than its underlying counterpart. This explicitly points to the inclusion of light element in chemical makeup with a greater concentration compared to other areas. In accordance to EDS analysis, the base layer is assigned to be Na-rich and the whole bi-layered tribofilm is considerably deprived of O. Furthermore, since B is the lightest element among the tribosystem, it is plausible that the upper layer is mainly compounded of vitreous boron oxides. The upper layer is then highly-concentrated in B but heavily depleted in O. This is a possible indication of

polymerization occurrence under the effect of stressed shearing. In principle, B exists in its most stable form when screened by O atoms in inorganic boron oxides [123] and the polymerization can be triggered through additional formation of bonding-oxygens. An illustrative schematic of the tribologically-driven process is proposed in Figure 4-18. The self-adaptation behavior can be considered as a smart response of the tribofilm to accommodate the shearing stress. The upper layer thus dominates the anti-wear capacity due to an increased cohesive strength of the tribofilm bulk. Besides, the friction reduction capability of the tribofilm can originate from the amorphous nature of the tribofilm. The O depletion not only provides reasonable evidence about the possible polymerization in the tribofilm, but also underlines the potential anti-oxidation.

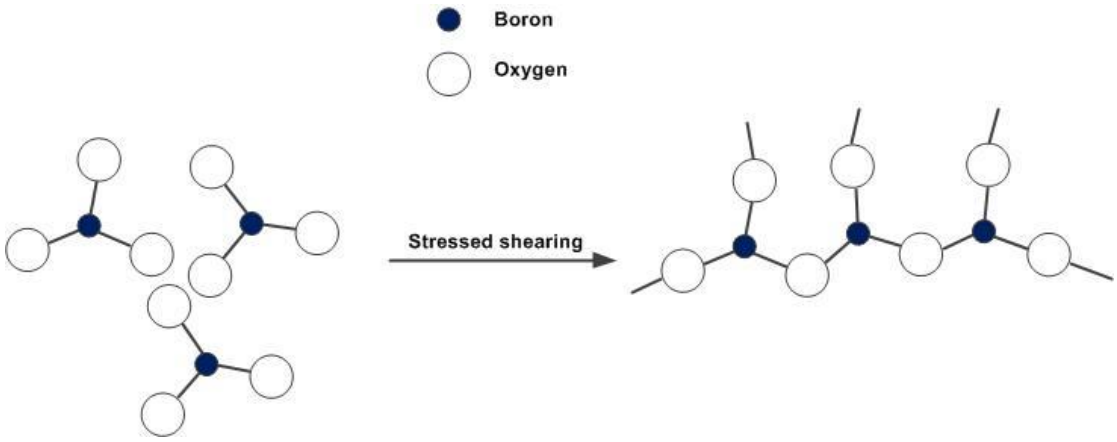


**Figure 4-18:** Simplified schematic of tribologically-induced polymerization in borate tribofilm

On the opposing contact surface, the interface structure is also complex with the formation of ultra-fine grained iron oxides beneath a boundary thin film. While the overlying film comprises mainly lubricant elements, the nano-grain oxide layer can also plays a crucial part in the properties of the sliding interface. It could be due to the combined effects of oxidation and surface deformation at high temperature. Ultrafine-

grained materials have been known for their unusual mechanical features including high yield strength, excellent impact toughness and good fatigue strength [124-126]. Superior mechanical characteristics are associated with the substantial boundaries density within the microstructure. Herein, the nano-grained oxides (average diameter of 50-150nm) can significantly enhance the mechanical strength of the rubbing interface and consequently increase its wear resistance [127, 128]. As shown previously, the astonishing smoothness observed can be attributed to the improved wear resistance when asperities contacts are minimized under such surface quality. The nanoscale grains neatly arrange themselves on the interface within a refinement range of ~200-300nm without being scattered outwards. Apart from reinforcement capacity, nano-size grains are also characterized by high boundary diffusion coefficient [129, 130] which can contribute to the complex chemistry of the overlying film. The film is chemically made up with expected melt elements (B, O, Na) with Fe and C. The inclusion of C and Fe could stem from the effect of high temperature as this always induces outward diffusion of Fe and decarburization. As the GCr15 ball consists of approximately 1% C, decarburization is reasonably likely [9]. The decarburization process corresponds to competitive oxidation of solute [C] species in the steel base which produces a mixture of carbonaceous gases as: $[C] + Fe_xO_y \rightarrow Fe + CO/CO_2$. Under the effect of constant tribological exposure and tremendous heat, complex reactions can take place which eventually transforms carbon-bearing gases into amorphous carbon. In the tribofilm, the amorphous carbon is considered intrinsic, given that thin lamellar was constantly kept in the vacuum condition until TEM examination, contamination was therefore very negligible. This is also supported by the total absence of C in the oxide scale as well as in the upper residual film indicated by the EELS analysis.

TEM micrograph of the steel substrate extracted from the ball scar displays continuous voids along the scale/steel base interface (Figure 4-19). Outward diffusion of iron through interstitial sites is considered rate-determining stage in scaling process when the oxide scale thickens [7]. Again, the nanograins can accelerate Fe diffusion and subsequently incorporate it into the tribofilm. With a variable coordination number, Fe has been known to increase the network connectivity of the glassy film which results in an increased strength [131]. As previously shown, the conversion from $BO_4$ to $BO_3$ is apparent which can be explained by the favorable formation of easy-to-shear species under sliding ($BO_3$ has much lower shearing strength than $BO_4$ due to its planar structure).

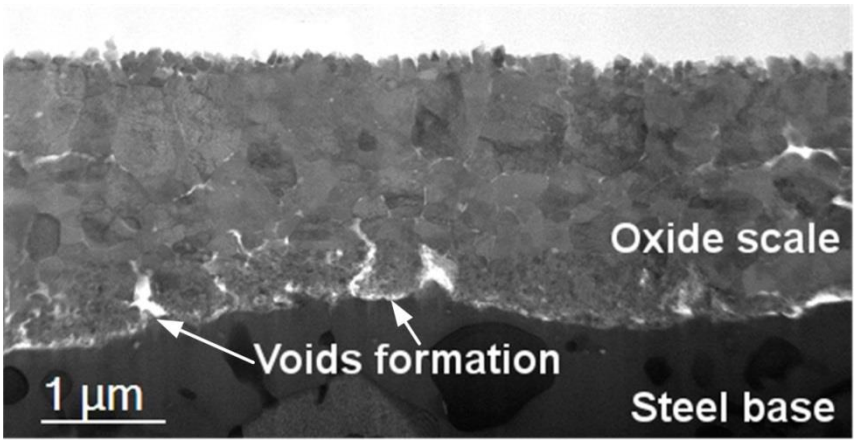


**Figure 4-19:** BF image of cross-sectional scale/steel interface of GCr15 ball after friction test.

Under borate lubrication, the boundary interfaces are microstructurally and chemically complex (Figure 4-20), due to tribological responses of borate which related closely to its physical chemistry at high temperature. There are some difficulties in attempting to understand the tribological reactions at this extreme condition. The highly kinetic aftermath has great chances to distort the actual state of the tribofilm structure. By

retrieving the steel components promptly after friction test, the interfaces were presumably "freezing" which makes subsequent analysis highly credible.

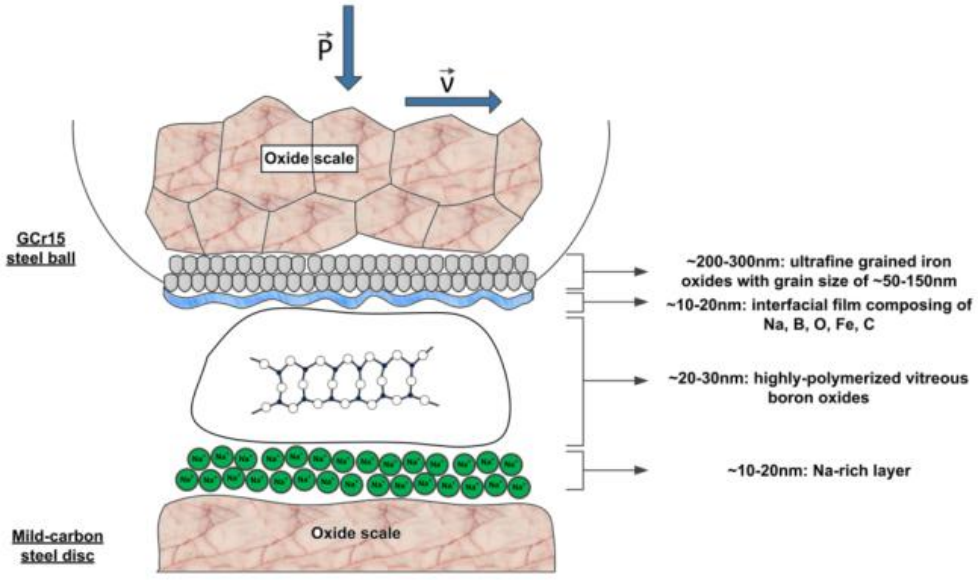


**Figure 4-20:** Simplified chemical structure of borate tribofilm and participating interfaces

## 4.4 Conclusions

Tribological performances of inorganic sodium borate were investigated by pin-on-disc testing over a wide range of conditions. Further analysis was carried out to reveal the chemical and microstructural complexity of the interfaces at 800°C. The concluding remarks can be found as followed:

- Sodium borate exhibits a very good lubricating properties above its melting point which is demonstrated by a significant reduction in friction and wear loss volume;
- On the disc surface, a dual-layered tribofilm is observed with a total thickness of ~50-60nm. While the lower part is enriched by Na, the increased concentration of B in the upper part indicates potential polymerization reaction under tribological stimulation;

- On the ball surface, a tribofilm composing of Na, O, B, C and Fe overlays on an ultra-fined oxides scale. There is a conversion from $BO_4$ into $BO_3$ species in the vitreous film;
- The physical chemistry of borate melt plays a critical role in its tribological responses.

# CHAPTER 5:

# Interface reaction of borate melt/oxidized steel and the anti-oxidation capacity of lubricant melt

** This chapter content was published in Corrosion Science, 2018, 140, 231-240.*

Like other engineering operations that involve high-temperature exposure, oxidation management is very critical in the hot rolling of steel, although it is sometimes overlooked. The intensive growth of oxide scale during reheating and subsequent deformation process accounts for a substantial amount of material loss. From a tribological perspective, oxide scale is considered as the major origin of abrasive/adhesive wear that deteriorates the surface conditions of both mating surfaces and increases chances of seizure [132]. After rolling, the unwanted oxide scale on the workpiece is often hard to remove, which requires costly downstream processes (such as pickling).

Fundamentally, the nature of oxidation depends on a number of factors including temperature, exposure duration, chemistry of the substrate and the corroding environment. The majority of oxidation sequences take place at the phase boundary with heterogeneous reactions. Glass-based coatings have been used to improve the high-temperature oxidation resistance of many alloys and steel [58, 60, 61]. The coating is expected to act as a hermetic seal which can physically separate metal substrate and oxidizing offenders. Apart from the restriction of oxygen diffusion through the coating bulk, redox reactions at the coating/base boundary result in the formation of an interlayer which governs the oxidation

kinetics. Ideally, the interlayers are characterized by a low oxygen diffusivity while their formation is based on thermodynamically-favored reaction which further inhibits corrosion of more valuable elements in the substrate [57, 59, 63-67, 133, 134]. Although there are plenty of studies associated with static oxidation at high temperature, only little attention is spent on the oxidation of sliding surfaces.

The present chapter discusses the chemical nature on the borate melt/oxidized steel interface and the influences of shearing stress on that particular confined region. As tribofilm formation was acknowledged previously (Chapter 4), further insights on the anti-oxidation capacity of such thin film are also given.

## 5.1 Experimental details

### 5.1.1 Material preparation

In the high-temperature friction test, material selection was kept the same as it was presented in Chapter 4 (GCr15 as the ball and mild steel as the disc). Surface conditions of the steel pair also remain unchanged. Aqueous solution of 5%wt. of sodium borate was prepared for the friction test.

### 5.1.2 Oxidation and tribological test

Both static oxidation test and tribological test were carried out on the UMT2-CETR ball-on-disc tribometer. Testing temperature was selected at 800$^{o}$C while the load was kept at 10N with a sliding speed of 0.1m/s. During lubrication test, the lubricant was fed onto the disc 2mins prior to contact engagement. Distilled water is only considered as a carrier which immediately vaporizes when the lubricant reaches the heated disc. The remaining

borate certainly melts at the testing temperature (given its transition temperature is 525$^{o}$C). After sliding test (which lasts 5mins), the steel disc was immediately retrieved and cooled in air to avoid further oxidation. It can be predicted that there are 2 distinct areas on the disc after test: non-contact and contact. The former is associated with the region where oxidized steel is coated with borate while the latter one refers to the worn track where the borate/steel interface was subject to shearing exposure.

### 5.1.3 Characterizations

The majority of characterization tools used in this chapter is similar to what described in section 4.1.4. In addition, Secondary Ion Mass Spectroscopy (SIMS) analysis was performed on a CAMECA IMS 5FE7 to determine elemental distribution across the lubricated interface, particularly B which is difficult to detect by EDS mapping. A focused 5.0keV $Cs^{+}$ primary ion beam with a current of 100nA was employed over a raster of 180x180 $\mu m^{2}$ area. The depth profile was obtained from sputtered $MCs^{+}$ (where M is B, Na and Fe) to minimize potential matrix effects.

## 5.2 Interfacial reaction between borate melt and oxidized steel

Figure 5-1 shows the top-view surface microstructure from non-contact area on the tribo-disc. It can be seen that the surface morphology appears glassy and smooth. The X-ray spectrum clearly indicates melt elements such as Na, O and B while Fe is not detectable. From the cross-sectional view (Figure 5-2), the total thickness of borate deposition is around 50μm.

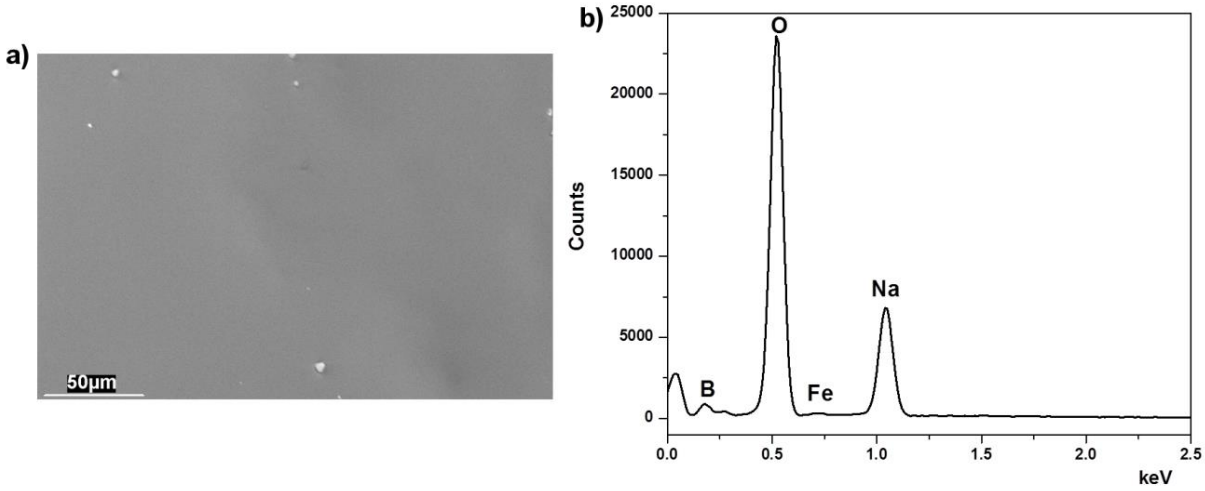


**Figure 5-1:** a) SEM micrograph of borate-coated oxidized steel from non-contact area and b) the corresponding EDS spectrum.

As the oxidation sequences occur mainly at the phase boundary, Figure 5-3 illustrates a STEM-BF image of the interaction zone (marked in Figure 5-2) together with the EDS phase and spectrum. From the BF image (Figure 5-3), there are 2 different phases which can be distinguished from their contrasts. The bright phase which looks uniform, is likely associated with the borate coating while its darker counterpart can be assigned to the oxide scale. EDS spectra were provided to differentate compositionally the contributing phases. According to the spectrum, Phase 1 with predominant composition of Fe and O is clearly attributed to the grown oxide scale. In contrast, Phase 2 consists mainly of B, Na and O which can be ascribed to the borate melt. At the glass/scale interface, a substaintial amount of sub-micron particles are in contact with the borate phase. Fluxing behavior of the borate melt is clearly illustrated as a fraction of borate melt infiltrates into oxide scale while the oxide particles appear to be pulled out of the substrate at the same time. This phenomenon could result in interface roughening which was shown in Figure 5-2. It is noted that the increased vertical intensity (top-to-bottom) is attributed to the increased thickness from the top to the bottom of the thin lamellar, rather than an intrinsic feature of the interface.

.

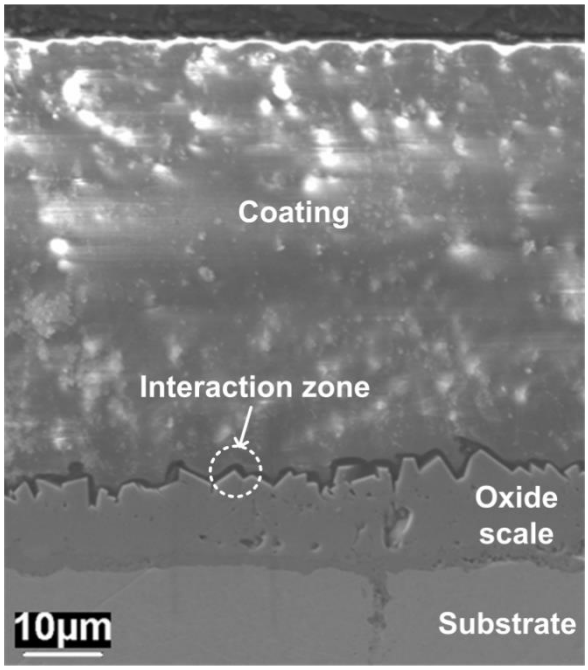


**Figure 5-2:** Cross-sectional view of borate-coated steel

In order to examine the immediate interface between the borate melt and oxide scales, BF image of higher magnification with corresponding EDS mapping and line scan are given in Figure 5-4. It is clear that O is present in both phases with a higher concentration in the iron oxide than that of the borate melt. In addition, there is a very small amount of Fe in the melt. Apart from uniform distribution in borate phase, it is notable that Na concentrates heavily on the interface of iron oxide as a continous thin film. The sudden increase of Na signal when it comes to the iron oxide interface justifies the presence of Na-rich film in Figure 5-4. This interface layer could be the result of heterogenous reaction between borate melt and iron oxides that governs the dissolution characteristic. Selected Area Electron Diffraction patterns from borate and oxide phase are shown in Figure 5-5a and 5-5b, respectively. As expected, the diffuse ring pattern (Figure 5-5a) reveals the amorphous nature of borate melt whereas the spot-like pattern (Figure 5-5b) is attributed to the (1 0 0) and (1 1 0) planes of cubic iron oxides.

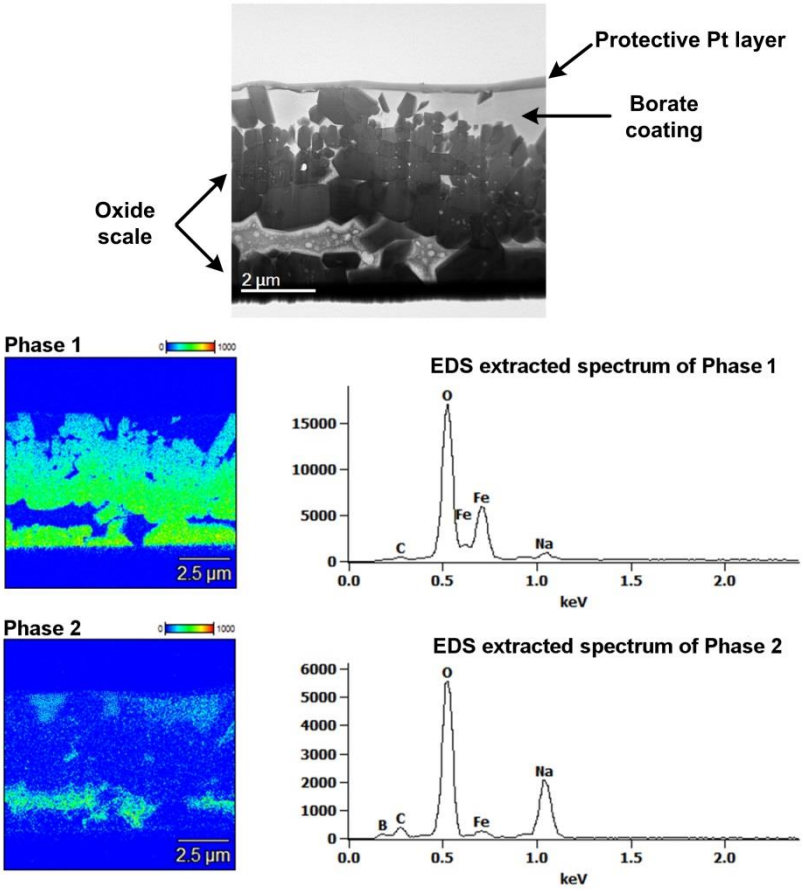


**Figure 5-3:** STEM-BF image of the borate-steel interface from unworn area and the corresponding phases determination with EDS spectrum.

Due to the limited sensivity toward X-ray detection, EELS was employed to identify the distribution of B and its intensity profile across the phase boundary is given in Figure 5-6a. It is clear that there is almost no trace of B in the oxide scale while the element becomes significantly abundant in the borate phase. Figure 5-6b presents the energy loss spectrum of B-K edge in the borate phase. There is a sharp peak located at 194.8eV followed by a broad hump B with maximum intensity at 202eV. The intense π* peak at 194e.8V corresponds to the transition of 1s electron to unoccupied $p_z$ orbital which defines trigonal $^{[3]}$B unit while the subsequent broad hump indicates a possible co-existence of trigonal $^{[3]}$B and tetrahedral $^{[4]}$B [114, 115]. Elemental distribution and microstructure characterization

suggest a potential interface reaction and microscopic fluxing of the protective iron oxide scale in the hot corrosion of borate melt.

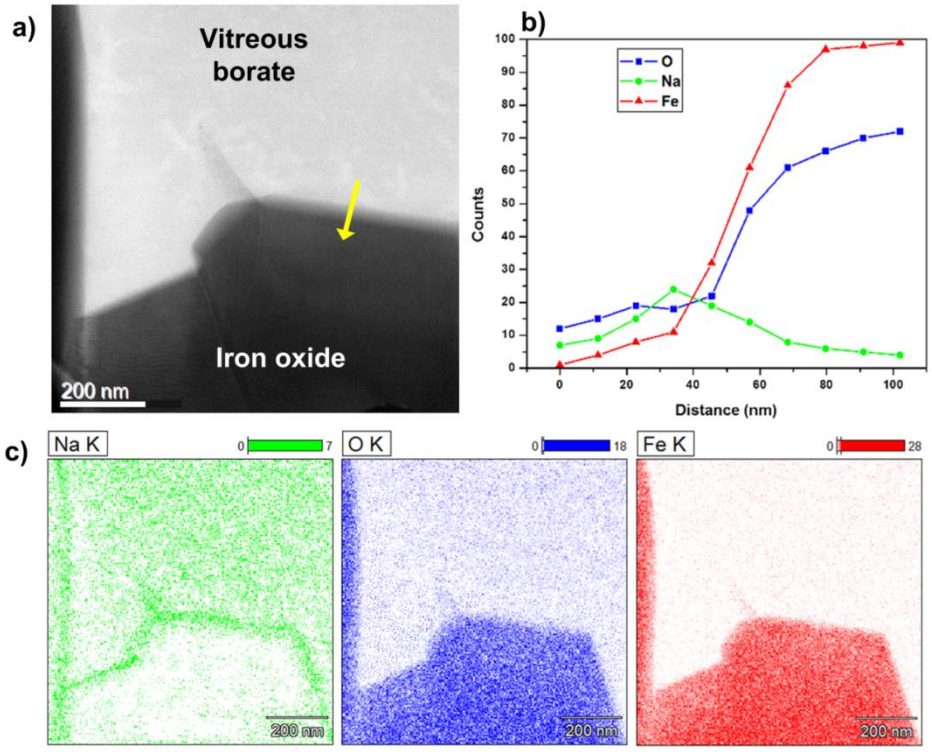


**Figure 5-4:** a) STEM-BF image of the borate-steel interface from unworn area, b) a scan profile across the interface and c) corresponding EDS mapping of Na, O and Fe. (Yellow line indicates scanning direction)

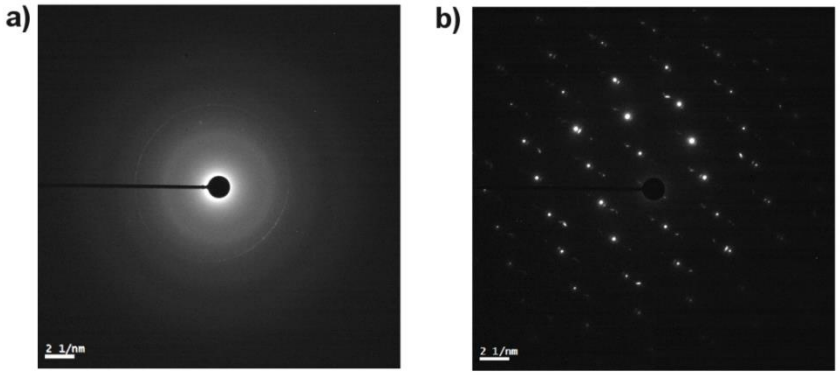


**Figure 5-5:** Electron Diffraction pattern of a) borate melt and b) oxide scale.

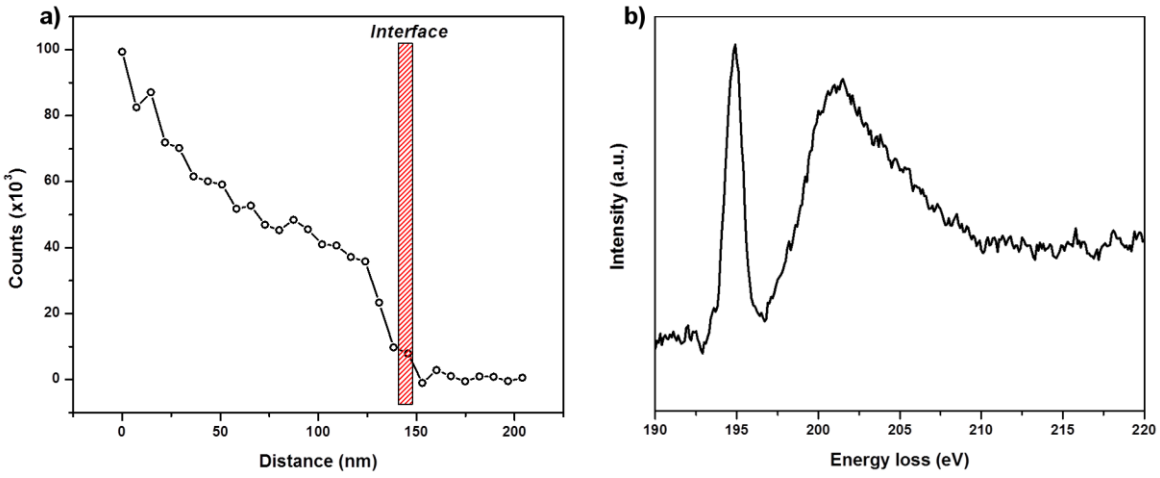


**Figure 5-6:** a) EELS B-K edge intensity profile of B across the interface and b) EELS spectra of B-K edge of the borate melt.

## 5.3 Effect of stressed shearing on the interface chemistry

The surface morphology of the area under tribological exposure is shown in Figure 5-7. The worn surface looks smooth while X-ray spectrum points to the presence of lubricant melts and Fe. In comparison to the coating case where Fe is very weak, this arises from a thin deposition of the borate melt on the wear track (<1µm, shown in Figure A-4) after the ball-on-disc test.

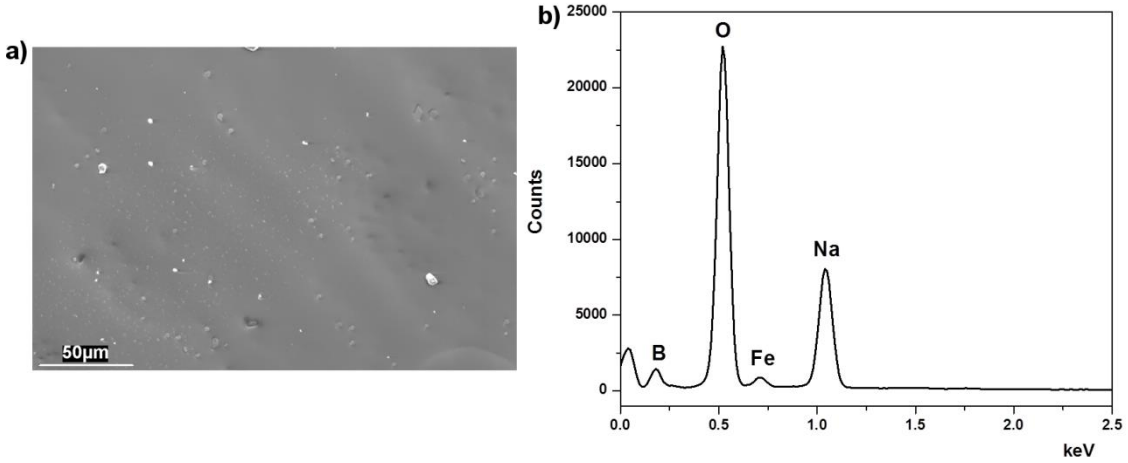


**Figure 5-7:** a) SEM micrograph of the wear track lubricated by borate and b) corresponding EDS spectrum.

Figure 5-8 details the STEM-HAADF image of borate-lubricated interface with corresponding EDS mapping and line scan. Although already presented in Chapter 4, it is worth recalling the image that highlights the effects of tribological exposure on the chemistry of borate/oxidized steel interface. A tribofilm (50-60nm) is found residing on top of the iron oxide surface. Similar to what observed in out-of-track area, Na highly localizes on the iron oxide interface as part of the inherent interfacial reaction. However, it is noteworthy that the boundary film is significantly depleted in O (Figure 5-8c) which was not seen in the case of static oxidation. A representative scan line across the interface further confirms an abrupt decrease in the intensity of O in the tribofilm bulk. As borate becomes viscous at testing temperature, it is likely that out-of-track melt flows into the worn area and eventually form a residual layer after the high-temperature test. By assuming uniform elemental distribution in the residual layer, compositional differences between the tribologically-generated boundary film and the reference glass bulk can be demonstrated. Therefore, it can be deduced that the interface chemistry experienced remarkable changes induced by the shearing effect.

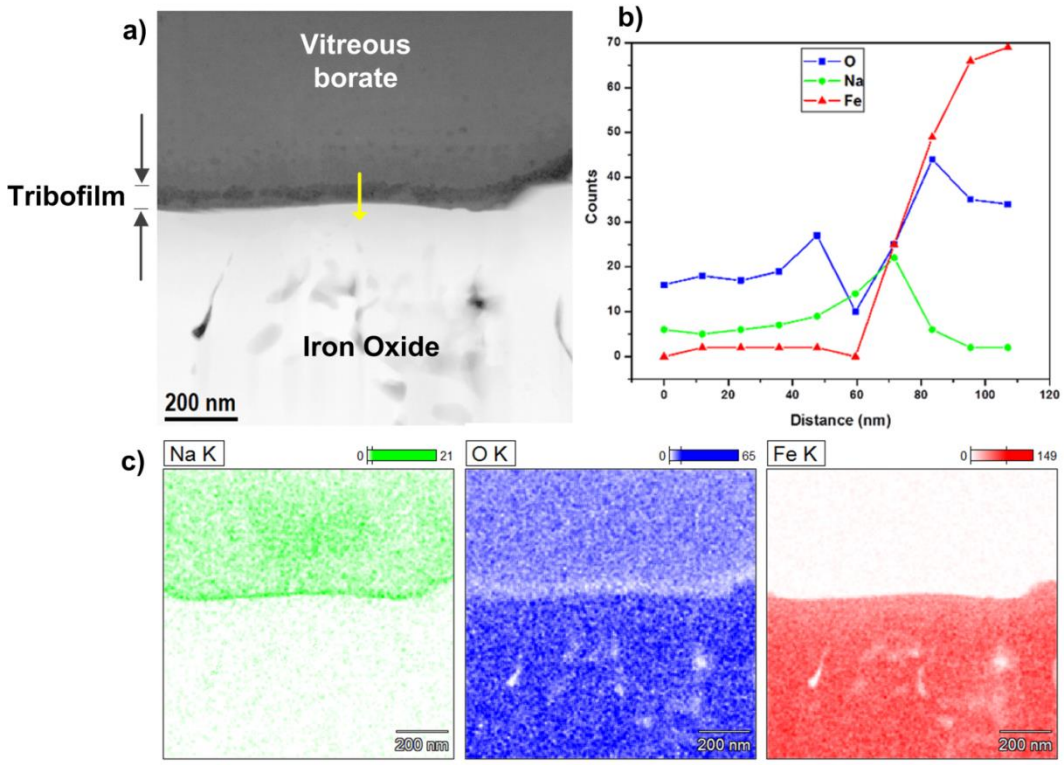


**Figure 5-8:** a) STEM-HAADF image of the worn track area, b) a scan profile across the interface and c) corresponding EDS mapping of Na, O and Fe. (Yellow line represents scanning direction)

As suggested that the interfacial film mainly comprises of B, SIMS was employed to provide supportive evidence. SIMS has been widely used in characterization of structurally layered materials. In this case, depth profiles of B and Na are given in respect to Fe to determine the gradient changes across the interface (Figure 5-9). As expected, the melt elements (B and Na) concentrate on the interface and their intensities share a similarly decreasing pattern as sputtering time increases. In contrast, Fe initially starts with negligible intensity which increases sharply to a stabilization stage after 1000s of sputtering. It is noted that the profile was extracted from the contact interface including a residual layer with an estimated sputtering rate of 0.43nm/s. The gradient changes are

attributed to not only element distribution within the residual film, but also to the inherently rough lubricant melt/oxide interface.

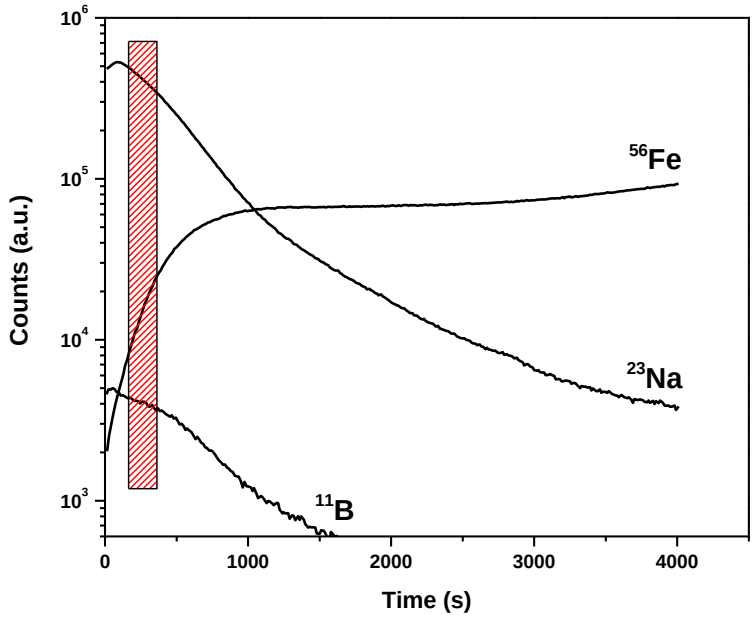


**Figure 5-9:** SIMS depth profiles of B, Na and Fe on the worn track (Dashed area approximates the interface).

## 5.4 Discussions

At elevated temperatures, oxidation of metals is accelerated by the deposition of melted salt [135]. The hot corrosion may involve fluxing action of the protective oxides initiated by potential chemical reactions between heterogeneous phases. The underlying mechanism is primarily governed by the physical chemistry of the melt. As previously stated in Chapter 4, the sodium borate melt is regarded as an ionic liquid above its melting point. The structural disassociation upon heating induces the formation of free Na cations and depolymerized boron oxide network. The equilibria correspond to the disassociations of borate melt components can be described as followed:

$$Na_2O \rightarrow Na^+ + O^{2-} \quad (1)$$

$$B_2O_3 + O^{2-} \rightarrow 2BO_2^- \quad (2)$$

According to the Lewis acid-base definition [136], the base is considered an electron donor and acid is an electron recipient when the pair is involved in a chemical reaction. Being analogous, the current sodium borate system therefore can exhibit base-acid chemistry where $O^{2-}$ is the charge carrier. In the binary oxides of $Na_2O$-$B_2O_3$, $Na_2O$ plays a role of a base whereas $B_2O_3$ is assigned an acid from (1) and (2). As a result, the resulting melt is then characterized as a conducting media with the coexistence of multiple ions induced by the chemical equilibria. It is suggested that both acidic and basic components have certain roles in the electrochemical reaction with iron oxides.

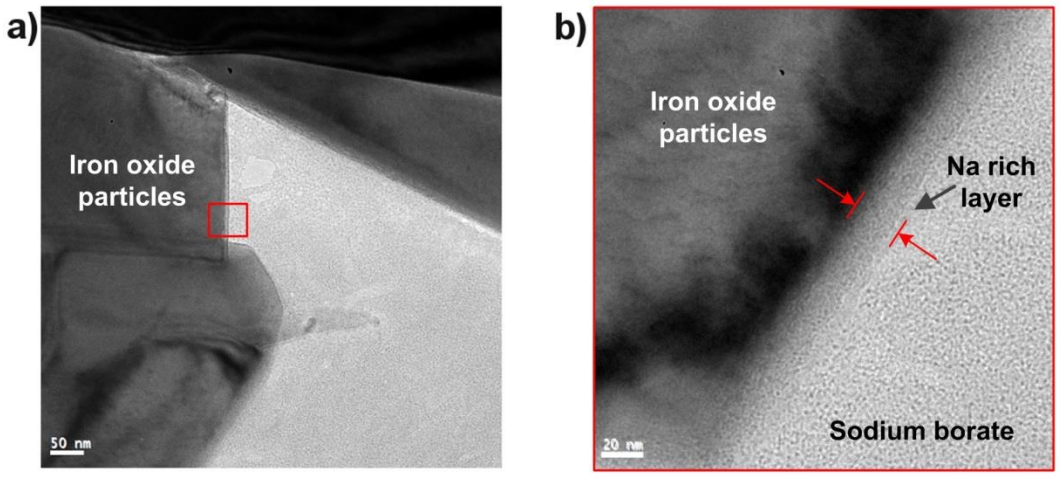


**Figure 5-10:** TEM image of the boundary interface showing a thin film of Na as a result of heterogeneous reaction**.**

If an interface reaction occurs, it is likely to commence on the phase boundary where the reactants are in contact. Previous characterization reveals an amorphous thin film (~20nm) which is rich in Na residing on the surface of iron oxide particles (Figure 5-10). This arises from a reaction between the basic component of borate melt and iron oxides. X-

ray powder diffraction was used to determine possible phase formation between borate melt and iron oxides powder (mainly $Fe_2O_3$) subject to heat treatment (Figure 5-11). The high specific area of oxide powder (particles size of 10~20μm) enables a higher conversion of the interface reaction. The mixture was heated at 800$^oC$ for 7 minutes which is equal to the exposure duration in tribological/oxidation test. It can be seen that apart from the expected dominance of $Fe_2O_3$, XRD pattern of the heat-treated mixture shows relevant peaks attributed to $NaFeO_2$ at 20.6$^o$ and 22.9$^o$ [137]. Due to the fact that the reaction layer is only confined on the oxide interface, the resulting phase constituent is thus inferior to the iron oxides. Ryutaro et al. [138] attempted to measure the solubility of $Fe_2O_3$ and $Cr_2O_3$ in a fused mixture of $Na_2B_4O_7$-$B_2O_3$ under air atmosphere. While $Cr_2O_3$ exhibits a negligible solubility due to its superior corrosion resistance, $Fe_2O_3$ displays a magnitudes-higher value caused by a proposed basic dissolution which aligns with the present study. The interfacial adsorption of Na can alternatively be attributed to the ionic attraction between positively-charged Na ions and the oxides surface featured with a high O density. This occurs regardless of the presence of external shearing and pressure. With respect to the acidic component, it is less likely for boron oxide to chemically react with $Fe_2O_3$. Theoretically, Hematite can be considered as a weak base due to its unwillingness to liberate oxygen while $B_2O_3$ is a weak acid, the reaction between such two reactants is not thermodynamically favorable. It can be deduced that the basic dissolution is the primary reaction in the hot corrosion of borate melt and can be described as followed:

$$Na_2O + Fe_2O_3 \rightarrow 2NaFeO_2 \quad (3)$$

As the interface reaction plays a critical role in inititating the dissolution of iron oxides, other factors can further facilitate the fluxing action of the grown scale microscopically. The metallography of the grown scale can determine the contact morphology when exposed to a borate coating. Figure 5-3 illustrates clearly the grain-like structure of the oxide scale coated by borate. Being a viscous liquid, the borate melt is able to infiltrate through the grain boundaries among sub-micron oxides particles aided by capillary force and density difference. Eventually, the fluxing action can result in an involvement of substantial oxide particles in the melt bulk, interface roughening and potential loss of the protective oxides scale.

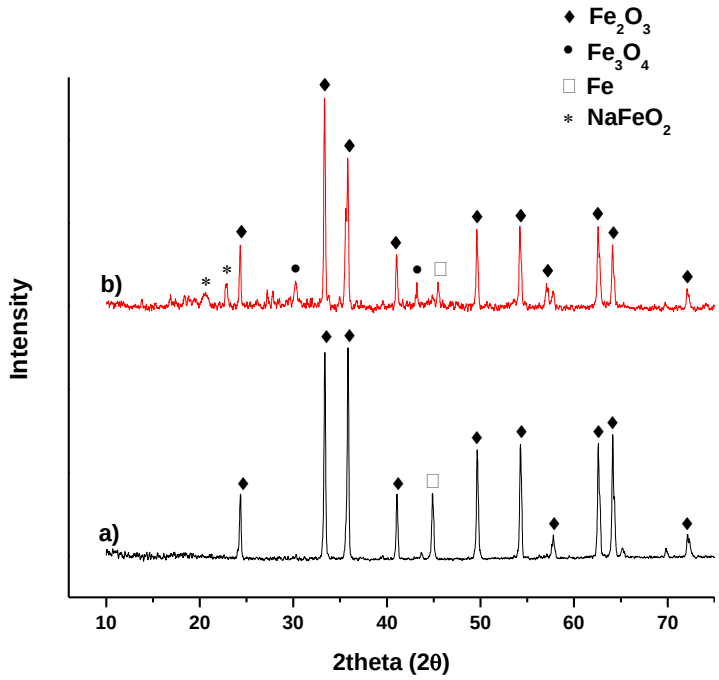


**Figure 5-11:** XRD pattern of a) iron oxides and b) thermally treated borate-iron oxides

In general, a tribo-test progresses in two consecutive stages: a running-in period followed by a more steady stage. The initial running-in period produces a high and unstable coefficient of friction (COF) where the contacting surfaces experience continuous changes in their primary topographies, microstructures and chemical compositions with

probable involvement of third-body particles. On the other hand, the steady stage indicates that the rubbing interfaces reach equilibrium state mechanically and chemically (Figure 5-12). Particularly under lubrication condition, the COF plays an important role in judging the lubricant performance which depends closely on the effective tribofilm formation. Detailed chemical analysis was performed from the lubricated area where interface equilibrium was reached with the tribofilm formation.

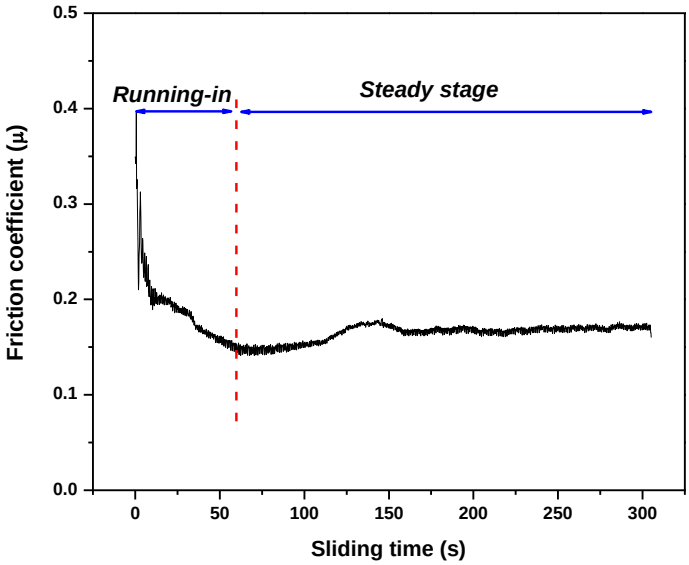


**Figure 5-12:** Friction coefficient curve from lubricationt test of borate on steel/steel contact (800$^{o}$C, 10N, 0.1m/s)

External oxidation occurs when the outwardly-migrating Fe ion reaches the interface and reacts with adsorbed oxidizing species while internal oxidation occurs when the oxidaizing species penetrate through the protective scale then react with the base metal [7]. As a result, the oxide scale thickens progressively. The borate tribofilm generated on the interface is characterized by a significantly low O density, thus has a great potential in mitigating the oxidation severity. The borate tribofilm is capable of inhibiting O diffusion onto the interface which is one determining factor in oxidation kinetic. If oxidizing species

manage to infiltrate through the boundary film, their adsorption probability wil be hindered by the dense and continuous film of Na. In addition, the outward migrating Fe is likely curbed by the Na film. By obstructing the pathway of reagents transport, the tribofilm can play a role as an effective anti-oxidation layer.

Figure 5-13 illustrates cross-sectional view of the steel substrate exposed to different conditions with corresponding element profiles. It can be seen that the grown scale under borate lubrication is the thinnest (8~10μm) despite signs of interface damages. In the case of borate-coated sample without tribology contact (Figure 5-13b), the melt/oxide scale interface appears rougher and the scale is 2~3μm thicker than that on the worn area. Lastly, the oxidation of bare steel substrate (no lubricant coating, no tribology contact) yields an uniform scale with the greatest thickness of 16μm. Compared to the unprotected substrate, borate coating can prevent the oxidation of steel substrate in some extent due to its ability to separate physically the substrate and oxygen in the atmosphere. On the lubricated substrate, the interface benefits substantially from the oxidation resistance of O-depleted boundary film and produces the thinnest oxide scale although the wear loss can not be underestimated. Ultimately, due to its favorable locality, the tribofilm not only imposes an anti-oxidation capacity on the disc surface but also on the opposing surface. When the normal load was increased up to 30N, the sodium borate melt still retains its oxidation resistance on the sliding surface, as shown in Figure 5-14.

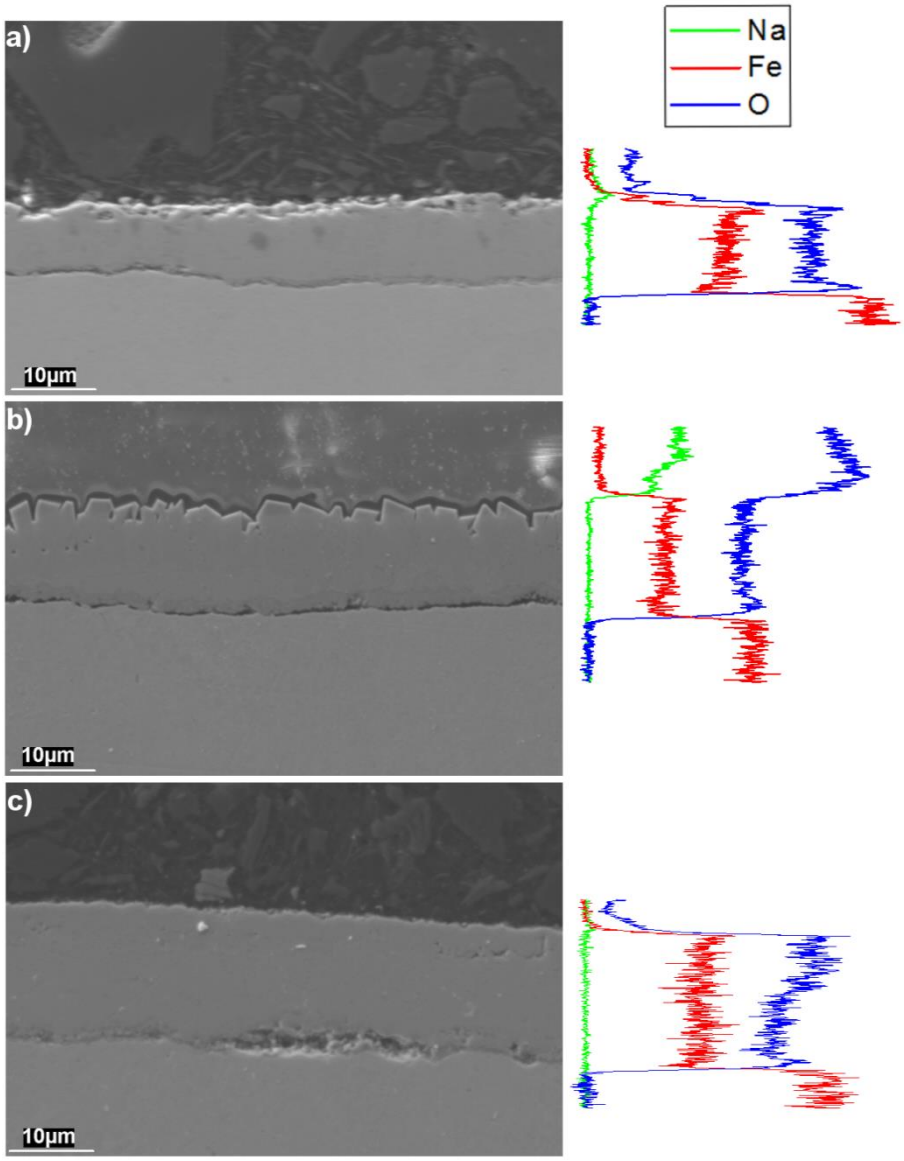


**Figure 5-13:** Cross-sectional view of the steel subtrate lubricated by borate (a), coated by borate (b) and under pure oxidation (c) at 800°C (Intensity unit is counts)

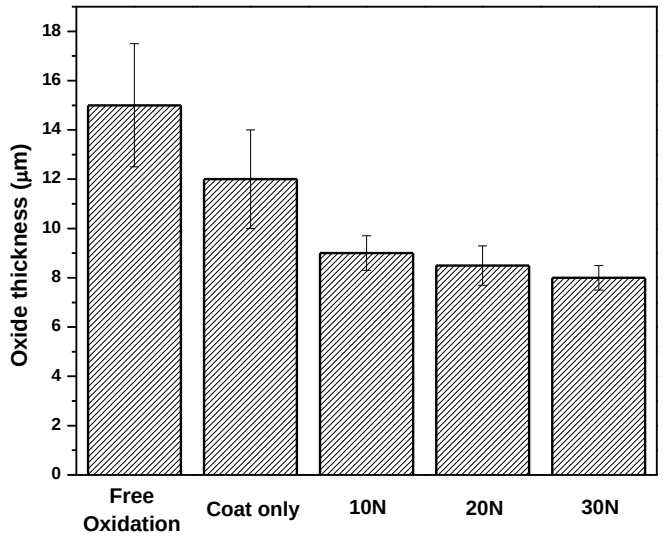


**Figure 5-14:** Variation of oxide scale thickness under free oxidation, borate-coating and borate lubrication at different loads (800$^{o}$C, sliding duration of 5mins, sliding velocity of 0.1m/s)

## 5.5 Conclusions

The interface chemistry of borate melt/oxidized steel was revealed and the influences of ribological exposure on the boundary region were also understood. Some conclusions can be drawn from this chapter as listed bellowed:

- The oxidation reaction of borate melt on oxidized steel is characterized by the interface reaction and fluxing action of the oxide particles;
- The formation of thin Na film on iron oxide interface is observed regardless of the presence of shearing stress;
- Tribological exposure leads to the tribofilm formation which is significantly depleted in Oxygen;
- The tribofilm formation enhances oxidation resistance by reducing the oxide growth.

# CHAPTER 6:

# The role of Na in the lubrication behavior of sodium borate

** This chapter content was published in RSC Advances, 2018, 8, 28847-28860.*

It has been acknowledged that the chemical makeup of the tribofilm, often quite complex in its nature, plays a crucial role in the lubricant performance at high temperature. The compositional complexity can originate from the diverse elements involved in the tribosystem (from lubricant, additives, contact surfaces and environment) and also the structural gradients that exist across the tribofim thickness. In engine oil, the ZDDP (Zinc DialkylDiothioPhosphate) additive creates a hierarchically-structural tribofilm in which functions of individual elements still draws plenty of debate till now [139].

As previously stated, melt lubricant can be formulated from two primary constituents: alkaline (or alkaline-earth) element and glass-forming compound. Each of the components has certain roles in defining the overall physico-chemical characteristics of the melt at elevated temperature. Condensed polyphosphate ($P_2O_5$), boron oxide ($B_2O_3$) and silicon oxide ($SiO_2$) are the most fundamental network-building blocks. These structural groups are the foundations of polymeric nature that renders thermal stability and high transition point. The introduction of cationic moieties modifies the degree of polymerization which helps tuning melting temperature and viscosity. The relative ratio between the two constituents dictates high-temperature behaviors of the melt and there have been plenty of

studies dedicated to this close relationship [111, 118, 140, 141]. On the rubbing interfaces, how each component responds to tribological stimulation might determine the overall lubrication mechanism. For instance, Cui et. al. found that depolymerization of phosphate network is associated with the good wear resistance of sodium polyphosphate as the tribo-chemical reactions can eliminate the formation of abrasive wear on sliding steel pair [142-144]. In addition, they also revealed differential polymerization/depolymerization tendency of a range of sodium polyphosphates (ortho-, pyro- and meta-) due to their original chemical structure which greatly affects the tribological behaviors.

Under sodium borate lubrication, the tribofilm formation was evident in previous chapters. The current chapter aims to investigate the tribological impacts of sodium (Na) in borate lubrication at elevated temperature by the pin-on-disk testing. Friction and wear characteristics under pure $B_2O_3$ lubrication were evaluated in comparison to those of its Na-bearing counterpart, the binary system of $Na_2O$-$B_2O_3$. The locality of the Na and its gradients on both sliding interfaces were analyzed to reveal its roles in the lubrication mechanism. Effects of the microstructure of the iron oxides on the interfacial phenomena were also taken into account.

## 6.1 Experimental details

### 6.1.1 Lubricant preparation

In the high-temperature friction test, boron oxide ($B_2O_3$) and sodium borate were chosen. XRD pattern indicates crystalline structure of the starting $B_2O_3$ at room temperature (Figure 6-1). Thermal behaviors of boron oxide were previously studied as the

material shows a well-defined transition point of 450°C [145, 146] while sodium borate has a melting point of 525°C as shown in Chapter 4 (Figure 4-3). An aqueous solution of 5% wt. was prepared for the friction test. Despite the formation of boric acid ($H_3BO_3$) by the reaction with water, the compound subsequently melts and results in a glassy boron oxide [145] at the testing temperature (here 800°C). The final composition of the sodium borate melt is simplified as $Na_2O$-$B_2O_3$ upon melting at 525°C (Figure 4-3). Thermal transitions of the concerning lubricants are described as followed:

$$2H_3BO_3 \xrightarrow{\text{Melting}} B_2O_3 + 3H_2O$$

$$Na_2B_4O_7.10H_2O \xrightarrow[\text{Dehydration}]{100-200^oC} Na_2B_4O_7 \xrightarrow{\text{Melting}} Na_2O.2B_2O_3$$

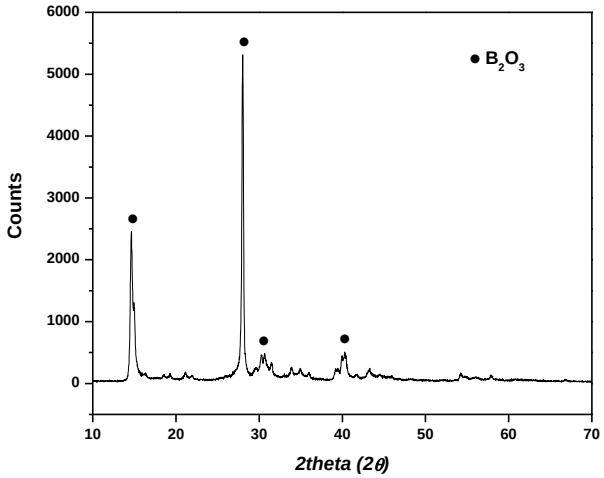


**Figure 6-1:** X-ray diffraction pattern of boron oxide

| C | Si | V | Cr | Mo | W | Ni | Mn | Fe |
|---|---|---|---|---|---|---|---|---|
| 2.0 | 0.99 | 4.00 | 4.85 | 4.47 | 3.40 | 0.78 | 1.26 | Remainder |

**Table 6-1:** Chemical composition of HSS (weight %)

### 6.1.2 Tribopair preparation

As High Speed Steel (HSS) has been commonly used as the work roll material in hot rolling practice [147-149], the current chapter employs HSS as the upper pin. The nominal chemical composition of HSS material is shown in Table 6-1. The fractional volume of metal carbides is estimated at around 9-12% by using phase compositional analysis from EDS mapping (AZtec 3.3 Oxford Instrument). The multi-alloyed material consists of metallic matrix and precipiated carbides as shown in the XRD pattern (Figure 6-2). It is noted that MC simply stands for Metal Carbides since XRD single-handedly is not able to distinguish carbides with different stoichiometry [150]. However, classification can be made through microstructure observation [151] and the signature morphologies of corresponding carbide are illustrated in Figure 6-3a, 6-3b and 6-3c. On a polished HSS substrate, AFM height profile (Figure 6-3d) details protruding drenditic features of the carbide from metallic matrix due to the greater hardness of the carbide. Figure 6-4 shows elemental distribution on a polished HSS in which the two abovementioned phases can be differentiated.

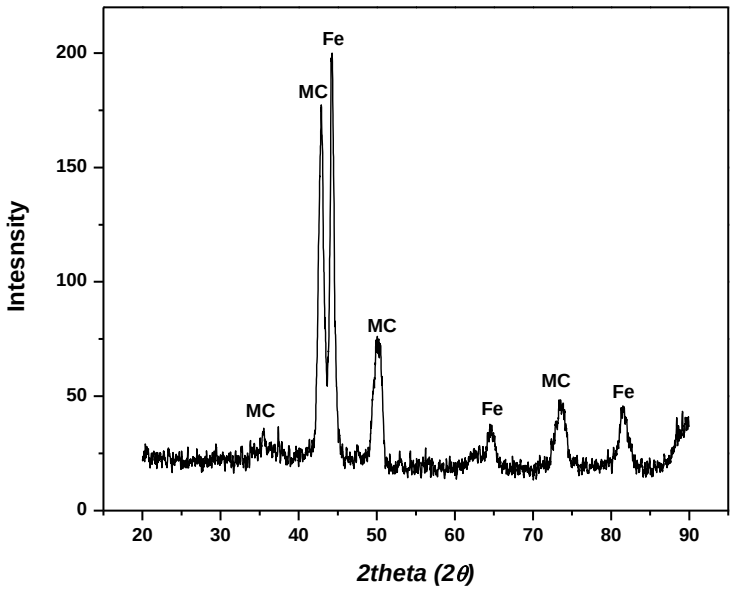


**Figure 6-2:** X-ray diffraction pattern of HSS

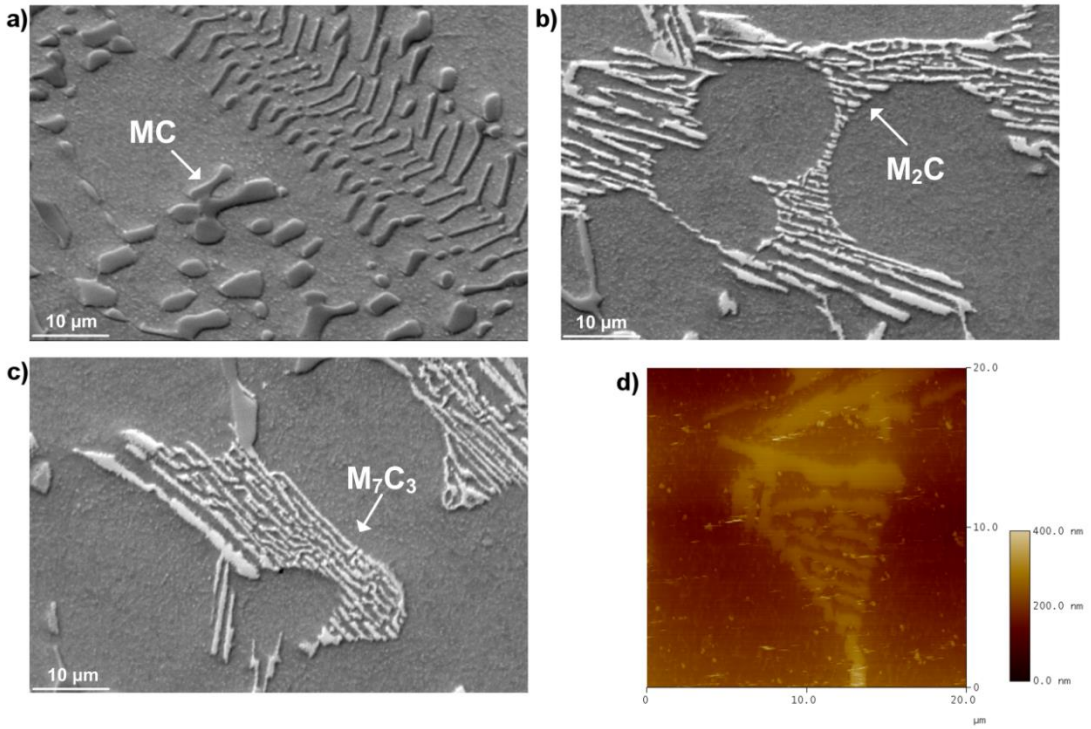


**Figure 6-3:** SEM micrographs of different carbide morphologies a) MC, b) $M_2C$, c) $M_7C_3$ and d) AFM height profile of a polished HSS subtrate

The HSS pins were fabricated out of an industrial work roll without heat treatment. They are wire cut into cylinders then one end is machined by a ceramic tip to achieve a 6.35mm-diameter hemispherical end with an average roughness of 1µm. Total length of the HSS pin is 4mm. The metallic matrix has a hardness of 8±0.6GPa and a Young modulus of 222±5GPa while the corresponding values for carbides are 19±3.26GPa and 300-373GPa depending on carbide type. Commercial stainless steel (SS316, hardness of 4.3GPa, Young modulus of 180GPa) was chosen as the rotational component in the hot friction test. The SS316 round disc is 3mm thick with a diameter of 50mm and its surface was polished to achieve a roughness of 1µm. Mild-carbon steel was also used in this work to reveal the effect of different oxide microstructure on lubrication. The steel pairs were ultrasonically cleaned by ethanol and acetone prior to each friction test.

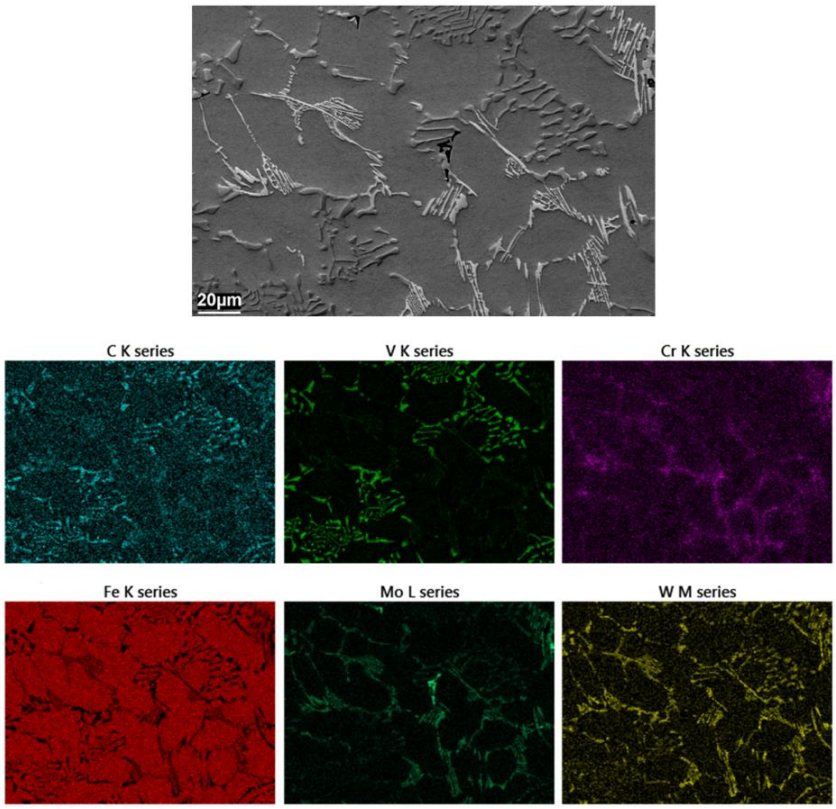


**Figure 6-4:** Elemental mapping of a polished HSS surface

### 6.1.3 Friction test

High-temperature friction test was performed on the Bruker UMT2-CETR ball-on-disc tribometer. The testing procedure was slightly different from previous chapter as the pin was pre-oxidized for a fixed duration prior to sliding. The SS316 disc was first installed into the furnace chamber followed by heating to 800$^{o}$C. Once the furnace temperature reached the set point, the upper stage carrying HSS pin was automated to descend to a distance of 3mm away from the disc surface. Pre-oxidation of HSS pin lasted for 10 minutes. During this stage, the disc rotated at 5rpm to ensure uniform heat distribution. Lubricant solution was dropped onto the heated disc at 2 minutes before contact engagement with a rate of 0.01ml/s. The sliding velocity was kept constant at 0.1m/s while

testing duration was fixed at 5 minutes. The applied load varied from 10-40N (with an interval of 10N) corresponding to the maximum Hertzian contact pressure ranging from 1.14GPa to 1.84GPa (Equation 4-1). When the friction test finished, the tribopairs were retrieved immediately and cooled in the air to prevent further oxidation and preserve the intrinsic chemical state of the contact interfaces.

### 6.1.4 Characterization

The wear loss volume of the track was measured by a Surface Profiler (Hommel Etamic W10, JENOPTIK). X-ray Diffractometer (GBC MMA) was used to determine crystalline structure of the as-received lubricant powders and HSS material. An Atomic Force Microscopy (Digital Instrument Dimensions 3100) was employed to generate height profiles of polished HSS substrate and lubricated track. Morphologies of the worn surfaces were examined by the same routine in Chapter 4 and Chapter 5. As EDS mapping is not effective in resolving the presence of Boron, EELS was used to detect the element on the lubricated sliding surfaces.

## 6.2 Result

### 6.2.1 Lubrication performances of $B_2O_3$ and binary system $Na_2O$-$B_2O_3$

Figure 6-5a illustrates friction coefficient curves of steel contact exposed to different lubricating melts: pure $B_2O_3$ and binary system $Na_2O$-$B_2O_3$. The normal load was kept at 10N in these tests. Under $B_2O_3$ lubrication, the curve displays an increasing trend accompanied by an intense fluctuation of the friction coefficient ranging from 0.4 to 0.6. The frictional behavior resembles unlubricated sliding contact between steel counterparts

which is typically characterized by high friction [24, 152]. Despite using different mating material, Chapter 4 also confirms high friction coefficient from unlubricated steel pair (GCr15/Mild steel). In stark contrast, after only 25 seconds of running-in period, the tribopair lubricated by Na-containing $B_2O_3$ exhibits a steadily low COF of 0.12 thorough the rest of the test. A comparison of wear volume losses (Figure 6-5b) indicates a significant difference in anti-wear capacity of the concerning lubricants. The sole $B_2O_3$ lubrication demonstrates a relatively poor wear resistance, yielding a volume loss of 0.34 $mm^3$ which is 9 times greater than the case where Na was involved in the melt. It can be deduced that the addition of Na exerts remarkable influences on $B_2O_3$ lubrication as the binary oxides outperforms the lone $B_2O_3$ in terms of friction and wear reduction.

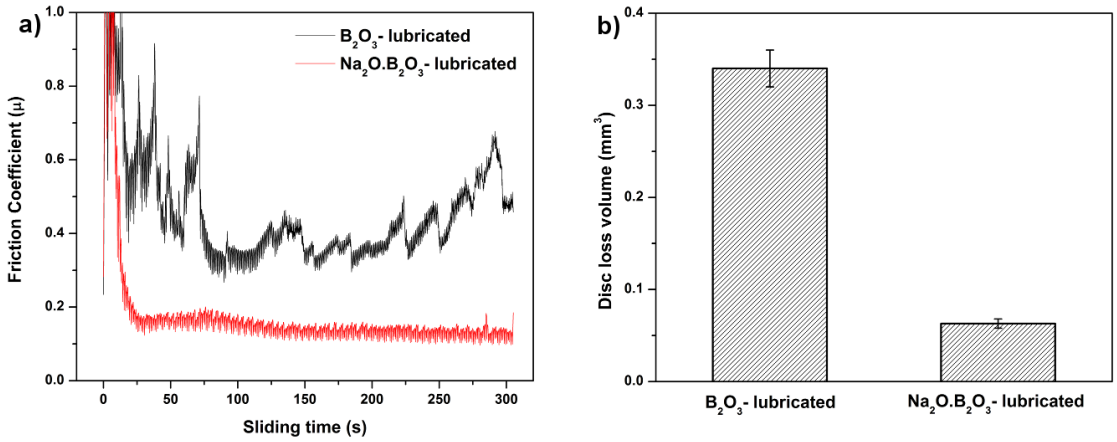


**Figure 6-5:** a) Friction coefficient curves of HSS/SS316 pair lubricated different melt systems and b) corresponding wear loss volumes on the disc

Figure 6-6 presents SEM micrographs and the relevant X-ray analysis of the disc worn surfaces lubricated by lone $B_2O_3$. The wear track appears broad and deep filled with surface damages parallel to the sliding direction. Higher magnification image (Figure 6-6b) reveals severe pitting and ploughing while scratching is considered as the most predominant damage type. EDS spectrum extracted from inside the wear track reveals no sign of B but only elements associated with oxidized steel including Fe, Ni and O. The

high intensity of O suggests adverse oxidation that occurred on the rubbing surface. Melt elements B and O are only detected outside of the worn area while there is no trace of Fe. A further examination of Figure 6-6a points out that the vicinity of the wear track looks much brighter than the contact area due to the charging effect of $B_2O_3$ whose electronic conductivity is very poor [153]. This stems from the accumulation of incident electrons on $B_2O_3$ surface which subsequently reflects all the incoming beam and eventually results in visually ambiguous contrast. It is deduced that $B_2O_3$ melt was unable to withstand the stressed shearing on the contact area and subsequently squeezed out to both sides of the sliding track. As a result, the steel tribopair became fully exposed without lubrication so direct asperities contacts evidently result in rising friction, excess wear loss and severe worn morphologies [24, 152, 154]. Figure 6-7 displays the contact surface of opposing SS pin lubricated by $B_2O_3$. A higher magnification image shows aggregation of smearing glaze which could be transferred from the countered surface. As the pin material is very hard, it does not wear significantly and results in a worn circle on the contact area similar to that in Chapter 4. Instead, the most dominating wear occurrence is adhesive wear and material transfer. EDS mapping reveals an oxidized pin surface without any trace of lubricant melt (Figure A-10).

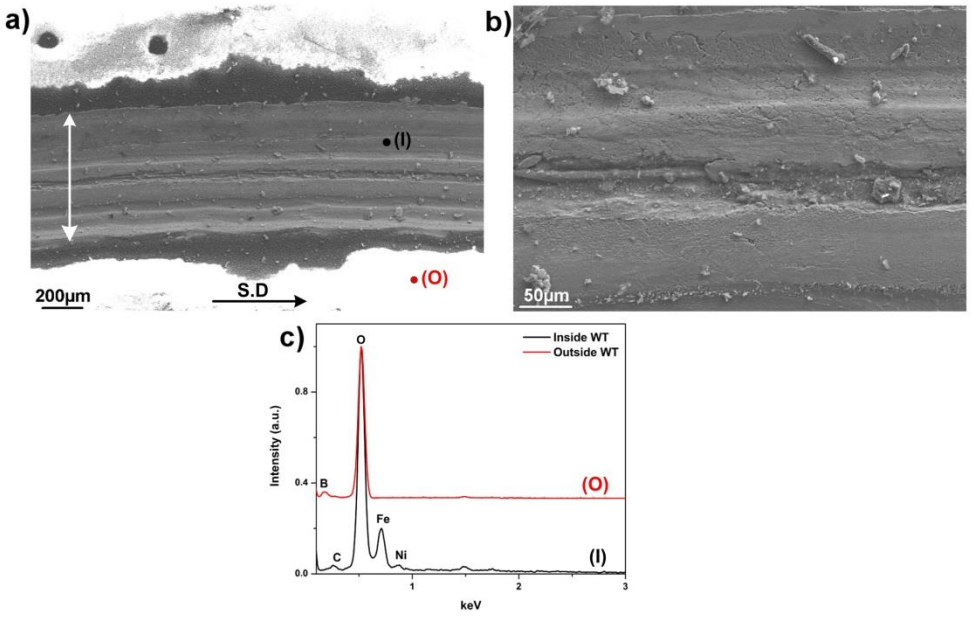


**Figure 6-6:** a) Worn morphologies of SS316 disc lubricated by $B_2O_3$, b) magnified image of the track and c) EDS spectrum collected from inside and outside the track

The lubrication failure of $B_2O_3$ is demonstrated by worn surface morphology coupled with underwhelming friction and wear behaviors. Despite having liquid-like behavior, $B_2O_3$ melt was not able to bear the shearing stress which could be due to its weak interaction with the mating surface [155].

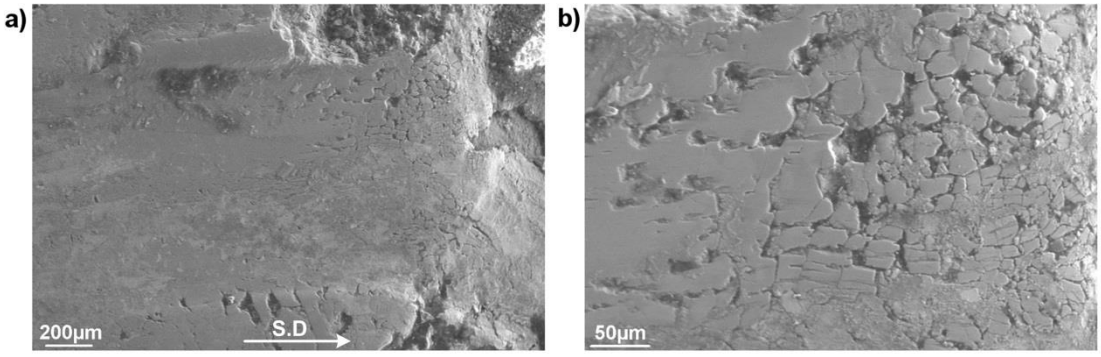


**Figure 6-7:** a) Worn morphologies of HSS pin lubricated by $B_2O_3$ and b) higher magnification of the contact area

Worn morphologies and the corresponding EDS analysis of the steel tribopair lubricated by binary system $Na_2O$-$B_2O_3$ are given in Figure 6-8. Contrary to what observed in $B_2O_3$ lubrication, both rubbing surfaces share a common theme of being free from any kind of

surface damages. X-ray spectrum clearly points out chemical fingerprints of the melt lubricant including B, O and Na alongside a minor trace of Fe on both worn surfaces. The presence of lubricant elements on the wear track after friction test suggests that the binary system $Na_2O$-$B_2O_3$ was able to endure the tribological exposure without being squeezed out. This attribute is the most critical factor for sodium borate superior lubrication compared to $B_2O_3$ melt. The addition of Na into $B_2O_3$ clearly has a significant impact on friction and wear behaviors of the lubricant.

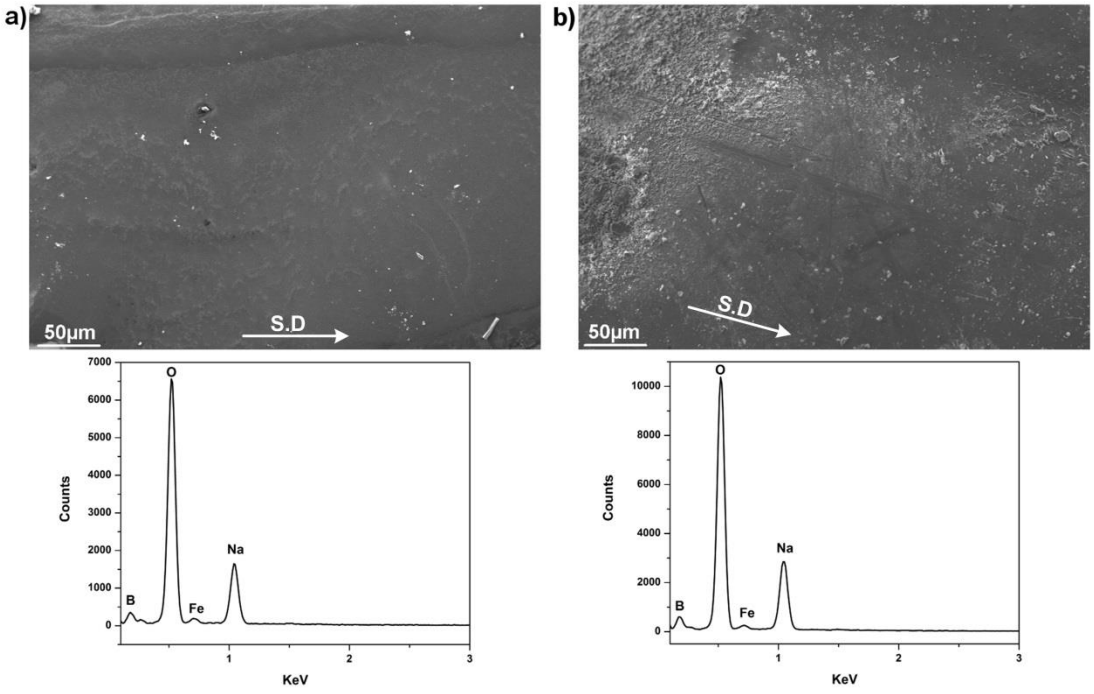


**Figure 6-8:** Worn morphologies of steel pair lubricated by binary system $Na_2O$-$B_2O_3$ and the corresponding EDS spectrum a) SS316 disc, b) HSS pin (S.D = sliding direction)

### 6.2.2 Load-carrying capacity of binary system $Na_2O$-$B_2O_3$

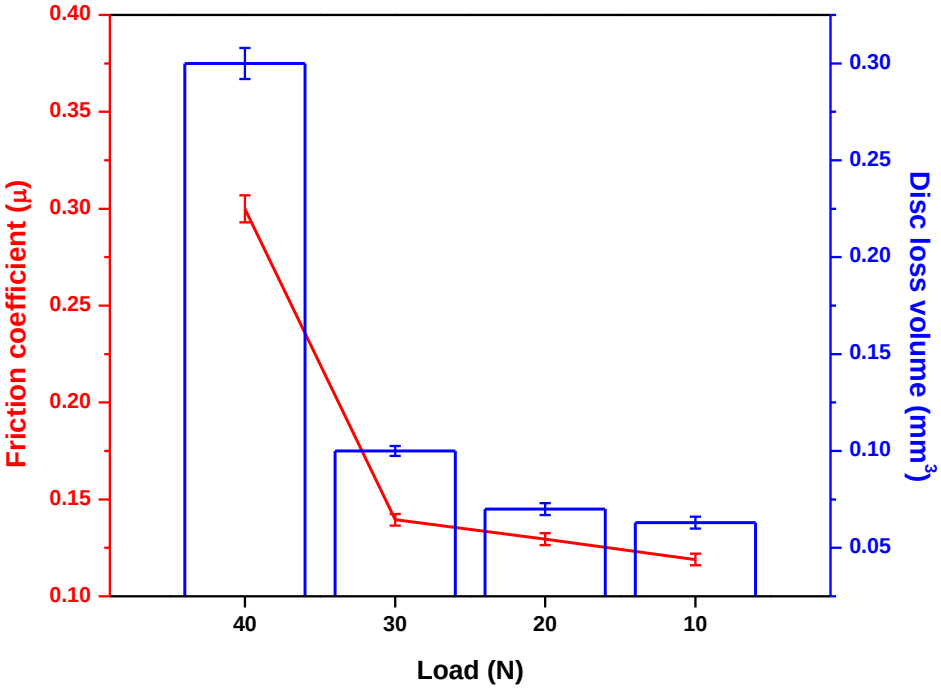


**Figure 6-9:** Variation of average friction coefficient and disc loss volume versus increasing load under $Na_2O$-$B_2O_3$ lubrication

A series of hot friction test with increasing load was conducted to determine the load-bearing capacity of Na-containing $B_2O_3$ melt. Figure 6-9 plots the average friction coefficients and disc loss volumes as a function of applying load while other parameters are kept unchanged. It is evident that both friction and wear loss volumes increase progressively as the load rises. Under 10N of normal load, the friction coefficient is recorded as the lowest value of 0.12 among those tested. Likewise, SS316 disc yields the least amount of worn loss volume of 0.063 $mm^3$. As the load increases, both figures exhibit a similar increasing trend. At 30N, the friction coefficient climbs to 0.14 while the worn loss volume nearly doubles compared to what recorded at 10N. Under the highest load (40N), the $Na_2O$-$B_2O_3$ melt seemingly fails to perform as the tribopair generates the highest coefficient of 0.31 which closely approaches the characteristic friction of

unlubricated contact [24]. Furthermore, the disc wears by an amount of 0.3mm$^3$ which is nearly 3-fold of the 30N testing point.

Characterization by SEM/EDS on the worn surfaces lubricated by $Na_2O$-$B_2O_3$ at 20N and 30N was performed and reported in Figure A-11 and A-12 (Appendices). Those worn morphologies display identical features to those at 10N with no sign of surface damages while being covered by the lubricant melt.

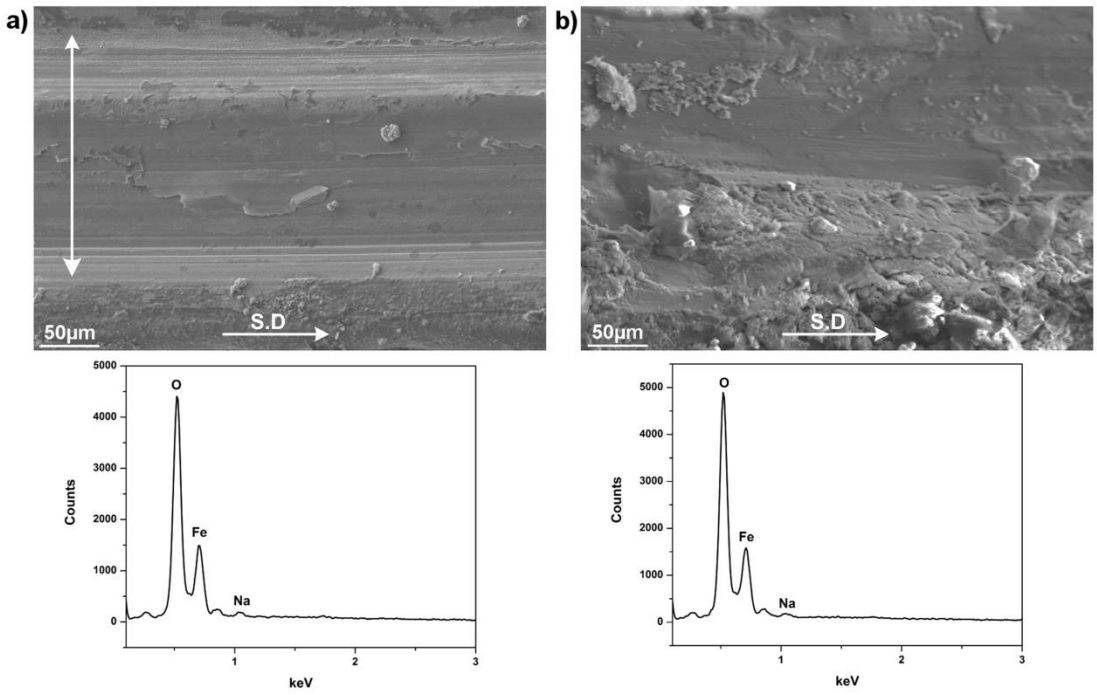


**Figure 6-10:** Worn morphologies of steel tribopair lubricated by $Na_2O$-$B_2O_3$ at 40N and the corresponding EDS spectrum a) SS316 disc, b) HSS pin

The sudden disruption in friction/wear behaviors at the highest load 40N suggests lubrication failure and surface examination of the worn pairs is given in Figure 6-10 to provide further evidences. It can be recognized that both contact surfaces reveal different worn morphologies compared to those under successful lubrication at lower loads. There are signs of scoring damages parallel to sliding direction in conjunction with minor delamination on the wear track (Figure 6-10a). The opposing surface exhibits several types

of damage ranging from adhesive wear to plastic smearing (Figure 6-10b). The corresponding EDS spectrum suggest oxidized contact areas with the absence of B and only small amount of Na. Figure 6-11 illustrates AFM image of the worn track at the point of lubrication failure (at 40N). The nano-grain morphology belongs to the exposed oxide scale grown on stainless steel [66] and will be confirmed in the following analysis. As the lubricant film was likely destroyed, the sliding contact became unlubricated which resulted in incremental friction and wear losses (Figure 6-9). As sole $B_2O_3$ evidently failed to lubricate at the lowest load, it can be predicted that the melt is not able to perform under harsher conditions. The addition of Na into $B_2O_3$ not only radically reverses the lubricity of the beneficiary, but also renders a stable lubrication performance over a certain range of load.

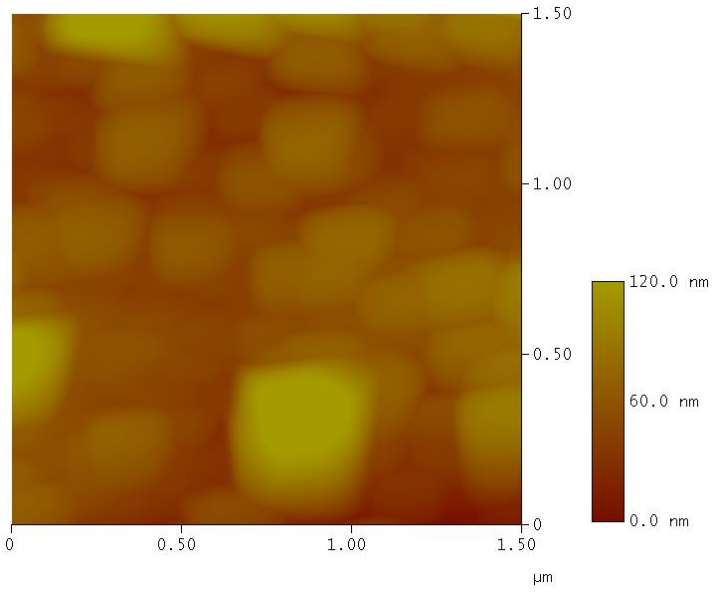


**Figure 6-11:** AFM height profile of the wear track after the friction test under $Na_2O$-$B_2O_3$ lubrication at 40N

### 6.2.3 Contact interfaces lubricated by binary system $Na_2O$-$B_2O_3$

In order to gain better insights into the positive influences of Na addition, microstructural and chemical analysis of the rubbing interfaces were provided. The examinations were carried out on both steel tribopairs lubricated at 30N while the binary system still exhibits acceptable lubrication performance.

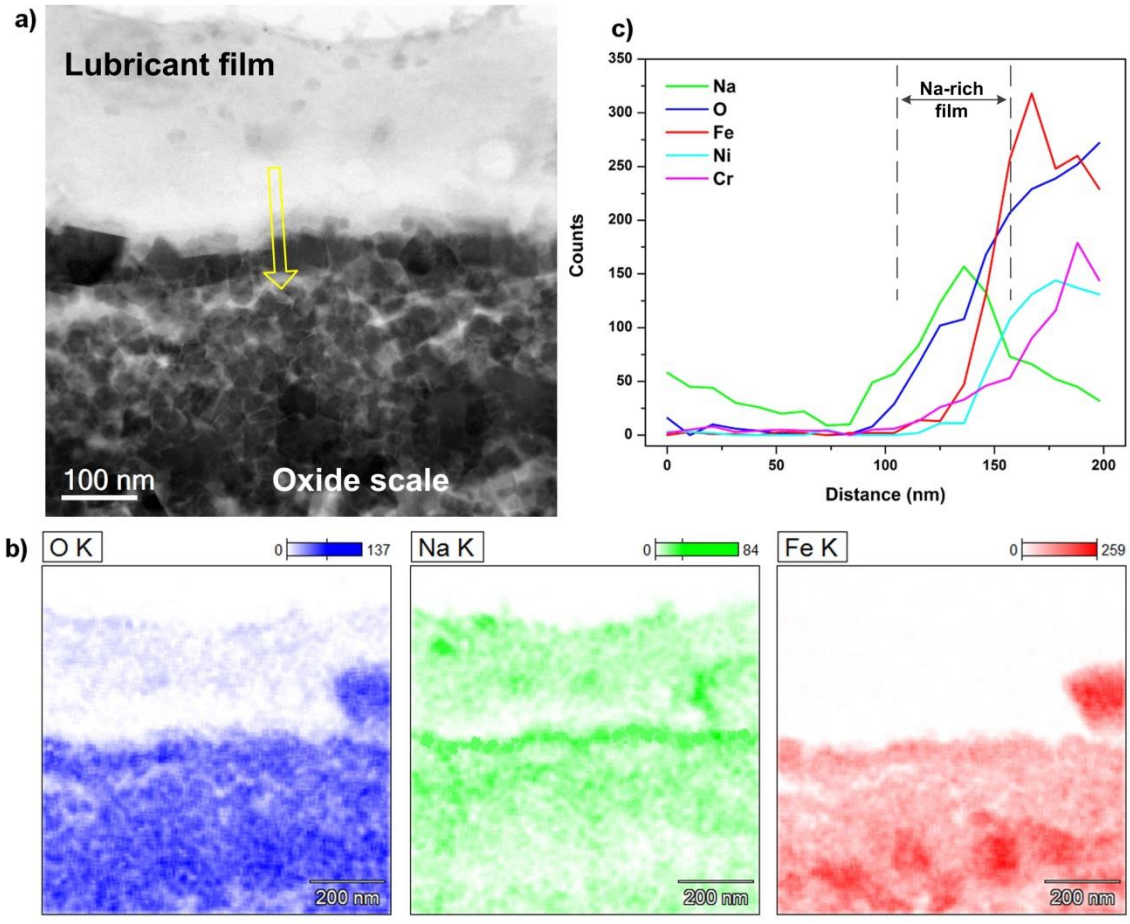


**Figure 6-12:** a) STEM-BF image of contact interface on SS316 disc lubricated by $Na_2O$-$B_2O_3$ at 30N, b) EDS mapping and c) EDS line scan across the interface (yellow arrow indicates scanning direction**)**

Figure 6-12 shows STEM-BF image and the associated EDS analysis of the immediate sliding interface on SS316 disc lubricated by the binary melt $Na_2O$-$B_2O_3$ (presence of B will be confirmed by the subsequent EELS analysis). There are two distinct regions which

can be differentiated by their contrasts. The bright upper layer can be assigned to the lubricant melt while the underlying counterpart with grain-like characteristic can be designated to the iron oxide scales. It can be observed that the immediate sliding surface is composed of fine oxide grains whose lateral dimension is below 50nm. In addition, there are also signs of voids and pores within the oxide scale which are considered as intrinsic features in the oxide microstructure grown on alloyed steel at high temperature. EDS mapping apparently differentiate the oxide scales from the overlying lubricant layer. Fe signal is more intense in the oxide scale while O density appears much higher in the oxide scale than in the lubricant melt. Na exhibits an interesting distribution pattern as the element concentrates heavily on top of the iron oxide surface to form a continuous film. The representative EDS scan is provided to underline the existence of Na-rich film by the sudden increase in the Na signal when it approaches the oxide scale. The thickness of this Na film is estimated around ~50nm. Due to its relative position on the sliding interface, the Na film can play a pivotal role in prohibiting immediate asperity contacts, particularly under boundary lubrication regime. In addition, Na is also detected underneath the immediate sliding surface. It tends to distribute among the subsurface voids and pores, although it is less dense than the interfacial film (Figure 6-12b). At high temperature, the inward infiltration of lubricant melt could be due to the extreme stressed shearing in combination with the voids formation within the oxide microstructure of SS316. On the other hand, O looks depleted just above the Na-rich film. Apart from the predominant iron oxides, the oxides of Ni and Cr are also formed since the elements are typically included in stainless steel composition for improved oxidation resistance.

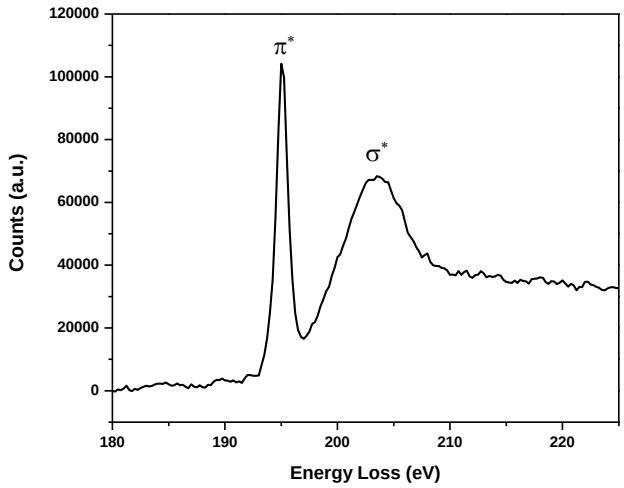


**Figure 6-13:** EELS spectrum of B K-edge on the contact interface of SS316 disc lubricated by $Na_2O$-$B_2O_3$ at 30N

Boron was detected at the sliding interface and its chemical fingerprint is given in the EELS spectrum (Figure 6-13). The characteristic excitation edges are located at 195eV and 204eV corresponding to the π* and σ* transition, respectively [113-115] which indicate the dominant presence of trigonal $BO_3$ species.

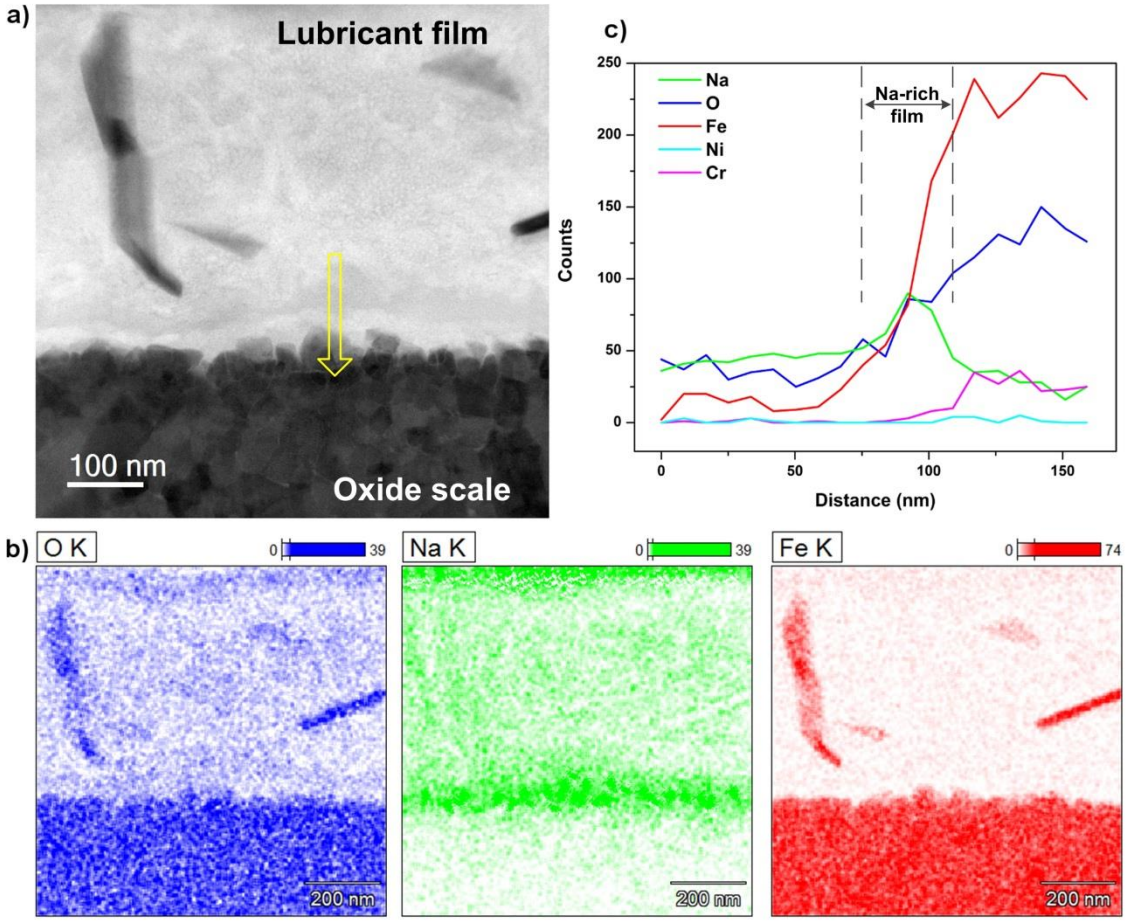


**Figure 6-14:** a) STEM-BF image of contact interface on HSS pin lubricated by $Na_2O$-$B_2O_3$ at 30N, b) EDS mapping and c) EDS line scan across the interface (yellow arrow indicates scanning direction)

A similar characterization routine was accomplished on the opposing HSS pin and the outcomes were shown in Figure 6-14. The BF image illustrates 2 different regions with varying contrasts, a top transparent layer of lubricant melt residing on the oxide substrate. In addition, there appears a very thin boundary film with a distinct contrast running along the oxide interface. Again, the grain-like morphology of the oxide scale is visible. However, the HSS oxide scale appears tightly compact as the oxide scale look very dense without any sign of internal porosity. This could be attributed to the superior oxidation resistance and excellent mechanical properties of HSS material. EDS mapping reveals the

apparent boundary between the two contacting phases as Fe and O are predominantly found in the oxidized surface while the upper layer contains a significant amount of Na. In accordance to the elemental mapping, the interfacial film in BF image turns to be rich in Na with an approximated thickness of ~50-60nm. The penetration of Na appears less significant compared to what occurred on the opposing SS316 surface. The chemical signature of boron on the interface was detected and presented in the EELS spectrum (Figure 6-15) with excitation edges identical to that extracted on the disc interface.

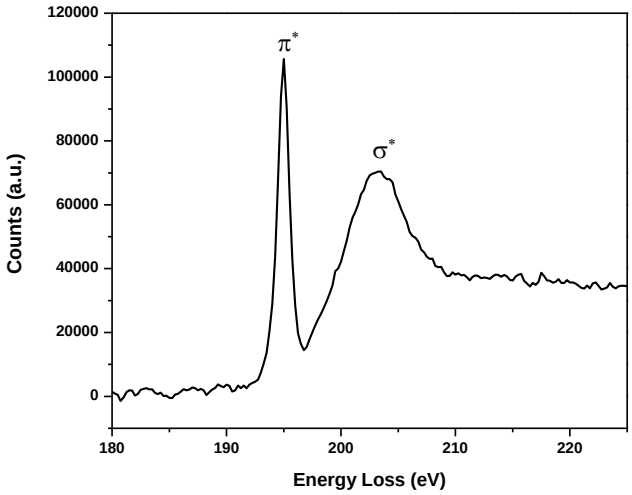


**Figure 6-15:** EELS spectrum of B K-edge on the contact interface of HSS pin lubricated by $Na_2O$-$B_2O_3$ at 30N

TEM image capturing the HSS contact interface on a wider field of view is given in Figure 6-16. Despite having a similar contrast with the lubricant layer, Na-rich film can be readily distinguished as a thin continuous layer superimposing on the oxide surface. In addition, it can be observed that the nano-sized grains are rigidly held together with no voids among them. Electron Diffractions (ED) of both contacting phases are shown in Figure 6-16. The lubricant layer expectedly produces a diffusive ring suggesting amorphous nature of the binary borate melt. On the other hand, a ring-like ED pattern was

collected on the oxides side which implies polycrystalline nature of the oxide scale. In this chapter, ED was only used to confirm the polycrystalline nature of the oxide scale without emphasis on further analysis. Chapter 7 uses extensively ED to investigate the oxide microstructure in which detailed ED pattern processing routine and other relevant analysis will be provided.

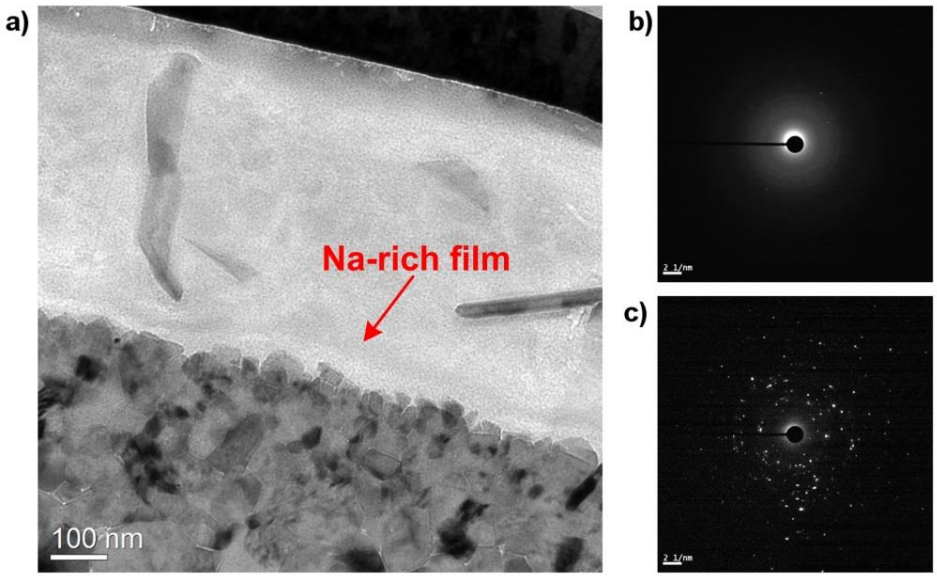


**Figure 6-16:** a) TEM image of the lubricated HSS pin showing the interfacial Na-rich film and Electron Diffraction of b) the lubricant film, c) the oxide scale

## 6.3 Discussion

One aspect that makes high temperature tribology distinct from that at a lower temperature is the oxidation of mating surfaces. In the air atmosphere, high temperature leads to growth of oxide scale which acts as a protective layer against further oxidation [7]. As a result, the tribology contact involves two oxidized surfaces whose chemistry was greatly altered by the abundant presence of Oxygen. Even at low/moderate temperature, an oxygenated surface could have a totally different reactivity towards additives elements

compared to an oxygen-free surface. Jun et al. discovered that treating a TiAlV alloy with an oxygen-diffusion process stimulates the formation of ZDDP-based tribofilm which in turn reduces the wear rate by up to six orders of magnitude [156]. In addition, mechanical properties and microstructure of the developed scale are also believed to play a significant role in the tribological behaviors.

As clearly stated in Chapter 4&5, there is a coexistence of covalent and ionic bonding in the binary system $Na_2O.B_2O_3$ upon melting. The former is assigned to B-O-B network while the latter refers to the Na-O interaction. The addition of Na introduces ionic characteristic into otherwise purely covalent $B_2O_3$ melt. With small atomic radius and high mobility, the electrophilic Na cations are attracted by the oxidized steel where electron density is high due to the presence of Oxygen. The strong adsorption of cationic Na renders the binary system a superior affinity towards iron oxide surface than its Na-excluding counterpart. It is exhibited by the formation of continuous Na-rich layers residing on both contact surfaces as observed in Figure 6-12 and Figure 6-14. On one hand, the interface reaction can enhance the wettability of the binary melt on oxidized surface in a similar fashion to hydro bonding on most hydrophilic surfaces [157, 158]. On the other hand, it also helps the $Na_2O$-$B_2O_3$ melt to sustain the stressed shearing on the interface and subsequently function as an effective lubricant. This is the primary foundation for the excellent lubricating properties of the binary melt including friction reduction, wear resistance and high load-bearing capacity. Under boundary lubrication, direct asperity contacts can be mitigated by the boundary film which results in low wear rate and low friction. The extended load-bearing capacity could be attributed to the robustness and resilience of Na thin film. At room temperature, electrolytic lubricating medium reportedly

demonstrates promising performance [120, 159-161] and surface adsorption is claimed to be the fundamental factor for such behaviors. In addition, some believed that the repulsion between similarly-charged atoms on opposing surfaces can further reduce frictional loss [159].

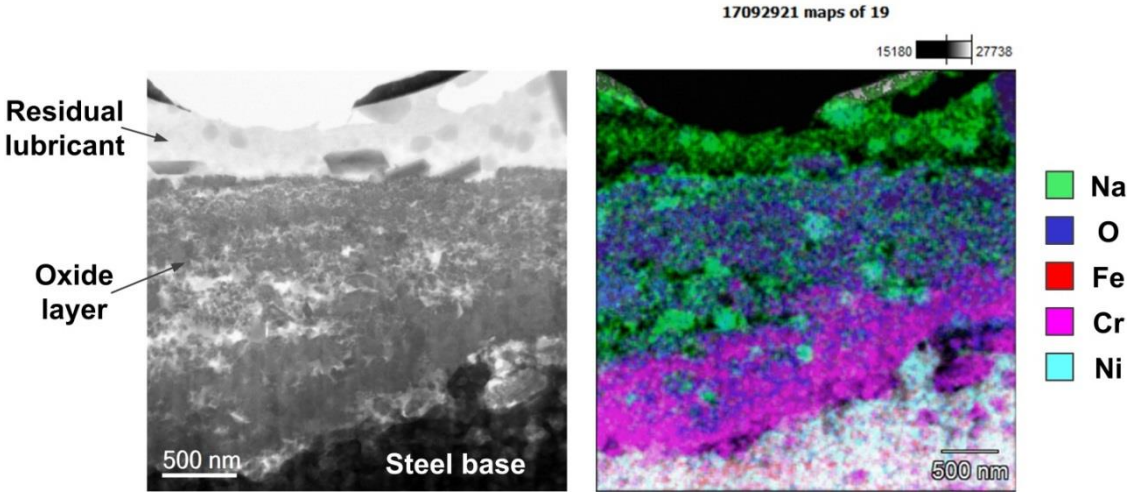


**Figure 6-17:** Infiltration of Na into the SS316 surface under $Na_2O$-$B_2O_3$ lubrication (at 30N)

Beside the chemical origin of the lubricant melt, the effects of microstructure of the grown oxide scale on lubrication mechanism also deserve consideration. It was evident that the mating surfaces are comprised of ultrafine oxide grains which are well-known for their high strength [124, 162]. On the sliding interface of the disc, disintegration of the scale microstructure was shown with voids formation among the oxide scale bulk (Figure 6-12). The liquid-like lubricant melt is drawn into the subsurface region evidenced by the migration of Na into the internal structure of the deformed scale (Figure 6-17). This could arise from intense capillary forces in combination with shearing stress. The lubricant infiltration effectively creates pocket reservoirs which could extend the loading capacity of the binary melt (Figure 6-9). When the outermost oxide surface wears out during sliding contact, the melt lubricant hosted in the subsurface scale emerges to provide healing effect.

In addition, this could also result in a lower shearing stress of the whole oxide scale. On the opposing HSS pin surface, the Na infiltration appears to be less significant as the oxide scale shows exceptional coherence despite experiencing constant tribological exposure. This is due to the inherent properties of HSS since the material composition enables strengthened oxidation resistance and mechanical attributes.

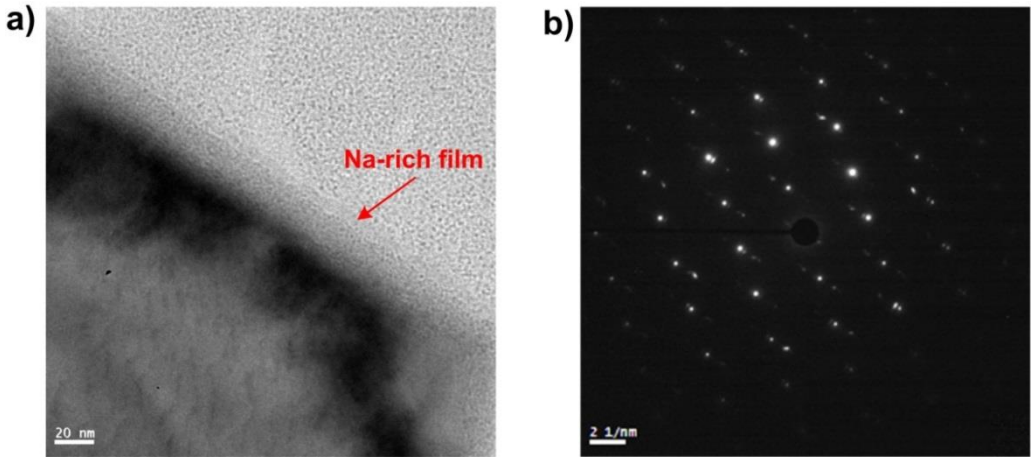


**Figure 6-18:** a) Na-rich film on oxidized mild-steel and b) the corresponding ED pattern of the oxide (Chapter 5)

The microstructure of the oxide scale evidently dictates the adsorption manner of Na cation. Chapter 5 revealed a thin layer of Na on oxidized mild-carbon steel with an estimated thickness of ~20nm (Figure 5-10b) which is less than what observed on both HSS and SS316 surfaces (~50-60nm). Since mild-carbon steel tends to develop large grains of single-crystalline oxides (Figure 5-10b) upon high temperature oxidation [163, 164], their specific surface area is implicitly lower than that derived from oxidized steel with nano-grain morphology. This is equivalent to lesser attractive sites for Na adsorption which leads to the development of a thinner Na film on oxidized mild steel. It is expected that the lubricant melt requires a robust supporting oxide scale to function effectively. Figure 6-19 illustrates difference in friction/wear behavior of different mating steel pair

under binary borate lubrication. While HSS/SS316 shows good lubricity and low wear rate at both testing load, the HSS/mild-carbon steel (MC) appears to fail at both conditions. As the oxide scale on SS316 has a good adherence with the steel base due to the formation of Cr-rich layer (evidenced in Figure 6-17), it provides a strong foundation for an effective lubrication. Plenty of studies have proved the superior adhesion strength of the oxide scale grown on Cr-containing steel [165-167]. On the other hand, oxide scale grown on mild or low-carbon steel often demonstrate weak adhesion with the steel base due to the absence of the reactive elements (Cr, Al, Si…) [7]. The lack of strong supporting oxide scale results in the lubrication failure which is indicated by high wear loss and high friction coefficient (Figure 6-19).

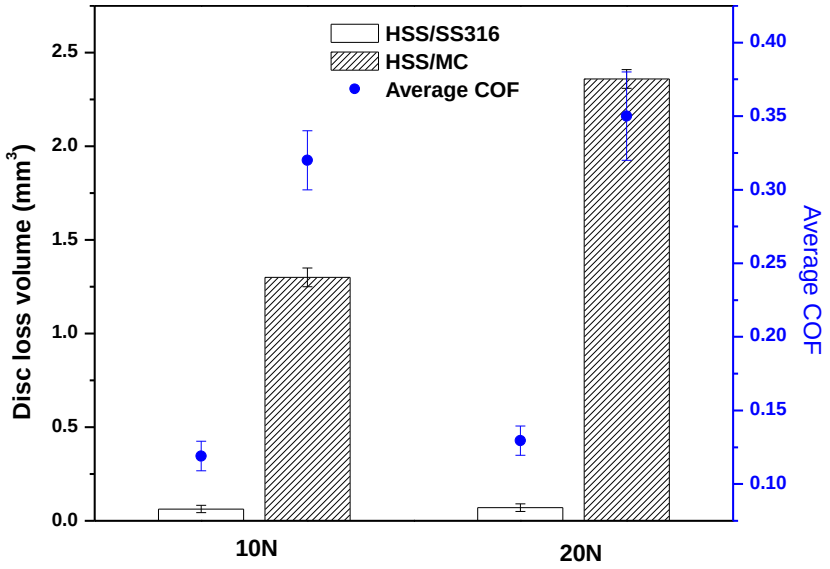


**Figure 6-19:** Friction/wear behaviors between different tribopair under borate lubrication at 800°C

$B_2O_3$ singly provides little or no lubrication effect and this poor behavior could be attributed to its inertness towards iron oxides. Since $B_2O_3$ is considered as a weak acid while iron oxides are also regarded as weak bases on the basis of chemical hardness theory

[168], reaction between those two bodies is unlikely due to unfavorable thermodynamic. By classifying the lubricity of different oxides systems based on a crystal-chemical model, Erdemir [155] found that $B_2O_3$ has little or no chemical interaction with other cations in the tribosystem due to its high ionic potential. However, the role of $B_2O_3$ in the lubrication performance of the binary system cannot be undermined. As a structural-building block, boron oxide provides the viscous characteristic with low shearing strength for the binary melt. The fluidity rendered by boron oxide also facilitates the transport of lubricant into the contact area and subsequently allows Na absorption on the oxidized surface, which has been proven critical for the lubrication performance.

## 6.4 Conclusions

The current chapter aims to refine the role of sodium on the tribological behaviors of binary oxides $Na_2O$-$B_2O_3$ on coupled steel pair HSS/SS316 at 800ºC. There are some concluding remarks which can be found as followed:

- Addition of Na into pure B2O3 drastically improves the lubrication performance of the beneficiary;
- The binary system Na2O-B2O3 also exhibits a good load-bearing capacity;
- Adsorption of Na onto both contact surfaces close to the iron oxide surface is the driving force for the excellent lubrication performance of sodium borate;
- There is a close relationship between Na film thickness and the oxide microstructure;
- Oxide scale grown from stainless steel proves a better foundation for lubricant adsorption.

# CHAPTER 7:

# Borate melt as a sticking-scale inhibitor on a High Speed Steel surface

** This chapter content was published in Tribology International, 2019, 140, 105860*

Apart from friction/wear concerns, material transfer between work roll and workpiece can result in detrimental consequences during tandem hot rolling. The roll surface can be covered by a layer of sticking oxide which originates from the workpiece surface in reheating stage. As the transferred scale thickens, it is prone to peeling-off which results in roll banding and the quality of rolled products is significantly deteriorated from the emerging defects [27, 169]. In fact, the sticking occurrence could be due to poor oxidation management in the reheating stage and ineffective lubrication in subsequent rolling proceses.

High speed steel (HSS) is a specialized micro-alloyed material which has been widely used as the work roll due to its high hot hardness and exceptional wear resistance at high temperature. Much effort have been made to evaluate the tribological properties of HSS in various operating conditions. By using a dry rolling-sliding configuration on HSS/carbon steel tribopair, Pellizzari [152] correlated the low wear rate of HSS roll with its high hardness while wear mechanism was claimed to be a complex combination of adhesion, abrasion and tribo-oxidation. On the contact surface, the formation of an oxide layer was believed to transition friction/wear characteristics into a milder regime which otherwise

would be severe if direct metal-metal contact occurs. In the case of pure sliding contact, transferred oxide scale is also observed on HSS surface when it pairs with mild steel [23, 24] and ferritic stainless steel [170, 171] at elevated temperature.

The current chapter specifically focuses on the wear characteristics of HSS surface under sliding contact at high temperature in the presence of sodium borate. Stainless steel is chosen as the counterpart material since it exhibits great sticking tendency in actual hot rolling process [169, 172]. The normal load was chosen (5N) to generate a maximum contact pressure of 0.9GPa which is close to actual parameters in hot rolling [173]. Besides, the effects of lubrication on oxidation behavior of the subsurface oxides are also revealed.

## 7.1 Experimental details

### 7.1.1 Materials preparation

Material selection for the tribotest is similar to Chapter 6 as HSS was chosen as the pin and Stainless Steel 316 (SS316) was selected as the disc material. The mechanical properties and chemical composition of the steel tribopair remain unchanged. The disc surface was ground and polished to achieve an average roughness of 0.1µm. The HSS pin has a hemispherical diameter of 6.35mm with a roughness of 1µm. The steel pair was cleaned with ethanol/acetone prior to friction test. A 5% wt. aqueous solution of sodium borate was prepared for lubrication test.

### 7.1.2 Friction test

Hot friction test was conducted on the UMT2-CETR pin-on-disc tribometer. The disc sample was first placed in the furnace followed by a series of heating sequences to avoid overshooting. Once the set temperature was reached, the HSS pin was lowered to a distance of 2-3mm above the SS316 disc surface. HSS pin was oxidized for 10 mins prior to sliding. A thermocouple was embedded into the pin body (with a distance of 2mm to the contact surface) to monitor its temperature. As illustrated in Figure 7-1, the temperature of the pin sharply rises after the first 5 mins followed by stabilization at 695$^{o}$C. An engagement of the steel pair further increases HSS surface temperature to nearly 700$^{o}$C. The heating program was designed to represent actual working condition in which HSS surface temperature typically lies between 650$^{o}$C and 750$^{o}$C during hot rolling [24, 174]. Lubricant was dropped onto the hot disc 2 mins at a rate of 0.01ml/s prior to sliding. Linear sliding velocity was kept at 0.096m/s with two different durations: 5 mins and 15 mins. The normal load was fixed at 5N corresponding to 0.9GPa (Equation 4-1). When friction test stops, the HSS pin was immediately retrieved from the furnace to avoid further oxidation. At least three tests were performed at each condition to ensure the repeatability.

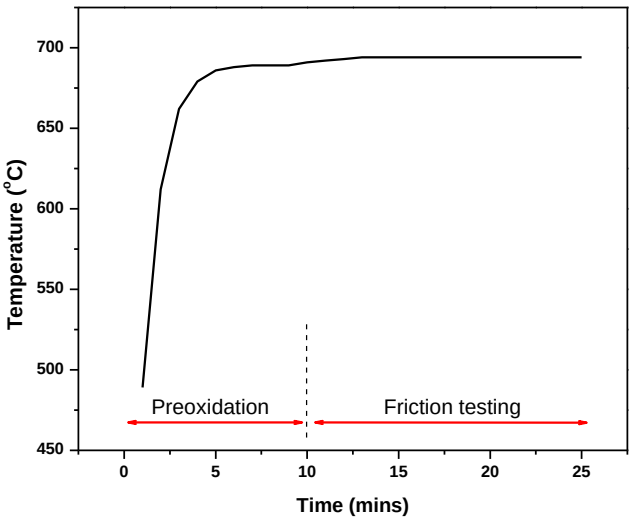


**Figure 7-1:** Temperature record of HSS pin during pre-oxidation and friction test

### 7.1.3 Characterization

An Atomic Force Microscopy (Digital Instrument Dimensions 3100) was used to generate height profiles of the polished HSS substrate. Worn morphologies on HSS pins were captured by the 3D Interferometer Optical Microscope (Bruker Contour GT-K).

Similar to Chapter 6, microscope works were conducted to observe the worn surface morphologies and the cross section of the contact area. During STEM/EDS, elemental phase mapping was achieved by the comparison of X-ray spectrum between pixels and those with similar statistic are collated into one specific phase. Selected Area Electron Diffraction (SAED) was performed on the FIB lamellas at several locations and three representatives are reported. All the calibrated diffraction patterns were processed by a suit of software tool (DiffTools) in Digital Micrograph, a widely-known platform software for TEM images processing [175, 176]. Intensity profiles as a function of reciprocal distance were then derived, normalized and compared between different testing conditions. Referenced d-spacings of relevant crystallites were collected from Powder Diffraction Files 4+ 2018.

## 7.2 Results

### 7.2.1 Microstructural evolution of HSS at high temperature and its tribological behaviors against SS316

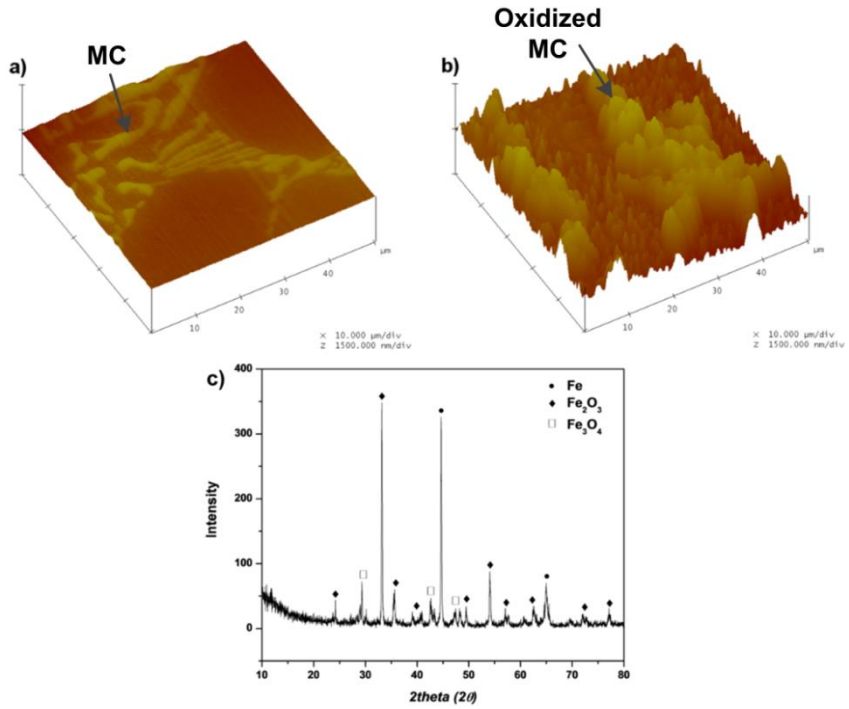


**Figure 7-2:** AFM image of HSS specimen before (a) and after oxidation (b) at 700$^{o}$C for 10 mins, (c) XRD pattern of the oxidized HSS

Since HSS is composed of two different phases (in Chapter 6), their individual oxidation behaviors at high temperature collectively contribute to the overall properties of the sliding surface. It has been acknowledged that oxidation of metal carbides are more thermodynamically favorable due to a low energy barrier [150, 177]. Carbide-free matrix is subsequently oxidized with the development of iron oxides. XRD pattern of oxidized HSS substrate at 700$^{o}$C for 10 mins reveals a major formation of $Fe_2O_3$ and a minor fraction of $Fe_3O_4$ (Figure 7-2c). AFM images (Figure 7-2b, 7-2c) clearly illustrate superior growing kinetic of metal carbides than that of metallic matrix during high temperature oxidation. Nevertheless, it is expected that the native oxide scale from the metallic matrix plays a critical role on the contact interfaces due to their dominating proportion in the starting material (volume fraction of carbide is around ~9-12%).

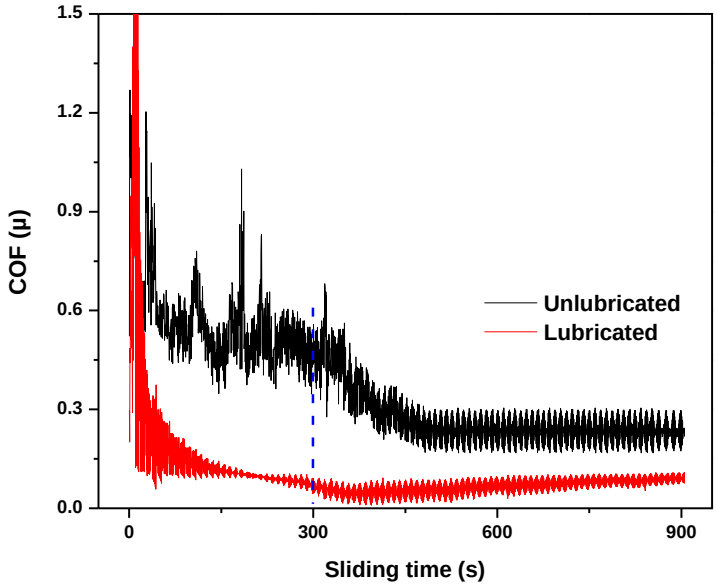


**Figure 7-3:** Friction coefficient curves from HSS/SS316 tribopair with and without lubrication

Friction coefficient curves generated from HSS/SS316 sliding contact are given in Figure 7-3. Under lubrication-free condition, it can be seen that friction coefficient fluctuates widely between 0.4-0.9 at the first 400 seconds before stabilizing at an average value of 0.23±0.05. During the running-in period, high friction coefficient is likely attributed to contact between hard metal oxides [171]. On the other hand, the following steady stage indicates potential formation of tribolayer with friction-reducing effect. It is evident in Figure 7-4 where transferred material on HSS pin is observable on both unlubricated tests, regardless of testing duration. At 5mins mark (Figure 7-4a), the worn morphologies are characterized by plateau build-up and progressive smearing of the adhered layer. As sliding test continues, the contact area enlarges with apparent flattening effect which consequently reduces the contact pressure. The complete formation of the tribo-layer significantly alleviates wear severity which can be indicated by smooth rubbing surface with the only damage being minor fracture in the sub-surface region (Figure 7-4d).

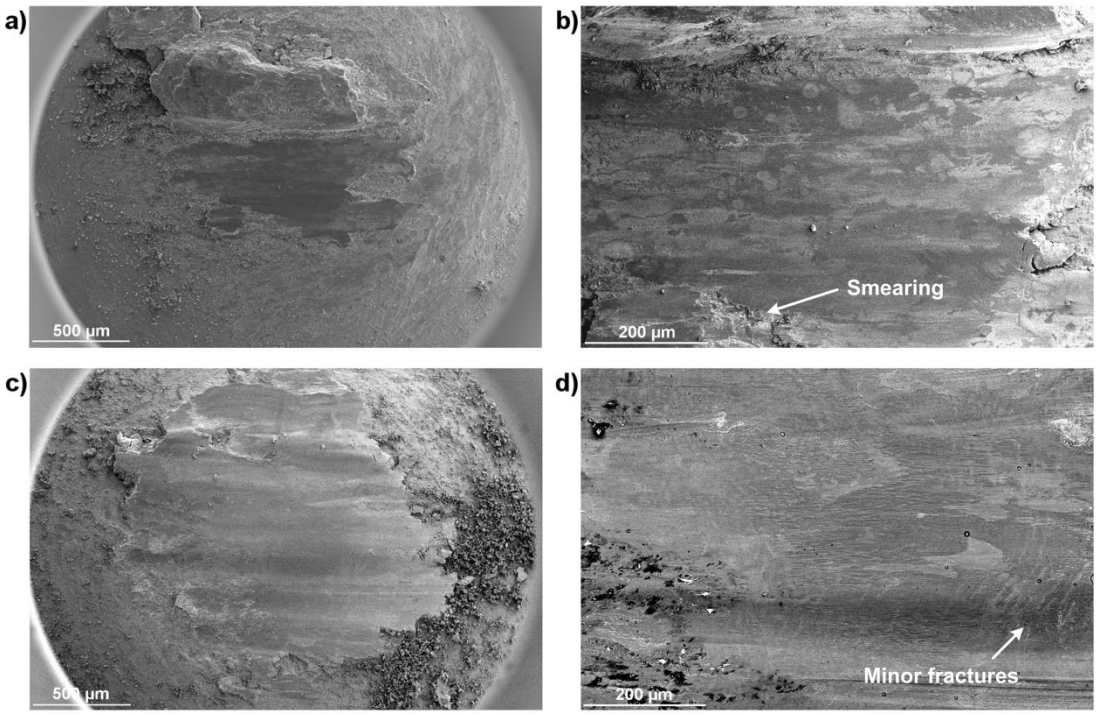


**Figure 7-4:** Worn morphologies of HSS pin without lubrication after 5 mins (a, b) and 15 mins (c, d)

Figure 7-5 illustrates cross-sectional views of HSS worn surfaces along with relevant elemental mapping after dry sliding tests. After 5mins, by contrast difference, the transferred layer can be distinguished from the HSS substrate which is characteristically filled with carbides chunks (Figure 7-5a). The transferred layer thickness ranges from 4.5 to 6.6µm at 5mins mark then it soars to roughly 34µm as sliding duration triples. The oxygen signal indicates that the adhered material is predominantly composed of oxides. However, there could be inclusion of stainless steel debrises in the transferred layer, although they were likely oxidized as the test progresses. It is noteworthy that the tribo-oxide layer which is exclusive of any sign of carbides implies the foreign nature of transferred material. Although the native oxide scale developed during pre-oxidation accounts for a definite fraction of the oxide scale, it is conclusive that transferred (and

adhesive) oxide scale to the pin is the most dominating wear occurrence on HSS surface sliding against SS316.

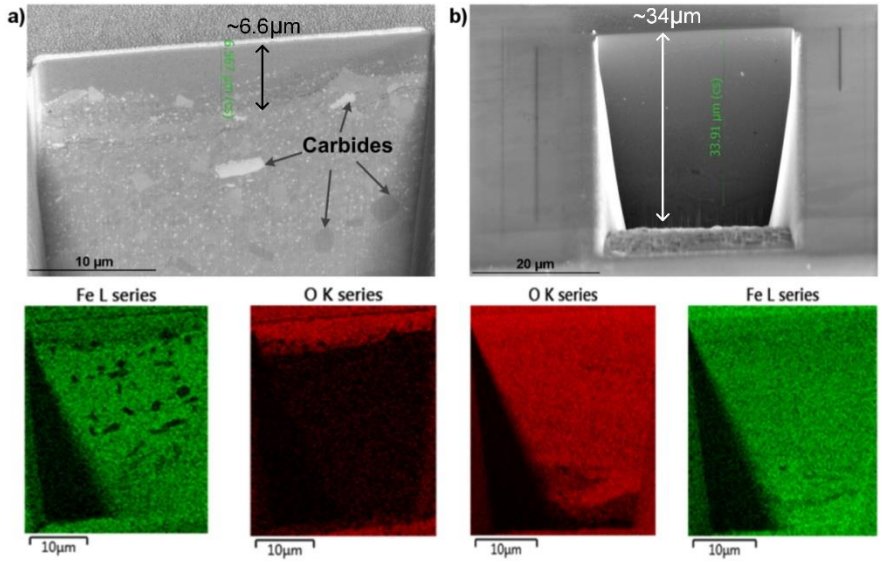


**Figure 7-5:** Cross-sectional views of HSS worn surfaces without lubrication after a) 5mins and b) 15mins (specimens were tilted at 54$^{o}$)

### 7.2.2 Effect of lubrication on the tribological behavior of HSS pin

As shown in Figure 7-3, frictional behavior of HSS/SS316 sliding contact clearly benefits from the borate lubrication. The use of melt lubricant clearly shortens running-period, as friction coefficient enters stabilization stage roughly after 200 seconds of sliding. The downward trend could be associated with the gradually decreasing shearing stress by the presence of the lubricant melt on the contact surface. In addition, the average friction is quite low at 0.1±0.02 during the steady period which is reduced by 2.3 times in comparison to unlubricated case. Figure 7-6 displays SEM micrograph of HSS pin surface after 5mins-lubrication test while the one after 15mins-test is not provided due to similarity. Worn morphology reveals no major damages but only a few scratches along sliding direction. Supporting EDS spectrum exhibits intense signals of lubricant elements

including B, O and Na with relatively weak peak of Fe which suggests a layered structure in which lubricant film resides on the iron oxide base.

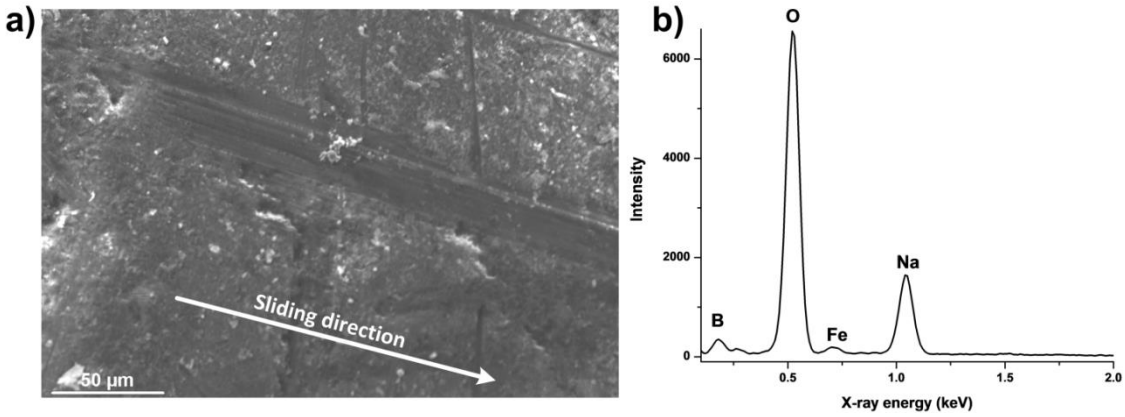


**Figure 7-6:** Worn morphology of HSS pin in lubrication test after 5 mins (a) and EDS spectrum (b).

In order to unfold the immediate sliding interface, cross-sectional observations of HSS pins exposed to lubrication are given in Figure 7-7. By a contrast difference, it can be seen that there are 3 distinct layers corresponding to the lubricant film, oxide scale and HSS substrate as denoted in each image. In the case of 5mins test, it is clear that the oxide scale is composed of nanoparticles in the range of ~20-100nm. This is in a good agreement with Chapter 6. The oxide structure remains remarkably compact with no sign of cavities or pores. In addition, the scale has an average thickness of 0.65 µm which is approximately 10 times lower than what observed with the lubricant-free test. There are signs of slight tearing damages in the HSS substrate which is likely to occur during the running-in process. As the sliding time increases, the scale on HSS thickens to approximately 6~6.5µm with some microstructure changes (Figure 7-7b). However, it is still significantly thinner than that observed in dry sliding counterpart (which is approximately 34µm). It is noteworthy that the immediate oxide/lubricant interface appears fairly smooth despite experiencing high local pressure during the friction test (Figure 7-7).

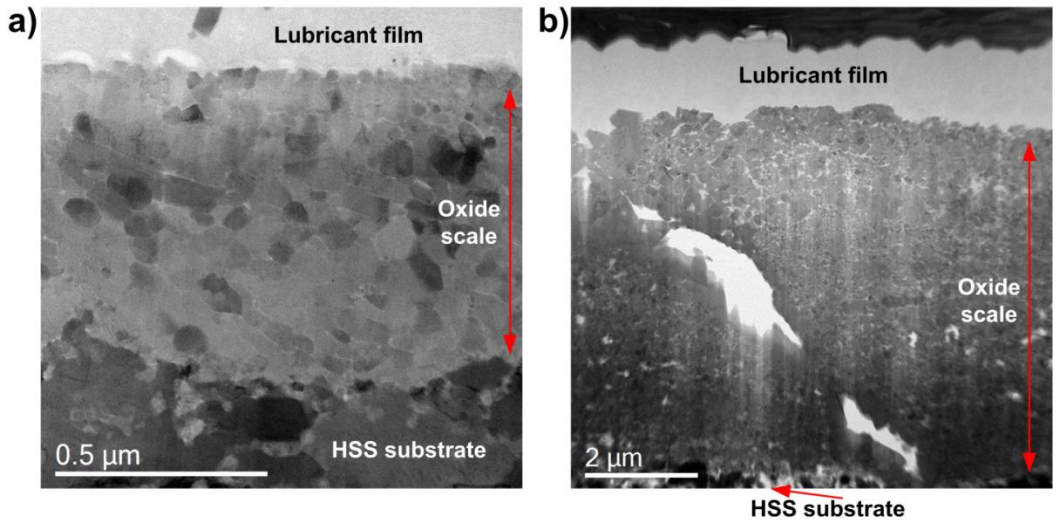


**Figure 7-7:** STEM-BF images of cross-sectional HSS pins after lubrication test a) 5mins and b) 15mins

Apart from friction-reducing effect, it is evident that sodium borate lubricant inhibits sticking oxide scale on HSS surface reflected by the oxide thickness reduction. After lubricant removal, 3D surface plots of HSS pin are given along unlubricated counterparts for worn morphology examination (Figure 7-8). Contrary to the apparent material transfer during dry sliding (Figure 7-8a, 7-8b), HSS pins practically shows no sign of adhered material across the whole contact areas exposed to the lubricant (Figure 7-8c, 7-8d), although some damages are visible in the longer duration. A closer examination reveals craters produced from FIB work, mostly on the top region of the worn area where oxide scale thicknesses were extracted.

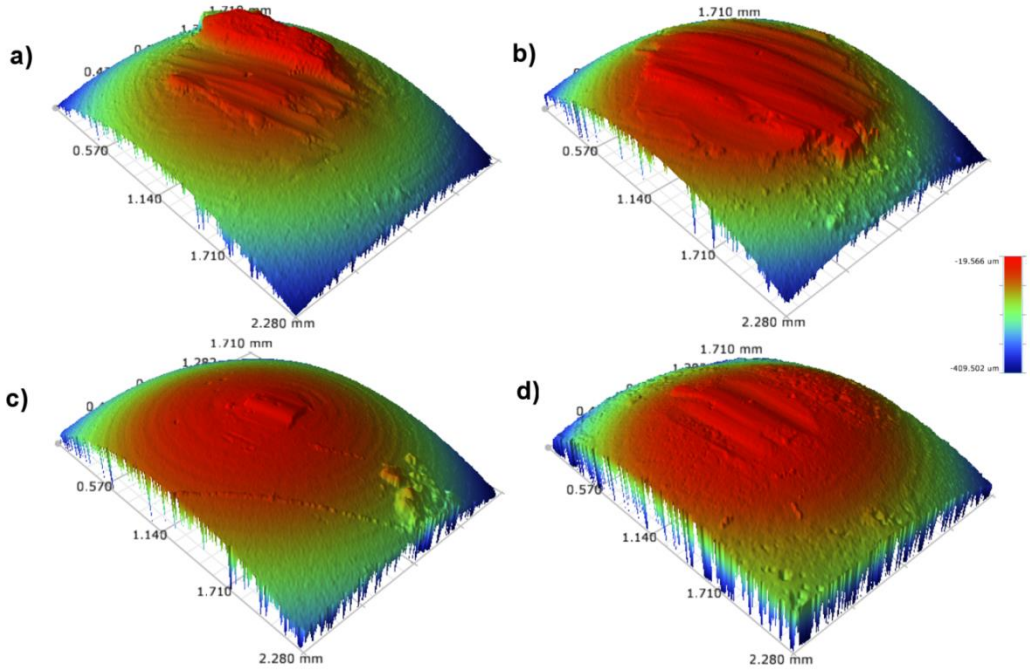


**Figure 7-8:** 3D profile images of HSS pin after dry sliding test (a-5mins, b-15mins) and lubrication test (c-5mins, d-15mins)

### 7.2.3 Effect of lubrication on iron oxides microstructure

It is expected that the presence of a lubricant film can exert certain influences on the high-temperature oxidation behavior of the underlying oxide scale. Figure 7-9 shows cross-sectional TEM micrographs of HSS surface under different lubrication/oxidation conditions. Electron diffraction was performed on the FIB lamellas and the processed intensity profiles are also provided to determine the crystal structure of iron oxides. In the case of 5mins lubrication test, it is clear that the oxide scale is composed of sub-micron particles with the major constituent being Hematite ($Fe_2O_3$) (Figure 7-9a). As sliding times triples, there emerges a phase evolution as Magnetite ($Fe_3O_4$) (mostly (102), (200) and (016)) replaces Hematite to become the most dominant phase as evidenced in the adjacent profile. Similar analysis routine was accomplished on purely oxidized HSS, which was

extracted from non-contact area after 15mins lubrication test (Figure 7-9c). There are 3 layers in top-to-bottom order: Pt cap, oxide scale and HSS substrate with the presence of carbides precipitates. The oxide layer thickness varies from 1 to 2µm across the whole lamella while the oxidescale is largely composed of Hematite with a minor fraction of Magnetite as evidenced in the complementary profile. This aligns well with X-ray diffraction result (Figure 7-2c). Chromia (110) ($Cr_2O_3$) is also present in a fair amount which likely concentrates on scale/substrate interface [177, 178].

The phase transformation over sliding time is further substantiated by the morphology change of iron oxide particulates. Figure 7-10 exhibits magnified TEM micrographs of the oxide scale formed under lubrication after increasing sliding durations. It can be seen that the iron oxide nanograins (with average dimension <100nm) appear to have poly facets when exposed to 5mins-lubrication test (Figure 7-10a). This could be the cause of the highly compact scale as each individual grain can accommodate geometry changes from the surrounding with ease, especially under the effect of shearing. The oxide grains from static oxidation test resemble the one achieved from 5mins lubrication test. On the other hand, prolonged exposure to lubrication evidently leads to shape transformation as the oxide nanoparticles exhibit an unambiguous cubic morphology (Figure 7-10b). The nanocubes seem to be geometrically distorted as a result from tribological effect. Figure 7-10c illustrates a typical cubic oxide particle with sharp edges and indicative d-spacing of Magnetite (102). The Magnetite nanoparticles with such characteristic shape were found across the whole scale. Contrary to a compact scale observed with the shorter test, the

loose oxide scale with emerging voids and porosity can be attributed to the phase transformation under extended sliding duration.

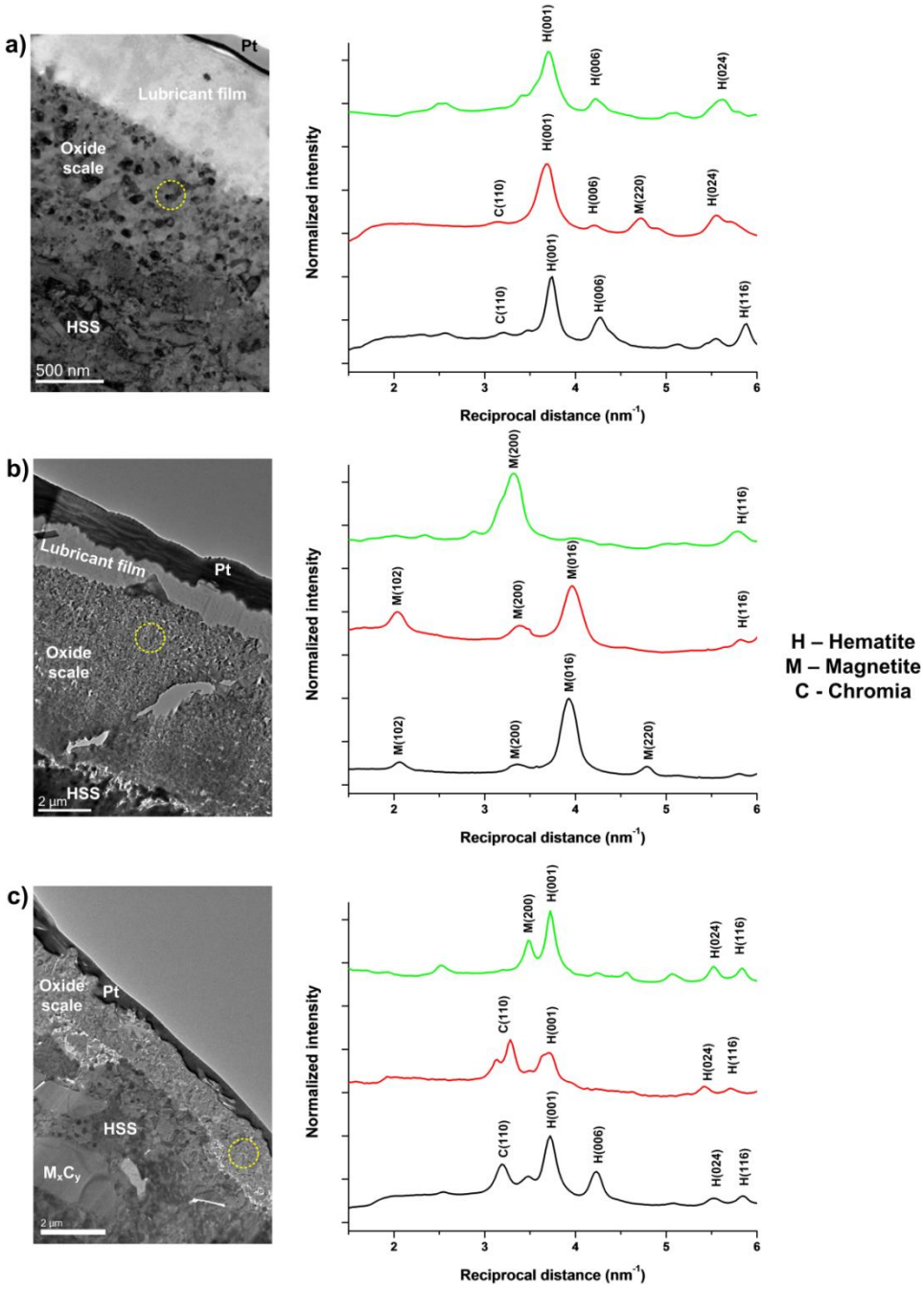


**Figure 7-9:** TEM images of HSS pin cross sections in a) 5mins lubrication, b) 15mins lubrication and c) 15mins static oxidation with corresponding intensity profiles from SAED

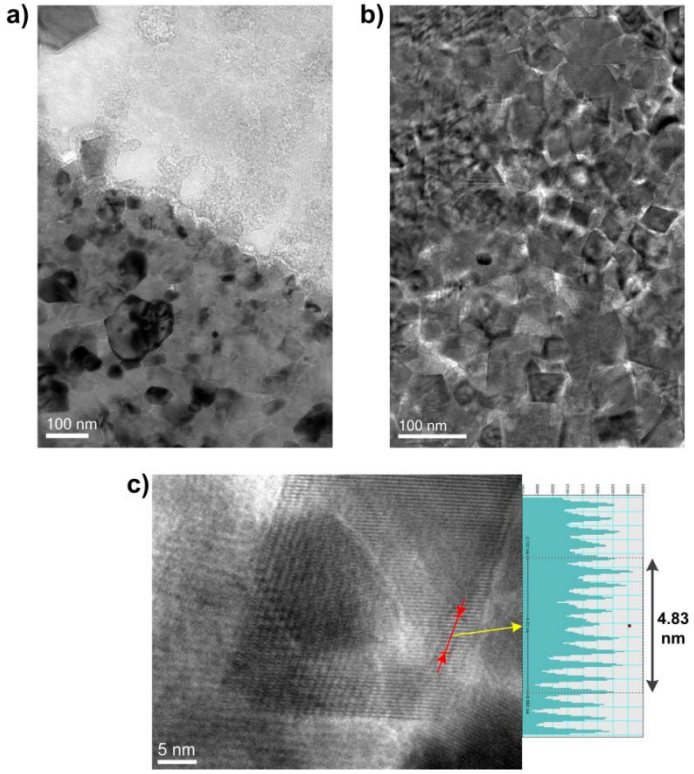


**Figure 7-10:** Magnified oxide microstructure after lubrication tests, a) 5mins, b) 15mins and c) $Fe_3O_4$ (102) nanoparticle with indicated d-spacing

## 7.3 Discussion

It has been shown (Figure 7-4) that carbides oxides are present on the pre-contact surface of oxidized HSS alongside iron oxide matrix. However, despite protruding through the oxide scale, those carbides oxide particles are likely to be ejected upon contact due to their poor adherence with the underlying substrate. This is justified by the total absence of carbides oxides on the sliding surface from cross-sectional observation (Figure 7-5). The current work is in good agreement with past literatures. In their study regarding oxidation behaviors of HSS at high temperature under dry and wet atmosphere, Qiang et al. [177, 178] observed various types of carbide oxides (mostly V-based) that are loosely held on top of a more compact scale. After conducting sliding test against mild-steel at high

temperature (900$^{o}$C), there was no sign of carbide-based particles on the front-most contact area [24]. On the other hand, the native oxide matrix is able to withstand the high shearing stress due to their excellent deformability and strong bonding with the metal substrate, mostly through the formation of anchoring $FeCr_2O_3$ spinels [150, 177, 178].

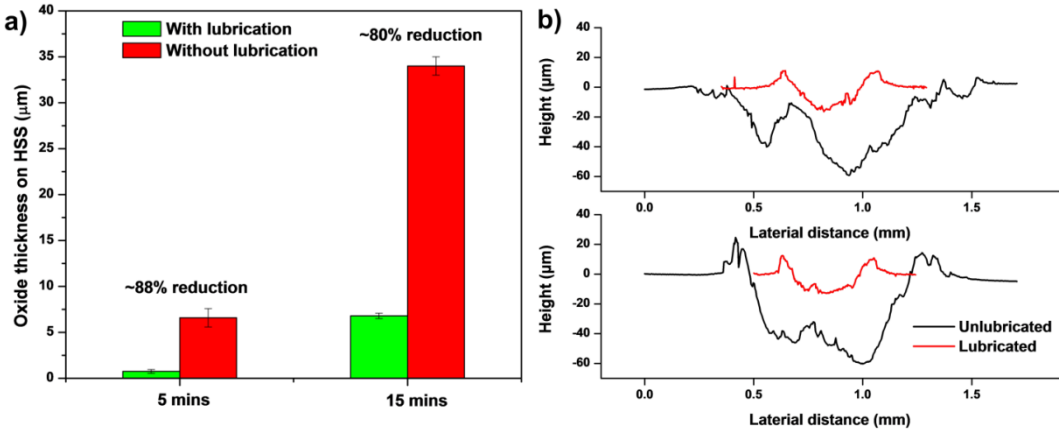


**Figure 7-11:** a) Variation of oxide thickness on HSS pin with various lubricating condition and b) wear track profiles on SS316 disc after 5mins (below) and 15mins (above) test

The formation of the tribo-layer (Figure 7-4) is likely originated from combined effects of adhesive wear, particles sintering and tribo-oxidation [179]. The development of such a layer is largely dominated by microstructural characteristics of the associated oxide particles while its endurance is also a function of loading amplitude and sliding velocity. Previous studies on sliding HSS/mild steel pair revealed tribo-oxide layer formation and its subsequent disintegration [22-24]. Particle omission by spallation leads to intermittent coverage of the glaze layer and increases friction coefficient as a result. This might arise from the fact that iron oxides tend to grow into coarse particles with poor deformability on mild steel which undermines the tribo-layer formability. In contrast, finer oxide particles have been shown to accelerate the tribo-layer formation on the sliding surface [25]. Native oxides of highly-alloyed steel reportedly grow as nano-scale grains [108, 180]. In addition,

Chapter 6 evidently revealed the nanograin oxide scale grown on SS316 which favors robust establishment of the glaze layer. The consolidation rate of the tribo-layer is believed to outweigh the omission rate of debris particles indicated by the growing thickness of glaze layer over time (by nearly 6 times as sliding time extends from 5mins to 15mins). Although the presence of tribolayer is commensurate with friction-reducing and -stabilizing effects, it is still considered unfavorable as it is developing at the expense of sacrificial wear of the opposing surface.

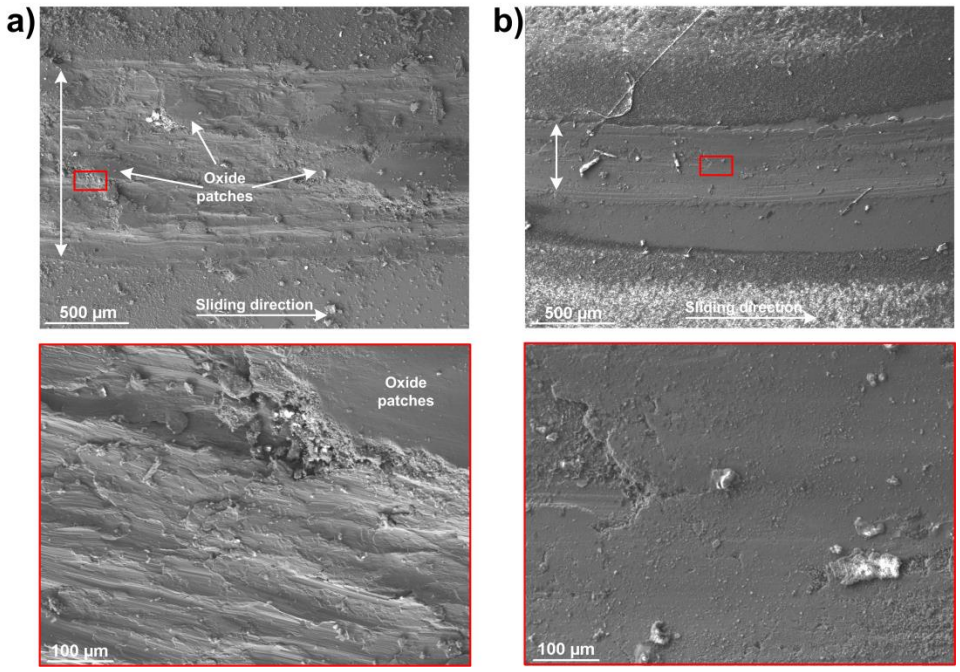


**Figure 7-12:** Worn morphologies of SS316 disc after 15mins test, (a) without lubrication and (b) with lubrication (below are magnified images, double-arrowed line indicates track width)

It is obvious that the employment of borate melt markedly inhibits adhered/transferred material on HSS pin as shown by the reduced scale thickness (Figure 7-11). The total reduction rate is estimated at ~88% after 5mins and ~80% after 15mins compared to unlubricated counterparts. Furthermore, the suppressed adhesive wear on HSS surface is indicative of a lower material loss on the opposing SS316 disc (Figure 7-11b) with the maximum reduction of 76% compared to unlubricated case. The exceptional wear resistance of borate lubricant is regarded as the most principle factor in the causation of anti-sticking behavior. Material transfer fundamentally occurs when there emerges either wear debris or third-body object on the contact interface. A reduced wear rate on the disc practically means less scale-sticking probability. Worn morphologies of SS316 disc after 15mins tests are given in Figure 7-12 to justify the wear mechanism under different lubrication conditions. In the absence of borate lubricant, catastrophic damages are visible including ploughing, abrasion coupled with a formation of discontinuous oxide patches. In contrast, the borate lubrication induces negligible wear severity as indicated by a reduced track width alongside a smooth worn surface (Figure 7-12b). It is noted that SEM micrograph was captured after the lubricant removal to reveal the true surface morphology.

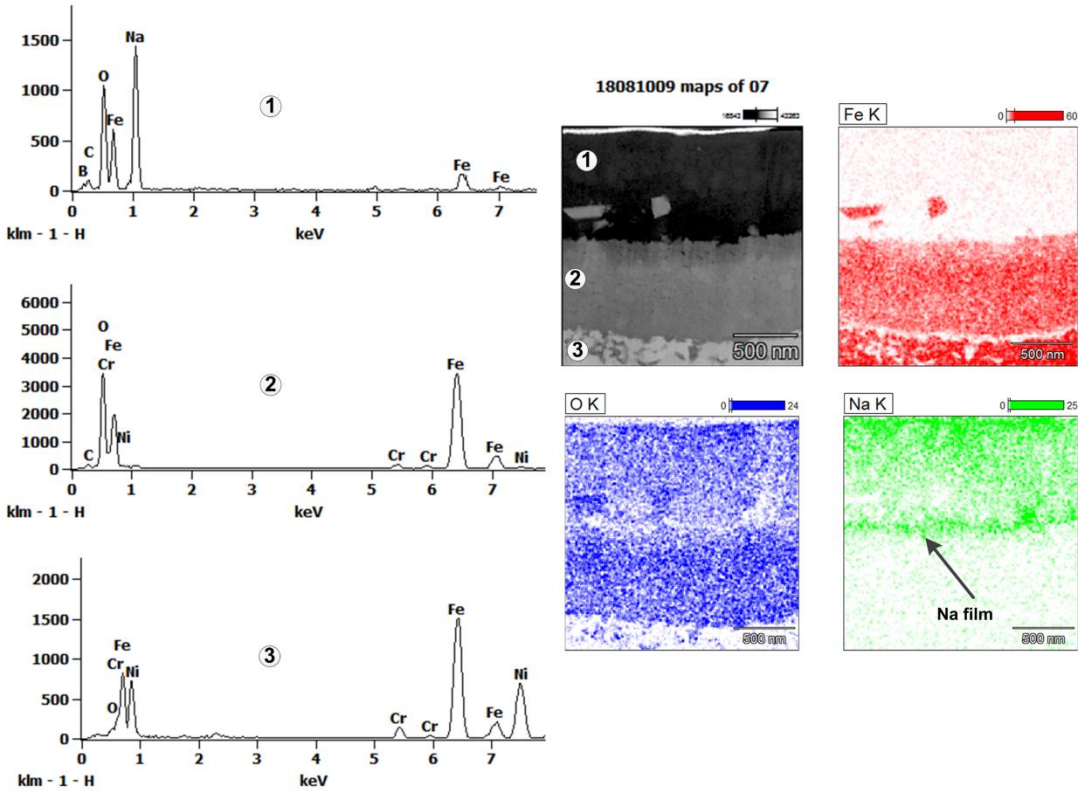


**Figure 7-13:** Individual phase spectrum and elemental distribution across the lubricated HSS pin after 5mins test

Beside friction-reducing effect (Figure 7-3), the resistance against adhesive wear arises from an effective lubrication and it is believed that the tribofilm plays a core role in these desirable behaviors. The surface chemistry of the immediate sliding interface is further examined to reveal the lubrication mechanism. Figure 7-13 shows the cross-sectional view of lubricated HSS interface after 5mins sliding test alongside relevant phase and elemental mapping. There are 3 different phases which can be compositionally distinguished by the complementary phase mapping. The uppermost layer (phase 1) is assigned to the lubricant layer with an abundance of Na, B and O while the two underlying layers are associated with oxide matrix (phase 2) and HSS substrate (phase 3), respectively. On the immediate

contact interface, a localization of Na is evident in the form of a thin film with an estimated thickness of ~50nm. Simultaneously, O is depleted in this region which certainly alters the oxidation behavior of the surface underneath. This is in good agreement with previous chapters (4,5 and 6). The robust adsorption of Na allows the tribofilm to sustain a high local shearing stress without failure and constantly provide an effective lubrication over the whole sliding duration. In addition, the durable lubricant film can act as a physical boundary which ultimately prevents possible segregation of wear debris on the sliding interface. In the circumstances where wear debris is formed, its oxidized surface would be subject to Na adsorption. This would effectively prevent them from being adhered onto the HSS surface due to the repulsion between 2 opposing Na-rich layers.

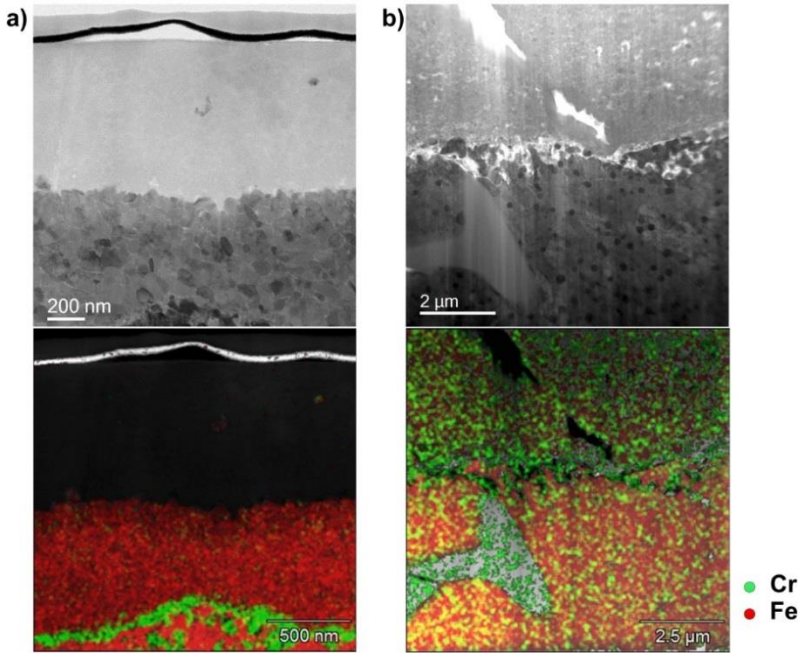


**Figure 7-14:** Localization of Chromia on HSS metal base/scale interface after 5mins lubrication test (a) and its disintegration after 15mins test (b)

As stated previously, the steel chemistry also plays a definite role in the high-temperature oxidation responses with alloying elements (Cr, Al, Si, Ni...) being introduced to enhance the oxidation resistance [7]. Due to their strong affinity with oxygen, oxidation of these sacrificial elements is more thermodynamically favorable with the development of an interlayer oxide [177, 178, 180-184]. Herein, SAED profiles are indicative of Chromia formation in the scales from static oxidation test and 5mins lubrication test (Figure 7-9). In addition, Figure 7-14 clearly illustrates a highly-localized Chromia film which continuously runs along the scale/substrate interface with a thickness of 100nm after 5mins lubrication test. The formation of Cr oxides interlayer (and possibly $FeCr_2O_3$ spinel) has been known for inhibiting further oxidation. The compact layer renders a low atomic diffusion rate which obstructs the outward migration of Fe ions. However, a prolonged sliding imposes the disintegration of Chromia layer as evidenced in Figure 7-14b where Cr signal is found scattering across the scale/base metal interface. The delocalization of Chromia is believed to free outward diffusion of Fe ions which occur along the grain boundary [7] and this could result in an increased oxidation (Fig. 10). Migrating Fe ions appeares to react with the existing Hematite to form Magnetite due to limited O activity on the interface (Figure 7-13). The resulting internal reduction of Hematite is evidenced by a rising proportion of Magnetite (Figure 7-9) with an apparent morphology evolution of the oxide nanoparticles (Figure 7-10). The reaction route is proposed as Fe (migrating) + $Fe_2O_3 \rightarrow Fe_3O_4$ which is greatly facilitated by a consistent lubrication effect and continuous tribological exposure on the HSS pin. However, as diffusion of atmospheric O into molten glass is well-acknowledged [185], one could not rule out its potential reaction with Fe ions which can thicken oxide scale over testing time despite the fully-formed

lubricant film. As the load-bearing capacity of sodium borate has been demonstrated in Chapter 6 (10-30N), it is likely that the lubricant can retain its anti-sticking characteristic over that range.

The current work used pin-on-disc platform to simulate the sticking occurrence between steel surfaces at high temperature and evaluate the influence of lubrication on such event. In real metal working processes where the fresh workpiece is continuously fed into the contact with the tool surface, the extent of sticking depends on many variables (temperature of steel piece, relative speed, steel grade…) and might be different from what observed in laboratory-scale testing. Thus, it is of necessity to justify the effectiveness of the concerning lubricant in actual working condition.

## 7.4 Conclusions

The current chapter aims to evaluate the effect of lubrication on wear behavior of High Speed Steel in contact with SS316 under high-temperature sliding condition. Several conclusions can be made as followed:

- HSS surface suffers negligible adhesive/transferred wear under borate lubrication contrary to the unlubricated case.
- The anti-sticking behavior is closely governed by the tribofilm formation on the immediate sliding.
- Adsorption of alkaline element (herein Na) on oxide surface has proved to be not only the foundation for effective lubrication but also the driving force to inhibit material transfer between pairing surfaces

- Prolonged exposure leads to phase transformation of iron oxides in which Hematite was transformed into Magnetite.

# CHAPTER 8:

# Tribological behaviors of sodium borate in rolling contacts

Surface characteristics of the workpiece change rapidly when passing from one mill to another due to differential rolling variables. To ensure a high surface quality of the rolled workpiece is one of primary priorities while consideration of the surface profile on the work roll is also equally important. However, the latter has not been often critically examined due to certain inconveniences, e.g. excessive physical dimension of the roll. Therefore, to have the capacity to evaluate both participating surfaces in the laboratory scale will provide significant benefit from the practical viewpoint. As the tribological behaviors of sodium borate have been extensively examined on sliding interfaces in previous chapters, the current chapter aims to determine its lubrication performance on rolling contacts with high pressure. A laboratory rolling platform was used to investigate surface-related occurrences of the rolling processes at high temperature. In addition, the effect of oxidation on the roll performance was also considered. It is noteworthy that the current testing configuration is not able to simulate the real hot rolling process. However, by setting loading amplitude close to actual processing parameter, complex interactions between lubricant and oxide scale on the rolling interface can be studied.

## 8.1 Experimental details

### 8.1.1 Material preparation

The present chapter employs High Speed Steel (HSS) as the work roll specimen. HSS roll specimens were cut from of an industrial roll into cylinder of 8.60mmxØ8.60mm with a ground surface (initial roughness of 0.2 μm, Table 8-4). X-ray diffraction pattern (Figure 8-1) of the starting HSS shows coexistence of metallic matrix and metal carbides. Microscopic image of a polished HSS (Figure 8-1) confirms the presence of two discrete phases with apparent morphology contrast. The chemical makeup of HSS is given in Table 8-1. The hardness and Young modulus of metallic matrix are 9.45±0.81GPa and 207±6.37GPa, while the corresponding figures of metal carbides are 24.41±4.43GPa and 275±12.53GPa. It is noted that this HSS material has slightly different chemical composition compared to that used in Chapter 6&7.

| C | Si | V | Cr | Mo | W | Ni | Mn | Fe |
|---|---|---|---|---|---|---|---|---|
| 2.0 | 0.94 | 5.61 | 4.69 | 5.83 | 3.97 | 0.87 | 0.95 | Remainder |

**Table 8-1:** Chemical composition of HSS (weight %)

Mild carbon steel (~0.3%C) was selected as the workpiece specimen with an initial roughness of ~1μm. The hardness and Young modulus of the material is 4.55±0.48GPa and 200±13.18GPa, respectively. The specimen shape and dimension are schematically depicted in Figure 8-2b with an effective length of rolling contact being 5mm. Prior to each test, both steel pairs were thoroughly cleaned by ethanol/acetone to remove contaminant. An aqueous solution of 5% wt. of sodium borate was prepared for lubricated rolling test

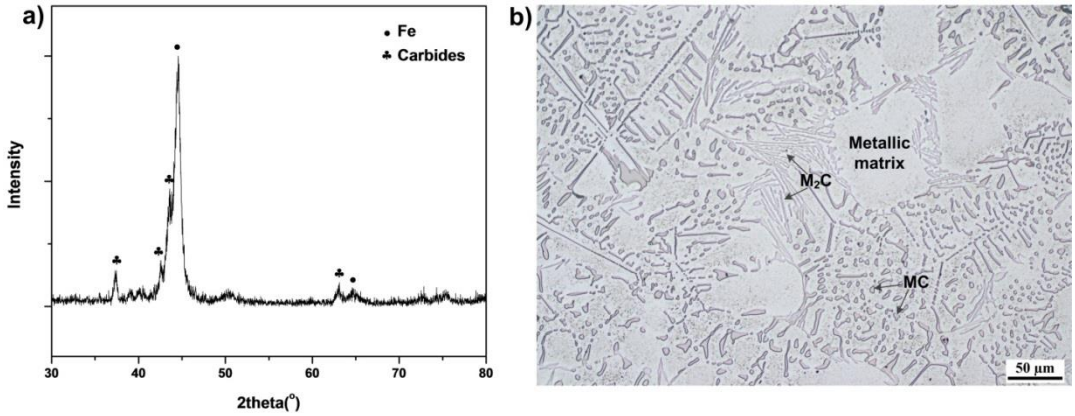


. **Figure 8-1:** a) XRD pattern of starting HSS and b) its microstructure

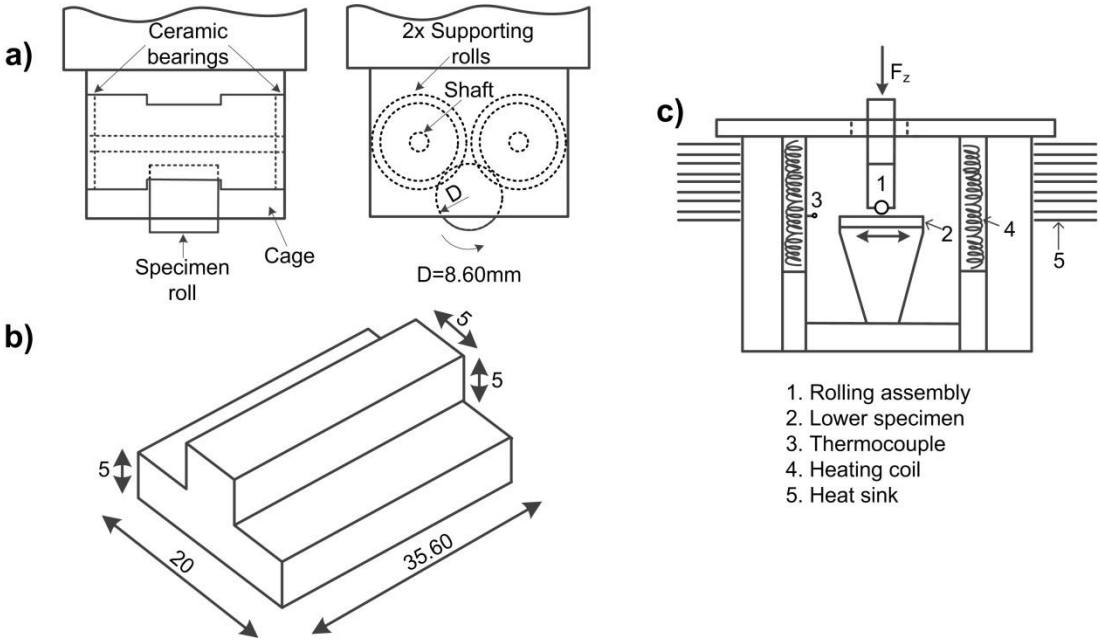


**Figure 8-2:** Simplified schematic of a) upper roll assembly, b) lower specimen and c) high temperature testing apparatus

### 8.1.2 Tribological test

Tribology test was conducted on the Bruker UMT3 high-temperature reciprocating module whose simplified schematic is given in Figure 8-2c. During the test, the HSS specimen was pressed against a lower specimen in a force-controlled mode and freely rolls as the lower specimen proceeds back-and-forth motion. The maximum contact pressure P

is calculated from the following Hertzian equation. For the sake of simplicity, Young modulus of the metallic matrix is chosen for the upper body because of its dominance in the starting material (fractional volume of carbide is only 12-15%)

$$P = \frac{2F}{\pi bL} (\text{Eq. } 8-1)$$

$$b = \sqrt{\frac{4F\left(\frac{1-v_1^2}{E_1}+\frac{1-v_2^2}{E_2}\right)}{\pi\left(\frac{1}{R_1}+\frac{1}{R_2}\right)}} (\text{Eq. } 8-2)$$

$v_{1,2}$: Poisson ratio of each component (0.3)

$E_{1,2}$: Young modulus of each component

F: applied force (N)

L: length of contact (mm)

Testing temperature was chosen from 550$^{o}$C to maximum 700$^{o}$C. The normal load was selected in the range of 50-150N corresponding to maximum contact pressure of 300-540 MPa which matches the rolling pressure in practice [174]. The traverse distance was set at 10mm with a frequency of 0.8Hz. These testing conditions were designed with careful consideration regarding operational limit of the ceramic bearings in the supporting rolls (Figure 8-2a). As the traverse length is less than half of the roll circumference, there is no material exchange (most likely oxide scale) between the supporting rolls and the specimen roll which could alter the roll contact surface after each cycle. The lower specimen was loaded into the furnace and heated to set temperature in 30minutes followed by 10 minutes of stabilization. In case of lubrication test, the lubricant solution was fed onto the testing area 2 minutes prior to the rolling with a flow velocity of 0.01ml/min. Next, the upper roll assembly was commanded to descend and press against the lower specimen, the normal load increased to a pre-determined point then the rolling subsequently proceeded in full 5 cycles. After the test finishes, both upper assembly and lower specimens were immediately retrieved out of the furnace and cooled in air to avoid further oxidation.

Since there is little slip and the rolling friction is generally very low, the determination of friction coefficient requires an extra care. In the current study, the 2-dimensional load cell used to detect the normal and lateral force has a minimum force resolution of 10mN. Contrary to tribotest in which relative movement is kept unchanged over the whole testing course (e.g. rotary pin-on-disc), the reciprocating direction reverses at the end of each stroke which normally involves increased uncertainty in lateral force. Herein, only 80% data in the middle of a single stroke is considered in the calculation of average rolling friction coefficient. Detailed description on friction coefficient acquisition can be found in supplemental information (Figure A-13)

### 8.1.3 Characterization

The characterization route is similar to what described in previous chapters. Viscosity measurement of sodium borate was carried out by a high temperature Rheometer (Physica MCR 301 Anton Paar). Firstly, the lubricant powders were dehydrated at 500$^{o}$C. Then pre-melting was performed in a Mo-crucible at 1000$^{o}$C with a holding time of half an hour. The molten material was then cooled at a rate of 10K/min.

The Bruker Contour GK-T 3D was used to examine the rolled surfaces and generate geometrical parameters. It is noted that the surface parameters are reported from an area perspective rather than a line profile perspective. There are 4 principle magnitude parameters being monitored including *Sa*, *Sq*, *Skw*, and *Sku*. *Sa* is the arithmetical mean height which could be considered as the extension of average roughness *Ra* to a surface. *Sq* is the root mean square length of the scale limited surface. *Ssk* (Skewness) reflects the symmetry of topography height distribution while *Sku* (Kurtosis) is an indication of height

profile sharpness. At least 5 separate measures were made on each specimen and the average values are reported.

## 8.2 Results

### 8.2.1 Effects of temperature and load on rolling characteristics at 550$^{o}$C-650$^{o}$C

To understand the effects of rolling parameters on surface characteristics of both steel components, tribology tests were conducted over a wide range of conditions. Temperature was selected at 550$^{o}$C, 600$^{o}$C and 650$^{o}$C while normal load varied from 50N to maximum 150N at each testing temperature. It is noted that a new HSS roll is used in each experimental subset. Figure 8-3 illustrates optical micrographs of mild steel surface after rolling test. While the non-rolling surface remains unchanged regardless of testing temperature, rolled area morphology displays dramatic changes across different temperature and loading condition. In contrast to dense parallel groves outside of the rolling area which is likely caused by machining, the rolled surface exhibits severe ploughing evidenced by deep scratches when the load is above 50N. Particularly at the highest load (150N), oxide delamination is observable at 550$^{o}$C and 600$^{o}$C while cracks were also visible at 650$^{o}$C. Areal parameters of the concerning specimens are given in Table 8-2 and Table 8-3. Outside rolling area, the surface roughness tends to increase with testing temperature (Table 8-2). In addition, it becomes increasingly rougher after rolling irrespective of temperature and loading amplitude (Table 8-3). The rolled surface appears to be skewed opposite to the original state by a combination of higher load and higher temperature. The change in Skw also indicates increasing proportion of protruding spikes

on the rolled surfaces. In addition, the increase in Sku suggests a spikey characteristic of the rolled surfaces (Table 8-3).

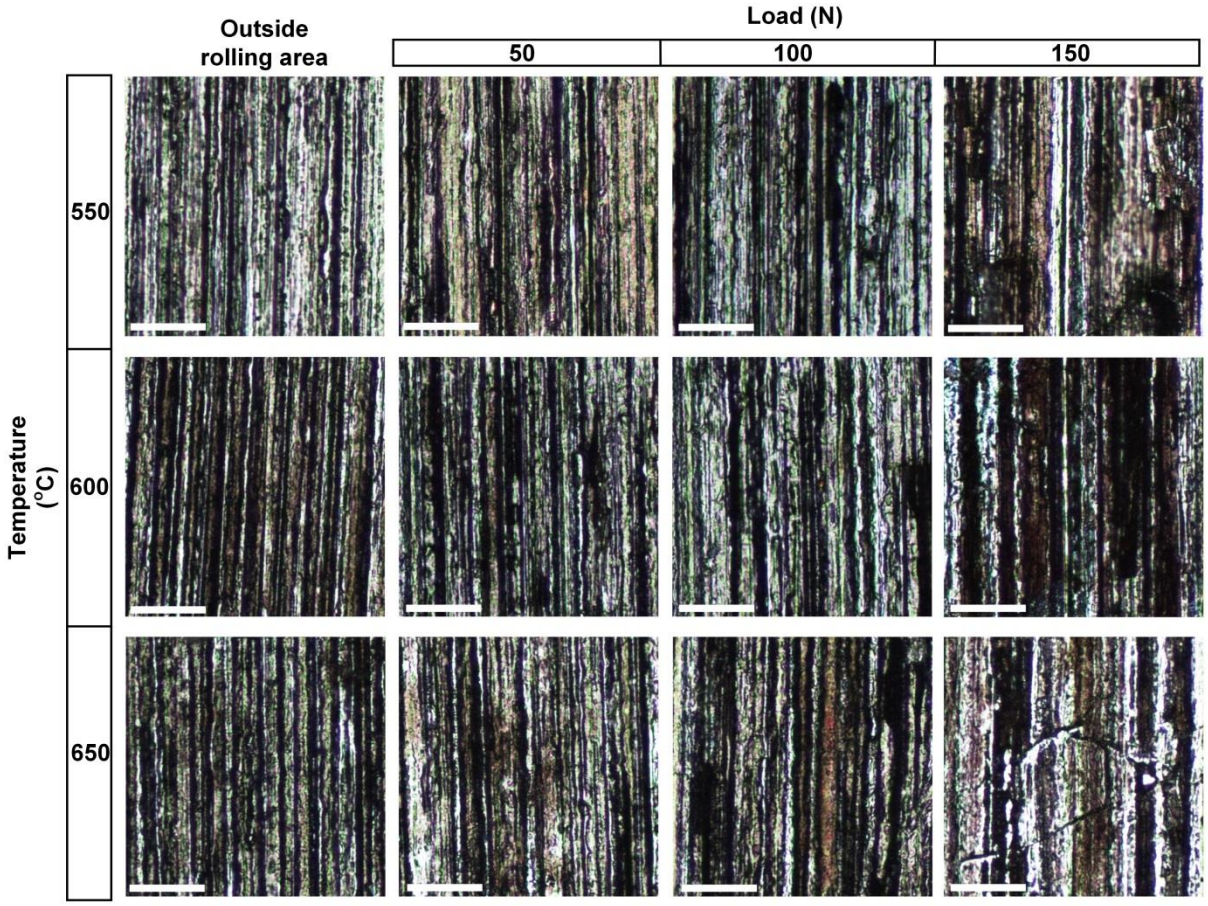


**Figure 8-3:** Optical microscope images of lower specimen surface after rolling test against fresh HSS roll (scale bar of 50 µm)

| | Outside rolling area | | | |
|---|---|---|---|---|
| | **Sa(µm)** | **Sq(µm)** | **Ssk** | **Sku** |
| **550ºC** | 0.99±0.05 | 1.27±0.05 | -0.55±0.13 | 3.8±0.37 |
| **600ºC** | 1.10±0.05 | 1.4±0.07 | -0.40±0.12 | 3.40±0.36 |
| **650ºC** | 1.26±0.04 | 1.57±0.05 | -0.26±0.05 | 2.90±0.09 |

**Table 8-2:** Variation of surface parameters from non-rolled area on lower specimen

| | **550ºC** | **600ºC** | **650ºC** | | **550ºC** | **600ºC** | **650ºC** |
|---|---|---|---|---|---|---|---|
| **Sa(µm)** | | | | **Sq(µm)** | | | |
| **50N** | 1.10±0.02 | 1.39±0.05 | 1.1±0.06 | **50N** | 1.43±0.03 | 1.88±0.08 | 1.49±0.1 |
| **100N** | 1.15±0.03 | 1.35±0.05 | 1.37±0.06 | **100N** | 1.47±0.05 | 1.78±0.09 | 1.8±0.1 |
| **150N** | 1.25±0.02 | 1.51±0.04 | 1.26±0.07 | **150N** | 1.65±0.04 | 2.03±0.06 | 1.7±0.1 |
| **Ssk** | | | | **Sku** | | | |
| **50N** | -0.36±0.23 | -0.40±0.15 | -0.44±0.24 | **50N** | 4.05±0.42 | 5.76±0.65 | 5.23±0.59 |
| **100N** | -0.07±0.01 | 0.60±0.17 | 0.45±0.26 | **100N** | 4.00±0.94 | 6.56±2.09 | 5.33±0.96 |
| **150N** | 1±0.1 | 0.83±0.12 | 0.91±0.07 | **150N** | 4.23±2.9 | 6.21±0.18 | 7.14±0.49 |

**Table 8-3:** Variations of surface parameters from rolled area on lower specimen across different testing conditions

Regarding the HSS roll surface, its relevant surface parameters across different testing conditions are given in Table 8-4 and Table 8-5. Contrary to mild steel whose surface roughness demonstrated a great sensitivity towards temperature and load, HSS surface roughness overall exhibits little change for all testing conditions. In fact, it slightly increases at lower temperature range and yields a minor decrease when loading increases at 650ºC. While Sku appears as similar as the starting state, the rolled HSS surface seems to experience a certain extent of skewing as figures are shifting towards zero, particularly at high load regime. This could be attributed to the oxide scale transfer from the lower specimen. Fig 8-5 shows optical micrographs of HSS surface before and after rolling tests. Oxide scale transfer is apparent with smeared reddish patches on a different background of the virgin surface. The extent of material transfer intensifies as testing condition becomes

progressively harsher as evidenced by the increasing coverage of adhered oxide scale. The variation of rolling friction coefficient as a function of testing condition is shown in Figure 8-4. The friction coefficient follows an upward trend with increasing load at any temperature, although the recorded figures are only in range of 0.01-0.025.

| Original surface | | | |
|---|---|---|---|
| **Sa(µm)** | **Sq(µm)** | **Ssk** | **Sku** |
| 0.19±0.01 | 0.29±0.01 | -0.71±0.01 | 8.12±0.14 |

**Table 8-4:** Surface parameters of pristine HSS

| | **550°C** | **600°C** | **650°C** | | **550°C** | **600°C** | **650°C** |
|---|---|---|---|---|---|---|---|
| **Sa(µm)** | | | | **Sq(µm)** | | | |
| **50N** | 0.21±0.01 | 0.22±0.02 | 0.23±0.01 | **50N** | 0.31±0.01 | 0.33±0.03 | 0.31±0.01 |
| **100N** | 0.25±0.01 | 0.23±0.01 | 0.19±0.01 | **100N** | 0.36±0.01 | 0.33±0.01 | 0.29±0.02 |
| **150N** | 0.21±0.15 | 0.21±0.01 | 0.16±0.01 | **150N** | 0.32±0.02 | 0.32±0.01 | 0.25±0.01 |
| **Ssk** | | | | **Sku** | | | |
| **50N** | -0.09±0.42 | -0.16±0.12 | 0.20±0.024 | **50N** | 7.93±0.50 | 7.34±0.58 | 7.83±0.35 |
| **100N** | -0.28±0.12 | 0.12±0.24 | 0.18±0.03 | **100N** | 6.47±0.91 | 8.29±2.59 | 7.37±0.30 |
| **150N** | -0.17±0.09 | -0.15±0.1 | 0.14±0.25 | **150N** | 7.38±0.53 | 7.51±0.79 | 9.04±1.28 |

**Table 8-5:** Variations of surface parameters from HSS across different testing conditions

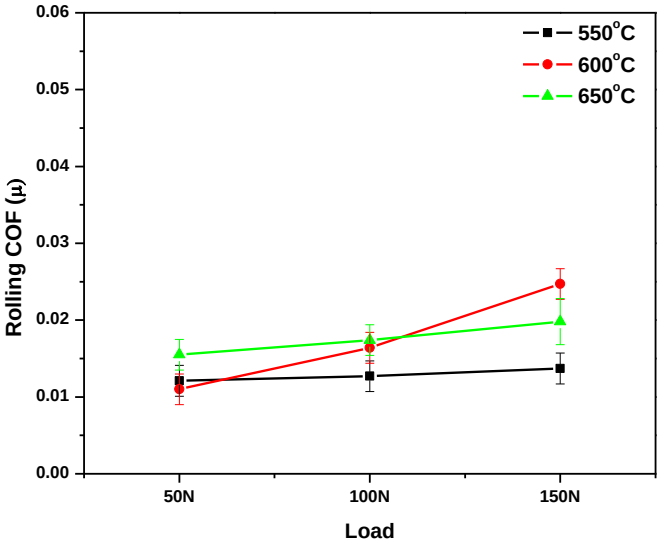


**Figure 8-4:** Rolling friction coefficient as a function of temperature and load in case of fresh roll

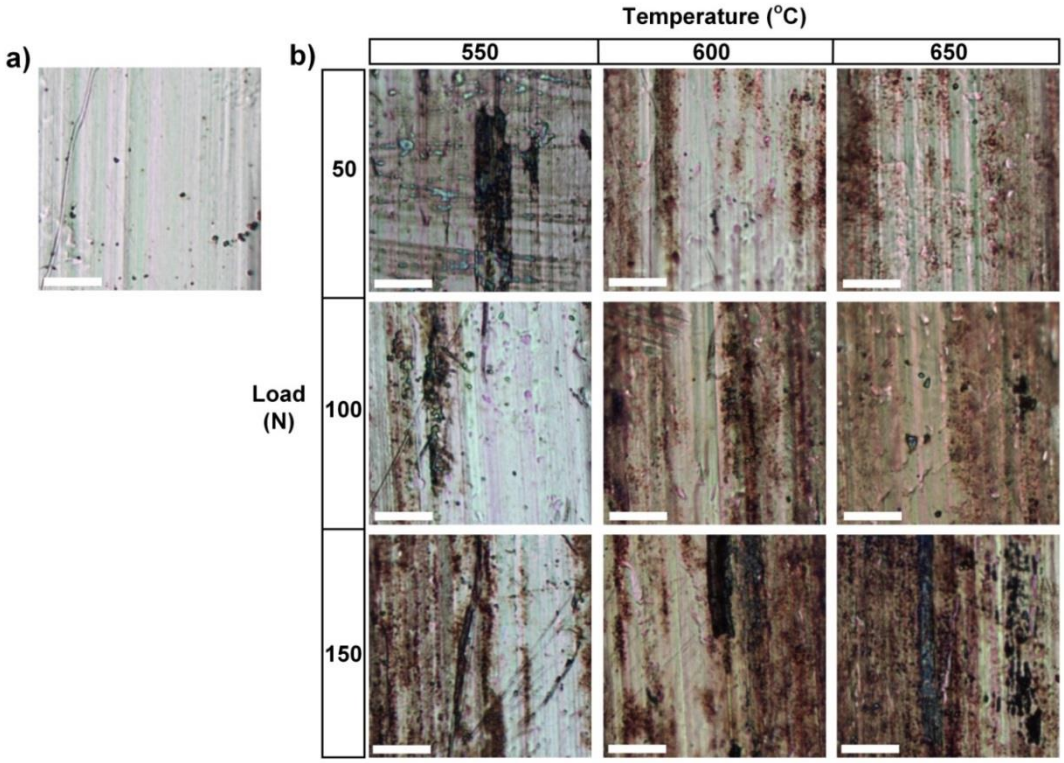


**Figure 8-5:** Optical microscope images of HSS surface
a) before and b) after rolling test (scale bar of 10µm)

### 8.2.2 Effects of oxidized HSS on rolling characteristics

In practice, work roll experiences a certain extent of oxidation during the warm/hot rolling process due to the heat transfer from the hot work piece. For instance, the maximum surface temperature of the work roll varies periodically in range of 550$^{o}$C-650$^{o}$C during the hot rolling of steel [174, 186]. Depending on the duration of exposure albeit for a very short time, this inevitably results in the formation of oxide scale on the contact surface with considerable changes in morphological nature and mechanical properties compared to the fresh surface. Several tests were carried out to determine the potential influences of oxidized roll surface on the rolling behaviors. The HSS roll specimens were pre-oxidized at 650$^{o}$C in a muffle furnace with durations of 0.5 hr, 1 hr and 2 hrs. The

testing temperature was kept at 650$^{o}$C with varying normal force (50-150N). Figure 8-6 illustrates surface morphology of oxidized rolls after different oxidation times and the corresponding X-ray diffraction patterns. After 0.5hr of oxidation, the HSS surface reveals island-like plateaus of protruding oxides which surround the lower matrix. Increased oxidation time causes rapid propagation of the island-like oxide patches. However, the fully-oxidized HSS surface (2hrs) shows a nearly homogenous morphology in which the previous two surface entities are no longer can be distinguishable. The island-like patches are likely associated with V-based oxides while the slowly-oxidized area is enriched by Cr which can be justified in complementary EDS mapping (Figure A-14, Figure A-15 and Figure A-16). Such non-uniform growing characteristics of oxide scale can be attributed to differential oxidation kinetics of metallic matrix and metal carbide on HSS which have been reported previously [150, 177, 178]. XRD patterns suggests the formation of iron oxides with $Fe_2O_3$ being the most dominating type as the oxidation progresses (Figure 8-6d). Geometrical parameters of pre-oxidized HSS surface at varying duration are given in Table 8-6. Compared to the virgin counterpart, the surface roughness increases rapidly with oxidation duration as the oxidized surface is twice as rough as the starting surface after 2hr of oxidation. In addition, the increase in Ssk and decrease in Sku are mainly associated with the formation of protruding oxides which are illustrated in Figure 8-6.

It is clear that the oxidation results in dramatic morphology changes on the roll surface. After rolling test at 650$^{o}$C, the roughness of the rolled area does not show any recognizable changes compared to that observed prior to rolling (Table 8-7). On the other hand,

marginal drops in both Ssk and Sku suggest a certain extent of flattening effect on the rolled HSS.

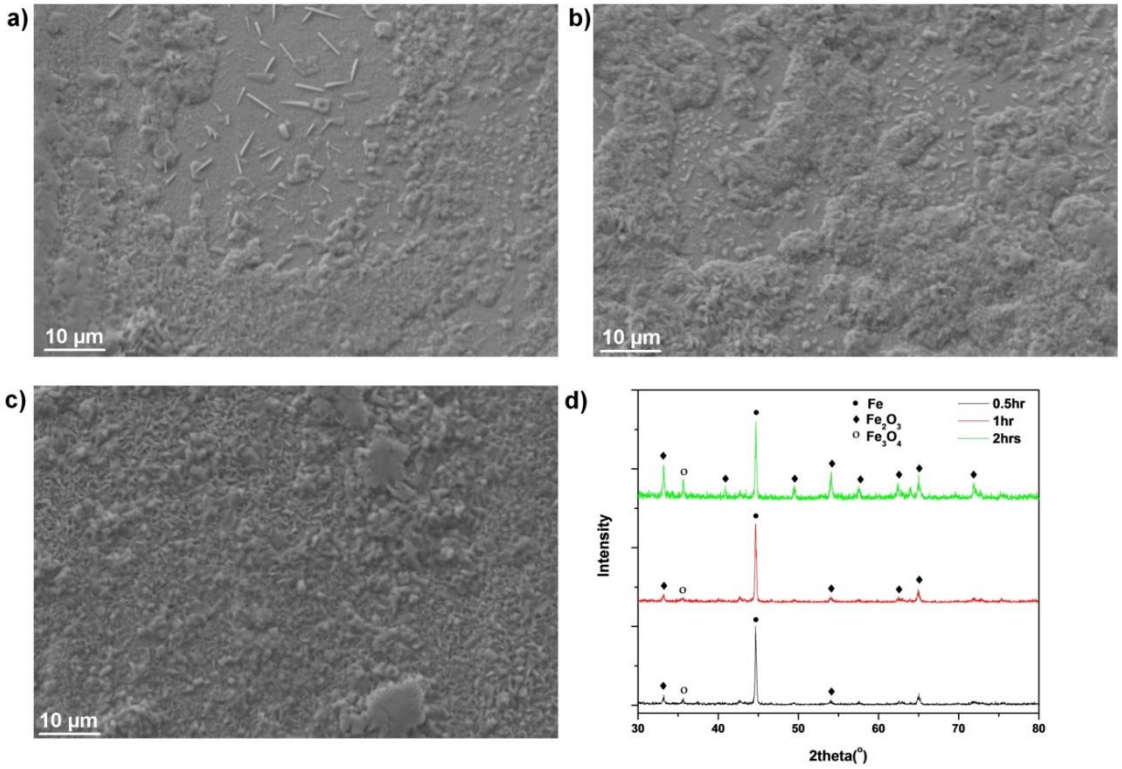


**Figure 8-6:** SEM micrographs of oxidized HSS surface with different oxidation duration, a) 0.5 hr, b) 1hr, c) 2hrs and d) their corresponding XRD patterns

Table 8-8 illustrates the geometrical changes on the lower specimen rolled against oxidized HSS. Compared to out-of-roll area (Table 8-2), surface roughness increases after rolling regardless of testing condition. Furthermore, rolled surface is skewed heavily in case of mildly oxidized HSS, even though the value is edging towards zero at high load range. For the fully-oxidized roll, Ssk shows a reverse tendency as it is close to zero in moderate load but jumps significantly when subject to 150N. Regarding Sku, it exhibits overall increases in most tests compared to the non-rolling area. The changes in surface parameters are indicative of increasing formation of spikes due to repetitive rolling

contacts. Rolled surface morphologies of the lower specimens are given in Figure 8-7. Quite similarly to what observed in case of fresh roll, ploughing- and scratching-related damages remain the most predominant. The damage severity appears to be amplified by increased load and longer oxidation time of the roll surface.

| | **Outside rolling area** | | | |
|---|---|---|---|---|
| | **Sa** | **Sq** | **Ssk** | **Sku** |
| **0.5hr** | 0.29±0.01 | 0.40±0.02 | 0.32±0.09 | 5.56±0.64 |
| **1hr** | 0.35±0.03 | 0.47±0.03 | 0.45±0.14 | 5.36±0.79 |
| **2hrs** | 0.43±0.03 | 0.56±0.04 | 0.24±0.07 | 4.29±0.53 |

**Table 8-6:** Variations of surface parameters on oxidized HSS prior to testing

| | **0.5hr** | **1hr** | **2hrs** | | **0.5hr** | **1hr** | **2hrs** |
|---|---|---|---|---|---|---|---|
| **Sa(μm)** | | | | **Sq(μm)** | | | |
| **50N** | 0.29±0.01 | 0.36±0.02 | 0.36±0.01 | **50N** | 0.39±0.02 | 0.48±0.03 | 0.47±0.02 |
| **100N** | 0.30±0.02 | 0.35±0.01 | 0.37±0.02 | **100N** | 0.42±0.03 | 0.46±0.01 | 0.49±0.03 |
| **150N** | 0.31±0.03 | 0.30±0.01 | 0.38±0.02 | **150N** | 0.42±0.03 | 0.41±0.02 | 0.51±0.02 |
| **Ssk** | | | | **Sku** | | | |
| **50N** | 0.27±0.06 | 0.33±0.07 | 0.23±0.07 | **50N** | 4.81±0.20 | 4.29±0.19 | 3.9±0.13 |
| **100N** | 0.50±0.14 | 0.22±0.03 | 0.37±0.07 | **100N** | 4.81±0.01 | 4.07±0.14 | 5.16±1.41 |
| **150N** | 0.26±0.03 | 0.39±0.07 | 0.12±0.05 | **150N** | 4.80±0.58 | 4.30±0.20 | 4.96±1.06 |

**Table 8-7:** Variations of surface parameters on oxidized HSS after testing at 650$^{o}$C

| | **0.5hr** | **1hr** | **2hrs** | | **0.5hr** | **1hr** | **2hrs** |
|---|---|---|---|---|---|---|---|
| **Sa** | | | | **Sq** | | | |
| **50N** | 1.48±0.06 | 1.25±0.06 | 1.19±0.02 | **50N** | 1.92±0.01 | 1.58±0.09 | 1.51±0.05 |
| **100N** | 1.48±0.01 | 1.50±0.03 | 1.50±0.05 | **100N** | 1.93±0.03 | 1.93±0.06 | 1.89±0.07 |
| **150N** | 1.27±0.02 | 1.13±0.05 | 1.45±0.04 | **150N** | 1.63±0.03 | 1.43±0.04 | 1.85±0.05 |
| **Ssk** | | | | **Sku** | | | |
| **50N** | 0.61±0.12 | -0.21±0.09 | 0.08±0.18 | **50N** | 4.9±0.48 | 3.45±0.18 | 4.12±0.62 |
| **100N** | 0.66±0.06 | 0.10±0.07 | 0.06±0.15 | **100N** | 4.9±0.51 | 4.14±0.67 | 4.08±0.07 |
| **150N** | 0.20±0.26 | 0.06±0.06 | 0.32±0.08 | **150N** | 4.10±0.39 | 4.5±0.26 | 4.1±0.28 |

**Table 8-8:** Variations of surface parameters from mild steel surface after rolling against oxidized HSS at 650$^{o}$C

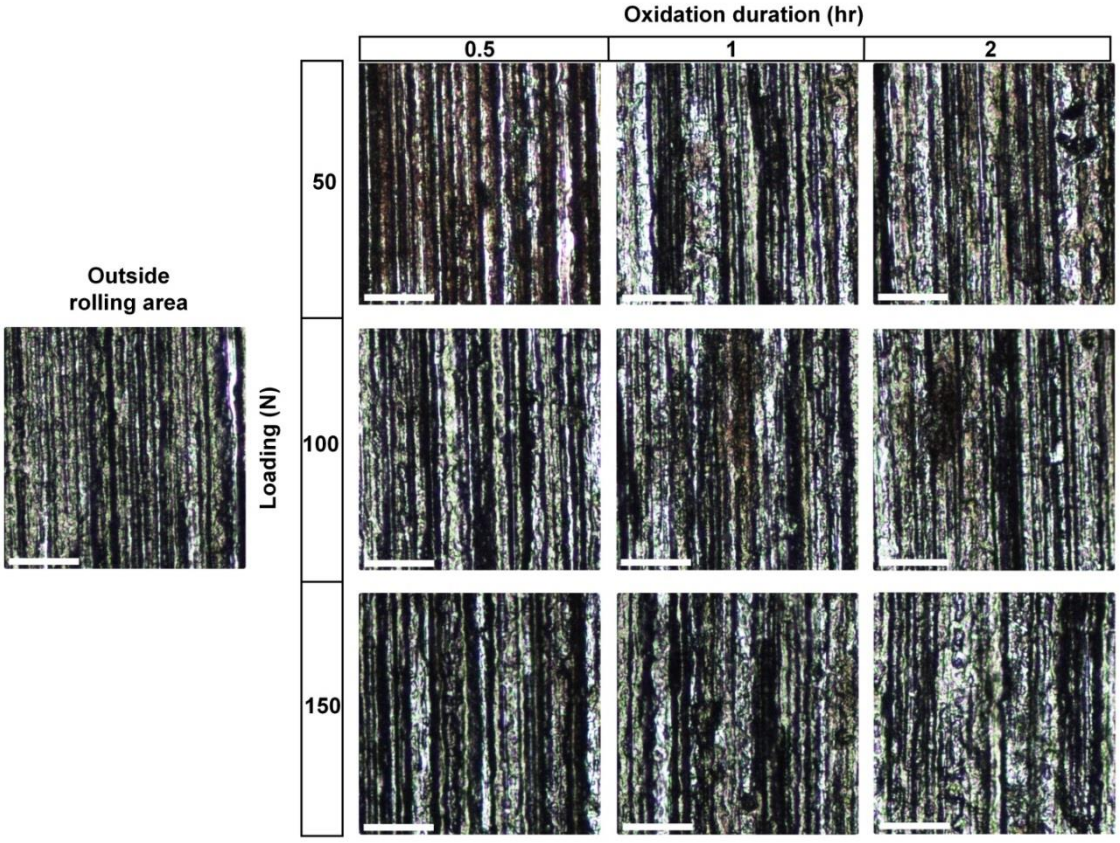


**Figure 8-7:** Optical images of lower specimen surface after rolling test against oxidized roll (scale bar of 50 µm)

Rolling friction coefficients of the subset experiments are shown in Figure 8-8. Although the test involves mildest oxidized roll (0.5hr) shows relatively similar COF as what seen in case of fresh roll, overall the friction coefficient is higher in comparison to the tests using fresh rolls. In fact, it exhibits a dramatic rise with the prolonged oxidation of the roll and loading amplitude. The maximum value of COF is recorded at 0.045, nearly as twice as the highest figure at the same testing condition using fresh roll.

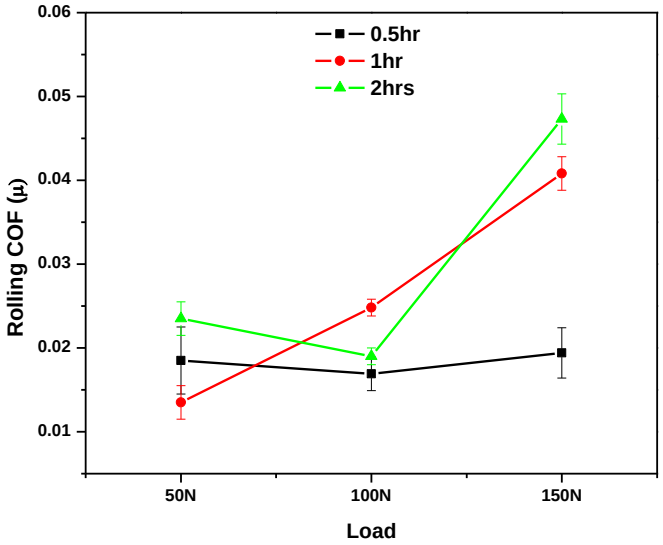


**Figure 8-8:** Rolling friction coefficient as a function of temperature and load using oxidized roll

### 8.2.3 Rolling under lubrication

Lubrication tests were performed at the temperature range of 600°C-700°C with a fixed load of 150N (~540MPa). The surface condition of the work roll is also taken into consideration by comparing fresh roll and oxidized roll (oxidation duration of 2hrs at 650°C). In addition, dry rolling tests were also carried out for direct comparison. Figure 8-9 illustrates rolling friction coefficient under dry and lubricated tests. Aligning with what seen previously, the fresh roll surface generates lower friction coefficient compared to fully-oxidized surface, except at 700°C in which there is no sizable difference between the two. Surprisingly, the introduction of lubrication yields higher friction coefficient compared to dry rolling irrespective of roll surface condition. At 600°C (lubricant melts at 525°C), fresh HSS/mild steel pair yields a COF of roughly 0.06 while using oxidized roll doubles the figure (~0.12). As the testing temperature rises further, lubricant viscosity

rapidly declines and the resulting COF follows a decreasing trend in both cases although the slope is much steeper in the case of oxidized roll.

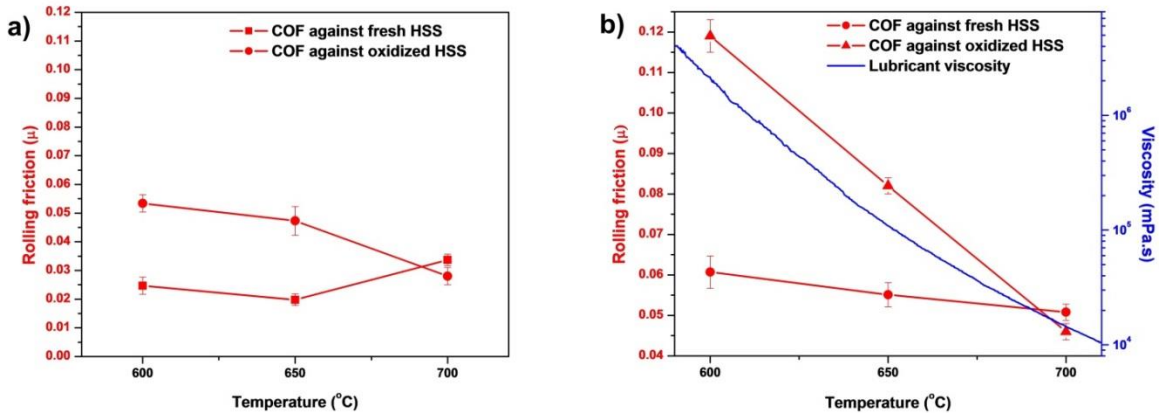


**Figure 8-9:** Rolling friction under a) dry and b) lubrication condition with respect to lubricant viscosity

Figure 8-10 shows optical images of fresh HSS roll surface after dry and lubricated test (with 150N). Again, dry rolling results in a considerable amount of adhered oxide scale on the roll surface and the transferred layer looks thicker as temperature rises. On the other hand, the introduction of lubricant completely inhibits the oxide pickup as evidenced at 600$^{o}$C and 650$^{o}$C. Specimen at 700$^{o}$C also does not show any sign of transferred oxide, although the lubricant appears to stick on the HSS surface after test. Experiments using oxidized HSS see relatively similar behaviors when the lubricant adherence only occurs at 700$^{o}$C. Figure 8-11 illustrates the morphology of adhered lubricant on the HSS roll (which occurred at 700$^{o}$C) with its characteristic chemical fingerprint. The viscous lubricant melt was likely stretched out by a shearing force which produces such feather-like appearance upon solidifying. SEM micrographs of rolled mild steel surfaces under different lubrication conditions are illustrated in Figure 8-12. Without lubrication, the rolled surfaces are

commonly characterized by parallel grooves and scratches which is quite similar to what observed previously (Figure 8-3 and Figure 8-7). Under lubrication, rolled surfaces show a stark contrast since the lubricant was able to remain on the rolled area after 5-cycles of rolling. The platelets lying on the rolled surfaces can be assigned to recrystallized borate upon cooling (similar to Chapter 4). This is also justified by the apparent changes in friction coefficient in the presence of lubricant (Figure 8-9). A detailed characterization in later part (section 8.3) will confirm the existence of the lubricant film after the rolling test.

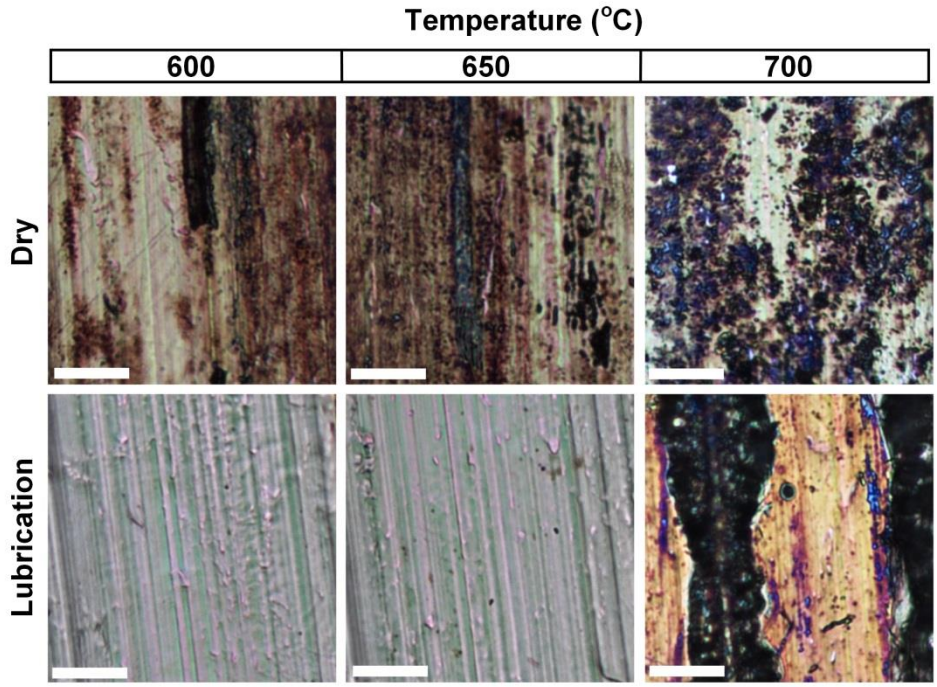


**Figure 8-10:** Optical images of HSS surface after test (scale bar of 10µm)

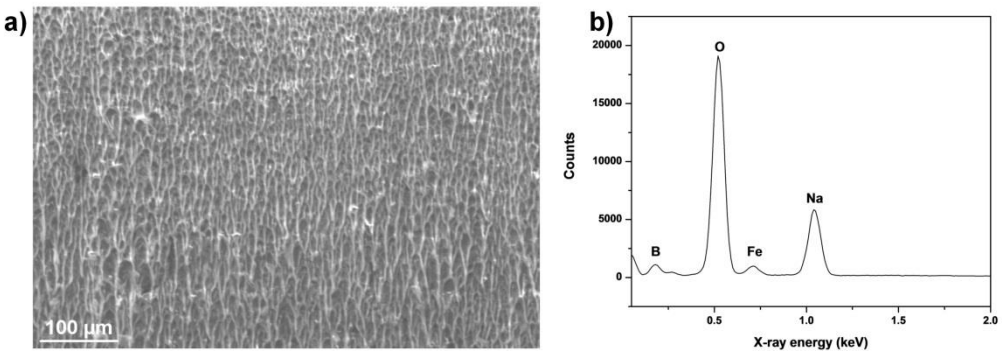


**Figure 8-11:** SEM micrograph of transferred lubricant (a) and the corresponding X-ray spectrum (b)

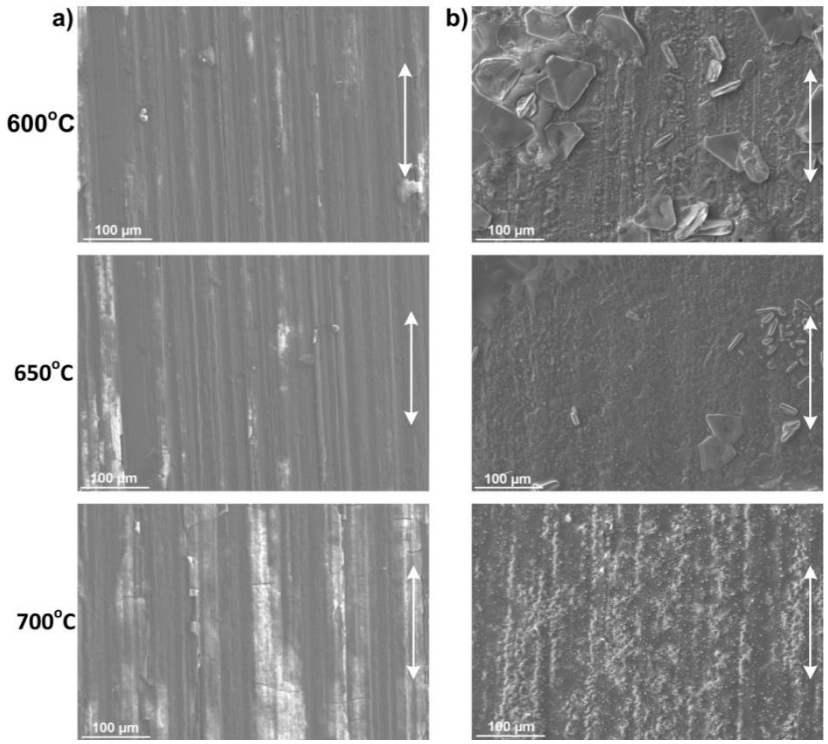


**Figure 8-12:** SEM micrographs of lower specimen surface after a) dry tests and b) lubrication tests (double-arrowed line indicates moving direction)

### 8.2.4 Pickling of rolled surfaces

The rolled surfaces under different lubrication conditions are subjected to pickling for scale removal. HCL (10% volume in distilled water) is chosen as pickling liquor. The rolled specimens were immersed into a becker of pickling liquor for 4 minutes at 28$^{o}$C and then washed rigorously 3 times by water and ethanol, respectively. The resulting surface parameters of pickled surfaces are reported in Figure 8-13. It is shown that lubricated rolled surfaces have a lower average roughness than unlubricated counterparts after pickling, particularly at high temperature range. Also, Ssk appears shifting towards zero at high temperature end although unlubricated surface has a larger deviation. Lastly, Skur is significantly lower when the lower specimen is rolled in the presence of lubricant. The changes in surface parameters suggest that exposure to borate lubrication results in a

smoother, less spikey surface after pickling. 3D surface plots of pickled surfaces are given in Figure 8-14 as marked difference is increasingly apparent as testing temperature rises.

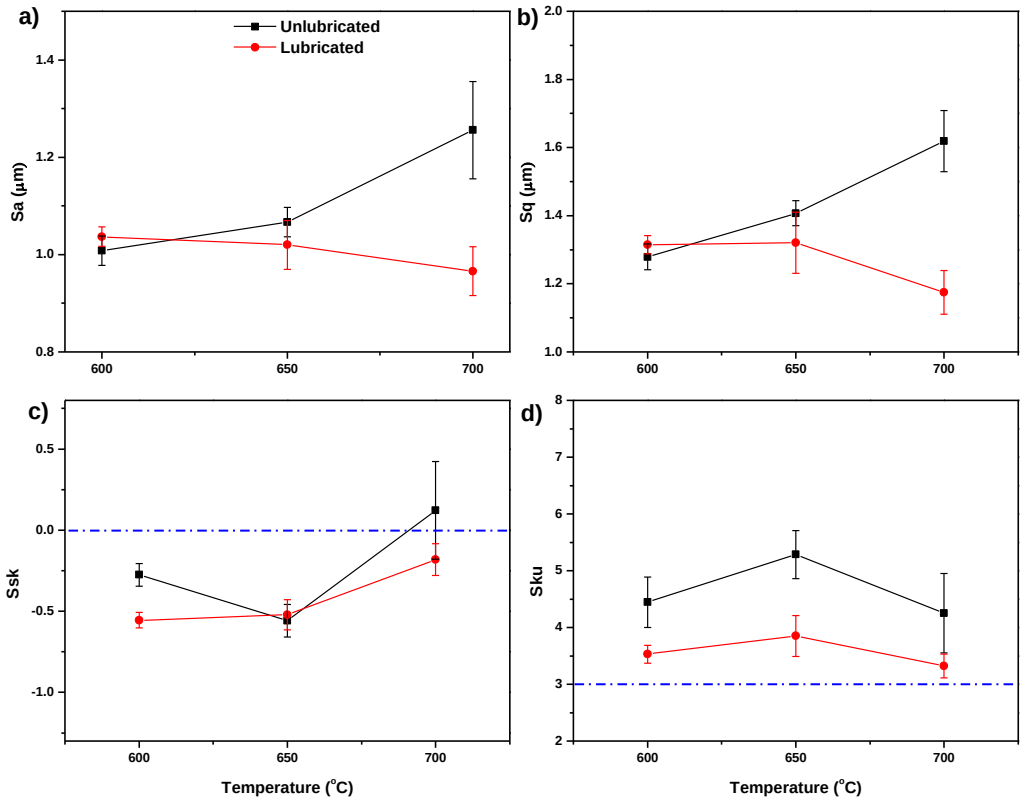


**Figure 8-13:** Areal surface parameters of lower specimen after pickling

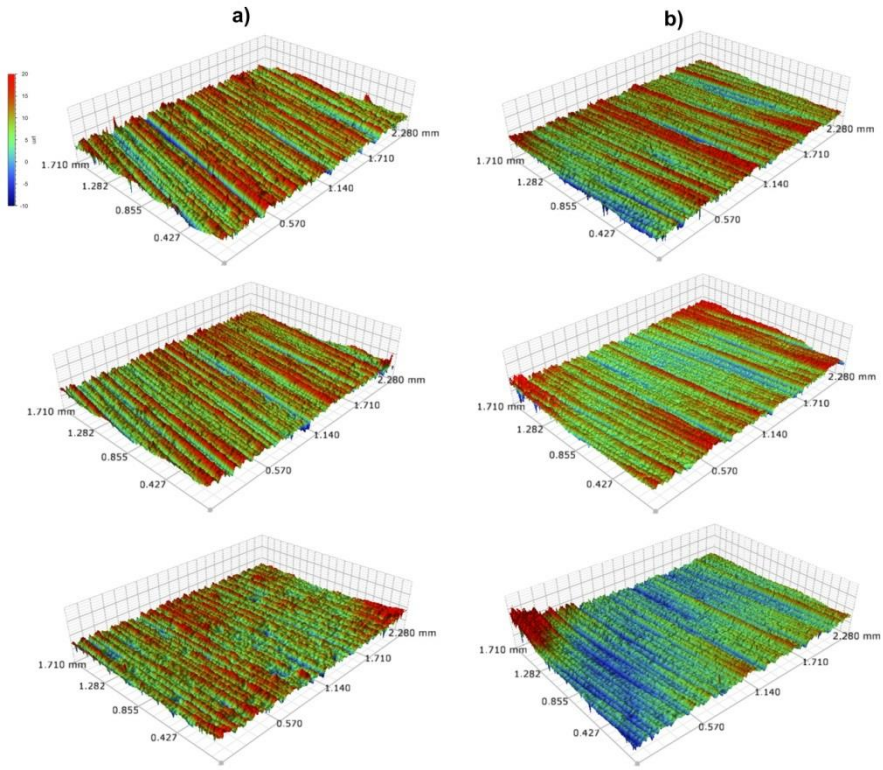


**Figure 8-14:** 3D images of rolled surfaces after a) dry rolling and b) lubricated rolling (top-to-bottom order: 600$^{o}$C, 650$^{o}$C, 700$^{o}$C)

## 8.3 Discussion

It has been demonstrated that the temperature of the work piece and loading amplitude collectively govern the oxide transfer occurrence on the roll surface. Increase in temperature leads to the formation of a thicker oxide scale as the specimen is heated in air atmosphere [7]. In fact the oxide scale thickness is roughly 2µm, 2.8µm and 3.8µm at 600$^{o}$C, 650$^{o}$C and 700$^{o}$C, respectively after the non-isothermal heating stage. This in turn amplifies the probability of scale sticking as evidenced by microscopy examination (Figure 8-4 and Figure 8-10). Moreover, higher loading magnitude can create a local spalling or even delamination of the grown scale (Figure 8-3) which consequently yields more intense material transfer. The continuous removal of oxide in combination with the mentioned

surface damages due to repetitive rolling contact increase the surface roughness and intensify the spikiness of the rolled surface regardless of roll surface condition (Table 8-3 and Table 8-8).

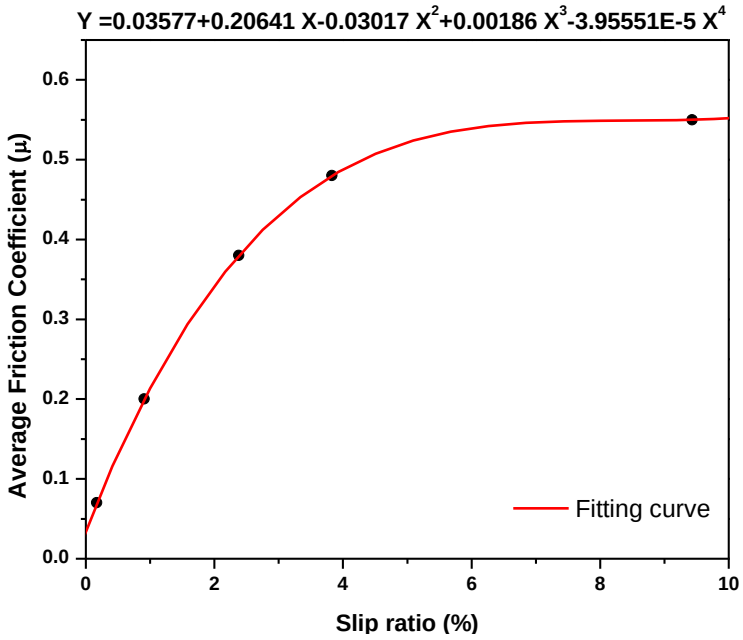


**Figure 8-15:** Rolling friction coefficient from roller-on-roller experiments as a function of slip ratio [187]

Ma et al. [187] conducted roller-on-roller experiments (between two mating steel surfaces) and revealed a close relationship between slip ratio and friction coefficient (Figure 8-15). By using extrapolation, there was little slip during the present rolling test (the slip ratio is less than 0.04% when friction coefficient is 0.044). In this work, the low slip ratio is the origin of low friction coefficient despite the heavy rolling load.

The surface condition of HSS roll plays a crucial role in friction behaviors of the rolling contact. While using pristine roll surface generates relatively low rolling COF which appears quite insensitive towards loading magnitude (Figure 8-5), oxidation of roll surface quickly escalates the friction coefficient (Figure 8-8). This could be attributed by the considerable changes in surface geometry induced by oxide scale growth upon high

temperature. It has been acknowledged that metal carbides and metallic matrix possess differential high-temperature oxidation kinetics as the former outgrows the latter due to favorable thermodynamics [177, 178]. This is justified by localized formation of oxides on carbide-based precipitates at the early stage of oxidation followed by the subsequent oxide growth on metallic matrix as oxidation progresses (Figure 8-6). As a result, this imposes surface roughening on HSS (Table 8-6) which consequently elevates the number of micro-asperities collisions and rolling resistance [188, 189]. While mild oxidation leads to an insignificant rise in friction coefficient, the effect becomes more obvious in the case of heavily oxidized roll as shown in Figure 8-8. This is in a good agreement with the past study [190].

It has been shown that the introduction of borate lubrication drastically change the rolling behaviors of the steel pair. The formation of the lubricating film was able to remain on the rolled area after test without being squeezed out as evidenced in Figure 8-12. This could be attributed to potential surface reaction between the lubricant melt and rolled surface which allows the lubricant to sustain such high contact pressure (>500MPa). The formation of the lubrication film can also be justified by the change in friction coefficient compared to the unlubricated tests (Figure 8-9b) regardless of the roll surface condition. This might arise from the adhesion between the lubricant film and the roll surface which potentially elevates the rolling resistance. Bulk properties of lubricant melt also play a crucial role on friction behaviors as lower viscosity induces lower friction. This partially reflects the hydrodynamic nature of the concerning lubrication system, although the inclusion of mixed or boundary lubrication is more likely. Previous chapters revealed

strong affinity between sodium borate melt and oxidized steel surfaces at elevated temperature. This could lead to a stronger lubricant adherence which consequently requires greater work to overcome the rolling resistance in the case of pre-oxidized HSS.

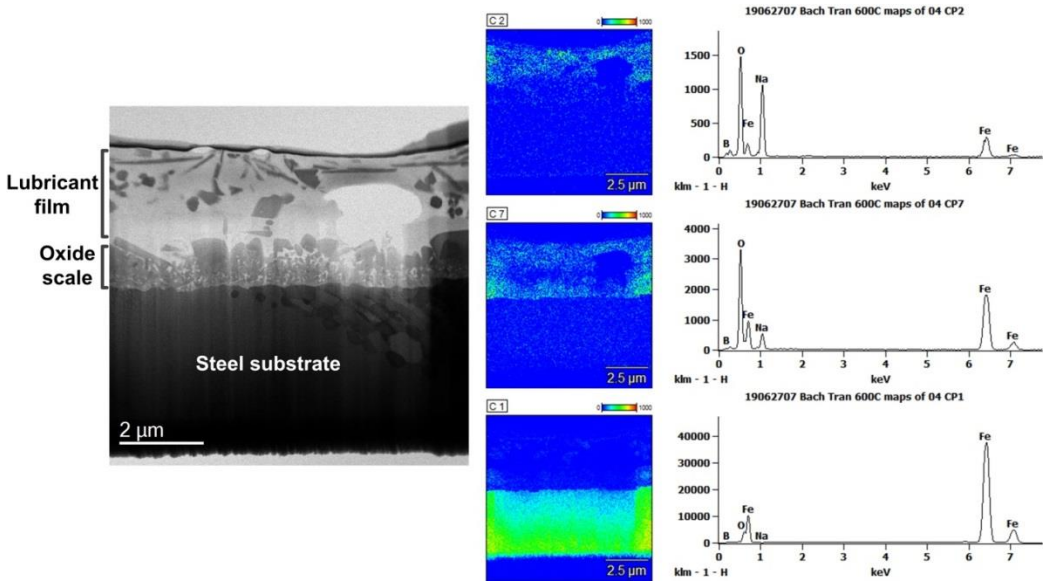


**Figure 8-17:** Cross-sectional views of mild steel surface and the corresponding compositional phase analysis after lubrication test at 600$^{o}$C, 150N

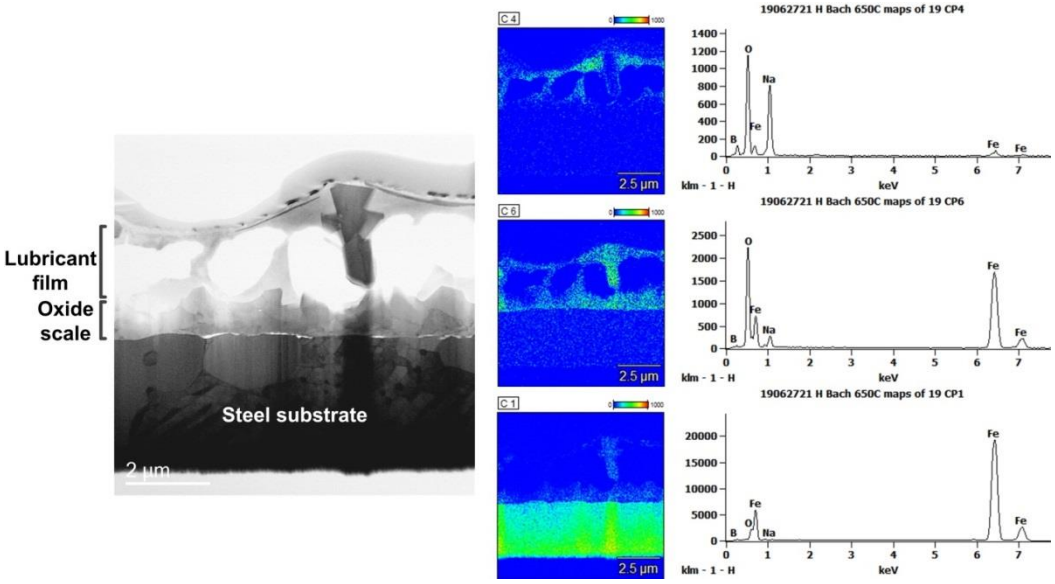


**Figure 8-16:** Cross-sectional views of mild steel surface and the corresponding compositional phase analysis after lubrication test at 650$^{o}$C, 150N

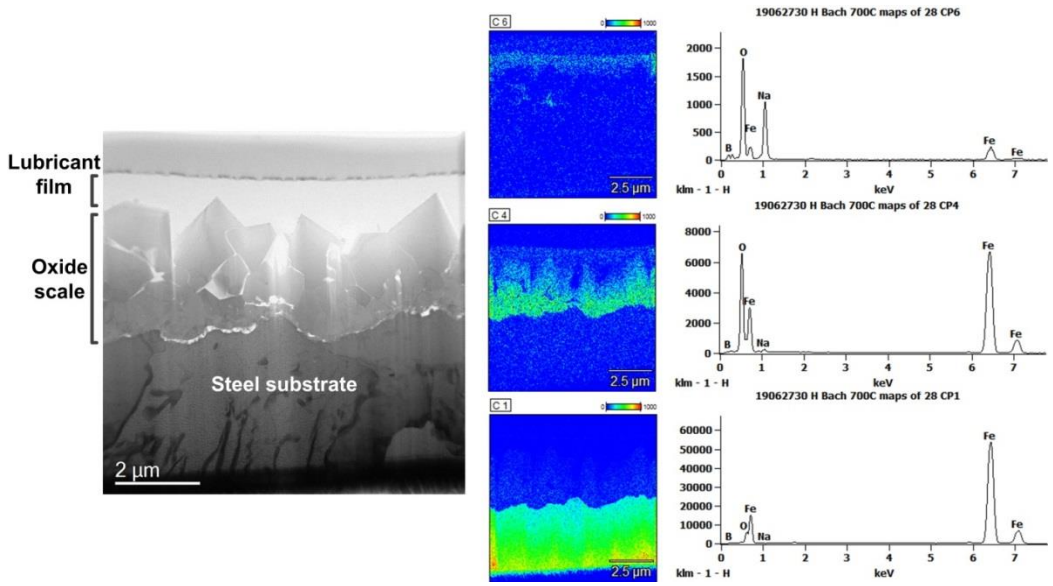


**Figure 8-18:** Cross-sectional views of mild steel surface and the corresponding compositional phase analysis after lubrication test at 700$^{o}$C, 150N

The use of borate lubricant evidently suppresses the material transfer which otherwise readily occurs during unlubricated tests (Figure 8-10). The oxide pickup has been known for its detrimental consequences in metal forming practice [27] . This positive effect is originated from the presence of lubricant film which can act as a physical boundary and minimize the chances of contact between the oxide scale and the work roll surface. Figure 8-16, 8-17 and 8-18 illustrate cross-sectional views of rolled area exposed to lubrication at different temperatures. There are 3 distinct layers in top-to-bottom order: lubricant layer, oxide scale and the steel substrate. The TEM lamellar specimen at 650$^{o}$C partially sacked due to overmilling during FIB process (Figure 8-17), although the boundary between layers is still recognizable. It is clear that the oxide scales are fully contained by the lubricant film which effectively prevents them from approaching the work roll surface.

There appears a microstructural evolution of the oxide scale exposed to lubrication. At the lowest testing temperature (600$^{o}$C), the oxide scale consists of an abundance of sub-micron particles which are heavily scattered. Since the oxide scale is thin prior to contact (2µm), it is likely shattered upon heavy loading and the formation of subsequent oxide scale is a result of complex reaction between the lubricant melt, shattered oxide scale and possible the outward-diffusing Fe from the steel substrate. At higher testing temperatures (650$^{o}$C and 700$^{o}$C), the oxide scale is formed in bulk and becomes thicker (Figure 8-19).

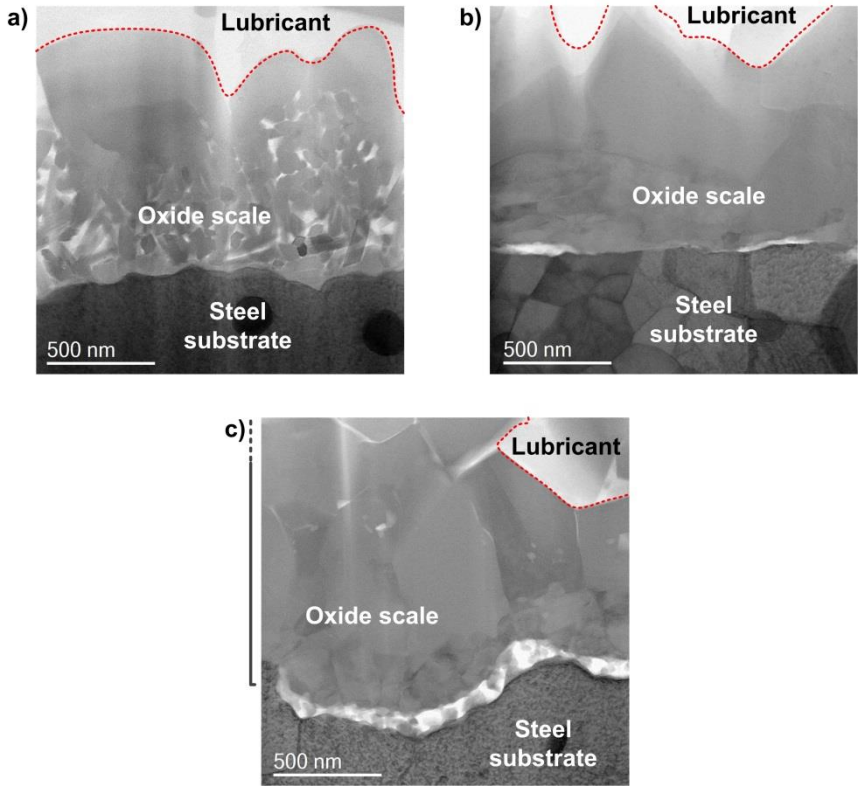


**Figure 8-19:** Magnified images of the oxide/steel substrate interface after lubricant test at a) 600$^{o}$C, b) 650$^{o}$C and c) 700$^{o}$C (load of 150N)

XRD analysis on the rolled area substantiates the apparent effect of borate lubricant on the formation of iron oxide scale (Figure 8-20). As expected, the untreated rolled areas are composed of 3 types of iron oxides (FeO, $Fe_3O_4$, $Fe_2O_3$) with Hematite ($Fe_2O_3$) being the most predominant constituent. In addition, the formation of complex compound

$FeO.FeBO_3$ is likely due to the reaction between the lubricant melt and the outward-diffusing Fe ions. Besides that, the use of borate lubricant evidently transforms the iron oxide structure characterized by the rising dominance of Magnetite ($Fe_3O_4$). The microstructure evolution of iron oxide by lubrication favor the subsequent pickling process since Hematite is considered hard-to-remove oxide due to its sluggish dissolution in pickling acid [191, 192].

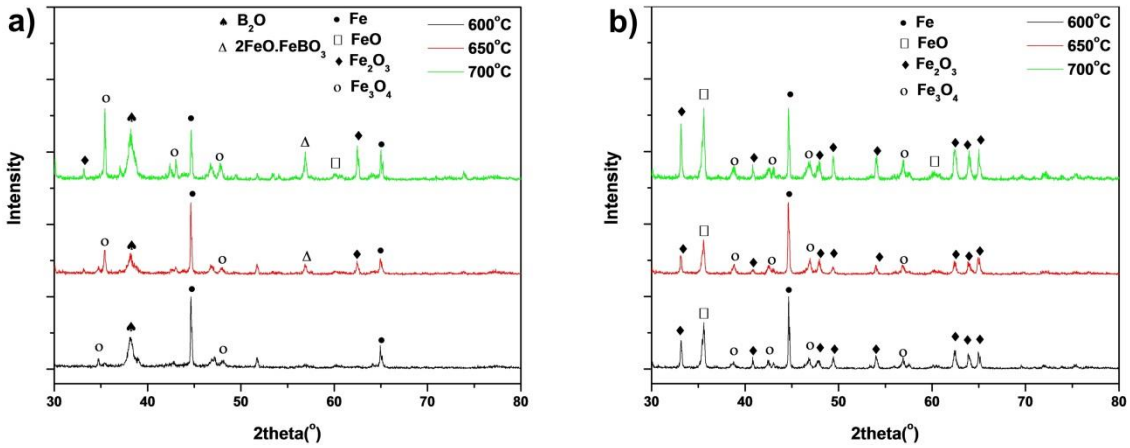


**Figure 8-20:** XRD patterns of rolled surfaces under a) lubrication and b) dry condition

It is noteworthy that the current rolling configuration is not representative of the actual hot rolling process in which there is a reduction of rolled workpiece thickness coupled with considerable deformation and 2-5% slip. However, as the contact pressure can be set closely to real processing parameter (>0.5GPa), the above results can be used to understand the complex interface reactions, particularly in the presence of lubricant.

## 8.4 Conclusions

In this study, a large volume tribology tests is conducted to study the surface interactions in rolling contacts over a wide range of conditions. There are some conclusions that can be found as followed:

- Oxide scale transfer occurs readily on the HSS surface under dry conditions and the extent grows with temperature and loading amplitude
- Pre-oxidation of HSS elevates the rolling friction coefficient compared to the case where fresh rolls are used
- The application of lubricant drastically hinders the material transfer on the HSS roll surface which is attributed to the formation of a lubricant film, although it raises the rolling friction coefficient
- Compared to dry rolling, the use of lubricant also transforms oxide microstructure on the rolled surface in which Magnetite replaces Hematite to become the most predominating phase. This conversion is beneficial for the subsequent pickling process.

# CHAPTER 9:

# Synthesis of potassium borate and its tribological behaviors above 800ºC

As shown in section 2.4, there is a fair amount of studies dedicated to the tribological behavior of sodium-based glass melt at high temperature. On the other hand, potassium-based glass melts have not received a reasonable attention. This chapter describes a simple method to synthesize potassium borate as a potential lubricant at high temperature. The tribological behaviors of synthesized potassium borate are compared with sodium borate at temperature up to 900ºC. Thorough characterization was performed to understand the molecular structure, thermal behavior and lubrication mechanism of synthesized material.

## 9.1 Material preparation

### 9.1.1 Synthesis of potassium borate

Potassium borate was synthesized by the condensation reaction between potassium hydroxide (KOH) and boric acid ($H_3BO_3$) in water. A 2.5g of KOH pellets was added into a 250ml of distilled water at 80ºC. Next, a 5.8g of $H_3BO_3$ in powder form was introduced into the KOH aqueous solution while the temperature was kept unchanged. The solution was vigorously stirred at roughly 300rpm for 8 hours. After that, temperature was increased to 200ºC to allow water vaporization and condensation. The product was retrieved in the white powder form with the nominal composition of $K_2O.2B_2O_3$. The condensation reaction is given as followed:

$$KOH + H_3BO_3 + H_2O \xrightarrow{80^oC} K_2O.2B_2O_3(a) \xrightarrow{200^oC} K_2O.2B_2O_3(s)$$

In hot friction test, High Speed Steel was chosen as the pin and Stainless Steel 316 (SS316) was selected as the disc material. The mechanical properties and chemical composition of the steel tribopair can be found in section 6.1.2. The disc surface was ground and polished to achieve an average roughness of 0.1µm. The steel pair was cleaned with ethanol/acetone prior to friction test. A 5% wt. aqueous solution of potassium borate was prepared for lubrication test.

### 9.1.2 Friction test

High-temperature friction test was performed on the UMT2-CETR ball-on-disc tribometer. The SS316 disc was first installed into the furnace chamber followed by sequential heating to set temperature (850ºC and 900ºC). Once the furnace temperature reached the set point, the upper stage carrying HSS pin was automated to descend to a distance of 3mm away from the disc surface. The pre-oxidation of HSS pin lasted for 5 minutes. Lubricant solution was dropped onto the heated disc at 2 minutes before contact engagement with a rate of 0.01ml/s. Sliding velocity was kept constant at 0.1m/s while the testing duration was fixed at 3 minutes with a fixed load of 10N. When the friction test finishes, the tribopairs were retrieved immediately and cooled in the air to prevent further oxidation.

### 9.1.3 Characterization

The 3D Interferometer Optical Microscope (Bruker Contour GT-K) was used to generate wear track profiles on the disc. Morphologies of the worn surfaces were examined

by the JOEL JSM-6490LV Scanning Electron Microscopy (SEM) equipped with Energy Dispersive Spectroscopy (EDS). Specimens for STEM work were prepared by the Dual Beam FEI Helios NanoLab G3 CX (FIB). The cross sections of the tribo-interfaces were observed by the aberration-corrected JOEL ARM 200F Scanning Transmission Electron Microscopy (STEM) at 200keV.

## 9.2 Results

### 9.2.1 Molecular structure and thermal behavior of synthesized potassium borate

Figure 9-1 presents a series of analysis on the synthesized potassium borate. It shows that the as-received potassium borate has a relatively poor crystallinity, evidenced by weak diffraction peaks and peak broadening in the XRD pattern. The material is likely constructed by plural constituents that possess short-range order structure. Unlike sodium borate, the synthesized potassium borate does not hold much adsorbed water as indicated by the absence of the peak at 3500cm$^{-1}$ in FTIR spectrum. The peak at 1336cm$^{-1}$ can be attributed to asymmetric stretching of B-O in trigonal $BO_3$ while the out-of-plane bending of B-O in $BO_3$ contribute to the peak of 708cm$^{-1}$ [102]. In addition, the peak located at 1024cm$^{-1}$ can be associated with terminal symmetric stretching of B-O while the peak at 922cm$^{-1}$ refers to the B-O ring stretching [193]. Compared to sodium borate (Figure 4-1), the synthesized potassium borate shows little trace of tetrahedral $BO_4$ presence. It can be seen from the GTA/DSC curve (Figure 9-1), only 8% mass loss is observed which confirms the lack of absorbed water molecules in the potassium borate structure, the corresponding figure in the case of sodium borate is >40% (Figure 4-1). Moreover, the DSC curve shows three consecutive endothermic peaks at 660$^{o}$C, 720$^{o}$C and 800$^{o}$C

respectively which corresponds to different melting point. This strongly suggests the compositional inhomogeneity of the synthesized potassium borate.

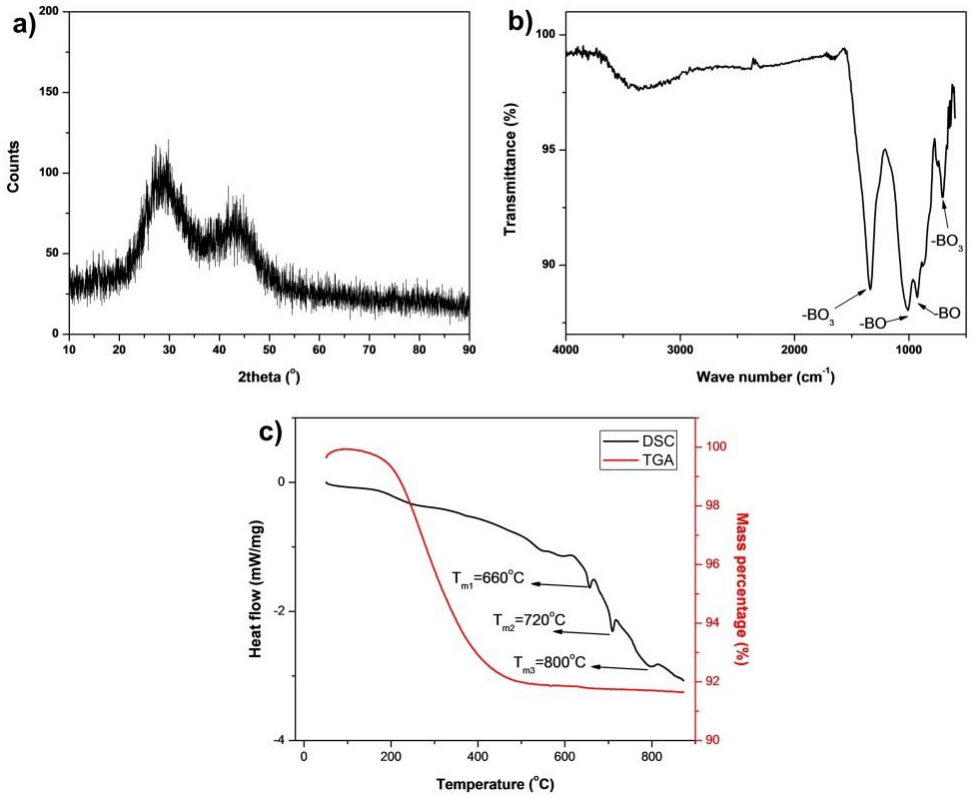


**Figure 9-1:** a) X-ray diffraction pattern, b) FTIR spectrum and GTA/DSC curve of synthesized potassium borate

### 9.2.2 Friction and wear behavior of K/Na borate

Friction coefficient curves of the sliding HSS/SS316 pair under different lubrication modes are illustrated in Figure 9-2. In the absence of lubricant, friction behavior is characterized by an initial period of fluctuation followed by a stabilization stage at both 850°C and 900°C. This is in line with what demonstrated in Chapter 7. However, a higher temperature enables a more rapid transition towards the friction stabilization as the running-in stage takes roughly 30 seconds at 900°C while it requires nearly 90 seconds to

approach the steady stage at 850ºC. The friction coefficient stabilizes at 0.19 and 0.18 at 850ºC and 900ºC, respectively. Alkaline borates lubrication clearly results in a much shorter running-in process regardless of the alkaline elements, although K borate produces a lower average friction coefficient than the Na counterpart, 0.14 versus 0.16 at 850ºC at the same sliding speed and load. However, Na borate appears to fail at 900ºC as the friction coefficient surges to 0.23. On the other hand, K borate retains its lubricity over the majority of sliding time with a steady friction coefficient of 0.13 despite a slight increase at the end of the test. Regarding the wear loss volume, the unlubricated contact leads to a higher material loss in comparison to the lubricated contact at both testing temperatures. At 850ºC, the unlubricated pair yields roughly 1.3$mm^3$ of wear volume on the disc while borate lubrication reduces the figure by at least 6 times (0.2$mm^3$) without any noticeable difference between the two alkaline elements. For the unlubricated case at 900ºC, the wear rate drops on lubrication-free case compared to 850ºC, although it is still higher than lubricated tests. In addition, there is a marked difference of wear resistance between the two alkaline borates, with K borate outperforming the Na counterpart. The volume loss resulted from Na borate lubrication is 1.5 times of that from K borate.

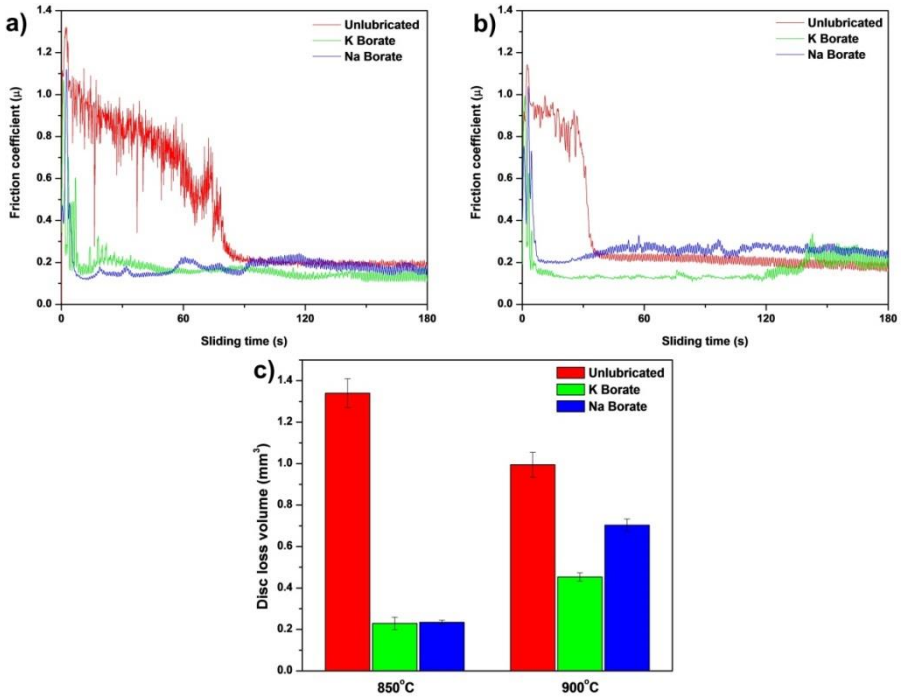


**Figure 9-2:** Friction coefficient curves at a) 850ºC, b) 900ºC and c) wear loss volume of SS316 disc in different lubrication conditions

### 9.2.3 Worn area analysis under dry sliding

Wear morphologies on the unlubricated steel pair at 850ºC and 900ºC are shown in Figure 9-3 and 9-4, respectively. Although the disc has a narrower wear track width at higher temperature, the worn morphologies are similar for both testing temperatures. It is predominantly characterized by ploughing, plastic deformation and adhesive wear. On the opposing surface, a fully-formed transferred layer is observed with a smooth contact surface and negligible damages. The more rapid transition in COF curve at the higher temperature (Figure 9-2) strongly suggests more rapid formation of a tribo-layer on the pin surface which leads to a reduced wear loss volume on the disc when the temperature reached 900ºC.

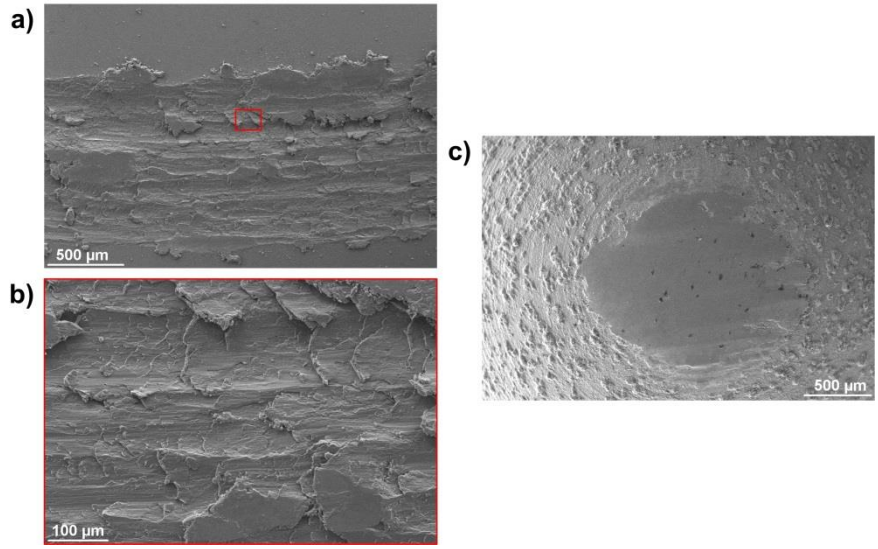


**Figure 9-3:** Worn morphologies on a) the disc, b) magnified image on the disc and c) the pin without lubrication at 850$^{o}$C

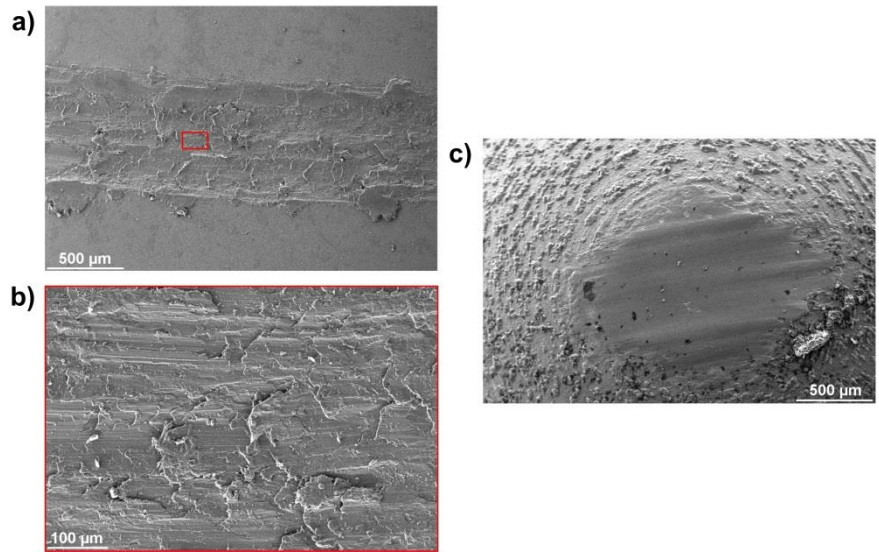


**Figure 9-4:** Worn morphologies on a) the disc, b) magnified image on the disc and c) the pin without lubrication at 900$^{o}$C

### 9.2.4 Worn area analysis under Na/K borate lubrication

Under Na borate lubrication, worn surface morphologies and corresponding X-ray analysis are shown in Figure 9-5 and 9-6. At 850$^{o}$C, there are signs of scoring and scratching on both sliding counterparts. This is quite different to what observed at lower

temperature (800$^{o}$C) in section 6.2.1 where the worn surfaces are covered by the residual melt without any clear surface features. Analysis collected from the worn areas suggests the presence of lubricant melt elements (Na, O, B) and a minor peak of Fe. The characteristic glassy appearance of lubricant melt is no longer seen at 900$^{o}$C, particularly on the disc surface. Instead, the worn surface is composed of solid-like particles as shown in the magnified image (Figure 9-6b). The corresponding EDS mapping (Figure 9-7) indicates that the solid-like particles are predominantly associated with oxides (Iron oxides and Chromium oxides). Although melt elements (Na & B) are still detected on the worn area, their intensities are significantly lower than what seen in lower temperature range. The changes in worn morphologies at 900$^{o}$C could be closely associated with potential lubrication failure of Na borate shown by increased friction and wear loss volume (Figure 9-2).

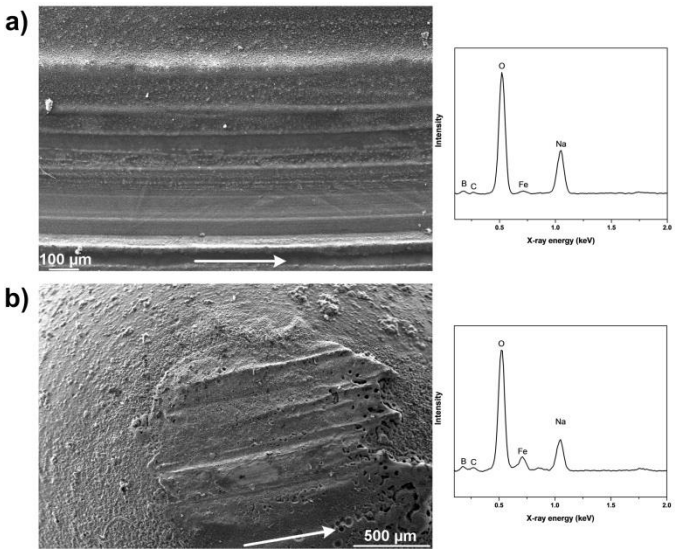


**Figure 9-5:** SEM micrographs of a) disc and b) pin after Na borate lubrication at 850$^{o}$C and the corresponding X-ray analysis

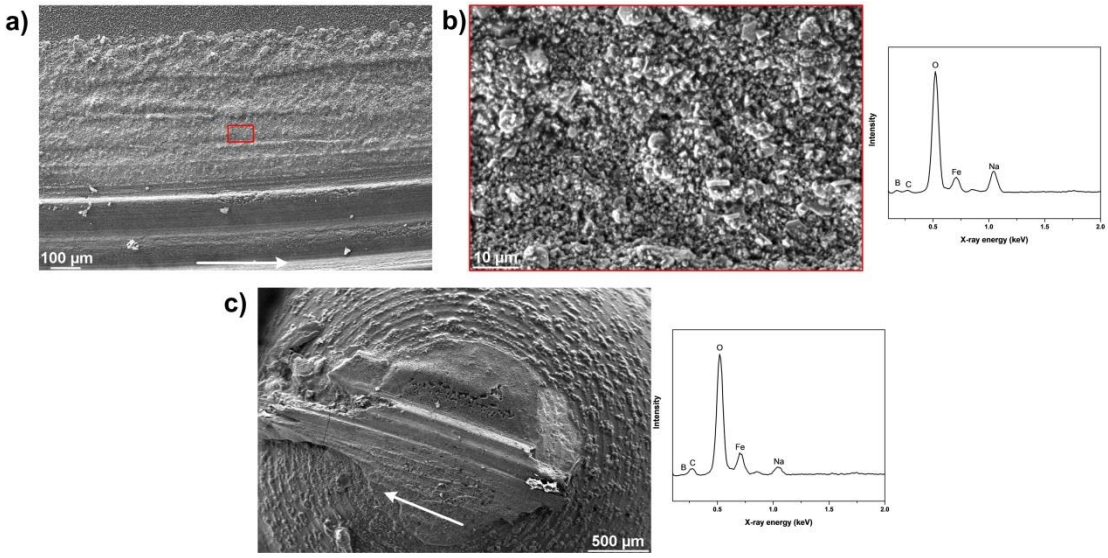


**Figure 9-6:** Worn morphologies of a) disc, b) magnified image of a, c) pin and the corresponding X-ray analysis after Na borate lubrication at 900$^{o}$C

Worn morphologies under K borate lubrication are given in Figure 9-8 and 9-9. At 850$^{o}$C, the worn disc is covered by patchy films with occasional disruption across the track width. When the testing temperature reach 900$^{o}$C, there emerges slight scoring features on both sliding surfaces (Figure 9-9). Despite that, the signature glassy appearances of lubricant melt is preserved up to 900$^{o}$C backed up by strong signals from lubricant elements (B, O, K).

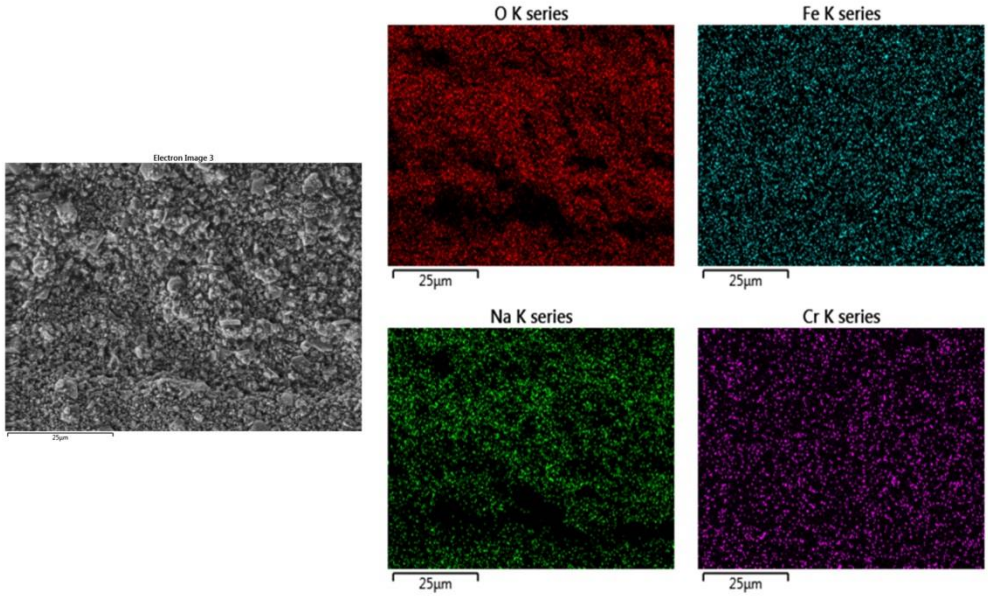


**Figure 9-7:** EDS mapping of SS316 surface lubricated by Na borate lubrication with solid-like particles

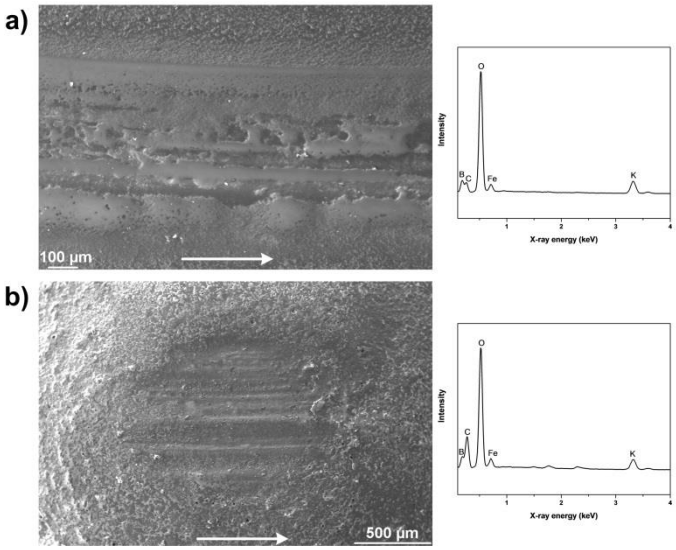


**Figure 9-8:** SEM micrographs of a) disc and b) pin after K borate lubrication at 850$^{o}$C and the corresponding X-ray analysis

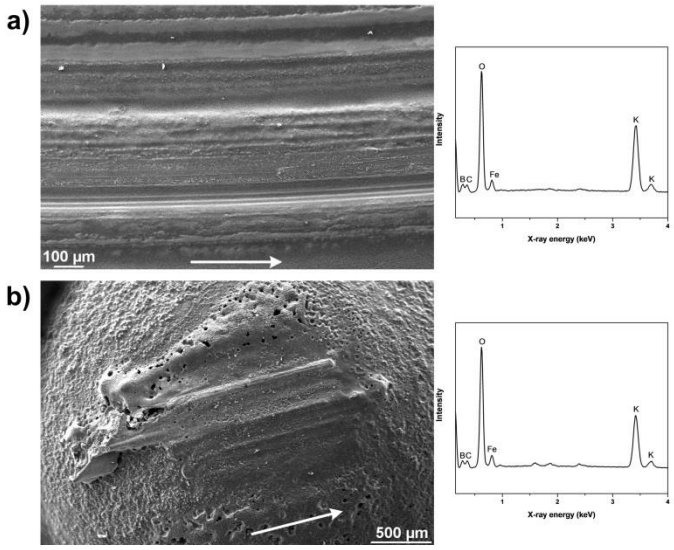


**Figure 9-9:** SEM micrographs of a) disc and b) pin after K borate lubrication at 900$^{o}$C and the corresponding X-ray analysis

## 9.3 Discussion

In order to understand the lubrication mechanism of the synthesized K borate at 900$^{o}$C, cross-sectional observation in combination with chemical analysis is given in Figure 9-10. From the STEM image, the upper transparent layer can be ascertained to the lubricant melt while the darker phase is assigned to oxide scale. The complementary phase compositional analysis (X-ray spectrum) clearly confirms the lubricant/oxide interface. Individual element mapping illustrates K enrichment on the immediate oxide interface. The behavior is identical to what observed in the case of Na borate lubrication. However, K does appear to infiltrate into the subsurface region, but in a limited manner and not as much an extent as with Na at lower temperature (Figure 6-17). The element is mostly confined above the oxide scale surface as shown in Figure 9-11.

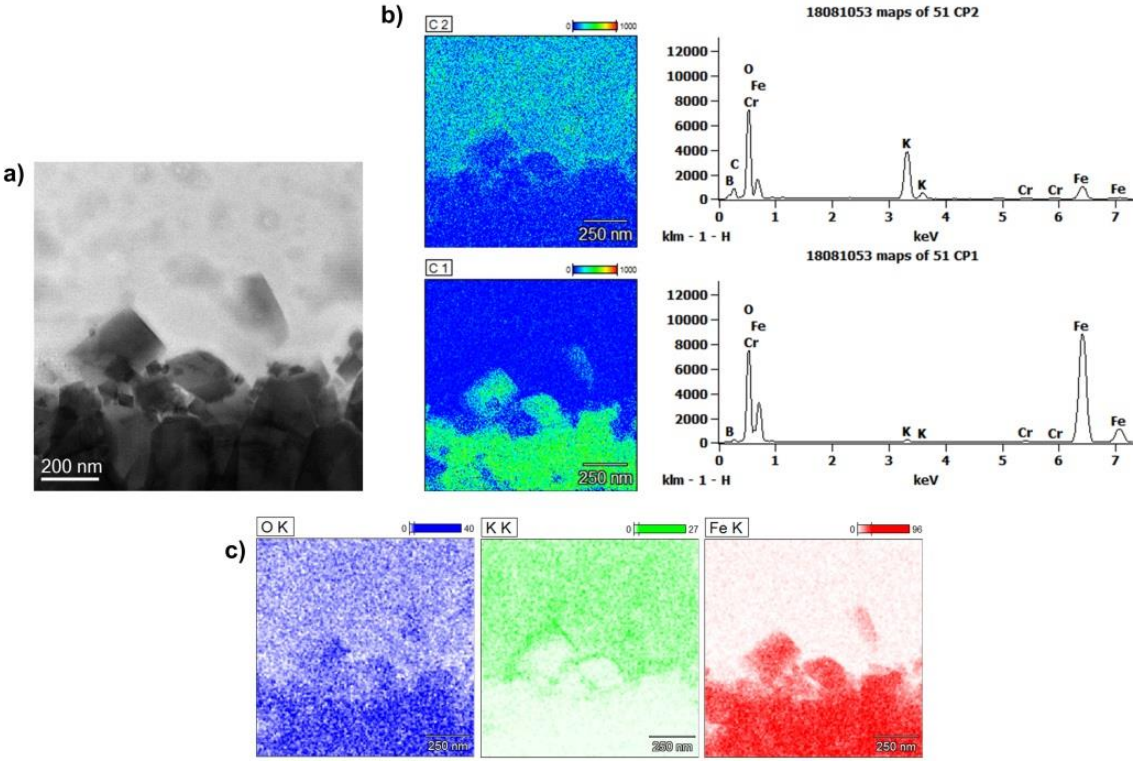


**Figure 9-10**: a) STEM-BF image of melt/oxide interface after K borate lubrication and b) phase composition, c) elemental mapping (at 900$^{o}$C)

It is expected that melting point of alkaline borate plays a crucial role in its working temperature range. For instance, having a transition point of 525$^{o}$C, sodium borate evidently functions well in the range of 600-850$^{o}$C which has been demonstrated throughout this study. The synthesized potassium borate has a multiple melting point due to its compositional inhomogeneity with the final melting point at 800$^{o}$C. Thus, it can potentially retain its lubrication performance from 800$^{o}$C upwards which was justified by the test at 900$^{o}$C (Figure 9-2). Both Na and K borate share a considerable similarity in their working principle as their strong absorption tendency on the oxide scale surface is repeatedly proved critical for desirable friction/wear behaviors. However, since the K atom radius is larger than that of Na (~1.86Å/1.52Å), this could have a certain impact on the

atom mobility upon interaction with the oxide scale. The charge-to-radius ratio of K is smaller than that of Na which can make the former element less mobile and less reactive towards the oxide surface. This is partly demonstrated by the lack of K borate infiltration towards the subsurface as shown in Figure 9-10, although the oxide scale stills show signs of cavities. It is expected that the lack of lubricant infiltration can result in poor load-bearing capacity. In contrast, the Na borate lubrication with good mobility results in a significant lubricant penetration into the subsurface associated with the formation of pocket reservoir (Figure 6-17).

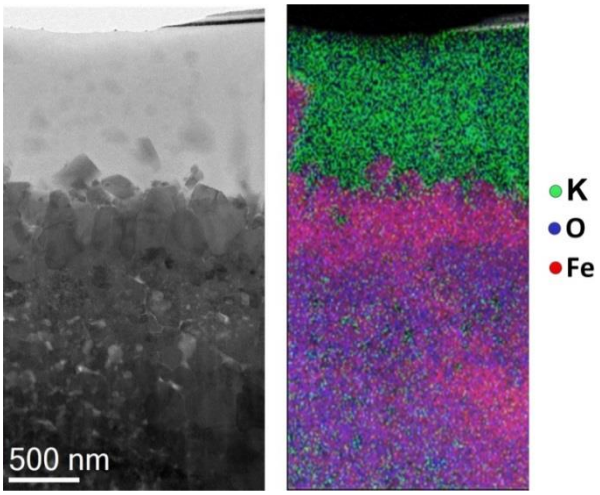


**Figure 9-11:** An STEM image of the immediate sliding surface with elemental mapping

Although the reactivity of alkaline elements is of paramount importance in the lubrication mechanism of alkaline borate, the role of viscosity should not be diminished. It provides the lubricant with the fluidity to move and remain on the contact surface. The low shearing stress of a fluid medium is mainly accountable for such low friction coefficient on the lubricated sliding surfaces. The lubrication failure of Na borate at 900$^{o}$C is likely associated with its low viscosity at this temperature range. Figure 9-12 plots the

dependence of friction coefficient on the viscosity of Na borate on the sliding HSS/SS316 pair. This follows well with the Stribeck principle and also confirms the mixed lubrication regime in the tribotest. The viscosity of K borate is not available, although the material exhibited a consistently low friction coefficient over the tested temperature (700-900$^{o}$C) (Figure 9-12b). The lubrication failure of Na borate at 900$^{o}$C also results in poor oxidation resistance on the sliding surface, as shown by the oxide scale thickness after lubrication tests in Figure 9-13. While both alkaline borates are similarly effective at 850$^{o}$C, K borate lubrication yields slightly better anti-oxidation performance at 900$^{o}$C. The anti-oxidation capacity of borate lubricants on SS316 is not as significant as what shown in Chapter 5 (where mild steel was used) which is due to the intrinsic oxidation resistance of SS316.

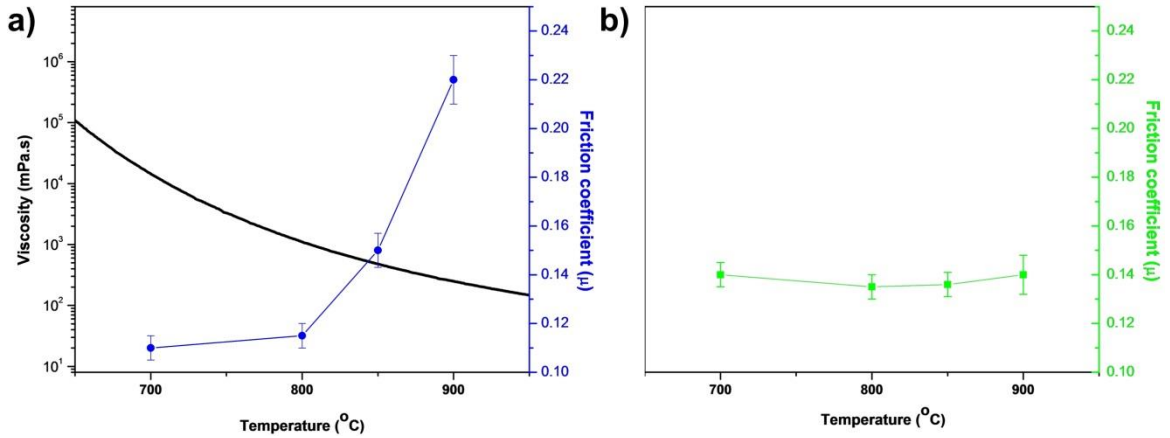


**Figure 9-12:** Variation of friction coefficient from HSS/SS316 lubricated (10N, 0.1m/s) by a) Na borate and b) K borate with temperature

The popularity of Na in complex glass lubricant composition is evident in Table 2-1 (Chapter 2). This could be mainly attributed to its abundant availability, high reactivity and high efficiency in adjusting the viscosity of the lubricant melt. Combined with previous chapters, it is highly credible to determine a universal working mechanism of alkaline

borates lubricant at high temperature. They can be also used to plot the prediction on the tribological response of alkaline earth borate or even more complex borate system.

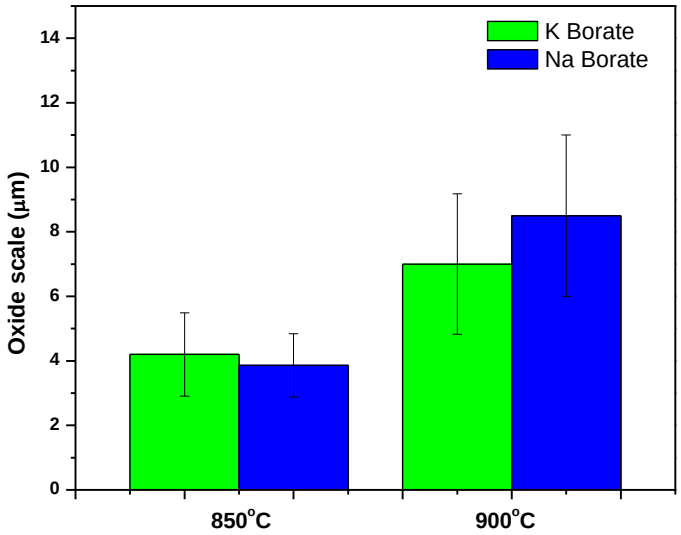


**Figure 9-13:** Oxide scale thickness on SS316 disc after lubrication tests at different temperatures

## 9.4 Conclusions

Potassium borate was successfully synthesized and its tribological behaviors are evaluated up to maximum 900°C. There are some concluding remarks from this chapter as listed below.

- Synthesized potassium borate works effectively up to 900oC, reduces friction coefficient and wear loss volume;
- Effective working temperature range of alkaline borate lubricant is determined by its melting point. K borate does not show significant penetration to the underlying oxide scale bulk;
- Sodium borate loses its performance when the testing temperature reaches 900oC which is mainly due to lack of viscosity.

# CHAPTER 10:

# General conclusions and recommendations for future work

The current dissertation thoroughly studied tribological properties of alkaline borates at elevated temperatures. By conducting a large volume of experimental work and detailed analysis, the lubrication mechanism and other fundamentals aspects of borate lubrication have been revealed. The final chapter aims to highlight general conclusions and suggestions for further work.

## 10.1 Tribological performance of sodium borate at high temperature

- During high temperature pin-on-disc testing on a steel tribopair (600$^{o}$C-800$^{o}$C), sodium borate demonstrated exceptional lubricating properties over its melting point which is reflected by a significant reduction in friction and wear loss volume in comparison to unlubricated test.
- At 800$^{o}$C, on the disc surface, a chemically hierarchical tribofilm is observed with a thickness of ~50-60nm. The tribofilm consists of 2 layers: the bottom layer is rich in Na with a thickness of ~20nm while B heavily concentrates in the upper part. The Na-rich film is believed to provide the necessary adhesion on oxidized steel surface while the self-adaptive polymerization of the upper part enhances the cohesive strength of the whole tribofilm.

- At 800ºC, on the ball surface, a complex tribofilm comprising of Na, O, B, C and Fe is found lying on a layer of ultra-fine grains of iron oxides. With exceptional toughness and strength, the ultra-fine oxide grains provide concrete ongoing support for the tribofilm. There is a conversion from $BO_4$ into $BO_3$ species in the tribofilm which is caused by the effect of shearing stress.

## 10.2 Thermally-activated and tribochemical reaction on borate-lubricated surfaces

- A formation of thin Na film on iron oxide interface is observed regardless of the presence of external shearing stress. This implies that the absorption of Na is thermally-driven. During the static oxidation, beside interface reaction, borate melt causes the disintegration of the oxide scale bulk by penetrating through the grain boundary which eventually roughens the melt/oxide interface.
- Tribological reactions result in the formation of tribofilm which is significantly depleted in Oxygen. This chemical feature enhances oxidation resistance by reducing the oxide growth considerably in comparison to static oxidation and untreated cases. It has been shown that shearing stress not only induces molecular structure changes in borate melt, but also the compositional change.

## 10.3 The role of Na in binary sodium borate lubrication and effect of oxide microstructure on adsorption behavior of Na

- The binary system $Na_2O$-$B_2O_3$ outperforms $B_2O_3$ in term of friction and wear reduction in pin-on-disc testing between High Speed Steel and Stainless Steel

316 surfaces. An addition of Na into pure $B_2O_3$ drastically improves the lubrication performance of the beneficiary. In addition, the binary system $Na_2O$-$B_2O_3$ also exhibits a good load-bearing capacity.

- The adsorption of Na onto both contact surfaces is the driving force for the excellent lubrication performance of binary sodium borate. However, the role of $B_2O_3$ in the binary system should not be diminished as it provides the polymeric/viscous nature of the lubricant upon melting.
- There is a close relationship between Na-adsorbed film thickness and the oxide microstructure. While it is ~20nm on an oxidized mild steel surface, it is estimated at 50~60nm on an oxidized alloyed steel (HSS and SS316). In addition, weakly-adhered oxide scale grown on mild steel did not support as an effective lubrication as the oxide scale grown on stainless steel.

## 10.4 Adhesive wear resistance of sodium borate on sliding HSS surface

- Under borate lubrication, High Speed Steel surface experiences no adhesive wear damages in comparison to lubricant-free case. The anti-sticking behavior is closely governed by the tribofilm formation on the immediate sliding. Adsorption of Na element on oxide surface is the main driving force to inhibit material transfer.
- The borate lubricant film alters significantly the oxidation characteristics of the underlying oxide scale on High Speed Steel. Extended exposure leads to Hematite-to-Magnetite conversion.

## 10.5 Tribological behavior of sodium borate in rolling contact and surface interaction with iron oxide scale

- Oxide scale transfer occurs readily on the HSS surface under dry conditions and the extent grows with temperature and loading amplitude. Pre-oxidation of HSS results in increase of rolling friction coefficient compared to the case where fresh rolls are used.
- The application of lubricant drastically hinders the material transfer on the HSS roll surface which is attributed to the formation of a lubricant film. The exposure to borate lubrication under rolling changes the oxide composition significantly, with Magnetite replaces Hematite to become the most dominating type. This favorable transformation can facilitate the pickling process.

## 10.6 Synthesis of potassium borate and understanding of alkaline borate lubrication

- Synthesized potassium borate lubricates effectively up to 900$^{o}$C by reducing friction coefficient and wear loss volume on Stainless Steel surface. On the other hand, Sodium borate loses its performance when the testing temperature reaches 900$^{o}$C which is mainly due to low of viscosity
- Potassium borate shares great similarity with sodium borate with respect to their lubrication mechanism at high temperature.

## 10.7 Recommendations for future work

- Although lubrication mechanism of sodium borate has already been revealed in great details in pin-on-disc testing and passivated rolling testing, further experimental work and analysis should be carried out on real hot rolling platform to justify the lubricant effectiveness.
- By accomplishing a firm understanding about glass chemistry, it is feasible to proceed the synthesis of other binary borate system such as alkaline earth borate (Mg, Ca) as potential candidates for high-temperature lubrication. It is expected that this family of borate glasses has a higher working temperature range than alkaline borate. Mixtures of different kinds of borate-based glasses should also be considered.
- The passivated rolling module has been successfully utilized. It can be modified further to represent actual hot rolling contact. However, there are a number of technical restraints that prevents wider range of testing condition. Efforts should be spent on finding better ceramic bearing material which can cope a with higher temperature and heavier load testing. In addition, slippage should be introduced to simulate realistically the rolling process
- The chemical state at the lubricant/surface interface can be readily distorted if the samples are still exposed to high-temperature condition after the tribology tests finish. Thus, it is of paramount importance to isolate the processed samples after high-temperature testing to ensure the credibility of the subsequent characterization.

# Bibliography

[1] Peterson MB, Murray SF, Florec K. Consideration of lubricants for temperature above 1000°F. ASLE Technical Publication. 1959;2:225-34.
[2] Wan S, Tieu AK, Xia Y, Zhu H, Tran BH, Cui S. An Overview of Inorganic Polymer as Potential Lubricant Additive for High Temperature Tribology. Tribology International. 2016;102:620-35.
[3] Sliney HE. Solid lubricant materials for high-temperatures. Tribology International. 1982;15:303-15.
[4] Allam IM. Solid lubricants for applications at elevated-temperatures - a review. Journal of Materials Science. 1991;26:3977-84.
[5] Hardell J, Hernandez S, Mozgovoy S, Pelcastre L, Courbon C, Prakash B. Effect of oxide layers and near surface transformations on friction and wear during tool steel and boron steel interaction at high temperatures. Wear. 2015;330-331:223-9.
[6] Zhu S, Cheng J, Qiao Z, Yang J. High temperature solid-lubrication materials: A review. Tribology International. 2019;133:206-23.
[7] Young DJ. High Temperature Oxidation and Corrosion of Metals: Elsevier 2016.
[8] Chen RY, Yuen WYD. Review of The High-Temperature Oxidation of Iron and Carbon Steels in Air or Oxygen. Oxidation of Metals. 2003;59:433-68.
[9] Malik AU, Whittle DP. Oxidation of Fe-C Alloys in The Temperature Range 600-850°C. Oxidation of Metals. 1981;16:339-53.
[10] Chang Y-N, Wei F-I. Review High temperature oxidation of low alloy steels. Journal of Materials Science. 1989;24:14-22.
[11] Dawson K, Tatlock GJ. High Temperature Crossoion of Low Alloy Steel: Elsevier B.V; 2010.
[12] Sun W, Tieu AK, Jiang Z, Lu C. High temperature oxide scale characteristics of flow carbon steel in hot rolling. Journal of Materials Processing Technology. 2004;155-156:1307-12.
[13] Chen RY, Yuen WYD. Oxide-Scale Structures Formed on Commercial Hot-Rolled Steel Strip and Their Formation Mechanisms. Oxidation of Metals. 2001;56:89-118.
[14] Pique B, Bouchard P-O, Montmitonnet P, Picard M. Mechanical Behavior of Iron Oxide Scale: Experimental and Numerical Study. Wear. 2006;260:231-42.
[15] Echsler H, ito S, Schutze M. Mechanical Properties of Oxide Scales on Mild Steel at 800 to 1000°C. Oxidation of Metals. 2003;60:241-69.
[16] Utsunomiya M, Hara K, Matsumoto R, Azushima A. Formation mechanism of surface scale defects in hot rolling process. CIRP Annals - Manufacturing Technology. 2014;63:261-4.
[17] Krzyzanowski M, Beynon JH, Farrugia DCJ. Oxide Scale Behaviour in High Temperature Metal Processing: Wiley-VCH; 2010.
[18] Luong LS, Heijkoop T. The influence of scale on friction in hot metal working. Wear. 1981;71:93-102.
[19] Munther PA, Lenard JG. The effect of scaling on interfacial friction in hot rolling of steels. Journal of Materials Processing Technology. 1999;88:105-13.
[20] Utsunomiya H, Nakagawa T, Matsumoto R. Mechanism of oxide scale to decrease friction in hot steel rolling. Procedia Manufacturing. 2018;15:46-51.
[21] Hidaka Y, Anraku T, Otsuka N. Deformation of Iron Oxide upon Tensile Test at 600-1250°C. Oxidation of Metals. 2003;71:S1282.
[22] Verge C, Boher C, Gras R, Levaillant C. Influence of oxides on friction in hot rolling: Experimental investigations and tribological modelling. Wear. 2006;2006:957-75.
[23] Verge C, Boher C, Levaillant C, Gras R. Analysis of the friction and wear behavior of hot work tool scale: application to the hot rolling process. Wear. 2001;250:322-33.

[24] Zhu H, Zhu Q, Tieu AK, Kosasih B, Kong C. A simulation of wear behaviour of high-speed steel hot rolls by means of high temperature pin-on-disc tests. Wear. 2013;302:1310-8.
[25] Kato H. Severe-mild wear transition by supply of oxide particles on sliding surface. Wear. 2003;255:426-9.
[26] Hiratsuka K, Muramoto K. Role of wear particles in severe-mild wear transition. Wear. 2005;259:467-76.
[27] Azushima A. Tribology in Sheet Rolling Technology: Springer International Publishing; 2016.
[28] Shirizly A, Lenard JG. The effect of lubrication on mill loads during hot rolling of low carbon steel strips. Journal of Materials Processing Technology. 2000;97:61-8.
[29] Shirizly A, Lenard JG. The effect of scaling and emulsion delivery on heat transfer during the hot rolling of steel strips. Journal of Materials Processing Technology. 2000;101:250-9.
[30] Imae T, Kanenari S. Symposium tex in division of processing for quality products of ISIJ (in Japanese). 1997:15-9.
[31] Azushima A, Xue WD, Yoshida Y. ISIJ International. 2009;49-6:868-73.
[32] Azushima A, Xue W, Yoshida Y. Influence of Lubricant Factors on Coefficient of Friction and Clarification of Lubrication Mechanism in Hot Rolling. ISIJ International. 2009;49:868-73.
[33] Bay N, Azushima A, Groche P, Ishibashi I, Merklein M, Morishita M, et al. Environmentally benign tribo-systems for metal forming. CIRP Annals-Manufacturing Technology. 2010;59:760-80.
[34] Tekkaya AE, Homberg W, Brosius A. 60 Excellent inventions in metal forming: Springer; 2015.
[35] Friedman PA, Luckey SG. 4 - High-temperature lubricants for superplastic forming of metals. Superplastic Forming of Advanced Metallic Materials. 2011:72-82.
[36] Erdemir A. Modern Handbook of Tribology - Chapter 22: Solid Lubricants and Self-Lubricating Films: CRC Press; 2001.
[37] Petrov A, Petrov P, Petrov M. Research into water-based colloidal-graphite lubricants for forging of carbon steels and Ni-based alloys. International Journal of Material Forming. 2010;3:311-4.
[38] Nagaile G, Botz F. Performance of Graphite and Boron-Nitride-Silicone Based Lubricants and Associated Lubrication Mechanisms in Warm Forging of Aluminum. Journal of Tribology. 2008;130:021801.
[39] Feher R. Graphite-based lubricants. Encyclopedia of Lubricants and Lubrication. 2014:758-69.
[40] Sliney HE. Rare Earth FLuorides and Oxides - An Exploratory Study of Their Use as Solid Lubricants at Temperatures up to 1800ºF. NASA TN D-5301. 1969.
[41] Shimotamai N, Ihara H, Nanao H. A Study of Hot Rolling Oil with Calcium Carbonate for Stainless Steel Process. Tribology Online. 2010;5:181-6.
[42] Xia W, Zhao J, Wu H, Huai S, Zhao X, Zhang X, et al. A novel nano-TiO2 additive Oil-in-water lubricant for hot steel rolling. Materials Science Forum. 2016;861:201-6.
[43] Xia W, Zhao J, Wu H, Zhao X, Zhang X, Xu J, et al. Effects of nano-TiO2 additive in Oil-in-Water Lubricant on contact angle and antiscratch behavior. Tribology Transactions. 2016:1-11.
[44] Zhu Z, Sun J, Wei H, Niu T, Zhu Z. Research on lubrication behaviors of nano-TiO2 in water-based hot rolling liquid. Advanced Materials Reserach. 2013;643:139-43.
[45] Hibi T. Aqueous high molecular weight polymer lubricant for hot forging. Technical Review by Forging Technology Institute of Japan. 1993;18:41-8.
[46] Dubois A, Dubar M, Dubar L, Tlili B. Tribological performances of two white lubricants in hot steel forging. Key Engineering Material. 2012;504-506:561-6.
[47] Schey JA. Tribology in Metalworking: Friction, Lubrication, and Wear. Journal of Applied Metalworking. 1984;3:173.

[48] A.S.M.E. Take Another Look at Lubrication in Metal Processing. Industrial Lubrication and Tribology. 1967;19:56-62.
[49] Kaplakjan S. Metal deformation process - friction and lubrication. 1970.
[50] Gupta AK, Hughes KE, Sellars CM. Glass-lubricated hot extrusion of stainless steel. Metal technology. 1980:324-31.
[51] Kovalev LK. The use of glass lubricants for hot deformation of chrome-nickel and titanium alloys. Glass and Ceramics. 1960;17:181-3.
[52] Kovalev LK, Ryabov VA. Glass lubricants in metallurgy. Glass and Ceramics. 1958;15:352-7.
[53] Feng Z, Hu X, Guo H, Yao Z, Lu Z, Gong P. Study on protective lubricant technology for isothermal super plastic forging of Ti-1023 titanium alloy. Forging and Stamping Technology. 2011.
[54] Li LX, Peng DS, Liu JA, Liu ZQ, Jiang Y. An experimental study of the lubrication behavior of A5 glass lubricant by means of the ring compression test. Journal of materials processing technology. 2000;102:138-42.
[55] Furugen M, Matsuo H, Fukuyasu T, Nakanishi T, Yanagimoto J. Characteristics of deformation in hot extrusion process of stainless steel tube. Tetsu-to-Hagane. 1999;85:801-5.
[56] Yoshida K. The Iron and Steel Institute of Japan. 2005:3-4.
[57] Chen M, Li W, Shen M, Zhu S, Wang F. Glass-ceramic coatings on titanium alloys for high temperature oxidation protection: Oxidation kinetics and microstructure. Corros Sci. 2013;74:178-86.
[58] Chen M, Li W, Shen M, Zhu S, Wang F. Glass coatings on stainless steels for high-temperature oxidation protection: Mechanism. Corros Sci. 2014;82:316-27.
[59] Chen M, Shen M, Zhu S, Wang F, Wang X. Effect of sand blasting and glass matrix composite coating on oxidation resistance of a nickel-based superalloy at 1000ºC. Corros Sci. 2013;73:331-41.
[60] Donald IW, Mallinson PM, Metcalfe BL, Gerrard LA, Fernie JA. Recent developments in the preparation, characterization and applications of glass- and glass-ceramic-to-metal seals and coatings. J Mater Sci. 2011;46:1975-2000.
[61] Frolenkov KY, Frolenkova LY, Shadrin IF. High-Temperature Oxidation of Low-alloyed Steel under Glass Coatings. Prot, Met Phys Chem Surf. 2010;46:103-9.
[62] Lefort HG, Friedberg AL. Quantitative High-Temperature Oxidation of Porcelain Enameled Iron. J Am Ceram Soc. 1958;41:216-26.
[63] Moskalewicz T, Smeacetto F, Cempura G, Ajitdoss LC, Salvo M, Czyrska-Filemonowicz A. Microstructure and properties characterization of the double layered glass-ceramic coating on near-α titanium alloy. Surf Coat Technol. 2010;204:3509-16.
[64] Ritchie D, Schaeffer HA, White D. The presence of an iron oxide layer at the enamel/steel interface in one-coat porcelain enamelling. J Mater Sci. 1983;18:599-604.
[65] Sarkar S, Datta S, Das S, Basu D. Oxidation protection of gamma-titanium aluminide using glass-ceramic coatings. Surf Coat Technol. 2009;203:1797-805.
[66] Shen M, Zhu S, Chen M, Wang F. The oxidation and oxygen permeation resistance of quartz particle-reinforced aluminosilicate glass coating on titanium alloy. J Am Ceram Soc. 2011;94:2436-41.
[67] Wang L, Meng C, Liu L, Wang L. Glass-ceramic protective coating for titanium alloys. J Am Ceram Soc. 2002;85:2867-9.
[68] Riaz S, Bugdol M, Farrugia D. Oxidation management in hot rolling processes. European Comission2013.
[69] Spikes H. The history and mechanism of ZDDP. Tribology Letters. 2004;17:469-88.
[70] Martin J-M, Onodera T, Minfray C, Dassenoy F, Miyamoto A. The origin of anti-wear chemistry of ZDDP. Royal Society of Chemistry. 2012;156:311-23.

[71] Nicholls MA, Norton PR, Bancroft GM, Kasrai M, Do T, Frazer BH, et al. Nanometer scale chemomechanical characterization of antiwear films. Tribology Letters. 2004;17:205-16.
[72] Demmou K, Bec S, Loubet JL, Martin JM. Temperature effects of mechanical properties of zinc dithiophosphate tribofilms. Tribology International. 2006;39:1558-63.
[73] Bec S, Tonck A, Georges JM, Coy RC, Bell JC, Roper GW. Relationship between mechanical properties and structures of zinc dithiophosphate anti-wear films. Proceedings of the Royal Society of London. 1998;455:4181-203.
[74] Martin JM. Antiwear mechanism of Zinc dithiophosphate: A chemical hardness approach. Tribology Letters. 1999;15:199-209.
[75] Minfray C, Mogne TL, Martin J-M. Experimental and molecular dynamics simulations of tribochemical reactions with ZDDP: Zinc phosphate-Iron oxide reaction. Tribology Transactions. 2008;51:589-601.
[76] Hoshino K, Yagishita K, Tagawa K, Spikes H. Tribological properties of sulphur-free antiwear additivies Zinc Diakylphosphate (ZDPs). SAE International. 2012;5:504-10.
[77] Minfray C, Martin JM, Tsujimoto T, Igarashi J. Alternative to ZDDP additive: Study of Zinc Diakylphosphate Lubricant Properties. STLE/ASME 2008 International Joint Tribology Conference: ASME Proceedings. 2008.
[78] Gauvin M, Dassenoy F, Belin M, Minfray C, Piecourt CG, Bec S, et al. Boundary lubrication by pure crystalline Zinc Orthophosphate powder in Oil. Tribology Letter. 2008;31:139-48.
[79] Crobu M, Rossi A, Spencer ND. Effect of chain-length and counterface on the tribochemistry of bulk Zinc Polyphosphate glasses. Tribology Letter. 2012;48:393-406.
[80] Kolesnikov VI, Savenkova MA, Bulgarevich SB, Chelokhyan AV, Bulavina EA, Boyko MV. Investigation of the triboengineering characteristics of plastic railway greases with inorganic polymeric additives. Journal of Friction and Wear. 2008;29:200-4.
[81] Kolesnikov VI, Ermakov SF, Sychev AP, Myasnikova NA, Savenkova MA, Luneva EI. Improvement of the triboengineering and physicochemical properties of Puma lubricating compositions with Lithium Molybdophosphate additive. Journal of Friction and Wear. 2009;30:182-7.
[82] Kolesnikov VI, Savenkova MA, Avilov VV, Migal YF. Properties of Luma and Buksol lubricants modified by inorganic additives of binary polyphosphates. Journal of Friction and Wear. 2014;36:205-12.
[83] Kolesnikov VI, Ermakov SF, Daniel F, Savenkova MA, Myasnikova NA, Luneva EI. Synthesis and study of triboengineering characteristics of a new nanosize ceramic Nickel Phosphoromolybdate additive to greases. Journal of Friction and Wear. 2009;31:426-32.
[84] Migal YF, Kolesnikov VI, Savenkova MA, Solodovnikova DN. Interaction of molecules of phosphorus-containing inorganic additives with iron surfaces: Quantum-chemical analysis and tribotechnical testing. Advances in Materials Physics and Chemistry. 2013;3:281-8.
[85] Kolesnikov VI, Migal YF, Savenkova MA, Mizhiritskaya SN. Adsorption of heteropolyphosphate of alkaline metals in iron surface. Journal of Friction and Wear. 2009;30:404-10.
[86] Matsumoto K, Izawa M, Nakanishi T, Tsubouchi K. Tribological properties of water glass lubricant for hot metalworking. Tribology Transactions. 2009;52:553-9.
[87] Tieu AK, Kong N, Wan S, Zhu H, Zhu Q, Mitchell DRG, et al. The Influence of Alkali Metal Polyphosphate on The Tribological Properties of Heavily Load Steel on Steel Contacts at Elevated Temperatures. Advanced Materials Interfaces. 2015;2:1-14.
[88] Tieu AK, Wan S, Zhu Q, Zhu H. Excellent melt lubrication of alkali metal polyphosphate glass for high temperature applications. Royal Society of Chemistry Advances. 2015;5:1796-800.
[89] Wan S, Tieu K, Zhu Q, Zhu H, Cui S, Mitchell DRG, et al. Chemical nature of alkaline polyphosphate boundary film at heated rubbing surfaces. Scientific Reports. 2016;6:1-16.

[90] Cui S, Wan S, Zhu Q, Tieu AK, Zhu H, Wang L, et al. Tribochemical Behavior of Phosphate Compounds at an Elevated Temperature Journal of Physical Chemistry C. 2016;120:25745-51.
[91] Cui S, Zhu H, Wan S, Tran B, Wang L, Tieu K. Investigation on different inorganic chemical compounds as hot metal forming lubricant by pin-on-disc and hot rolling. Tribology International. 2018;125:110-20.
[92] Huong TTT, Tieu AK, Zhu H, Yu H, Ta TD, Wan S, et al. Chemical Origin of Sodium Phosphate Interactions on Iron and Iron Oxide Surfaces by First Principle Calculations. Journal of Physical Chemistry C. 2018;122:635-47.
[93] Le MH, Tieu AK, Zhu H, Ta DT, Yu H, Ta TTT, et al. Depolymerization of sodium phosphates on an iron oxide surface at high temperature. Physical Chemistry Chemical Physics. 2018;20:7819.
[94] Tran NV, Tieu AK, Zhu H, Ta HTT, Ta TD, Le MH. First-Principles Study of the Adsorption and Depolymerization Mechanisms of Sodium Silicate on Iron Surfaces at High Temperature. Journal of Physical Chemistry C. 2018;122:20827-40.
[95] Griesser S, Pierer R, Reid M, Dippenaar R. SolTrack: an automatic video processing softwar for in-situ interface tracking. Journal of Microscopy. 2012;248:42-8.
[96] https://www.uow.edu.au/research-and-innovation/our-research/research-institutes-and-facilities/australian-institute-for-innovative-materials/uow-electron-microscopy-centre/emc-facilities/.
[97] Williams DB, Carter CB. Transmission Electron Microscopy A Textbook for Materials Science: Springer; 2009.
[98] Mitchell DRG, Schaffer B. Scripting-Customised Microscopy Tools for Digital Micrograph™. Ultramicroscopy. 2005;103:319-32.
[99] Wan S, Tieu AK, Zhu Q, Zhu H, Cui S, Mitchell DRG, et al. Chemical Nature of Alkaline Polyphosphate Boundary Film at Heated Rubbing Surfaces. Scientific Reports. 2016;6:26008.
[100] Shah FU, Glavatskih S, Antzutkin ON. Boron in Tribology: From Borates to Ionic Liquids. Tribology Letters. 2013;51:281-301.
[101] Konijnendijk WL, Stevels JM. The Structure of Borate Glasses Studied by Raman Scattering. Journal of Non-Crystalline Solids. 1975;18:307-31.
[102] Goel N, Sinha N, Kumar B. Growth and properties of sodium tetraborate decahydrate single crystals. Materials Research Bulletin. 2013;48:1632-6.
[103] Morrel R. Handbook of Properties of Technical and Engineering Ceramics: HMSO, London; 1987.
[104] Williams JA, Dwyer-Joyce RS. Modern Handbook of Tribology - Chapter 3: Contact Between Solid Surfaces: CRC Press; 2001.
[105] Otten MT. High-Angle Annular Dark-Field Imaging on a TEM/STEM System. Journal of Electron Microscopy Technique. 1991;17:221-30.
[106] Araujo D, Alegre MP, Pinero JC, Fiori A, Bustarret E, Jomard F. Boron Concentration Profiling by High Angle Annular Dark Field-Scanning Transmission Electron Microscopy in Homoepitaxial Doped Diamond Layers. Applied Physics Letters. 2013;103:042104.
[107] Utsunomiya S, Ewing RC. Application of High-Angle Annular Dark Field Scanning Transmission Electron Microscopy, Scanning Transmission Electron Microscopy-Energy Dispersive X-ray Spectrometry, and Energy-Filtered Transmission Electron Microscopy to The Characterization of Nanoparticles in The Environment. Environmental Science Technology. 2003;37:786-91.
[108] Inman IA, Datta S, Du HL, Burnell-Gray JS, Luo Q. Microscopy of Glazed Layers Formed During High Temperature Sliding Wear at 750ºC. Wear. 2003;254:461-7.

[109] Stott FH, Lin DS, Wood GC. The Structure and Mechanism of Formation of The "Glaze" Oxide Layers Produced on Nickel-Based Alloys During Wear at High Temperatures. Corrosion Science. 1973;13:449-69.
[110] Lundberg S-E, Gustafsson T. The Influence of Rolling Temperature on Roll Wear, Investigated in A New High Temperature Test Rig. Journal of Materials Processing Technology. 1994 42:239-91.
[111] Shartsis L, Capps W, Spinner S. Viscosity and Electrical Resistivity of Molten Alkali Borates. Journal of American Ceramic Society. 1953;36:319-26.
[112] Sauer H, Brydson R, Rowley PN, Engel W, Thomas JM. Determination of Coordinations and Coordination-Specific Site Occupancies by Electron Energy-Loss Spectroscopy: An Investigation of Boron-Oxygen Compounds. Ultramicroscopy. 1993;49:198-209.
[113] Garvie LAJ, Craven AJ. Parallel Electron Energy-Loss Spectroscopy (PEELS) Study of B in Minerals: The Electron Energy-Loss Near-Edge Structure (ELNES) of The B K Edge. American Mineralogist. 1995;80:1132-44.
[114] Yang G, Mobus G, Hand RJ. Cerium and Boron Chemistry in Doped Borosilicate Glasses Examined by EELS. Micron. 2006;37:433-41.
[115] Cheng S, Yang G, Zhao Y, Peng M, Skibsted J, Yue Y. Quantification of Boron Speciation In Alkali Borosilicate Glasses by Electron Energy Loss Spectroscopy. Scientific Reports. 2015;5:17526.
[116] Murooka Y, Tanaka N, Hirono S, Hibino M. Electron Energy-Loss Spectroscopy of Carbon Films Prepared by Electron-Cyclotron-Resonance Plasma Sputtering. Materials Transactions. 2002;43:2092-6.
[117] Havenbergh KV, Turner S, Driesen K, Bridel J-S, Tendeloo GV. Solid-Electrolyte Interphase Evolution of Carbon-Coated Silicon Nanoparticles for Lithium-Ion Batteries Monitored by Transmission Electron Microscopy and Impedance Spectroscopy. Energy Technology. 2015;3:699-708.
[118] Mackenzie JD. The Physical Chemistry of Simple Molten Glasses. Chemical Reviews. 1956;56:455-70.
[119] Ehrt D, Keding R. Electrical Conductivity and Viscosity of Borosilicate Glasses and Melts. Physics and Chemistry of Glasses. 2009;50:165-71.
[120] Minami I. Ionic Liquids in Tribology. Molecules. 2009;14:2286-305.
[121] Ito K, Martin J-M, Minfray C, Kato K. Low-friction tribofilm formed by the reaction of ZDDP on iron oxide. Tribology International. 2006;39:1538-44.
[122] Miyajima M, Kitamura K, Matsumoto K. In Situ Raman Tribometry for the Formation and Removal Behavior of FeS2 Tribofilm in the Scuffing Process. Tribology Online. 2016;11:382-8.
[123] Lee SK, Eng PJ, Mao H-K, Meng Y, Newville M, Hu MY, et al. Probing of Bonding Changes in $B_2O_3$ Glasses at High Pressure with Inelastic X-Ray Scattering. Nature Materials. 2005;4:851-4.
[124] Leinonen JI. Superior Properties of Ultra-Fine-Grained Steels. Acta Polytechnica. 2004;44:37-40.
[125] Valiev RZ. Structure and Mechanical Properties of Ultrafine-Grained Metals. Materials Science & Engineering A. 1997;A234-236:59-66.
[126] Valiev RZ, Korznikov AV, Mulyukov RR. Structure and Properties of Ultrafine-Grained Materials Produced by Severe Plastic Deformation. Materials Science & Engineering A. 1993;A168:141-8.
[127] Nie X, Zhang P, Weiner AM, Cheng Y-T. Nanoscale Wear and Machining Behavior of Nanolayer Interfaces. Nanoletters. 2005;5:1992-6.

[128] Shakhvorostov D, Gleising B, Buscher R, Dudzinski W, Fischer A, Scherge M. Microstructure of Tribologically Induced Nanolayers Produced at Ultra-Low Wear Rates. Wear. 2007;263:1259-65.
[129] Divinski S, Wilde G. Diffusion in Ultrafine Grained Materials. Materials Science Forum. 2008;584-586:1012-7.
[130] Sauvage X, Wilde G, Divinski SV, Horita Z, Valiev RZ. Grain Boundaries in Ultrafine Grained Materials Processed by Severe Plastic Deformation. Materials Science & Engineering A. 2012;540:1-12.
[131] Mosey NJ, Woo TK, Kasrai M, Norton PR, Bancroft GM, Muser MH. Interpretation of Experiments on ZDDP Anti-Wear Films Through Pressure-Induced Cross-Linking. Tribology Letters. 2006;24:105-14.
[132] Schey JA. Tribology in Metalworking: Friction, Lubrication and Wear: American Society for Metals; 1983.
[133] Borom MP, Pask JA. Kinetics of Dissolution and Diffusion of the Oxides of Iron in Sodium Disilicate Glass. J Am Ceram Soc. 1968;51:490-8.
[134] Xiong Y, Zhu S, Wang F, Lee C. Effect of vitreous enamel coating on the oxidation behavior of Ti6Al4V and TiAl alloys at high temperatures. J Coat Technol Res. 2008;5:93-8.
[135] Rapp RA. Hot corrosion of materials: a fluxing mechanism? Corros Sci. 2002;44:209-21.
[136] Sun K-H, Silverman A. Lewis acid-base theory applied to glass. J Am Ceram Soc. 1945;28:8-11.
[137] Zou X, Gu S, Cheng H, Lu X, Zhou Z, Li C, et al. Facile Electrodeposition of Iron Films from $NaFeO_2$ and $Fe_2O_3$ in Alkaline Solutions. J Electrochem Soc. 2015;162:D49-D55.
[138] Toki R, Doi T, Otsuka N. Solubility measurements of $Fe_2O_3$ and $Cr_2O_3$ in fused $Na_2B_4O_7$-$B_2O_3$ in air at 1173K. Mater Trans. 2016;57:143-7.
[139] Soltanahmadi S, Morina A, Eijk MCPv, Nedelcu I, Neville A. Experimental observation of zinc dialkyl dithiophosphate (ZDDP)-induced iron sulphide formation. Applied Surface Science. 2017;414:41-51.
[140] Kuppinger CM, Shelby JE. Viscosity and Thermal Expansion of Mixed-Alkali Sodium-Potassium Borate Glasses. J Am Ceram Soc. 1985;68:463-7.
[141] Gaylord S, Tincher B, Petit L, Richardson K. Viscosity properties of sodium borophosphate glasses. Mater Res Bull. 2009;44:1031-5.
[142] Cui S, Wan S, Zhu Q, Tieu AK, Zhu H, Cowie BCC, et al. Tribochemical Behavior of Phosphate Compounds at an Elevated-Temperature. J Phys Chem C. 2016;120:25742-51.
[143] Le HM, Tieu AK, Zhu H, Ta DT, Yu H, Ta TTH, et al. Depolymerization of sodium polyphosphates on an iron oxide surface at high temperature. Phys Chem Chem Phys. 2018;20:7819-35.
[144] Ta HTT, Tieu AK, Zhu H, Yu H, Ta TD, Wan S, et al. Chemical Origin of Sodium Phosphate Interactions on Iron and Iron Oxide Surfaces by First Principle Calculations. J Phys Chem C. 2018;122:635-47.
[145] Sparado F, Rossi A, Laine E, Hartley J, Spencer ND. Mechanical and tribological properties of boron oxide and zince borate glasses. Phys Chem Glasses B. 2016;57:233-44.
[146] Balc S, Sezgi NA, Eren E. Boron Oxide Production Kinetics Using Boric Acid as Raw Material. Ind Eng Chem Res. 2012;51:11091-6.
[147] Iwadoh S, Mori T. Effect of Work Roll Materials and Progress of Manufacturing Technology on Cold Rolling and Future Developments in Japan. ISIJ Int. 1992;32:1131-40.
[148] Nilsson M, Olsson M. An investigation of worn work roll materials used in the finishing stands of the hot strip mill for steel rolling. Proc Inst Mech Eng J Eng Tribol. 2013;227:838-44.
[149] Belzunce FJ, Ziadi A, Rodriguez C. Structural integrity of hot strip mill rolling rolls. Eng Fail Ana. 2004;11:789-97.

[150] Kim H-H, Lim J-W, Lee J-J. Oxidation Behavior of High-Speed Steels in Dry and Wet Atmospheres. ISIJ International. 2003;43:1983-8.
[151] Vitry V, Nardone S, Breyer J-P, Sinnaeve M, Delaunois F. Microstructure of two centrifugal cast high speed steels for hot strip mills applications. Mater Des. 2012;34:372-8.
[152] Pellizzari M, Cescato D, Flora MGD. Hot friction and wear behaviour of high speed steel and high chromium iron for rolls. Wear. 2009;267:467-75.
[153] Kim KH, Akase Z, Suzuki T, Shindo D. Charging Effects on SEM/SIM Contrast of Metal/Insulator System in Various Metallic Coating Conditions. Mater Trans. 2010;51:1080-3.
[154] Tran BH, Tieu AK, Wan S, Zhu H, Mitchell DRG, Nancarrow MJ. Multifuntional Bi-Layered Tribofilm Generated on Steel Contact Interfaces under High-Temperature Melt Lubrication. J Phys Chem C. 2017;121:25092-103.
[155] Erdemir A. A Crystal-Chemical Approach to Lubrication by Solid Oxides. Tribology Letters. 2000;8:97-102.
[156] Qu J, Blau PJ, Howe JY, Meyer HM. Oxygen diffusion enables anti-wear boundar film formation on titanium surfaces in zinc-dialkyl-dithiophosphate (ZDDP)-containing lubricants. Scripta Materialia. 2009;60:886-9.
[157] Wu X, Sacher E, Meunier M. The effects of hydrogen bonds on the adhesion of inorganic oxide particles on hydrophilic silicon surfaces. J Appl Phys. 1999;86:1744-8.
[158] Drelich J, Chibowski E, Meng DD, Terpilowski K. Hydrophilic and superhydrophilic surfaces and materials. Soft Matter. 2011;7:9804-28.
[159] Klein J. Hydration lubrication. Friction. 2013;1:1-23.
[160] Raviv U, Giasson S, Kampf N, Gohy J-F, Jerome R, Klein J. Lubrication by charged polymers. Nature. 2003;425:163-5.
[161] Ma L, A.G-Kipnis, Kamps N, Klein J. Origins of hydration lubrication. Nat Commun. 2015;6:1-6.
[162] Valiev RZ, Korznikov AV, Mulyukov RR. Structure and Properties of Ultrafine-Grained Materials Produced by Severe Plastic Deformation. Mater Sci Eng, A. 1993;A168:141-8.
[163] Juricic C, Pinto H, Cardinali D, Klaus M, Genzel C, Pyzalla AR. Evolution of Microstructure and Internal Stresses in Multi-Phases Oxide Scales Grown on (110) Surfaces of Iron Single Crystals at 650ºC. Oxid Met. 2010;73:115-38.
[164] Sun W, Tieu AK, Jiang Z, Zhu H, Lu C. Oxide scales growth of low-carbon steel at high temperatures. J Mater Process Technol. 2004;155-156:1300-6.
[165] Cheng X, Jiang Z, wei D, Wu H, Jiang L. Adhesion. friction and wear analysis of a chromium oxide scale on a ferritic stainless steel. Wear. 2019;429-427:1212-21.
[166] Jianian S, Longjiang Z, Tiefan L. High-temperature oxidation of Fe-Cr alloys in wet oxygen. Oxidation of Metals. 1997;48:347-56.
[167] Li MS, Hou PY. Improved Cr2O3 adhesion by Ce ion implantation in the presence of interfacial sulfur segregation. Acta Materialia. 2007;55:443-53.
[168] Martin JM, Onodera T, Bouchet M-IDB, Hatakeyama N, Miyamoto A. Anti-wear Chemistry of ZDDP and Calcium Borate Nano-additive. Coupling Experiments, Chemical Hardness Predictions, and MD Calculations. Tribol Lett. 2013;50:95-104.
[169] Jin W, Choi J-Y, Lee W-Y. Nucleation and Growth Process of Sticking Particles in Ferritic Stainless Steel. ISIJ International. 2000;40:789-93.
[170] Cheng X, Jiang Z, Kosasih B, Wu H, Luo S, Jiang L. Influence of Cr-Rich Oxide Scale on Sliding Wear Mechanism of Ferritic Stainless Steel at High Temperature. Tribol Lett. 2016;63:28.
[171] Hao L, Wu H, Wei D, Cheng X, Zhao J, Luo S, et al. Wear and friction behavior of high-speed steel and indefinite chill material for rolling ferritic stainless steels. Wear. 2017;376-377:1580-5.

[172] Son G-Y, Kim CK, Ha DJ, Lee S, Lee JS, Kim KT, et al. Mechanism of Sticking Phenomenon Occurring during Hot Rolling of Two Ferritic Stainless Steels. Metallurgical and Materials Transactions A. 2007;38A:2776-87.
[173] Spuzic S, Strafford KN, Subramanian C, Savage G. Wear of hot rolling mill rols: an overview. Wear. 1994;176:261-71.
[174] Spuzic S, Strafford KN, Subramanian C, Savage G. Wear of hot rolling mill rolls: an overview. Wear. 1994;1994:261-71.
[175] Mitchell DRG. Circular Hough transformation diffraction analysis: A software tool for automated measurement of selected area electron diffraction patterns within Digital Micrograph™. Ultramicroscopy. 2008;108:367-74.
[176] Mitchell DRG. DiffTools: Electron Diffration Software Tools for DigitalMicrograph™. Microsc Res Tech. 2008;71:588-93.
[177] Zhu Q, Zhu HT, Tieu AK, Kong C. Three dimensional microstructure study of oxide scale formed on a high-speed steel by means of SEM, FIB and TEM. Corros Sci. 2011;53:3603-11.
[178] Zhu Q, Zhu HT, Tieu AK, Reid M, Zhang LC. In-situ investigation of oxidation behaviour in high-speed steel roll material under dry and humid atmospheres. Corros Sci. 2010;52:2707-15.
[179] Pearson SR, Shipway PH, Abere JO, Hewitt RAA. The effect of temperature on wear and friction of a high strength steel in fretting. Wear. 2013;303:622-31.
[180] Higginson RL, Jepson MAE, West GD. Use of EBSD to characterise high temperature oxides formed on low alloy and stainless steels. Mater Sci Technol. 2006;22:11:1325-32.
[181] Ha DJ, Lee JS, Kim NJ, Lee S. Effects of Alloying Elements on High-Temperature Oxidation and Sticking Occurring During Hot Rolling of Modified Ferritic STS430J1L Stainless Steel. Metall Mater Trans A. 2012;43A:74-86.
[182] Segerdahl K, Svensson J-E, Johansson L-G. The high temperature oxidation of 11% chromium steel: Pat I - Influence of $pH_2O$. Mater Corros. 2002;53:247-55.
[183] Zou D, Zhou Y, Zhang W, Han Y. High temperature oxidation behavior of a high Al-containing ferritic heat-resistant stainless steel. Mater Charact. 2018;136:435-43.
[184] Trindade V, Christ H-J, Krupp U. Grain-Size Effects on the High-Temperature Oxidation Behaviour of Chromium Steels. Oxid Met. 2010;73:551-63.
[185] Bach H, Baucke FKG, Krause D. Electrochemistry of Glasses and Glass Melts, Including Glass Electrodes: Springer-Verlag Berlin Heidelberg; 2001.
[186] Pellizzari M, Molinari A, Straffelini G. Tribological behavior of hot rolling rolls. Wear. 2005;259:1281-9.
[187] Ma L, He CG, Zhao XJ, Guo J, Zhu Y, Wang WJ, et al. Study on wear and rolling contact fatigue behaviors of wheel/rail materials under different slip ratio conditions. Wear. 2016;366-367:13-26.
[188] Azushima A, Nakata Y, Toriumi T. Prediction of effect of rolling speed on coefficient of friction in hot sheet rolling of steel using sliding rolling tribo-simulator. J Mater Process Technol. 2010;210:110-5.
[189] Cross R. Effect of surface roughness on rolling friction. European Journal of Physics. 2015;36:065029.
[190] Tieu AK, Zhu Q, Zhu H, Lu C. An investigation into the tribological behaviour of a work roll material at high temperature. Wear. 2011;273:43-8.
[191] Jatuphaksamphan Y, Phinichka N, Prapakorn K, Supradist M. Pickling kinetics of tertiary oxide scale formed on hot-rolled steel strip. Journal of Metals, Materials and Minerals. 2010;20:33-9.
[192] Yamaguchi S, Yoshida T, Saito T. Improvement in Descaling of Hot Strip by Hydrochloric Acid. ISIJ International. 1994;34:670-8.

[193] Job CB. Growth and Characterization of Sodium Penta Borate Crystal. International Journal of ChemTech Research. 2015;8:898-904.

# Appendices

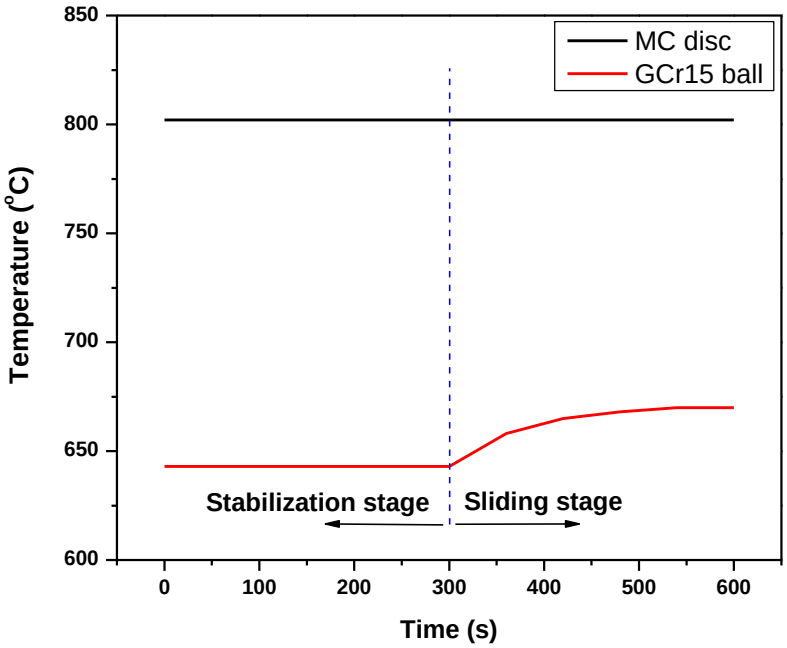


**Figure A- 1:** Temperature evolution of steel counterparts during stabilization stage and sliding stage.

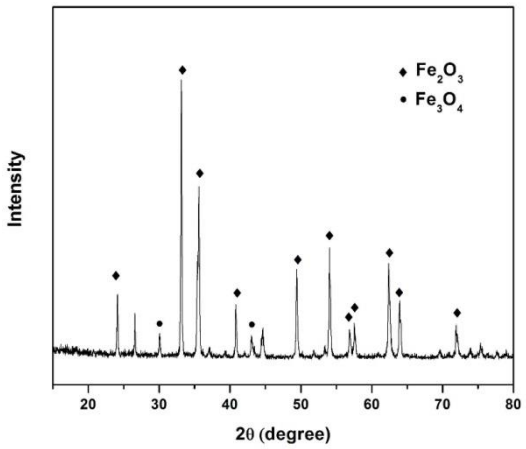


**Figure A- 2:** XRD pattern of wear debris collected from dry sliding test (at 800°C, 10N, 0.1m/s).

.

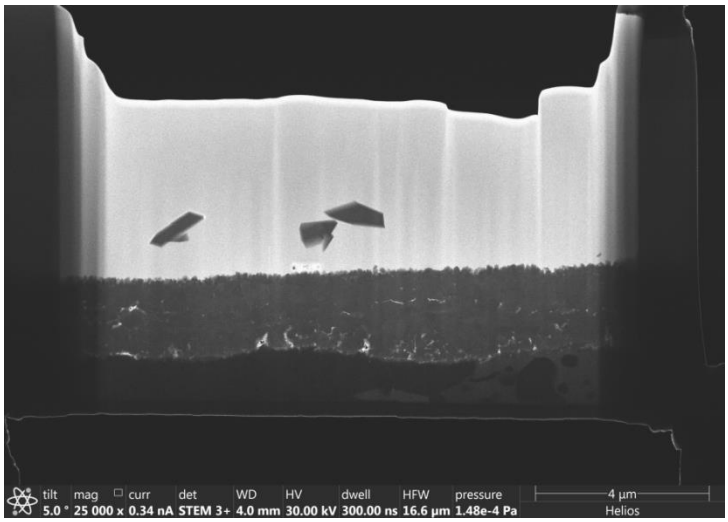


**Figure A- 3:** SEM image of thin lamellar extracted from the ball scar after lubrication test

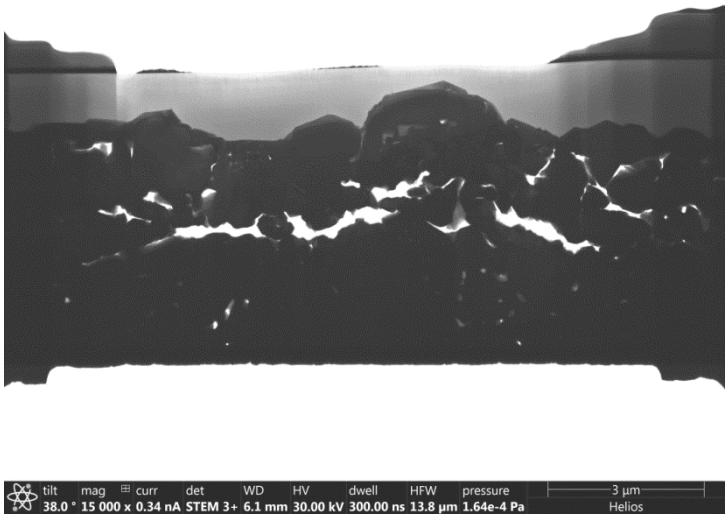


**Figure A- 4:** SEM image of thin lamellar extracted from the wear track after lubrication test.

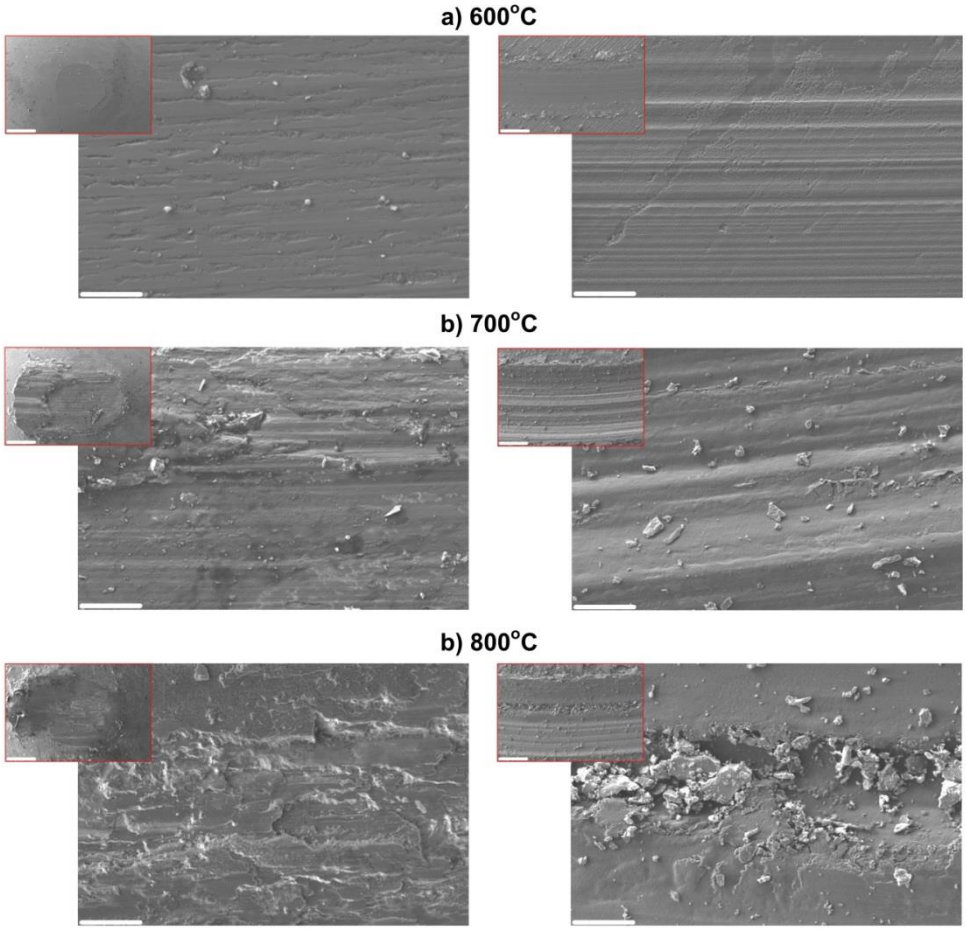


**Figure A- 5:** SEM micrographs of the worn surfaces after dry sliding test at (a) 600ºC, (b) 700ºC and (c) 800ºC (ball scars are on the left, wear tracks are on the right, the scale bar is of 500 µm and 20µm) (30N, 0.1m/s)

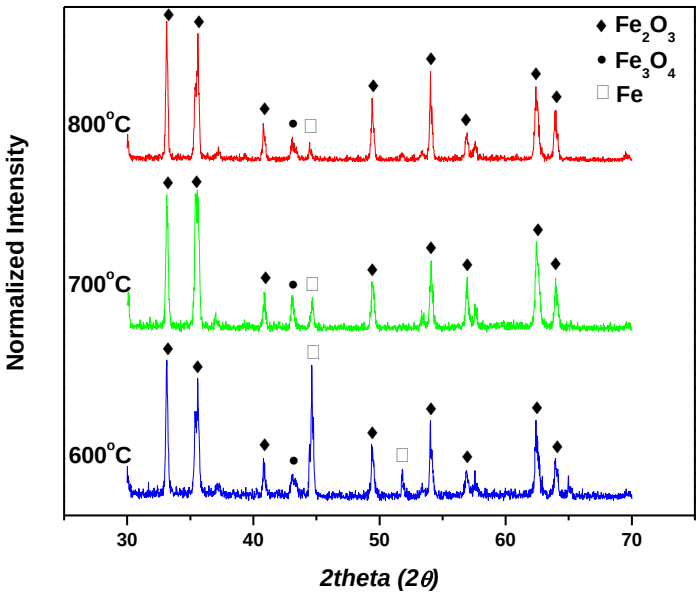


**Figure A- 6:** X-ray powder diffraction of wear debris collected from dry sliding test at different temperatures.

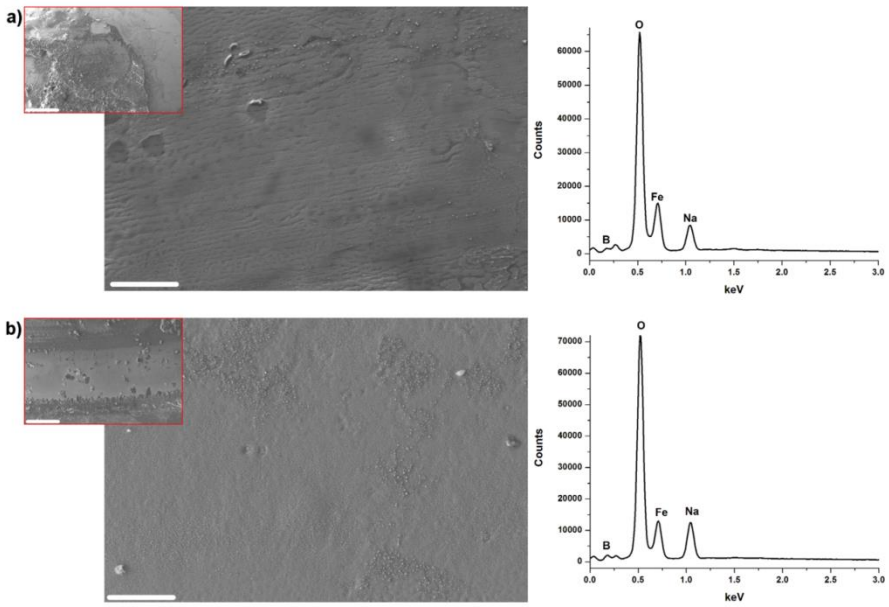


**Figure A- 7:** Worn morphologies and corresponding X-ray spectrum of lubricated tribopairs at 600°C: a) ball, b) disc (scale bar is of 500 µm and 20µm) (30N, 0.1m/s)

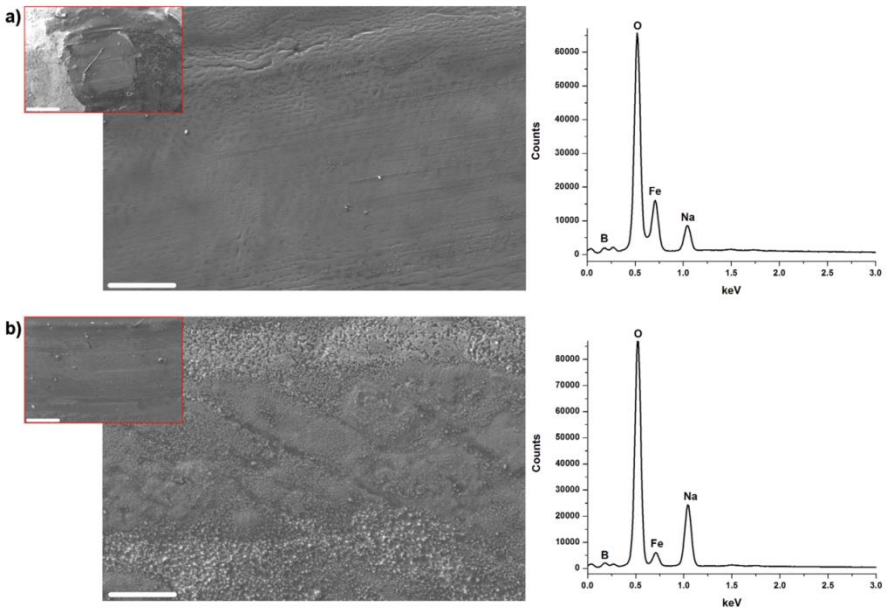


**Figure A- 8:** Worn morphologies and corresponding X-ray spectrum of lubricated tribopairs at 700$^{o}$C: a) ball, b) disc (scale bar is of 500 µm and 20µm) (30N, 0.1m/s)

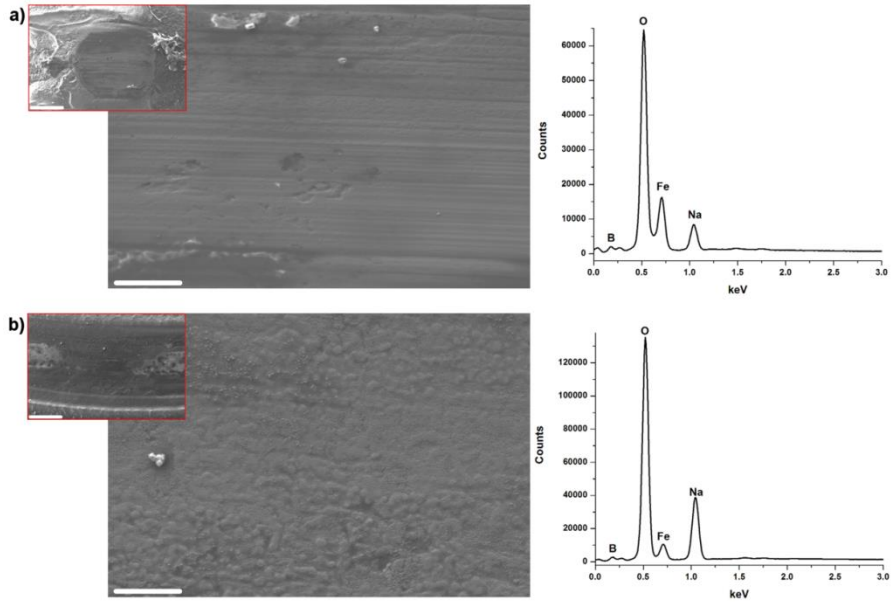


**Figure A- 9:** Worn morphologies and corresponding X-ray spectrum of lubricated tribopairs at 800$^{o}$C: a) ball, b) disc (scale bar is of 500 µm and 20µm) (30N, 0.1m/s)

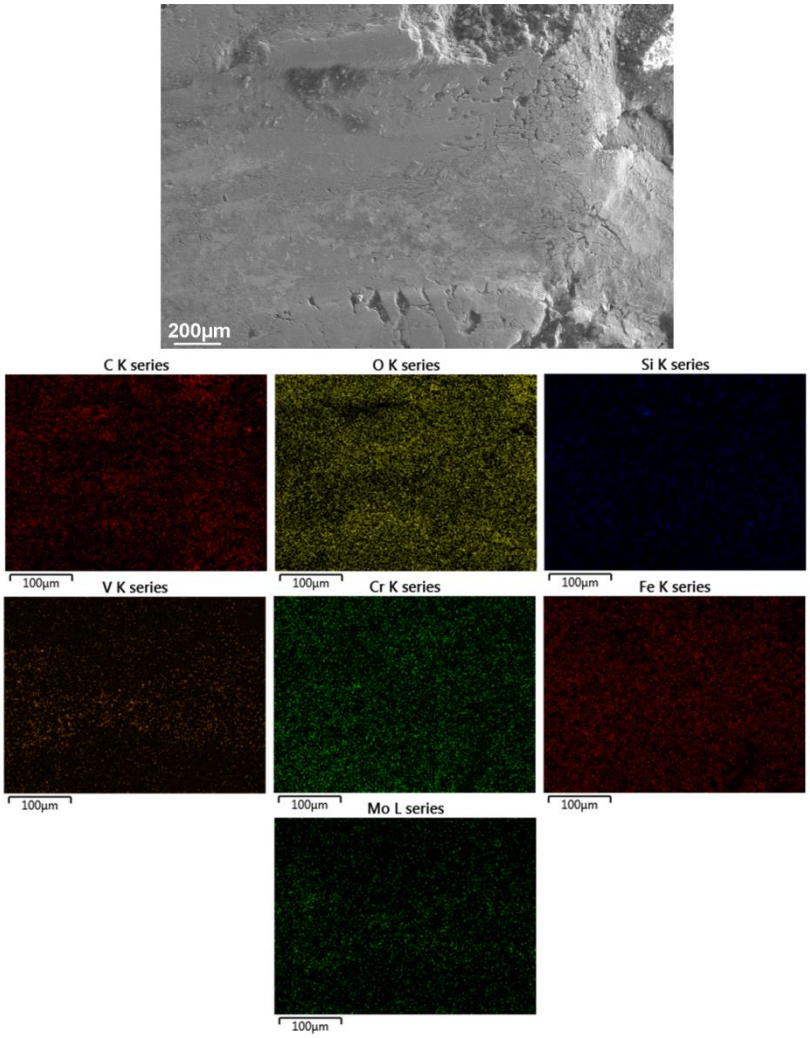


**Figure A- 10:** SEM image the EDS mapping of HSS pin lubricated by $B_2O_3$ at 10N

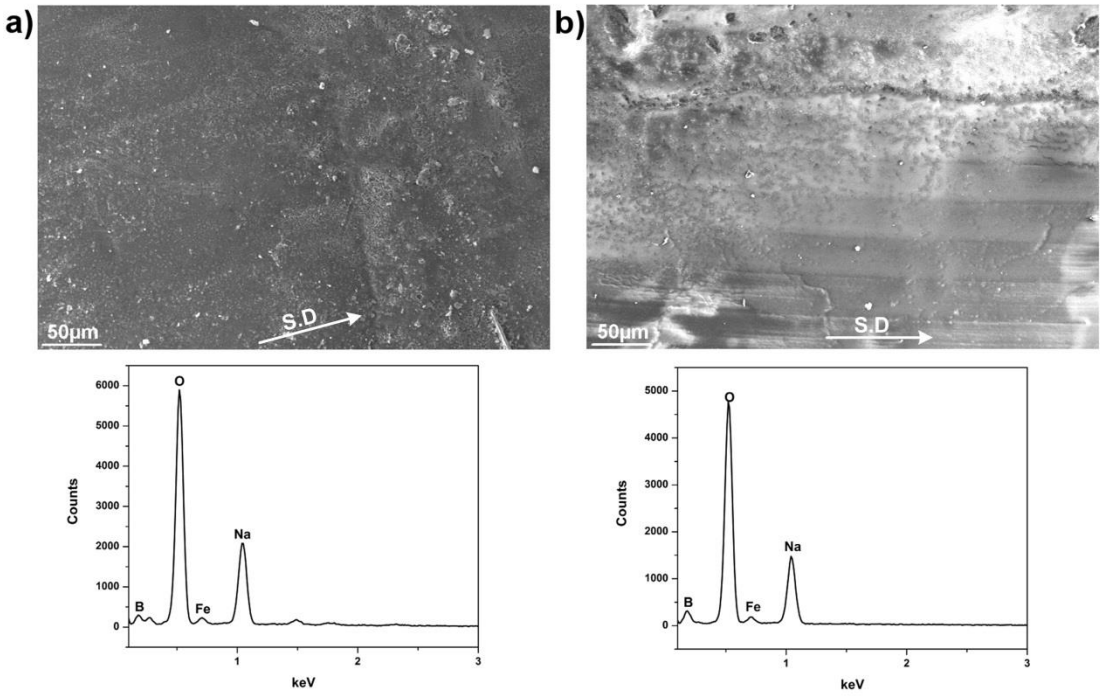


**Figure A- 11:** Worn surface morphologies and corresponding EDS spectrum of tribopair lubricated by $Na_2O$-$B_2O_3$ at 20N a) pin, b) disc

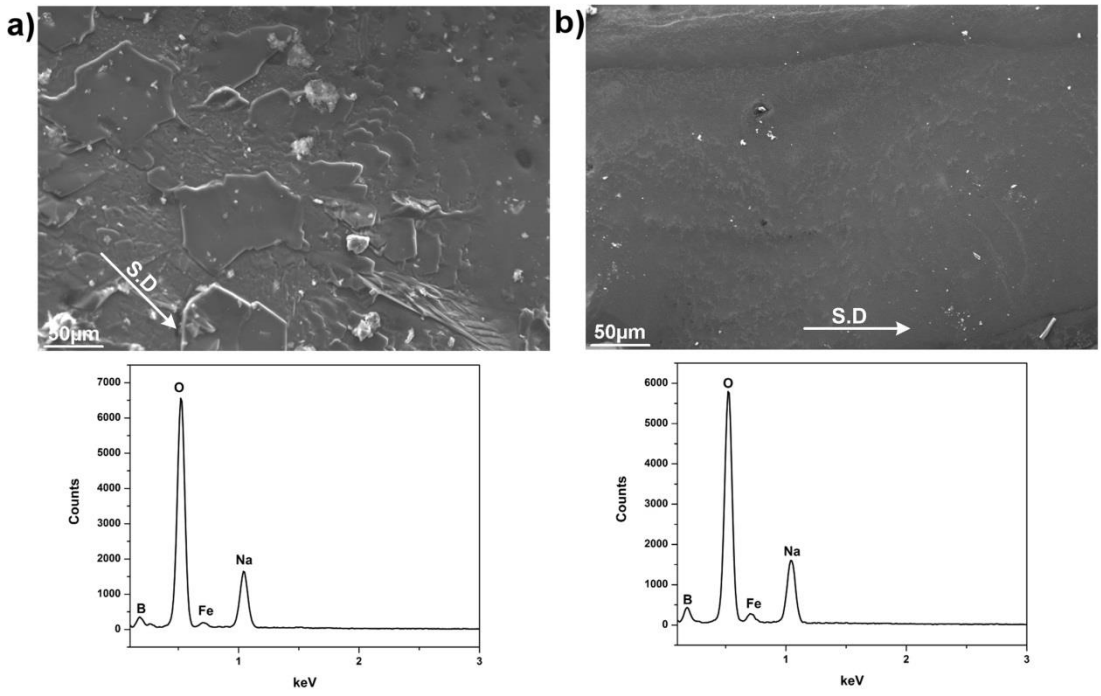


**Figure A- 12:** Worn surface morphologies and corresponding EDS spectrum of tribopair lubricated by $Na_2O$-$B_2O_3$ at 30N a) pin, b) disc

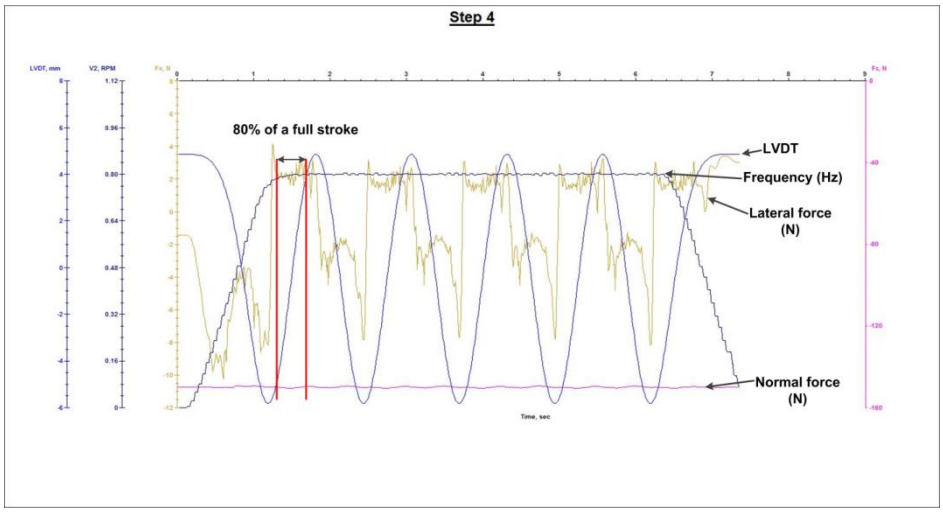


**Figure A- 13:** A typical data window from reciprocating test

Only 80% in the middle of each stroke was taken into calculating the average rolling friction. Lateral force tends to rise at the end of a stroke which increases the uncertainty of data acquisition. Also, the first and last strokes were also excluded due to the frequency change.

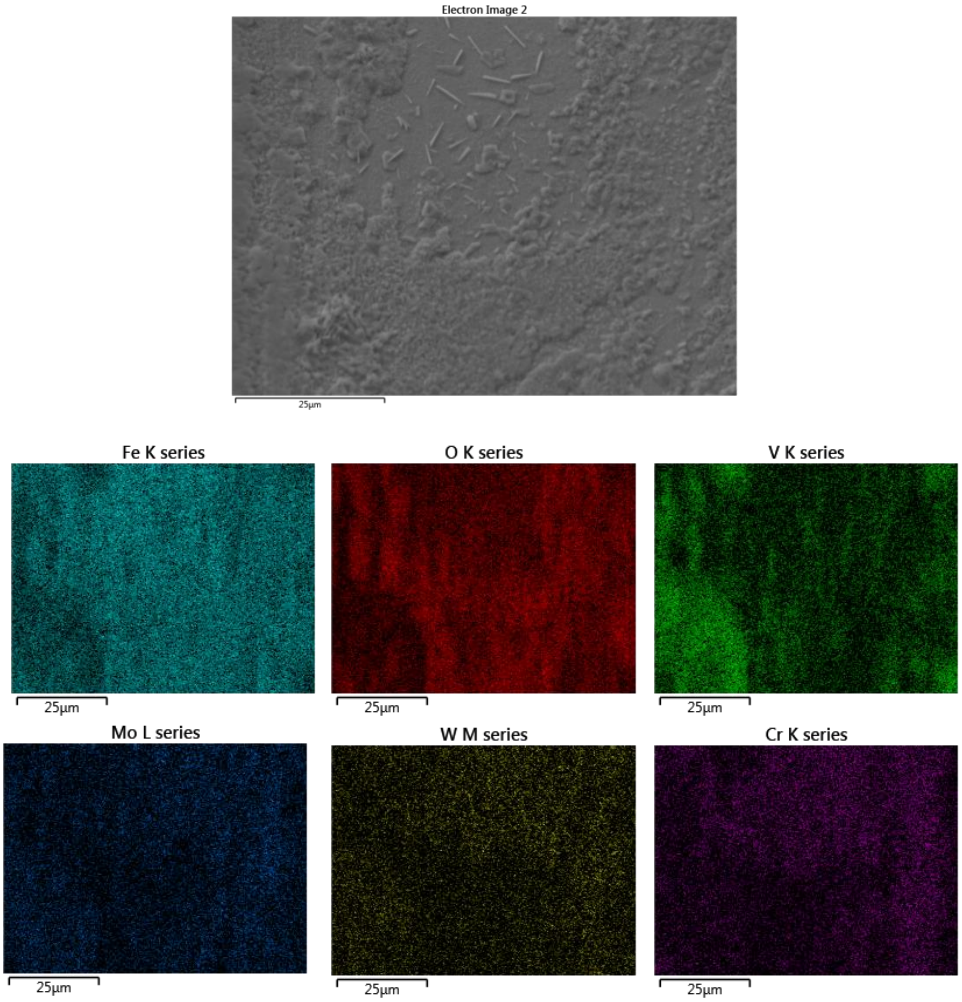


**Figure A- 14:** SEM micrographs of HSS surface being oxidized at 650$^{o}$C for 0.5hr and the corresponding elemental mapping

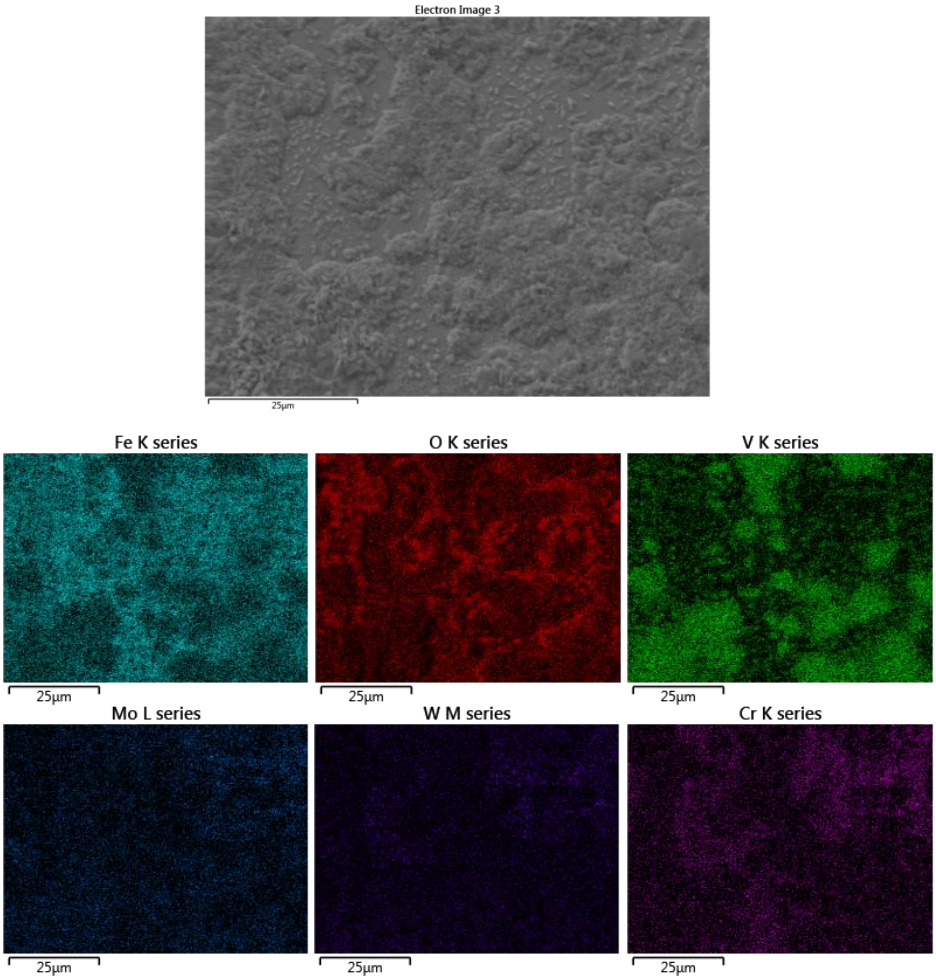


**Figure A- 15:** SEM micrographs of HSS surface being oxidized at 650$^{o}$C for 1hr and the corresponding elemental mapping

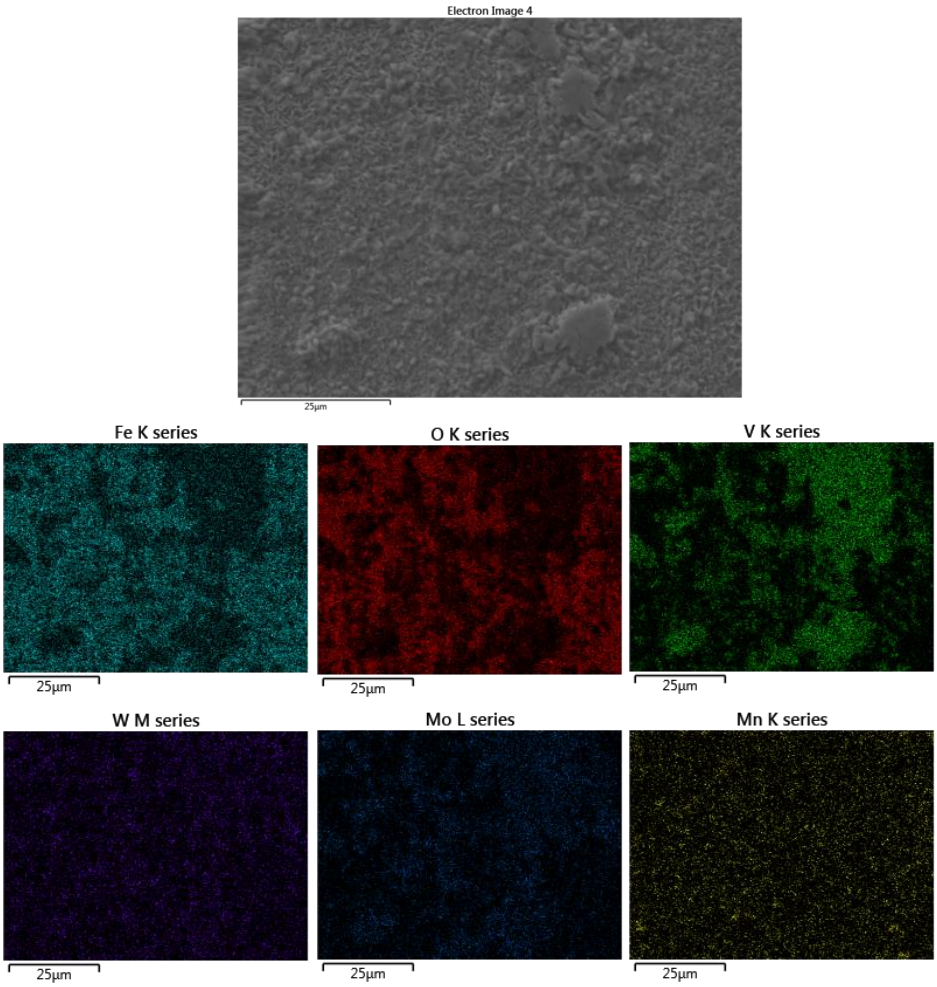


**Figure A- 16:** SEM micrographs of HSS surface being oxidized at 650°C for 2hr and the corresponding elemental mapping

| | | Temperature (°C) | | | | | |
|---|---|---|---|---|---|---|---|
| | | 600 | | 700 | | 800 | |
| | | Ball | Disc | Ball | Disc | Ball | Disc |
| Load (N) | 10 | 0.002093 | 0.00035 | 0.006067 | 0.000413 | 0.008533 | 0.00046333 |
| | 20 | 0.001218 | 0.000188 | 0.00345 | 0.00022 | 0.0058 | 0.00023667 |
| | 30 | 0.00091 | 0.000136 | 0.002611 | 0.000161 | 0.004822 | 0.00018111 |

**Table A- 1:** Specific wear rates of steel tribopair under borate lubrication in Chapter 4 (the unit is $10^{-2}$.$mm^3$/(N.m) and $mm^3$/(N.m) for GCr15 ball and mild steel disc, respectively)

| | 600°C | | 700°C | | 800°C | |
|---|---|---|---|---|---|---|
| | Ball | Disc | Ball | Disc | Ball | Disc |
| Lubricated | 0.0091 | 0.001356 | 0.026111 | 0.001611 | 0.048222 | 0.00181111 |
| Unlubricated | 0.0106 | 0.027778 | 0.053778 | 0.110722 | 0.077222 | 0.06171111 |

**Table A- 2:** Specific wear rate of steel tribopairs under unlubricated and lubricated conditions in Chapter 4 (the unit is $10^{-2}$.$mm^3$/(N.m) and $mm^3$/(N.m) for GCr15 ball and mild steel disc, respectively)

| | 10N | 20N | 30N | 40N |
|---|---|---|---|---|
| Borax lubrication | 0.00021 | 0.000117 | 0.000111 | 0.00025 |
| $B_2O_3$ lubrication | 0.001133 | | | |

**Table A- 3:** Specific wear rate of SS316 disc lubricated by sodium borate and $B_2O_3$ at 800°C in Chapter 6 (the unit is $mm^3$/(N.m))

| | 850°C | 900°C |
|---|---|---|
| Unlubricated | 0.007444 | 0.0055 |
| Lubricated by NaB | 0.0013 | 0.003889 |
| Lubricated by KB | 0.001267 | 0.002516 |

**Table A- 4:** Specific wear rate of SS316 under different lubrication conditions in Chapter 9 (the unit is $mm^3$/(N.m))